UNIVERSITY OF LIVERPOOL

Department of Engineering

PhD Thesis

Selective ablation of thin films with ultra short pulses

Thesis submitted in accrodance with the requirements of the University of Liverpool for the degree of Doctor in Philosophy

Paul Fitzsimons

October 2012

Laser Group
Department of Engineering
University of Liverpool
Brownlow Hill
L69 3GH
UK

Declaration

I declare that of all the work contained herein are the results of my investigations and collaborations with partner organisations.

Signed:

Paul Fitzsimons

Date:

Abstract

The micro processing of materials using ultra short pulse (USP) lasers with durations in the low picosecond (ps) and femtosecond (fs) range allows for the possibility of precision material removal on both nanometre and micron scales. Precision material removal can be achieved due to the near diffraction limited focus spot size and ultra-short pulse durations, which provide extremely high peak intensities with minimal thermal impact on the surrounding area.

The work presented in this thesis is primarily concerned with the selective ablation of thin films deposited on various surfaces, using lasers with picosecond temporal pulse lengths at 1064 nm. As a result, damage to the substrate is negated through exploitation of the difference in linear absorption coefficients between the thin film and substrate.

To elucidate the mechanism of selective processing with USP lasers; absorption, single and multi-pulse ablation effects were investigated in both fixed and variable beam positions. A sample of white float glass vacuum coated with indium tin oxide (ITO) was chosen as the material for this study. Experimental results demonstrate that linear absorption (α (λ)) of the ITO and substrate plays a key role in achieving selective thin film ablation. As a direct consequence of the difference in absorption coefficients at 1064 nm, the single (ϕ_{th}^{1}) and multi (ϕ_{th}^{n}) pulse ablation thresholds of both materials are altered during the high peak intensity exposure. Selective processing was achieved by exploiting the difference between the ablation thresholds of ITO and glass. When irradiated with multiple pulses the ablation threshold of the substrate was observed to decrease with increasing pulse number. This change in threshold fundamentally limits the selective processing window; therefore incubation (S) effects must be considered when determining the viability of selective processing. For the purpose of practical applications, a series of case studies are also presented which attempt to utilise selective materials processing. These investigations were split into industrial and conservation. Industrial case studies focused on successfully micro processing a small thin film ITO circuit using a Spatial Light Modulator and a new low cost solar cell (F doped SnO_2); whilst in conservation, the restoration of a pair of Royal gloves and the removal of unwanted bronze gilding is presented. The application of USP lasers in conservation represents a relatively new field of study where little previous research has been carried out. These case studies not only showcase the wide range of USP applications in which selective processing can be applied but also highlight the limitations of this method.

Acknowledgements

Firstly, I would like to thank my supervisors Professor Ken Watkins and Dr Geoff Dearden for their help and support throughout my PhD. In addition, special thanks go to Dr Walter Perrie for providing his guidance and support during my research and in the preparation of this document.

I would also like to thank the other members of the laser group Olivier Allegre, Stuart Edwardson, Eammon Fearon, Doug Eckford, Leigh Mellor, Joe Croft, Shuo "Spencer" Shang, Zheng Kuang, Dan Welburn, Dun Liu and Jian Cheng for the fun, football and occasional drinks. Thanks also to Andy Snaylam and Dave Atkinson for help with every crazy idea or question I had. Special thanks go to Denise Bain for all her help, advice and generally taking care of me for the last four years.

I would like to thank Juan Jacobo Angulo, Nick Underwood, David Vallespin, Elizabeth Christie, Marina Carrion, Savio Varghese, Cathy Johnson, Samuel Bautista Lazo, Giorgio Zografakis, Simao Marques, Marco Prandina and Yazdi Harmin for their friendship, the brilliant nights out and the random conversations at lunch.

I would like to reserve a special mention for Jonathan Griffiths who I have undertaken all my studies with during my time at Liverpool University; I count myself lucky to have had such a great colleague and gained an even better friend.

To Laura Clews there is no way for me to express how grateful and lucky I am to have had your love and support during the last four years; without you I would not be writing these acknowledgements. I love you.

Finally, I would like to thank my family and friends for their support. I would especially like to thank my Mum (Juanita Fitzsimons), Dad (Francis Fitzsimons), Aunty Margaret and my beautiful little sister Gia. This work is as much yours as it is mine.

Table of contents

List of Figures

List of Tables

List of Symbols

Symbol	Description	Units
$\Delta\omega_{H,D}$	Linewidth of laser transitions	nm
Φ_{th}	Ablation threshold	Jcm^{-2}
$\Phi_{th}(1)$	Single pulse ablation threshold	Jcm^{-2}
$\Phi_{th}(N)$	Ablation threshold for N pulses	Jcm^{-2}
C_e	Electron heat capacity	
$D_{\min}$	Minimum beam diameter	m
D_{in}	Input beam diameter	m
Φ	Average Fluence	Jcm^{-2}
Φ_P	Peak Fluence	Jcm^{-2}
F_i	Force on an atom	N
I	Average Intensity	Wcm^{-2}
I_P	Peak Intensity	Wcm^{-2}
I_0	Initial intensity	Wcm^{-2}
K_e	Electron thermal conductivity	
M^2	Beam quality factor	-
T_d	Pulse width	s
T_e	Electron temperature	K
T_l	Lattice temperature	K
V_i^T	Thermal velocity of atom	
f_{lens}	Focal length	m
m_e	Mass of an electron	Kg
m_i	Mass of atom	Kg
r_i	Position of atom	
η_c	Critical plasma density	
θ_i	Angle of incident rays	Degrees
ω_0	Focussed beam diameter	µm
ω_L	Laser frequency	$Rads^{-1}$
ϵ_0	Permittivity of free space	Fm^{-1}
D	Absorption depth	m
D	Diameter	m
E	Charge on an electron	C
I	Atom	-
K	Extinction coefficient	-
N	Refractive index	-
N	Number of pulses	-
R	Reflectivity (metals)	-
R_P	Reflectivity p polarisation	-
R_s	Reflectivity s polarisation	-
T	Time	S
Z	Distance from first boundary	m
Ξ	TTM+MD simulation coefficient	
Φ	Fluence	Jcm^{-2}
S	Absorbed laser energy	Jcm^{-3}
g	Electron – phonon coupling constant	-
α	Absorption coefficient (Linear)	cm^{-1}
ζ	Incubation effect	-
λ	Wavelength	nm

1 Introduction

1.1 Motivation and problem analysis

Thin film is a term applied to layers of materials which range from nanometres up to a millimetre in thickness, with such a broad definition this means that the composition and properties of these materials are wide ranging; for example thin films have been widely adopted in microelectronics (e.g. flat screen displays) and optical coatings, such as high k dielectrics for anti-reflection lens coatings. In contrast, thin films observed in conservation can damage or ultimately destroy items which can be of high value but more importantly are irreplaceable.

The uses of thin films in microelectronics are widespread and they are a key component in many electronic devices, such as high-density circuit boards, touch screen panels, photovoltaic cells and strain gauges.

The main manufacturing steps in micro fabrication are high temperature substrate modification, thin film deposition, patterning and bonding; within these four basic operations there can be several further fabrication steps. Currently, manufacturing methods for these devices are time consuming and expensive.

The market for electronic products continues to grow; therefore to successfully compete manufacturers need to provide the latest technology at the lowest possible cost to the consumer. One method of achieving this is through improvement of current manufacturing methods; this offers several advantages including: a reduction in cost, increased process efficiency, improved throughput, less waste and potential new functionality.

To date, the application of lasers in thin film removal has mostly been undertaken using short pulse (≥ns) or continuous wave lasers. The main drawback of using these systems has been high thermal input at the surface and shockwaves generated on or near the surface resulting in thin film removal but also substrate damage.

Thin films do not always provide beneficial properties; in some instances the film causes deterioration of the substrate. This detrimental effect is most easily observed in conservation. Over time films form on the surface of art and heritage objects with the composition and thickness of the film being dependent upon the environment in which the piece is displayed. A good example is the many statues located in urban areas, the contaminants on which consist mostly of carbon and sulphur deposits [1] produced by motorised transport; figure 1 highlights the beneficial effect of laser treatment. Before processing the surface of the statue was covered in surface deposits (left) and after irradiation with a pulsed ns laser (right) all of the contaminant was removed. The effects of

these films can vary from reduced aesthetics to partial corrosion and ultimately destruction of the object; therefore removal of these films is of significance in preserving art and heritage pieces.

Traditional restoration techniques involve the use of either physical abrasives or chemical breakdown of the layer; these methods of removal are time consuming, can be difficult to implement and are not always effective. The application of lasers to conservation began in the late 70s and has since become a key tool for conservators; resulting in the publishing of several books on the subject [1, 2] and establishing the LACONA conference dedicated to the application of lasers in restoration.

Figure 1: Laser cleaning of the statue of Linnaeus, the statue is displayed at the Palm House, Sefton Park, Liverpool. The image shows the statue before restoration (left) and after laser treatment (right). The contaminant layer consisted mainly of sulphur deposits [3].

In subtractive processes, selective processing describes the removal of individual layers from a multi-layer substrate as a consequence of the difference in absorption. Using long pulse (LP) or continuous wave (CW) lasers, selective material removal has been applied to both macro fabrication and laser conservation; for example the first restoration mechanism identified was named selective removal [4]. Through selective material removal laser processing of thin films becomes much easier and quicker as the user no longer has to consider substrate effects beyond knowing the damage threshold.

Ultra-short diode pumped solid state lasers emit pulses with durations of typically twenty picoseconds (ps) or less; the short pulse width combined with micron scale beam diameters produces pulses with very high output intensities ($I \geq 10^9$ Wcm^{-2}). When compared to more conventional systems such as pulsed (nanosecond) or continuous wave lasers ultra-short systems can provide significant advantages; especially in the ablation of thin films [5]. Thermal loading incurred as result of irradiation using ultra short pulses is negligible and in some cases can be neglected. As a result, less thermal damage will occur and the heat affected zone (HAZ) generally observed during laser processing will be minimised. Finally,

using an ultra-short laser source it is possible to ablate most materials, including diamond [6], which due to the high peak intensities can be mediated by both linear and non-linear absorption. All of these advantages can be attributed to ultra-short pulse (USP) laser systems.

Due to recent advances in ultra-short laser technology the commercial application of USP systems has increased. When combined with high accuracy CNC tables it is possible to fabricate extremely small and complex structures on thin films. Figure 2(a) and 2(b) show micro-components fabricated using ultra short pulse lasers. Both these figures highlight the ability of ultra-short pulses to generate clean, precise and complex structures. Similarly, in restoration this high precision can be utilised to only irradiate the necessary areas of an object, preventing unwanted exposure of other parts.

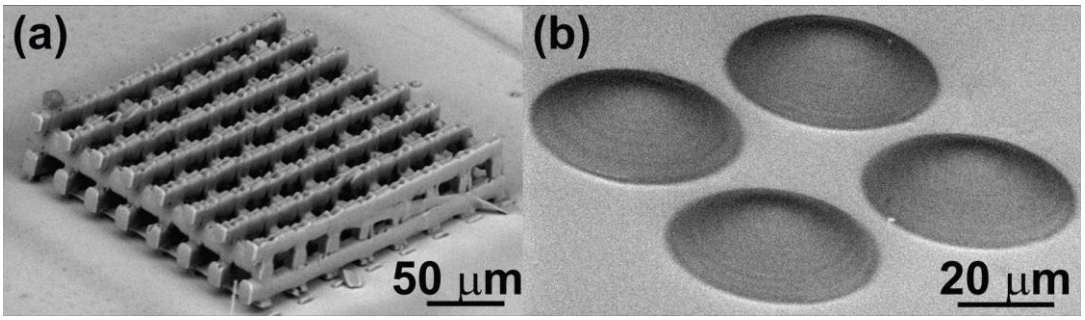

Figure 2: 3D structures fabricated using 8 ps pulses and at 532nm with irradiances of 0.7 $TWcm^{-2}$ (a) and 0.35 $TWcm^{-2}$ (b). (a) is a scaffold for cell cultures and (b) a micro lens array [7].

1.2 Primary objectives

The aim of this thesis is to highlight the capabilities of ultra-short picosecond pulse lasers as a disruptive technology for selective ablation of thin films; research was focused on the factors controlling selective removal, methods of manufacturing functional devices and the restoration of art and heritage items. The main objectives of this thesis are:

- To elucidate the factors controlling selective removal of thin films using ultra short pulses.
- To demonstrate the use of selective removal in micro-processing.
- To demonstrate the use of selective removal in laser conservation.
- Identify selective operating parameters on various thin films.

This was achieved through a series of planned experiments and process optimisation described in the subsequent chapters of this thesis.

1.3 Thesis Roadmap

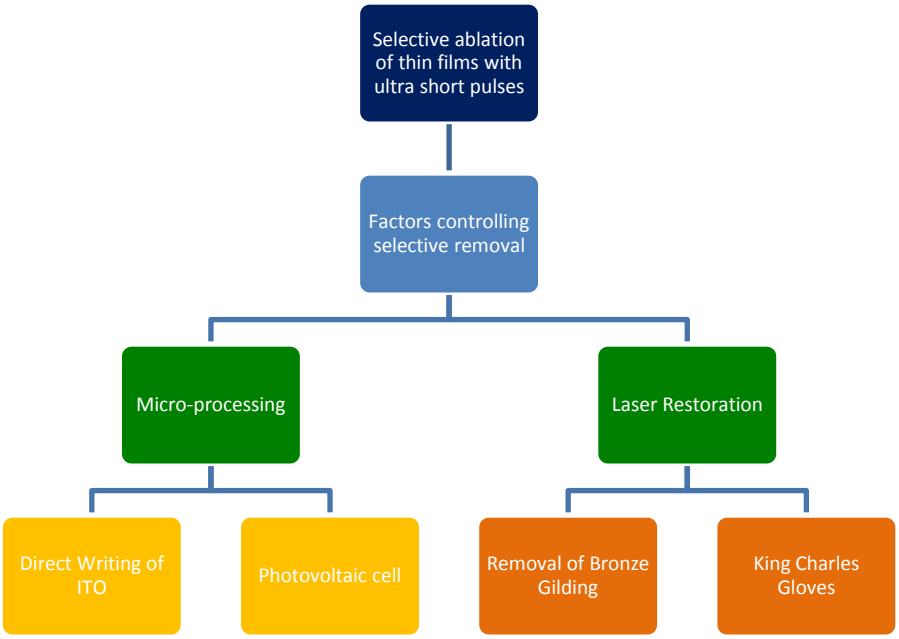

1.4 Thesis structure

This thesis is presented as follows:

Chapter 2 provides an introduction to relevant background information on selective processing, thin film micro-processing and laser conservation. A literature review of ultra-short pulse laser technology and its application in micro fabrication and restoration is included. Ultra-short pulse laser ablation mechanisms, related experiments and results are analysed.

Chapter 3 provides a description of the experimental equipment, setup and methodology used to implement and analyse the experiments described in this thesis. Details of the materials used in testing are also provided.

Chapter 4 presents the results obtained from an investigation into the factors governing selective processing. Using an ITO thin film adhered to a glass substrate the effects of absorption, ablation threshold; multi-pulse irradiation and beam shaping are investigated. The contribution of these factors to the selective removal process is discussed.

In **chapter 5** the selective removal processes identified previously are applied to a four case studies. These studies investigate the applicability of selective processing in fabricating a functional circuit, manufacturing a solar cell, restoration of a Royal heritage item

and the removal of unwanted bronze gilding. Through these case studies the usefulness of selective processing techniques, advantages and limitations are identified.

Chapter 6 concludes this thesis, providing a summary of its findings and achievements. Suggestions are provided for future research directions based on the work presented herein.

1.5 Summary

Currently, thin film devices are expensive to design and manufacture due to economies of scale, the availability of suitable materials and technological readiness. However, market demand for new products which utilise thin films is extremely strong (e.g. LCD TVs and mobile phones). As such new methods of manufacturing these devices that can reduce costs and improve throughput are highly sought after.

Similarly, in conservation practice ultra-short lasers have the potential to become an extremely useful tool; this is due to development of new more robust systems which can operated outside controlled laboratory conditions. The cost of these systems is reduced making these lasers more accessible to conservators. Current non-laser restoration techniques are labour intensive, require hazardous chemicals and are time consuming; whilst current laser techniques have been limited in scope due to the thermal input at the surface.

Presently, the use of selective removal using ultra-short pulse lasers has received little attention. However, by using this technique in conjunction with precise material removal associated with ultra-short pulse laser there are several potential benefits including: greater efficiency, lower costs and higher throughput whilst ensuring no substrate damage occurred.

This would improve the micro fabrication process and offer conservators a new tool for art and heritage restoration projects.

2 Literature review

This chapter presents some relevant background to lasers and ultra-short pulse (USP) laser processing. Reviews of laser technology, laser-material interaction mechanisms and the micro-processing techniques currently available in the literature are presented. In this thesis the author focuses on two specific areas: the micro-processing of thin films and restoration treatments. In addition, a state of the art review is conducted on the current applications of laser technology in both thin film processing and restoration.

2.1 Laser fundamentals

2.1.1 Origin

The physics underlying stimulated emission where first postulated by Einstein in 1917 [8] and confirmed experimentally by Ladenburg in 1928 [9]. However, it was not until May 1960 that the first laser was demonstrated by Theodore Maiman; this system used a Ruby crystal as the gain medium and can still be operated today, 50 years after it was first constructed [10,11].

Soon after, many different laser systems were invented. Javan *et al* [12], at Bell laboratories, developed the first gas laser from a mixture of helium and neon in 1961. Two years later, in 1963, Patel [13] also from Bell laboratories invented the CO_2 laser, which has become one of the most powerful and widely used industrial lasers. Today, CO_2 lasers are used in welding [14], cutting [15], forming [16,17], cladding [18] and repair [19].

The application of solid-state ultra-short pulse lasers in selective materials processing is the primary focus of this study; the development of these laser systems from their origin is subsequently discussed.

The Ruby laser developed by Maiman [3, 4] was the first solid-state system as well as the first working laser. Solid-state lasers (SSL) utilise a gain medium such as crystals (Ruby laser) or glasses doped with a rare earth or transition metal ions (for example Nd:YAG) [20]. A simplified energy level diagram of a Nd:YAG SSL is shown in figure 3. Initially, the gain medium is pumped using flash lamps or diodes, the latter being the most commonly used today, to excite electrons to a higher energy level (figure 3 (level 3)). The close proximity of several energy manifolds within this level allows for broad optical pumping in the range of 300 – 800 nm, these manifolds are also relatively closely spaced in relation to the maximum phonon energy (850 cm^{-1}). Consequently, through non-radiative transitions, excited ions cascade down until they reach the metastable level (figure 3 (level 2)). At this level the spacing between manifolds increases (separation of 4698 cm^{-1}, greater than 5 phonons) [21] and the rate of decay is slowed, leading to population inversion. As a result decay back to level 1 occurs almost exclusively via radiative decay, producing a 1064 nm laser output. The

separation between the levels of 0 (figure 3 (ground state)) and 1 are also closely spaced, resulting in a rapid relaxation to the ground state, with no output radiation.

Diode pumped solid-state lasers are often referred to as DPSS or all-solid-state lasers. DPSS systems are generally preferred to flash pumped systems (FPSS) as they have a longer operating life and a higher conversion efficiency, whilst consuming less power when compared to FPSS lasers.

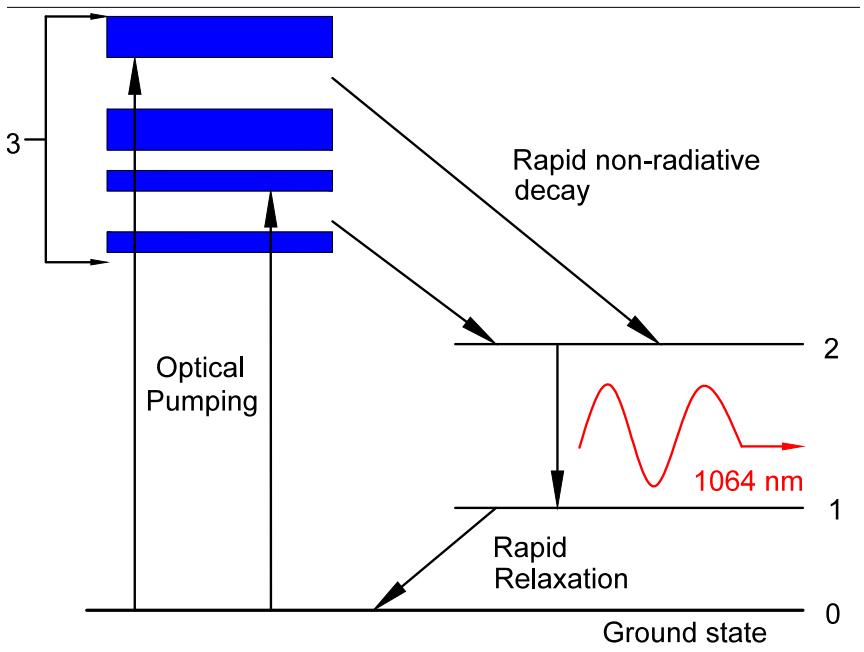

Figure 3: Simplified energy level diagram for obtaining stimulated emission from an Nd:YAG crystal. The radiative transition from level 2 to 1 produces light with a wavelength of 1064 nm.

Population inversion is key to producing a laser output and requires the majority of atoms in the lasing medium to be in the metastable level. Photons are emitted when electrons spontaneously decay (spontaneous emission) to a lower level (figure 3 (level 1)) before undergoing a further non-radiative decay back to the ground state.

If the photon released has an energy ($E_2 - E_1$) it can stimulate another atom in the metastable state to release a photon with the same phase, energy and momentum as the original; this process is called stimulated emission [1, 2, 7]. The vast majority of these stimulated photons are lost through collisions with the sides of the lasing medium. However, some photons will travel parallel to the optical axis of the cavity and are trapped by mirrors positioned at either end. One mirror is a totally reflecting surface whilst the other is partially reflecting; this allows a small proportion of the photons to pass through and out of the cavity. Photons that do not pass through are reversed back to continue the stimulated emission process. The lasing action continues as long as energy is supplied to the gain medium.

If the lasing medium is continuously pumped eventually equilibrium is established between the number of atoms at the metastable state and the number of emitted photons, resulting in a continuous emission.

2.2 Pulsed laser outputs

Through modulation of the lasing cavity output, it is possible to generate "flashes" of light; also known as an optical pulse. A pseudo method of producing a pulsed output can be achieved via beam blocking or using a spinning prism. Pulsed laser systems have been found to be able to generate light pulses with temporal pulse durations from micro- to femto-seconds and more recently pulse durations of attoseconds [22] with high spatial coherence; allowing for near diffraction limit focused beam diameters ($2\omega_0$ < 30 μm). The combination of these properties allows for extremely high peak powers from commercial laser systems (P ≥ GW) and ultra-high focussed intensities (I >> 10 $TWcm^{-2}$) even with modest pulse energies.

There are several different methods for generating laser pulses; the technique used varies depending on the pulse requirements. As this study utilises ultra-short pulse lasers the following section will focus on describing the techniques commonly used to generate these pulses.

2.2.1 Q-switching

Maiman's laser [3, 4] is an example of a pulsed laser. Further work by Collins *et al.* on Ruby lasers demonstrated pulses emitted on millisecond (ms) timescales [23]. This sparked further interest among researchers to produce more defined pulses. The first solution was proposed in 1961 by Hellwarth *et al.* [24] and was later confirmed experimentally by McClung *et al*. (1962) [25] with the production of low order nanosecond pulses (ns); this technique was referred to as Q-switching.

Q-switching is used to obtain high-energy short (>ns) but not ultra-short pulses. Pulse durations between one and several hundred nanoseconds can be generated with this method. Using a Q-switching laser it is possible to generate peak powers many times greater than the average powers produced by continuous wave (CW) lasers. These powers range from MW to GW. These lasers have proven to be particularly useful in several applications including laser cutting, welding and cleaning or as a pump source in other systems [26].

Q-switching generates pulses through modulation of intracavity losses. Initially, losses are kept high by using a device that prevents propagation of photons between mirrors in the cavity; resulting in a higher population of electrons at the metastable energy level. Then, cavity losses are reduced, rapidly, to very low levels, leading to a high rate of

stimulated emission. Once the gain in the cavity is saturated, the maximum pulse energy has been reached and is emitted as an output pulse. Figure 4 shows the temporal evolution of gain and losses in both active and passive Q-switched lasers.

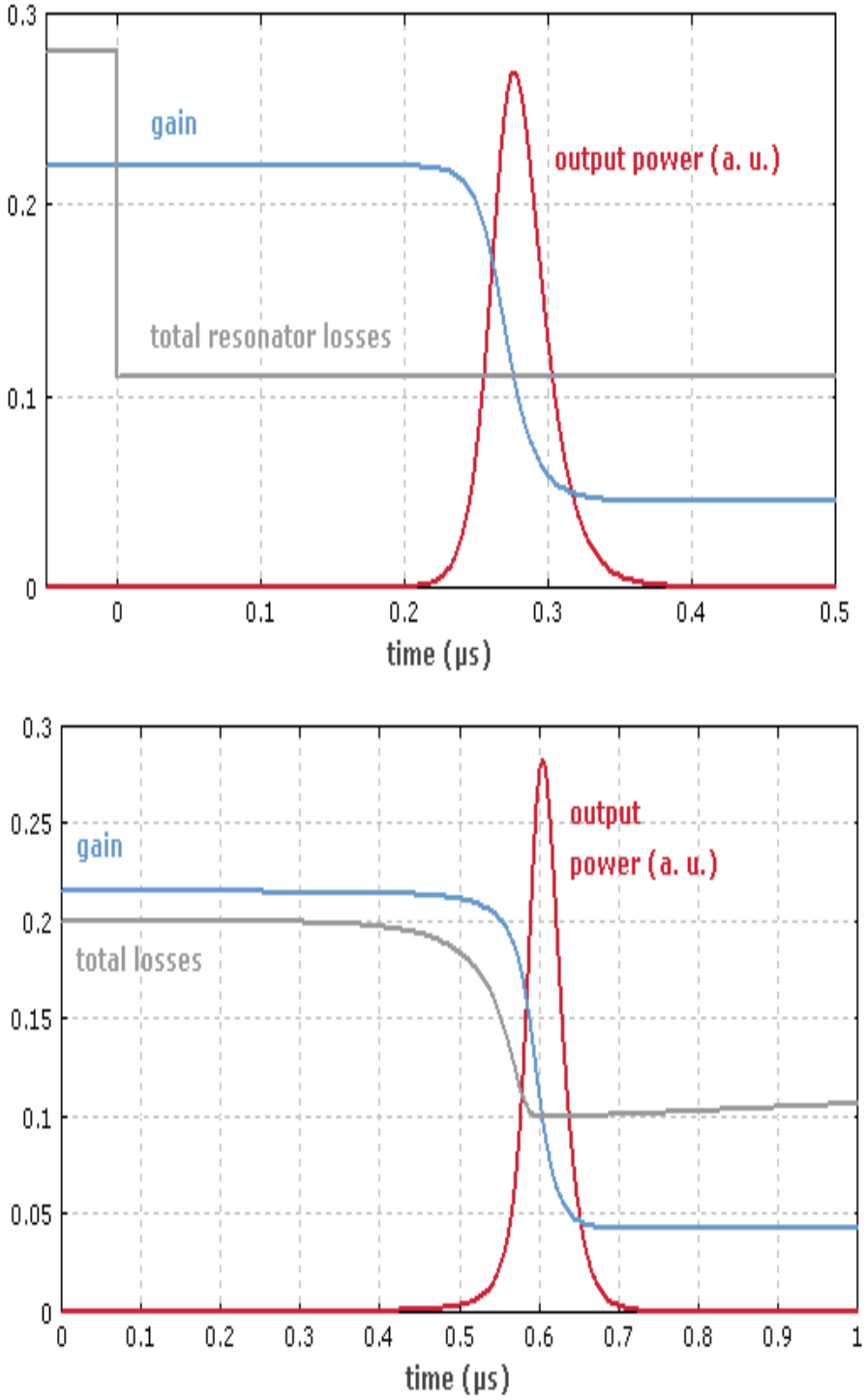

Figure 4: Oscilloscope trace showing active (top) and passive (bottom) Q-switching. Modulation of losses inside the cavity is used to generate ns pulses [27].

Control of the cavity losses is achieved through either passive or active Q-switching. Active control requires the use of a modulating device, which is triggered by an external source (outside the cavity). In contrast, the losses in passive Q-switching are self-modulated through the use of a saturable absorber. In this technique losses are minimised when the energy in the lasing medium reaches a sufficiently high intensity.

Q-switched lasers utilising this method of pulse generation have found widespread use in industry and conservation. Whilst it is not possible to generate ultra-short pulses with this technique it is currently one of the most common techniques used in commercially available laser systems.

Laser systems that can generate optical pulses with a temporal duration ranging from picoseconds (10^{-12} s) to femtoseconds (10^{-15} s) are classified as ultra-short pulse lasers. To generate ultra-short laser pulses, mode-locking (active or passive) combined with chirped pulse amplification (CPA) are often employed.

2.2.2 Mode-locking

Mode-locking refers to a group of techniques developed for the generation of ultra-short laser pulses. This method of generating ultra-short pulses (USP) was first proposed by Lamb Jr. in 1964 [28], before being observed experimentally by Hargrove *et al*. [29] later that year.

Inside the laser cavity each longitudinal mode will oscillate randomly with no fixed relationship to one another; this gives rise to the continuous output observed in CW lasers. To generate ultra-short pulses, these modes are forced to operate with a fixed phase relationship between one another; when operating in this manner the laser output is drastically altered as shown below in figures 5 and 6. Such lasers are said to be mode-locked and can be used to emit ultra-short optical pulses.

The pulse duration produced is dependent upon the number of modes oscillating within the laser cavity; therefore lasing mediums with a large gain bandwidth are able to generate the shortest pulses. The methods of mode locking are discussed in the following paragraphs.

2.2.3 Active mode-locking

There are two techniques available for generating actively mode-locked pulses: amplitude modulation (AM) and frequency modulation (FM); both these methods alter intracavity losses to produce the output pulses [30].

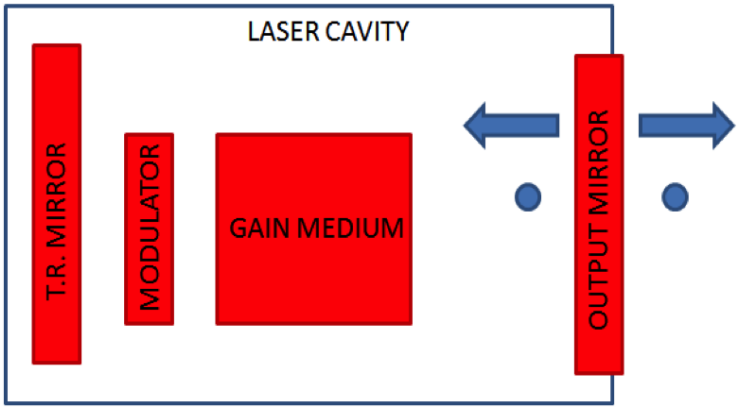

Figure 5: Schematic representation of mode-locking in a USP laser system. A modulating device is inserted into the cavity to alter the losses.

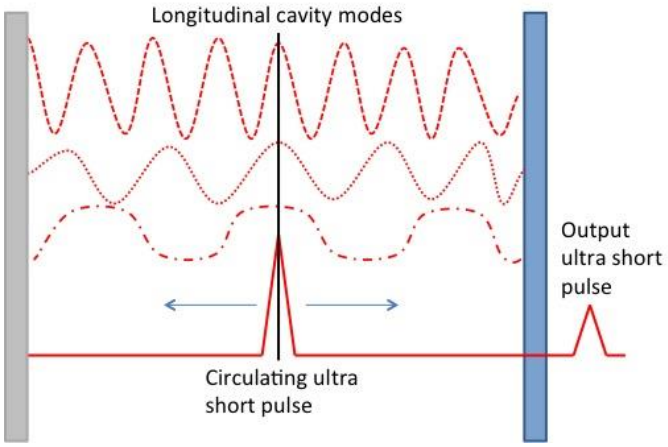

Figure 6: A number of longitudinal modes in the laser cavity produce the resultant output ultra-short pulse.

AM involves altering resonator losses within the cavity using a modulating device such as an electro-optic or acousto-optic modulator; this acts as a 'shutter' allowing synchronised ultra-short pulses to pass through whilst stopping longer pulses. Short pulses that pass through the modulator whilst it is 'open' are subjected to small losses and can complete another cavity round trip increasing the number of short pulses. Conversely, radiation outside of this time frame is subjected to large losses.

If a pulse arrives too early the leading edge is reduced in intensity, moving the remaining peak of the pulse to later times and closer to synchronisation with the AM device. Intensity attenuation on each round trip causes shortening of the pulse duration until equilibrium is reached (figure 7). Equilibrium is reached when pulse shortening is offset by other effects such as gain narrowing; the minimum pulse duration attainable is established when equilibrium is reached. A pulse arriving after the opening window has closed experience losses greater than the round trip gain and is reabsorbed.

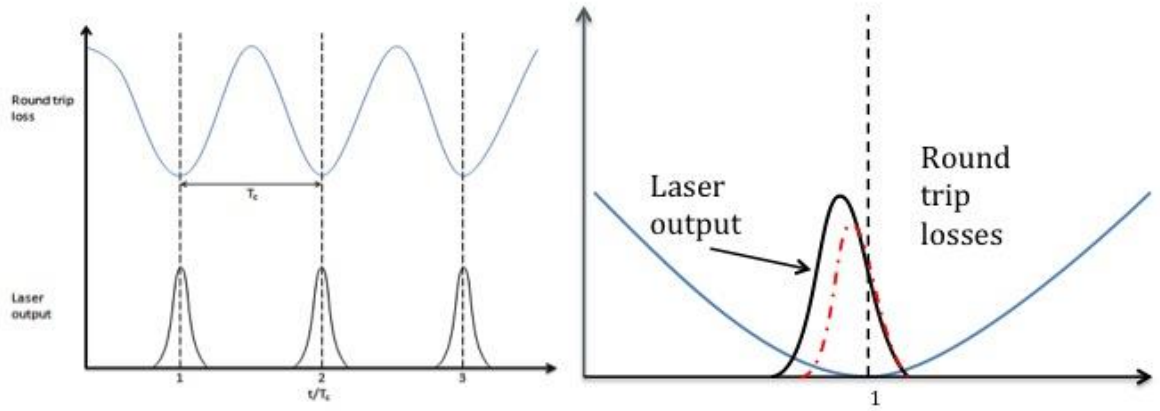

Figure 7: Amplitude modulating to produce ultra-short pulses (left). The image on the right shows how modulating the pulse when slightly out of synch with modulator causes pulse shortening to produce the ultra-short pulses [31].

FM mode-locking (figure 8) is achieved by modulating the refractive index of the intra-cavity component; as light passes through the device a small shift in frequency is induced. When the round trip time is synchronised with the frequency modulator some light is shifted to longer or shorter wavelengths; after several round trips these are removed from the cavity as the wavelength is outside the gain bandwidth.

However, when the induced frequency shift is zero, light is allowed to pass through and complete another cavity round trip; eventually after several round trips narrow ultra-short pulses are produced.

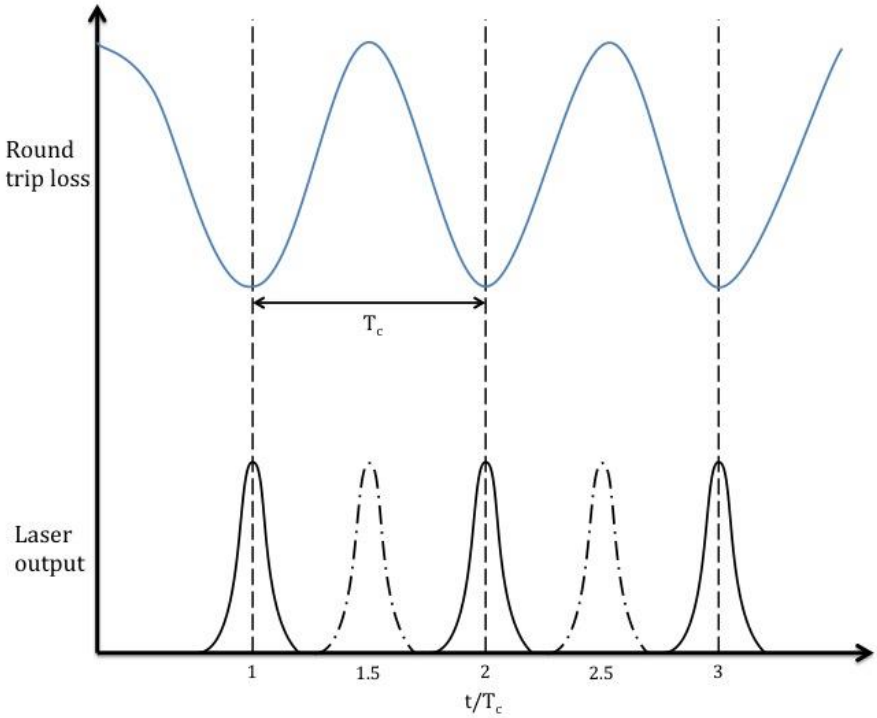

Figure 8: Example of frequency mode-locking. Modulation is achieved through modification of the refractive index of an intra-cavity component [32].

2.2.4 Passive mode-locking

Passive mode-locking was initially called Q-switched mode-locking, as it was first demonstrated together with Q-switching by Mocker *et al.* (1965) [33]. Passive mode-locking has a key advantage over active mode-locking; with this technique it is possible to produce pulses of a much shorter duration. All laser systems in this study produce ps pulses *via* passive mode-locking. Generally, determining the pulse width of a passively mode-locked laser is more difficult and must be considered on a case-by-case basis. However, the lower limit of attainable pulse widths (Td) can still be determined using equation 1.1:

$$T_d = \frac{2\pi}{\Delta\omega_{H,D}} \tag{1.1}$$

Where $\Delta\omega_{H,D}$ is the linewidth of the laser transition. The arrangement for passive mode-locking is the same as an active system; however in a passive system the optical element is not actively modulated with an external driver. The transmission properties observed during passive mode-locking are dependent upon the intensity of the incident radiation. The temporal variation observed during passive mode-locking using a fast saturable absorber is shown in figure 9.

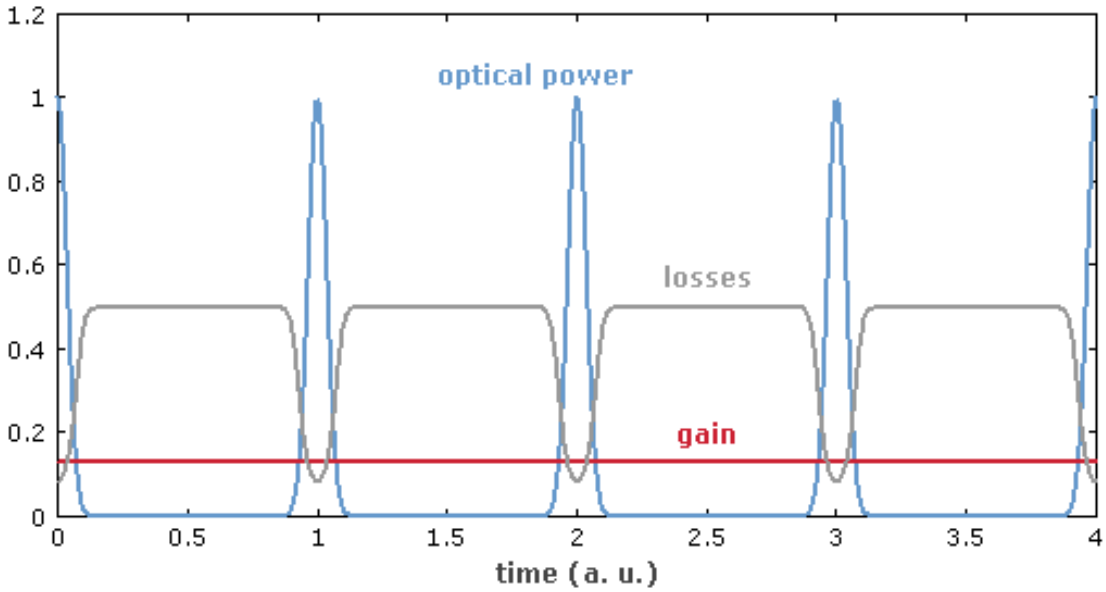

Figure 9: Example of passive mode-locking. A saturable absorber placed in the cavity is used to modulate the light. Low intensity pulses experience high losses and are reabsorbed; whilst the high intensity pulses are allowed to pass through experiencing low losses [34].

Saturable absorbers [35] are commonly used to modulate signals in passive mode-locking. There are three main types: fast, slow and artificial. To be effective the recovery

time of the saturable absorber must be shorter than one cavity round trip. Slow saturable absorbers have a recovery time near to, but still less than, the cavity round trip time.

There are several methods of creating artificial absorbers; one example of this is Kerr lens mode-locking. In this technique an artificial saturable absorber is created by exploiting the Kerr effect [36]; wherein a change in the refractive index of a material is observed in response to an applied electric field. Using this technique it is possible to generate pulses of < 10 fs [37].

Fast saturable absorbers have a recovery time significantly shorter than the round trip time, typically a few picoseconds or less [22]. When placed in a cavity the saturable absorber induces low losses for high intensity pulses and high losses for low intensity ones. This produces a single high intensity pulse within the cavity; other lower intensity pulses are reabsorbed.

Semiconductor saturable absorber mirrors (SESAM) are an example of a fast saturable absorber, displaying recovery times of the order of 100 fs [23]. This extremely fast response time is a key factor in determining the final pulse duration.

A SESAM comprises a semiconductor material encased between two mirrors; a typical SESAM is shown schematically in figure 10. The spacing of the mirrors within the SESAM device is crucial to prevent damage to the semiconductor material, which typically has a low saturation and damage threshold.

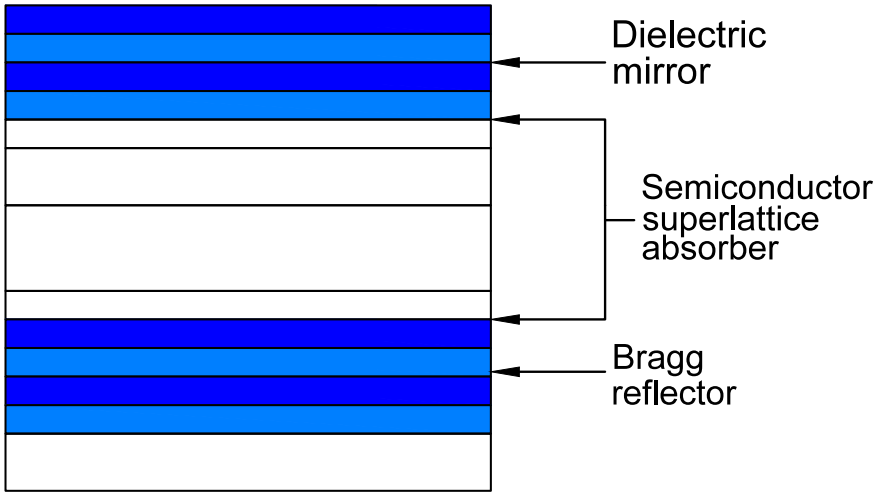

Figure 10: Schematic representation of a typical SESAM device.

2.2.5 Chirped pulse amplification (CPA)

For ultra-short pulse (USP) lasers with high repetition rates, the pulse energy produced can be of the order of nano-Joules (nJ). This is too low for materials processing to be viable, consequently these pulses must be amplified. However, the resulting amplified pulses pose a problem, as the peak intensity is extremely high (>TW), leading to effects such as non-linear pulse distortion (self phase modulation and self focussing) and damage to the gain medium or other optical components. To overcome this, chirped pulse amplification (CPA) is utilised (figure 11). This technique was first demonstrated by Mourou and Strickland [38] and can be used to amplify fs pulses up to petawatt peak powers (10^{15} W) without any of the deleterious effects mentioned.

In this technique pulses are initially passed through a dispersive element, such as a grating pair or long fibre, which stretches the pulse temporally, reducing the peak intensity to well below the non-linear threshold avoiding damage. The stretched pulse then passes into the amplifier were the energy is increased to much higher levels (G ≈10^6), more suitable for materials processing (≈µJ). After amplification the pulse enters a dispersive compressor (typically a grating pair) which has the opposite dispersion to the stretcher, removing the chirp. This returns the amplified pulse to high intensities before being emitted. This method is only applicable to extremely short pulse lengths from the low femtosecond regime to a few picoseconds.

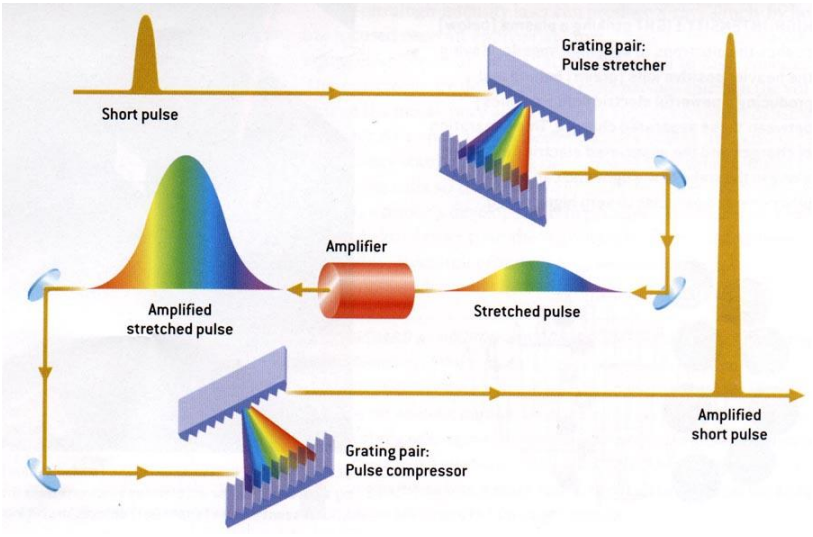

Figure 11: The process of chirped pulse amplification. The short pulse is initially stretched before undergoing amplification. After the stretched pulse has been amplified it is recompressed to match the input pulse [39].

2.3 Characteristics of laser light

Laser light has many unique characteristics which make lasers valuable and indispensable in many applications including medical, spectroscopy and materials processing. Some key properties of laser light are listed below:

2.3.1 Monochromatic

Laser outputs, whether they are CW or pulsed, are highly monochromatic meaning that the all the photons emitted are of the same frequency. True monochromatic beams are not achievable as amplified spontaneous emission leads to a broadening of the emission spectrum. In many instances the line width produced by a laser is extremely difficult to measure. The narrow laser line width makes the laser useful in various applications including those discussed previously and investigated in this thesis.

2.3.2 Directionality

Conventional light sources emit omnidirectional photons preventing them from being focused into a small spot. Laser light in contrast is unidirectional and displays only a tiny amount of divergence. Due to the high spatial coherence it is therefore possible to focus the laser beams down to the small spot sizes (cm, mm and µm) required in materials processing. Using this low divergence it is possible to calculate the diffraction limited spot size, i.e. the smallest size that the beam can focused down to.

2.3.3 Diffraction limited spot size

A laser beam with a finite diameter can be focused down to a small spot size; however, there is a limit to the degree of focussing achievable. Once the minimum for a particular wavelength has been reached the beam is said to be diffraction limited. By operating as close to this limit as possible this allows the user to increase the energy density in the target area. The diffraction limited spot size of a laser beam with a finite width can be estimated using equation 1.2:

$$D_{\min} = \frac{4 f_{lens} \lambda M^2}{\pi D_{in}} \qquad (1.2)$$

Wherein f_{lens} is the focal length, λ is the laser wavelength, D_{in} is the input beam diameter before focusing and M^2 is the laser beam quality factor [40]. With the laser beam focused onto such a small area, the intensity will be extremely high, causing most materials to be immediately melted, vaporised or sublimated.

2.4 Ultra-short pulses (USP)

The most fundamental difference between long pulse and continuous wave lasers in comparison to ultra-short systems are the extremely high intensities that arise as a consequence of the ultra-short pulses. The pulse duration is often considerably shorter than the time required to thermalise the substrate. This results in so-called "cold ablation". In reality, there is always some thermal by-product of laser interaction but the use of ps and fs pulses reduces this to negligible amounts. The key differences between CW/LP and USP material interaction is summarised in figure 12.

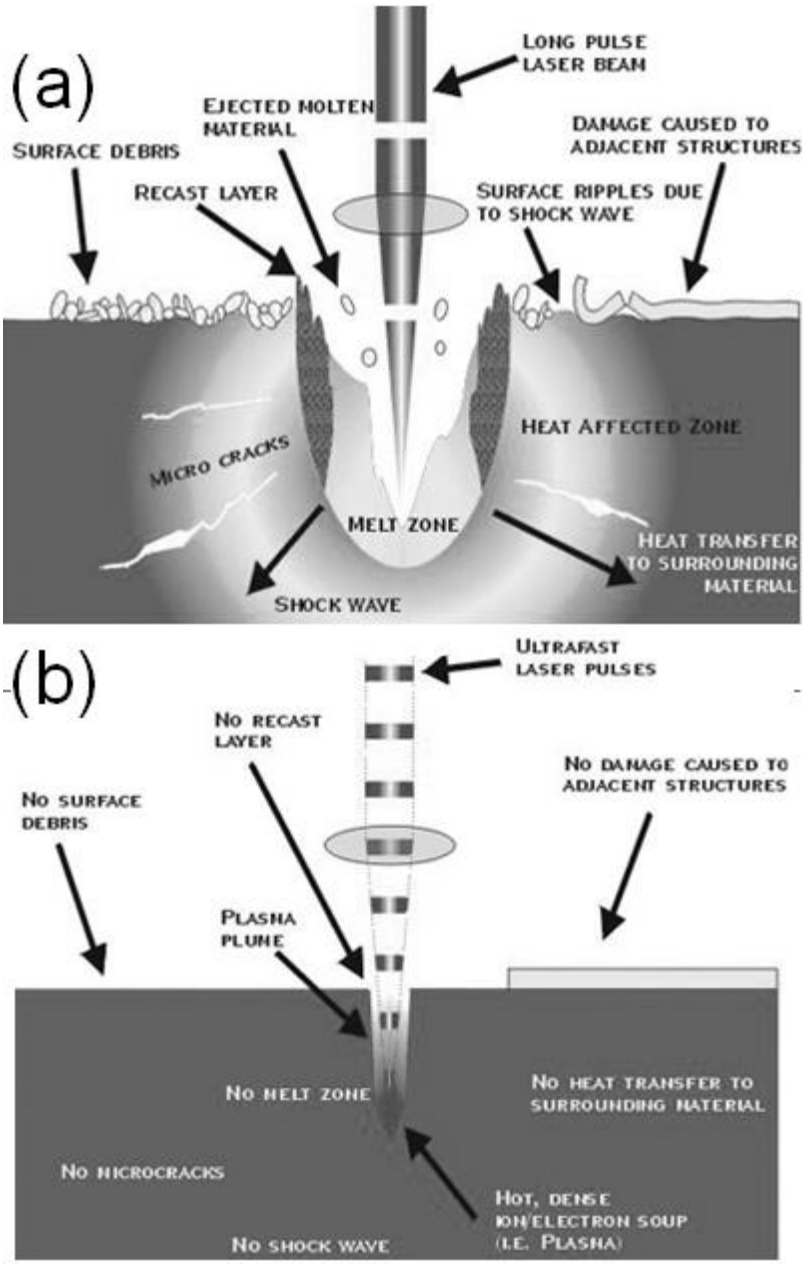

Figure 12: Comparison between (a) continuous wave/long pulse and (b) ultra-short pulse laser material removal [41].

Ultra-short pulse (USP) interactions will be discussed in the following order:

- Absorption processes
- Energy transfer between electrons and lattice
- Mechanisms of ablation
- Ablation threshold

Absorption plays a key role in successful materials processing. When using ultra-short pulses both linear and non-linear regimes are available. Linear absorption is dependent upon the properties of the material being subjected to laser processing. However, if there is sufficient intensity (>10^{12} Wcm^{-2}) then nonlinear absorption processes could occur. In these instances the properties of the material (e.g. wavelength dependency of absorption) becomes negligible and absorption is almost wholly dependent on the pulse intensity.

Since the pulse length is considerably shorter than the thermalisation time, removal is not dependent upon melting and vaporisation, as seen with CW or LP lasers, but on ionisation leading to sublimation of the surface layer [42].

The process of USP light-matter interaction is subsequently discussed including previous experimental work. The beginning of any light-matter interaction starts with absorption; i.e. the amount energy taken in by the material with which it is interacting. This provides an excellent starting point for the USP discussion.

2.4.1 Absorption processes

When a laser pulse strikes the surface of an opaque material it is either reflected or absorbed. Ideally, when materials processing one would prefer 100% absorption of the incoming pulse as this maximises process efficiency. In practice, this is not achievable and some reflectivity and absorption will always occur; the preference for one over the other is determined by either the properties of the material (linear absorption) or in some instances the extremely high intensity of the incoming pulse (nonlinear absorption). Generally, linear absorption is most widely observed in materials processing as it is the dominant method in CW down to ps (> 50 ps) [43].

2.4.2 Linear absorption

When light strikes the surface of a material it will be absorbed into a thin layer of the material, as the light passes through the medium the irradiance of the pulse will decrease exponentially with distance. This decay in irradiance is dependent on the absorption

coefficient (α) of the material and the distance (z) the light needs to pass through; this is described using Beer-Lamberts' law (equation 1.3) [44].

$$I = I_0 exp^{-\alpha z} \quad (1.3)$$

Wherein I_0 (Wcm^{-2}) and I (Wcm^{-2}) are the impinging and transmitted intensity respectively.

Using this equation it is possible to determine which wavelength would be most suitable for processing different materials. The absorption depth (d) within a material can be approximated using equation 1.4.

$$d = \frac{1}{\alpha} \quad (1.4)$$

2.4.3 Nonlinear absorption

Non-linear absorption (NLA) occurs when two or more photons are absorbed, simultaneously exciting the atom from its ground state across the band gap to a higher electronic level. This phenomenon was first predicted by Goeppert-Mayer (1931) [45]. When the intensity of an incoming pulse becomes sufficiently high it is possible to induce absorption in even low absorbing materials such as glasses [46, 47] *via* direct pumping of electrons across the band gap.

2.4.4 Reflectivity

As mentioned above, a laser pulse can either be absorbed or reflected at the surface of an opaque medium. Regardless of the mechanism or degree of absorption there will always be some light reflected. In laser materials processing, determining how much light is absorbed is important in ensuring the process efficiency and therefore the suitability of laser processing. Under ambient atmosphere or vacuum, normal reflectivity (R) of a conducting surface can be determined from Fresnel's relations as shown in equation 1.5 [48].

$$R = \frac{((n-1)^2 + k^2)}{((n+1)^2 + k^2)} \quad (1.5)$$

Wherein *n* is the refractive index and *k* is the extinction coefficient.

Although the Fresnel equation provides an excellent approximation of the reflectivity, the process is complicated by the electrical conductivity of semiconductors and metals. In

these materials an abundance of free electrons can affect the electromagnetic wave, giving rise to differences in reflectivity measurements. This is especially prevalent when utilising USP if one considers the magnitude of the electric field of the incoming pulses.

In dielectrics, the Fresnel law is modified to account for the fixed relationship between the light and electrons, as there are no delocalised electrons, unlike a metal or semiconductor. Wherein θ_i is the angle of the incident rays.

$$R_p = \left(\frac{\sqrt{\left(n^2 - sin^2\theta_i - (n^2 \cos\theta_i)\right)}}{\sqrt{(n^2 - sin^2\theta_i + n^2 \cos\theta_i)}} \right)^2 \quad (1.6)$$

$$R_s = \left(\frac{\left(\cos\theta_i - \sqrt{n^2 - sin^2\theta_i}\right)}{\left(\cos\theta_i + \sqrt{(n^2 - sin^2\theta_i)}\right)} \right)^2 \quad (1.7)$$

There are several different techniques available to accurately examine reflectivity such as pump-probe spectroscopy [49] and harmonic generation [50].

Finally, the surface condition can affect the reflectivity. As surface roughness (Ra) increases the surface will become less reflective and more diffuse, assuming a laser beam may undergo two or more reflections. Results by Vorobyev *et al.* have shown that the presence of macro, micro and nano structures can enhance absorption at the surface, thus reducing reflectivity [51,52].

2.5 Mechanisms of ablation

Ultra-short pulse laser ablation is, generally, dependent upon a variety of factors including the material properties, pulse duration and fluence [5,53,54,55,56,57]. In this section the general mechanism of USP laser ablation will be discussed. It is commonly accepted that there are three major material classifications: metals, semiconductors and dielectrics. These three materials show different mechanisms of ablation due primarily to their individual band structures; a simplified diagram of the different bands gaps for each material is shown in figure 13.

2.5.1 Metals

The energy absorbed from the pulse is deposited into the electron subsystem *via* the inverse Bremsstrahlung effect [58]. The electrons within the subsystem have a low heat capacity, which causes the electron temperatures to rise to tens of thousands of degrees Kelvin very quickly. At this point, the lattice remains at low temperatures (near ambient); this

results in a transient non-thermal equilibrium between the electrons and lattice [59, 60]. To rebalance this equilibrium, energy is exchanged between the electrons and lattice. The time taken to reach equilibrium varies depending on the material but is typically of the order of from one to tens of ps. Re-establishing the equilibrium causes both a temperature and kinetic energy rise in the lattice, resulting in ablation of the metal.

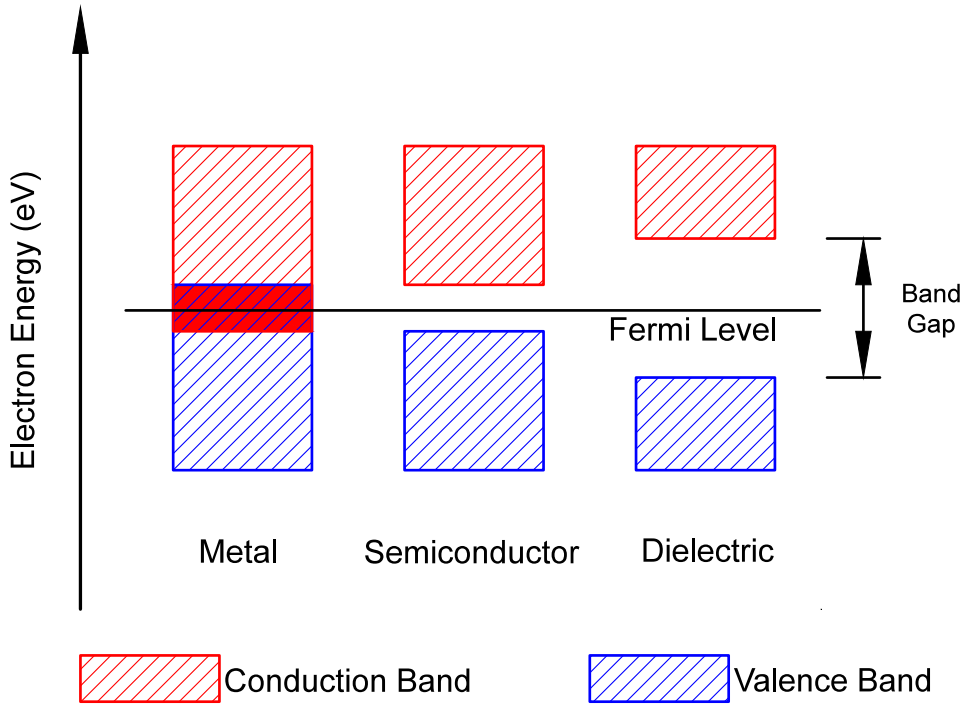

Figure 13: Schematic image of the band structure of three major groups of materials. The black line represents the Fermi level.

2.5.2 Dielectrics

In dielectric materials, the mechanism of ablation is different to that of a metal as the electrons used to initiate ablation are bound as opposed to delocalised, as observed in metals [61]. Dielectric ablation proceeds *via* optical breakdown, in this mechanism impinging ultra-short pulses induce multi photo-ionisation within the irradiated region. In this instance several photons with an energy below the band gap of the dielectric are used to promote electrons from the valence into the conduction band of the material. These seed electrons initiate an electron avalanche due to impact ionisation, creating many electron-hole pairs; this causes an irreversible change in the structure of the irradiated region [62,63,64,65,66].

The free, ionised electrons generated in this manner produce a plasma, which is visible to the naked eye. Ablation is initiated when the plasma reaches a critical density (η_c); which can be described by equation 1.8.

$$\eta_c = m_e \epsilon_0 \omega_L^2 / e^2 \quad (1.8)$$

Wherein m_e is the electron mass and ω_L is the laser frequency in rads^{-1}. Ablation is initiated when (η_c) is reached; therefore it is natural to link the critical electron density to the ablation threshold fluence of materials. This indicates that the threshold fluence is the minimum energy input required to produce the critical electron density. A realistic value of (η_c) is described as being the point at which the plasma generated becomes reflective to incoming pulses (approximately 10^{21} cm^{-3} for 1053 nm [67]), since it is just below this density that the pulse is strongly absorbed.

2.5.3 Ablation threshold (Φ_{th})

As discussed above, the ablation threshold (Φ_{th}) is said to be equivalent to (η_c). In this section the ablation threshold, which is determined using fluence, is calculated. The fluence of a pulse is described using equation 1.9. This equation was derived by Mannion *et al.* and relates the square of an ablated crater diameter (D) to the peak fluence (Φ_P).

$$D^2 = 2\omega_0 \ln\left(\frac{\Phi_P}{\Phi_{th}}\right) \quad (1.9)$$

Wherein ω_0 is the beam diameter and Φ_{th} is the fluence threshold (ablation threshold).

2.5.4 Incubation effect

During experimental processing with USP lasers it was noted that the ablation threshold (Φ_{th}) of a material decreased with increasing pulse number on the surface. The incubation effect (ζ) describes the dependence of the ablation threshold, for a given material, on the number of pulses (N) as shown in equation 1.10. The lowering of the ablation threshold was observed in most materials including dielectrics [61 – 63], semiconductors [68], metals [69] and polymers [70].

$$\Phi_{th}(N) = \Phi_{th}(1) N^{\zeta - 1} \quad (1.10)$$

Where $\Phi_{th}(1)$ is the single pulse ablation threshold of the material.

In this equation ζ characterises the degree of the incubation effect on the threshold value; if ζ is equal to 1, the ablation threshold of that material is independent of the pulse number. The lower the ζ value is the greater the effect of incubation.

Generally, ζ is higher for metals than dielectrics. This is attributed to the ready abundance of free electrons in the surface of a metal, which makes it easier to initiate ablation than in a dielectric were the electron must first be promoted to the conduction band. The incubation effect is explained by the formation of cumulative defects in the surface of the material [71]. These defects are induced by previous pulses and create colour centres which absorb slightly more energy than the surrounding material. The absorption increases with the number of pulses until there is sufficient energy absorbed by the material to initiate ablation.

2.6 Mathematical models used in USP

When modelling laser materials processing with USP, it is not possible to use traditional thermal models, as these cannot account for the high temperatures of the electron gas and the non-thermal equilibrium initially established. This leads to predicted surface temperatures across the material of several thousand Kelvin, which are inaccurate. Therefore, new modelling techniques were required; several models have been developed for understanding USP-matter interaction.

2.6.1 1D two temperature model for metals

As discussed in section 2.5, the ablation of metals with USP proceeds in three distinct steps; absorption, energy transfer between the electrons and lattice and an increase in lattice temperature and kinetic energy resulting in ablation.

After their initial work, Anisimov *et al.* proposed a two-step model to describe the transfer of energy between the electrons and lattice for metals; using the assumption that electron and phonon energy transfer can be described using Fourier's law [72, 73]. Qiu and Tien later derived this model from the Boltzmann energy transport equation [74].

Assuming a uniform fluence across the irradiated area allows the consideration of temperature change in only the z plane. The 1D two-temperature model (TTM) can be described using two partial differential equations [61].

$$C_e(T_e)\frac{\delta T_e}{\delta t} = \left(K_e \frac{\delta}{\delta z} T_e\right) - g(T_e - T_l) + S(z,t) \qquad (1.11)$$

$$C_l(T_l)\frac{\delta T_l}{\delta t} = g(T_e - T_l) \qquad (1.12)$$

Wherein (T_e) and (T_l) are the electron and lattice temperatures respectively. (C_e) is the electron heat capacity, (C_l) is the lattice heat capacity, (K_e) is the electron thermal conductivity, g is the electron-phonon coupling constant and $S(z,t)$ is the absorbed laser

energy. The effect of the diffusive term in equation 1.12 is negligible and thus is neglected in temperature calculations.

One of the assumptions made in this model system is that the metal properties remain constant throughout the irradiation process. Within this model the electron heat capacity, thermal conductivity and electron-phonon coupling constant are all temperature dependent variables.

2.6.2 Molecular dynamics (MD)

This technique was proposed by Alder whilst working at the Lawrence radiation laboratory [75]. Since then, it has found widespread use in physical, chemical and biological studies. One application has been the study of USP material ablation [76]; where the mechanisms of spallation and nucleation have been verified.

MD is a method used to visualise molecular and atomic interactions and predict their behaviour. Due to the vast number of particles in atomic systems it is impossible to deduce the properties of these highly complex systems analytically. MD circumvents this problem by applying algorithms to the system; the atoms and molecules will abide by some theoretical approximations, such as Newtonian dynamics and the Born-Oppenheimer approximation.

Using this technique the velocity, temperature, pressure and structure can be probed. Rapaport published a simplified flow chart describing the MD simulation steps. Figure 14 shows a flow chart of the steps involved in MD simulations.

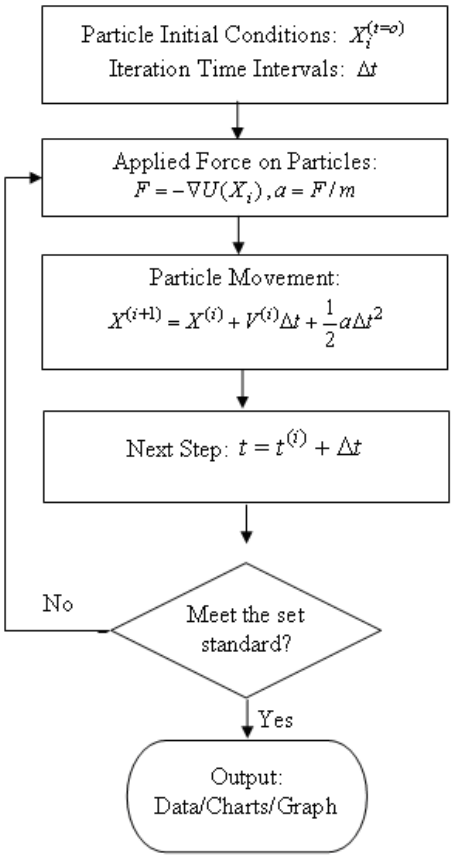

Figure 14: Flow chart showing the steps in MD simulations [77].

2.6.3 Combined TTM and MD simulations

By combining these two simulation methods, it is possible to negate some of the limitations inherent in both processes. In this hybrid model the TTM and MD simulations are combined within the absorption depth of the beam. This allows for determination of the molecular effects of irradiation and the thermal effects resulting from the non-equilibrium thermal gradient. Outside the absorption depth only the TTM is used; this is due to the long computational time that would be required to determine the molecular effects and the limited effect observed for such a small absorption depth. When combined, the equations governing this model are described in equations 1.13 – 1.15 [78].

$$C_e(T_e)\frac{\delta T_e}{\delta t}=\left(K_e\frac{\delta}{\delta z}T_e\right)-g(T_e-T_l)+S(z,t) \tag{1.13}$$

$$F_i=m_i\frac{\delta^2 r_i}{\delta t^2}-\xi m_i v_i^t \tag{1.14}$$

$$\xi = \frac{1}{n}\sum_{k=1}^{n} gV_n\left(T_e^k - T_l\right) / \sum_i m_i\left(v_i^t\right)^2 \quad (1.15)$$

Wherein (m_i) and (r_i) are the mass and position of an atom (i), and (F_i) is the force acting on the atom (i). The second part of equation 1.14 describes the contribution of the electrons to atomic motion. The thermal velocity of the atoms raised by electron movement is represented by $\left(V_i^T\right)$. The coefficient (ξ) is defined for each cell of the volume.

2.7 Applications

The following section discusses some of the current applications of USP lasers, state of the art work in thin film micro-processing and competing processes are discussed. A review of laser restoration with current, previous work and mechanisms is presented.

2.8 Micro-processing

Micro-processing is used to describe the modification of materials, which are within the nanometre to millimetre range [79]. Micro-processing can be used to describe any fabrication or manufacturing method on a micron scale.

The original micro-processing techniques can be traced back to the design and manufacture of integrated circuits (IC). Integrated circuits have found widespread applications in both consumer and scientific markets; ICs are found in TVs, DVDs and other consumer electronic devices. For scientific applications, ICs have been used to control equipment and spectrometers. More recently, the techniques of IC fabrication have been applied in the manufacture of micro-electromechanical systems (MEMS) and nano scale systems. This has resulted in the production of devices such as gears, valves, tweezers and electronic circuits of less than 100 μm [80]. These devices have been utilised as sensors for pressure, temperature, velocity and chemical composition; and have been incorporated into devices such as a lab-on-a-chip, robots, micro-engines and heat pumps [81].

The market for products that include micro-processed devices continues to expand with the advent of smartphones and tablet computers, which require high performance within a small form factor. This means that research in to new methods of miniaturisation and wholly new devices, gives rise to a variety of interdisciplinary research.

2.8.1 Thin film processing

Within the micro-processing field, the use of thin films for the creation of integrated circuits has been widely utilised; most prevalently in personal computers and displays. Thin films are also used in flow measurements [82], electroluminescence [83], radio frequency identification (RFID) [84] and photovoltaic cells [85].

First manufactured in the 20th century [87], transparent conductive oxides (TCOs) which are electrically conducting and transparent to visible light have undergone continuous development, resulting in the production of several different types including: Al-doped ZnO, SnO_2, F-doped In_2O_3 and others.

Indium tin oxide (Sn-doped In_2O_3), also known as ITO, is a commonly used TCO material. First manufactured in the 1960s, ITO has become very popular with manufacturers due to its excellent conductivity, transmission and stability in most environments. ITO is a semiconducting material with a wide band gap of ≈ 4 eV and a refractive index of ≈ 1.76 [88].

Tin dioxide (SnO_2) is another semiconducting material commonly used transparent conductive oxide, due to its excellent transmission and electrical conductivity. In addition, its relatively low cost and high mechanical, chemical and environmental stability has resulted in its widespread application. Similar to ITO, tin dioxide also has a wide band gap of between 3.4 – 4 eV and a refractive index of ≈2.0 [89].

2.8.2 Competing micro-processing techniques

Many types of micro-processing techniques have been developed over the past century. These methods can be applied in a wide variety of processes but are ultimately dependent upon the requirements of the part being fabricated. To remain within the scope of this work, the competing processes discussed here pertain to the micro-processing of thin films. Traditionally, these films have either been patterned using a physical tool (mechanical force) or undergone etching; however more recently direct writing using lasers has become a popular technique.

2.8.3 Removal by mechanical force

Using conventional milling procedures, new machines were developed that could utilise ultra-fine tips to remove material from the surface [90]. By tracing the tips over the sample the required patterns were scribed on to the surface of the thin film. This technique can be used to produce extremely fine holes or scribed lines on the surface of thin films; however the ultra-fine tips are prone to wear through constant application of forces in three dimensions (XYZ). This fatigue means that the tips are prone to high failure rates and require replacement regularly.

2.8.4 Removal by etching

Thin film removal through chemical breakdown is the most popular technique for patterning thin films, due to the high quality structures produced even at micron scales. Under the title etching there are several different techniques.

2.8.4.1 Dry

In this technique the material being etched is exposed to either reactive ions or a vapour phase etchant. A mask is used to protect the areas of the film that do not require processing. Exposure to the ions/vapour results in dissolution or sputtering of the surface. After the etching process is finished, the mask is removed to reveal the desired pattern on the substrate. One drawback of this process is the difficulty in removing the mask after processing. Dry etching is particularly useful in situations were wet etching is not possible, such as when the material is chemically resistant [91].

2.8.4.2 Wet

In wet etching [92] the target surface is exposed to a chemical, which dissolves the thin film in the exposed areas. Similar to dry etching, areas that do not require etching are covered using a mask, which does not react with the chemical etchants. After processing is complete, the mask is removed leaving the required pattern behind.

Despite the simplicity of this technique, it does suffer from some drawbacks. The chemicals required are harmful and are controlled by strict health and safety regulations. The non-dissolvable mask used to protect part of the film is difficult to deposit on the surface and remove after completion. The processing of single crystal materials (e.g. silicon) is also difficult due to preferential etching rates in some orientations, causing under or over etching in certain areas. Finally, at the end of the process the waste toxic material must be disposed of in accordance with strict health and safety regulations [93]. Figure 15 compares two structures fabricated on aluminium using dry and wet etching; in this case wet etching produces superior features on the surface.

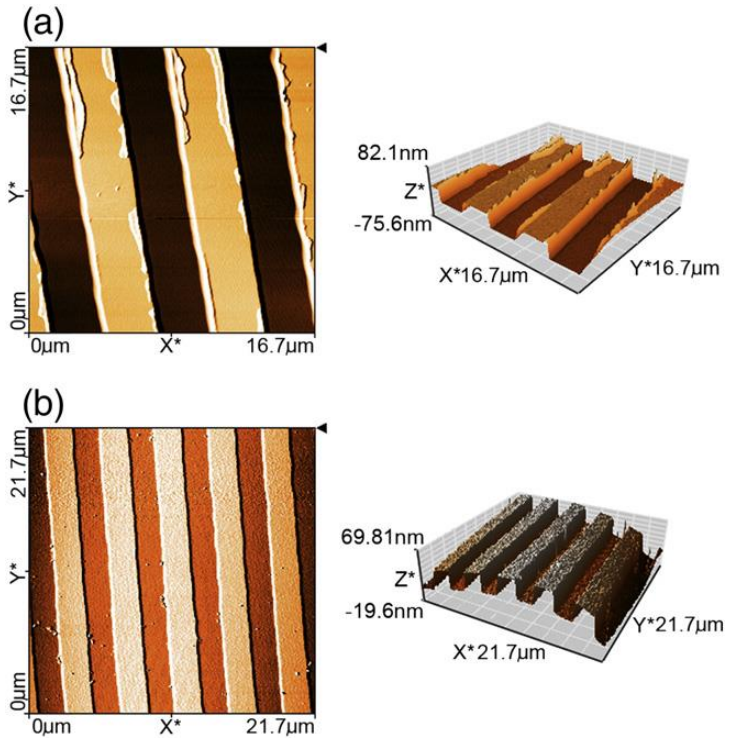

Figure 15: AFM images comparing two aluminum electrode structures (thickness ≈ 60 nm) fabricated (a) with a dry-etch procedure and (b) with a wet-etch procedure [94].

2.8.4.3 Reactive Ion etching (RIE)

RIE [95] is one of the most popular and widely used etching techniques due to its ability to produce high resolution 3D structures. High etching depths of greater than 100 µm can be achieved with near vertical walls [96]. RIE, also called plasma etching, is a hybrid method of etching surfaces combing techniques used in dry and chemical etching. Figure 16 shows the mechanism for RIE processing. A low-pressure chamber and an electromagnetic field is used to generate chemically active plasma; the reactive ions are accelerated towards the sample were interaction with the surface results in material removal. The plasma source used in the etching process can be varied depending on the material being etched and the resolution required. The combination of wet and dry techniques allows for the production of deep, high quality etched structures, an example of a RIE fabricated structure is shown in figure 17.

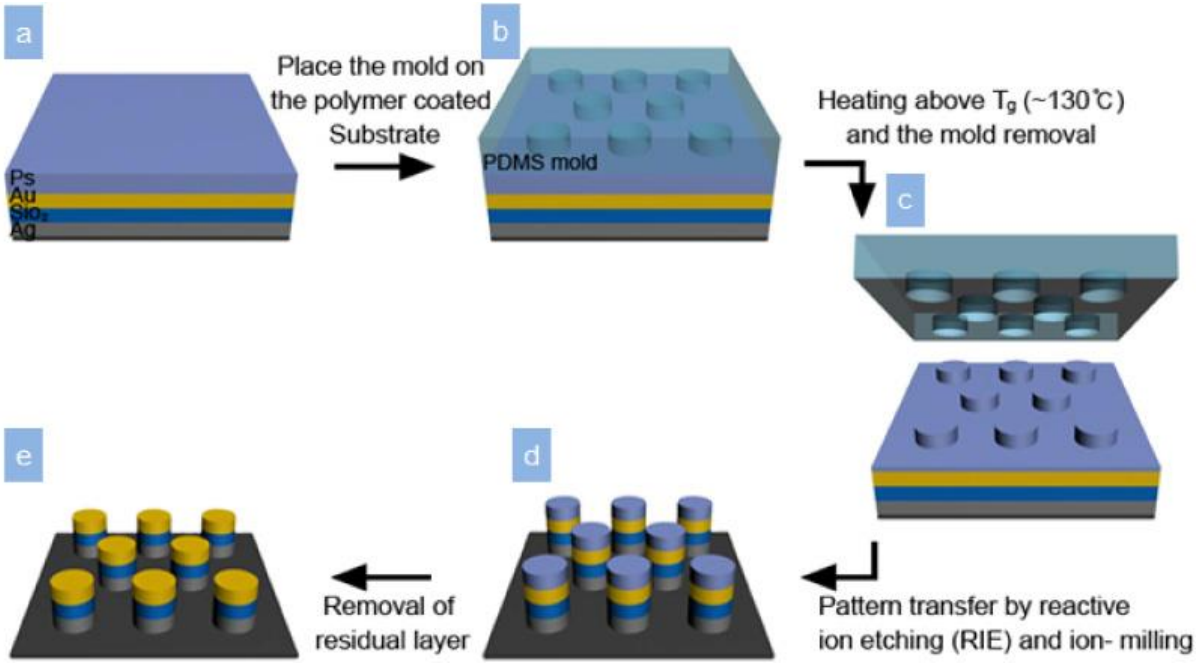

Figure 16: An image showing how the RIE process can be used to fabricate cyclinder shaped Ag/SiO_2/Au multi-segment nanopatterns. (a) PS on the Ag/SiO_2/Au multi-segment surface. (b) Pattern transfer using a PDMS mold above the glass transition temperature of PS (Tg ~ 273.15 K). (c) Patterned PS film on the Ag/SiO_2/Au multi-segment surface. (d) Removal of the residual layer by a reactive ion etching (RIE) and ion-milling process. (e) Removal of the residual PS on top of the pattern [97].

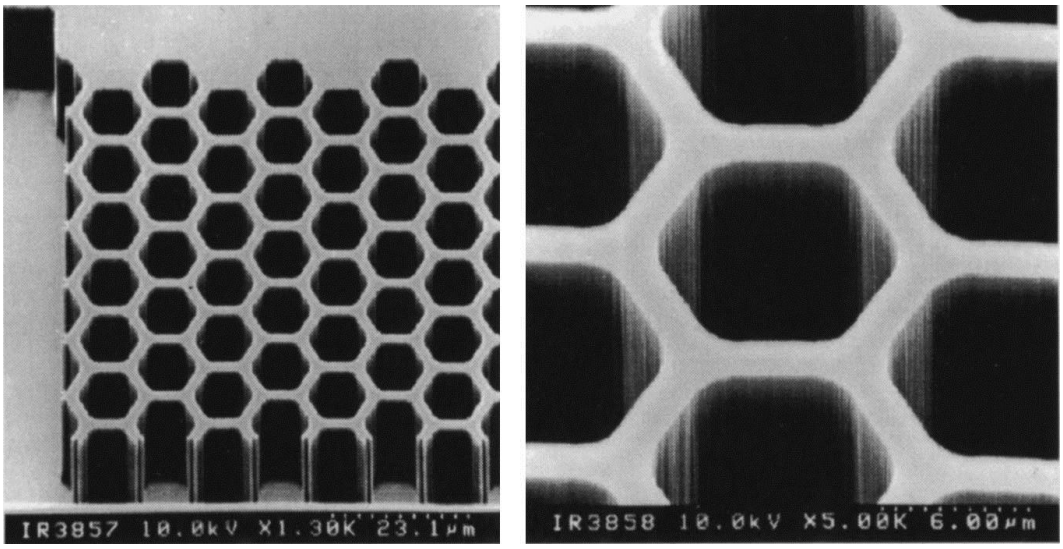

Figure 17: Microfilter structures etched in silicon with BCl_3/Cl_2/HBr plasma [98].

2.8.5 Removal using lithography (LIGA)

Lithography, electroplating and moulding, also known as LIGA (taken from the German equivalents), describe a micro-processing technique used to create structures with high aspect ratios [99]. Currently, there are two main LIGA processes used in micro-processing, X-ray and UV LIGA. X-ray LIGA being able to produce structures with the highest aspect ratios.

LIGA micro-processing techniques use a photosensitive material (resist), which is exposed to a radiation source, causing a change in its physical properties. By selectively exposing certain areas of the material the desired pattern can be transferred to the resist. After exposure, this is placed into a developer solution, which selectively etches leaving only the unexposed part of the resist behind (positive resist). This process can also be completed in the opposite manner with only the exposes parts of the resist remaining (negative resist). Figure 18 shows some micro structures fabricated using LIGA; this shows the high quality finishes (Ra ≈10 nm) and aspect ratios (100:1) achievable with this technique.

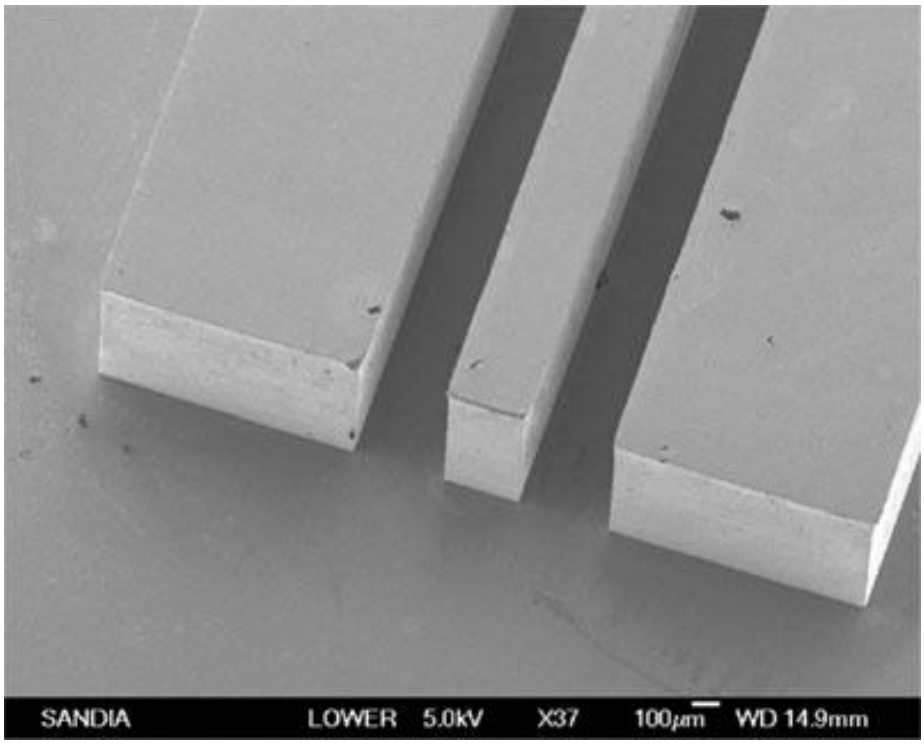

Figure 18: A 517 μm tall copper waveguide fabricated using the LIGA process [100].

2.8.6 Direct writing applications (DW)

More recently, the application of laser systems in the patterning of thin films has been undertaken using CW or LP laser systems. In this method, the desired pattern is programmed into a specialist software package or computer numerically controlled (CNC) stage in order to expose the desired areas to laser radiation. The laser beam is focused to a small, highly intense spot capable of raising the localised temperature of the film above its vaporisation point (Δvap); if the intensity is sufficient it is also possible to induce sublimation (Δsub) [101].

The use of CW/LP lasers induces heat within the irradiated zone and the area immediately surrounding it. This heat diffuses away in the time between pulses or when the beam is moved to another irradiation point. Heat diffusion in micro-processing reduces the efficiency of fabrication [46]. During processing plasma is formed above the irradiated region and whilst this improves the coupling of light into the interaction zone, micro-processing quality is reduced due to a laser induced detonation wave near the surface.

More recently, with the advent of more robust USP laser systems the direct writing of different films with fs and ps sources has increased. The potential benefits are clear, no harmful chemicals or vacuum chambers are required and the pattern is software generated making it easier to alter. USP lasers can be focussed to near diffraction limited and due to the timescales that these systems operate on, any heat generated during the pulse is not transferred from the electrons to the lattice. This minimises heat effects making processing more efficient. These benefits allow USP lasers to produced high resolution, aspect ratio structures with minimal thermal effects; figure 19 shows some structures fabricated using USP lasers.

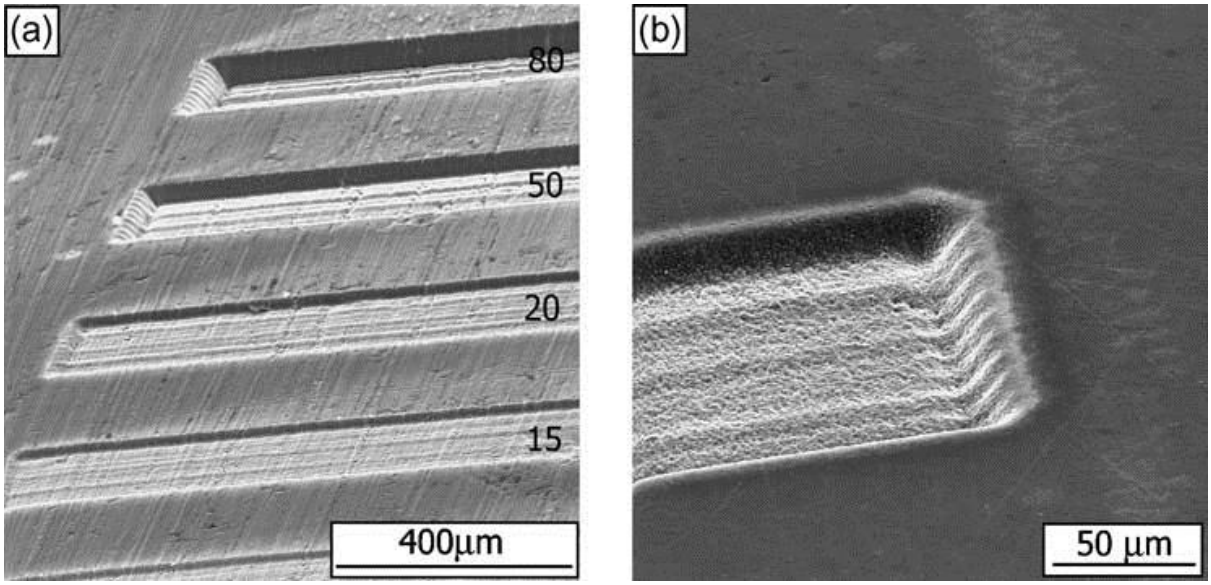

Figure 19: Femtosecond micro-machining of aluminum under helium at 1 kHz repetition rate and 3.3 Wcm^{-2} average powers (1.4 Jcm^{-2}/ 10 mm s^{-1}). (a) 10 mm raster with 10/15/20/50/80 over scans. (b) 240 mm wide, 25 mm deep channel on polished aluminum sample micro-machined at 3.3 Wcm^{-2} average powers [102].

2.8.7 Direct applications

Due to the inherent versatility of laser systems there is a wide variety of micro-processing applications in which USP lasers can be utilised. The following are a few examples of relevant micro-processing applications.

2.8.8 IC and PCB industry

The use of lasers in the direct writing of circuits has already been seen using CW and LP lasers; this was originally investigated in the 1980's. More recently, the application of ultra-short pulses in the IC and PCB has become widespread and these systems are now a key technology in the current revolution in information technology [103]. These lasers can be used to create circuits on both rigid and new flexible [104] substrates with high resolution and reproducibility. In addition, with the near diffraction limited beam sizes of these systems, it is possible to drill holes down to several microns in size. This ability will be an important technology in the fabrication of semiconductors as interconnect densities increase. Figure 20 shows cavities engraved on silicon to produce a circuit.

The scribing of an integrated circuit using parallel processing is discussed in detail in the experimental section (chapter 5) of this thesis.

2.8.8.1 Scribing of thin films

Thin film coatings on different substrates can be used for a variety of functions including the hardening of machining tools and improving charge transfer and collection efficiency.

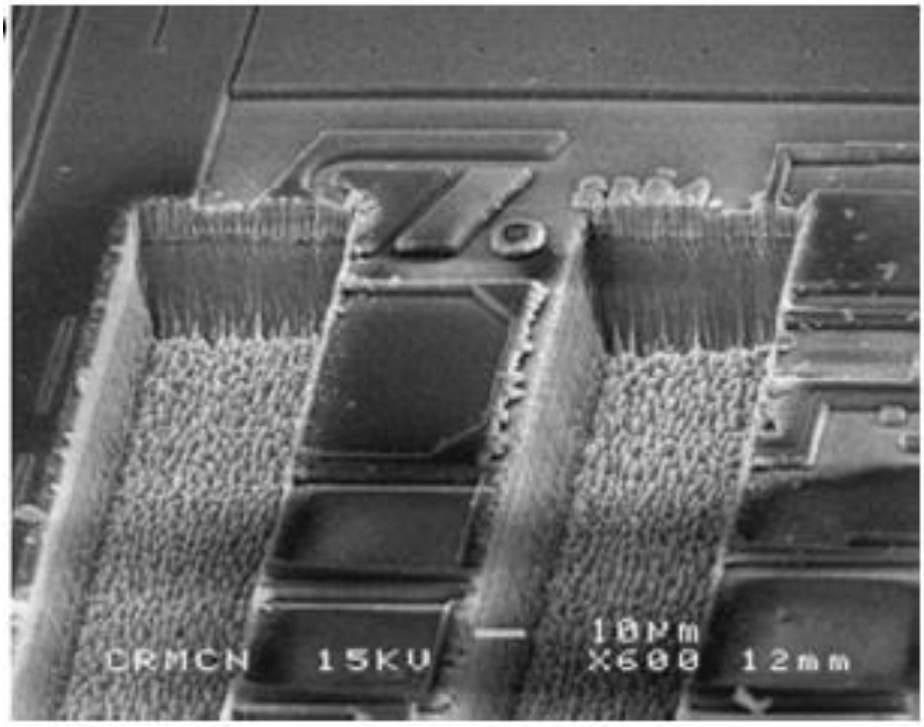

Figure 20: SEM image of engraved micro-cavities in an integrated circuit [105].

A common application of lasers in scribing has been in the manufacture of various types of photovoltaic cell [106]. In this application, lasers are used to isolate charge generation regions, these areas are subsequently interconnected and the charge generated is extracted. To achieve high efficiency in charge generation these scribes must be as small as possible whilst maintaining the high electrical resistivity between collection strips. Initially, CW/LP lasers were used in PV cell manufacture, now USP systems with the extra advantages have become a very attractive tool for manufacturing these cells.

Figure 21 shows how a solar cell generates useable current, which can be extracted as electricity. This can be used to power individual devices or fed back into the national grid. One of the drawbacks of using solar energy is the low conversion efficiency between solar energy and useable electricity [107]. Researchers in this field generally aim to either improve efficiency or reduce manufacturing costs.

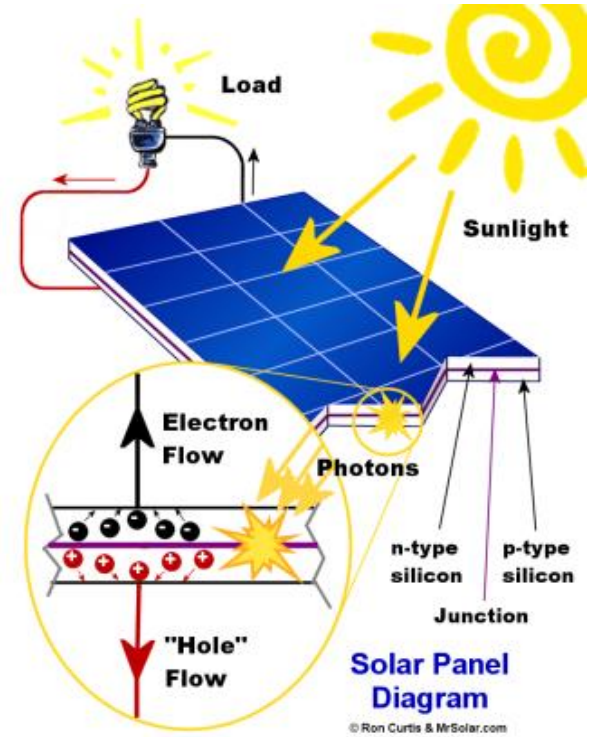

Figure 21: Simplified diagram of how a photovoltaic cell converts light into electricity [108].

When sunlight strikes the cell, the energy in the photons promotes electrons from the valence band to the conduction band; creating many electron-hole pairs. The electrons and holes begin to move toward the PN junction, when they reach this junction the recombination that occurs generates a small voltage, which can be extracted as useable electricity.

2.8.8.2 Bioscience, chemistry and medical applications

The application of lasers in the manufacture of biological, chemical and medical reactor technology; also called lab-on-a-chip or microfluidic devices is expected to increase due to the high quality and precision of the devices that can be manufactured in this way [109, 110]. Examples of the use of microfluidic systems include:

- Blood analysis for disease/drug identification or determining blood-sugar levels.
- Detection of harmful chemical or biological agents.
- Targeted drug delivery, when combined with MEMS devices.

2.8.8.3 MEMS and MOEMS

Micro-Electro-Mechanical Systems (MEMS) and Micro-Opto-Electro-Mechanical Systems (MOEMS) are batch manufactured integrated systems [111]. MEMS devices can convert a physical stimulus into electrical, mechanical or optical signals and vice versa. These devices can be utilised in actuation, sensing and other functions. Generally, fabricated MEMS and MOEMS devices are significantly smaller, lighter, more functional and

more reliable than the components they are replacing. The cost of fabricating these devices with USP lasers is also favourable due to the versatility and high throughput of high energy and repetition rate lasers. Figures 22 and 23 shows two MEMS structures, these where produced using ns and fs lasers respectively.

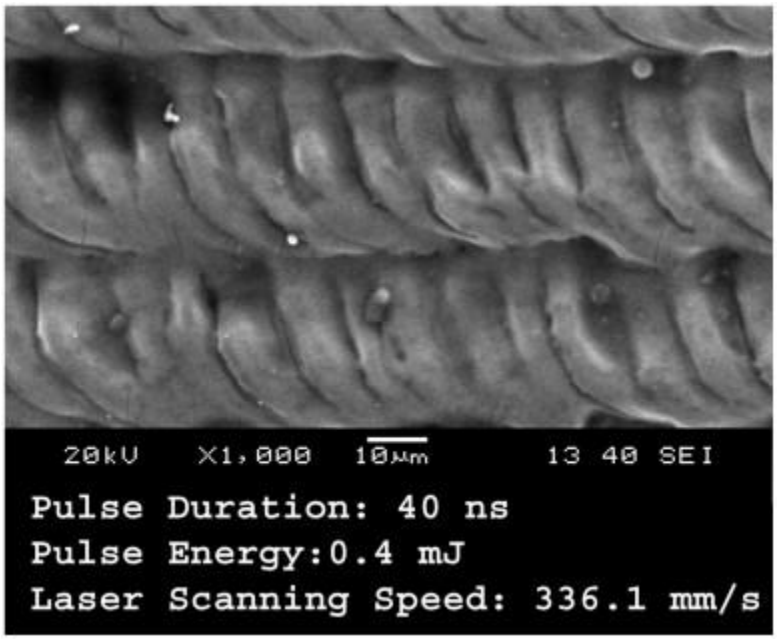

Figure 22: SEM image of a laser machined MEMS structure. This coil structure was designed to improve cooling performance [112].

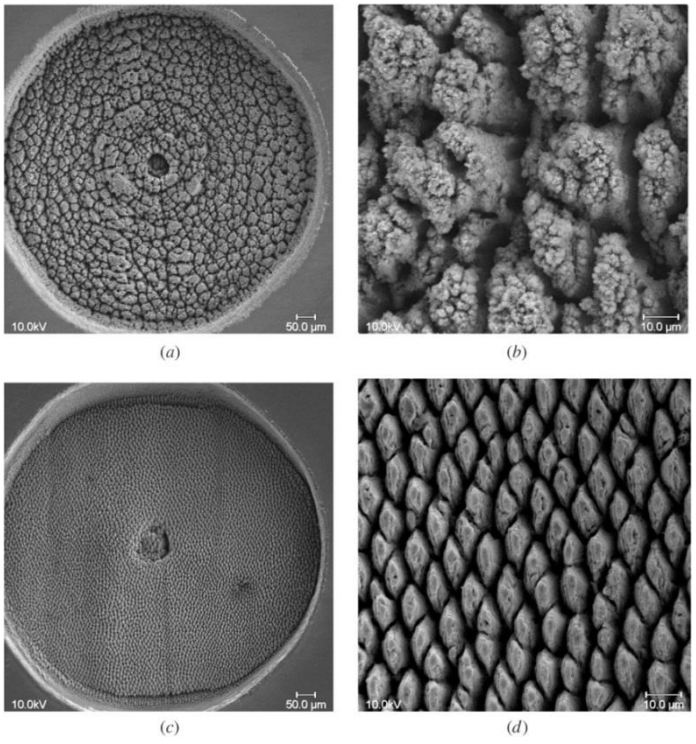

Figure 23: Scanning electron micrographs showing nominal 1 mm diameter diaphragms fabricated in 4H–SiC using a femtosecond pulsed laser: (a) profile using 0.15 mJ, 12 pulses per spot; (b) bottom of the profile shown in (a); (c) profile using 0.05 mJ, 36 pulses per spot; (d) bottom of the profile shown in (c) [113].

2.9 Laser cleaning

Laser cleaning is a process term applied to the removal of unwanted or contaminant material from the surface of a substrate. To date, laser cleaning has been mostly used in the conservation of artwork and heritage items and in the removal of debris from semiconductors.

The idea of using lasers to remove material was first presented by Arthur Schawlow, who patented the "laser eraser" [114], a device designed to remove mistakes from typewritten documents. This was in reality an attempt to highlight the use of lasers as a non-military weapon [115], however the invention never found widespread use due to the rise of word processors.

One of the two major applications of laser cleaning is art and heritage restorations, the items that have undergone laser cleaning are varied and include: sculptures [116], paintings [117] and even some buildings [118]. Lasers were first applied to the cleaning of artworks in 1972 by John Asmus [119], whilst working on laser holography in Venice. Asmus noticed that the darker encrustation on the statues he was studying was removed without damaging the statue itself. This gave rise to the selective vaporisation mechanism in laser cleaning (discussed in chapters 2 and 5) and initiated the use of lasers in conservation.

Not long after, in the early 1980s, Bell laboratories working with Susan Allen and her group at Florida State University, developed several techniques for the removal of surface contaminants from semiconductors and silicon wafers [120,121]. Given the increased use of personal computers at the time it can be intimated that this work assisted in reducing the cost associated with fabricating the silicon processors used in PCs, thus making them more affordable and accessible to consumers. This work produced a patent for a high efficiency laser cleaning technique in which a thin layer of a water-alcohol mixture was deposited on the surface just before irradiation took place; this was laser steam cleaning which is discussed further in the next section.

2.9.1 Mechanisms of laser cleaning

Since the inception of laser cleaning, a range of mechanisms have been determined that allow for removal of unwanted material from the surface of a substrate. There are a wide range of mechanisms, which can be categorised generally into three groups; however surface removal is not limited to a single mechanism and there may be an overlap with other cleaning processes.

1. Evaporation processes: this includes mechanisms were vaporisation is used to remove material, such as selective vaporisation and ablation.

2. Impact processes: in these processes a physical force imparted leads to material removal. These include spallation, shock, dry and steam cleaning.
3. Vibration processes: an acoustic or thermo-elastic force is used to remove material. Examples of this type of cleaning are transient thermal heating and angular laser cleaning.

2.9.1.1 Selective vaporisation

This mechanism of laser cleaning was uncovered during Asmus' original work in Venice (mentioned above) [122]. By operating with either CW or LP lasers at relatively low intensities (10^3 – 10^5 Wcm^{-2}) removal of surface encrustation could be achieved selectively; whilst leaving the substrate almost wholly unaffected by the treatment. The principle underlying this process was attributed to the difference in linear absorption coefficients between the encrustation, which was usually dark, and the substrate, which was white and had a low absorption coefficient (figure 24). When irradiated with a laser the darker layer absorbed a greater proportion of the incoming beam; this lead to a localised increase in temperature to a value above the vaporisation point. Meanwhile the lighter substrate would absorb a lower amount of energy and therefore experience only a small temperature rise; well below the damage threshold. It is possible to account for the temperature differential and determine the self-limiting effect using a 1D heat equation [123].

One drawback of this process is the degree of thermal loading required. Whilst it may be suitable for materials such as marble, which can handle a sharp temperature increase; it is not suitable for more fragile artworks such as pictures, wooden carvings and gilded frames.

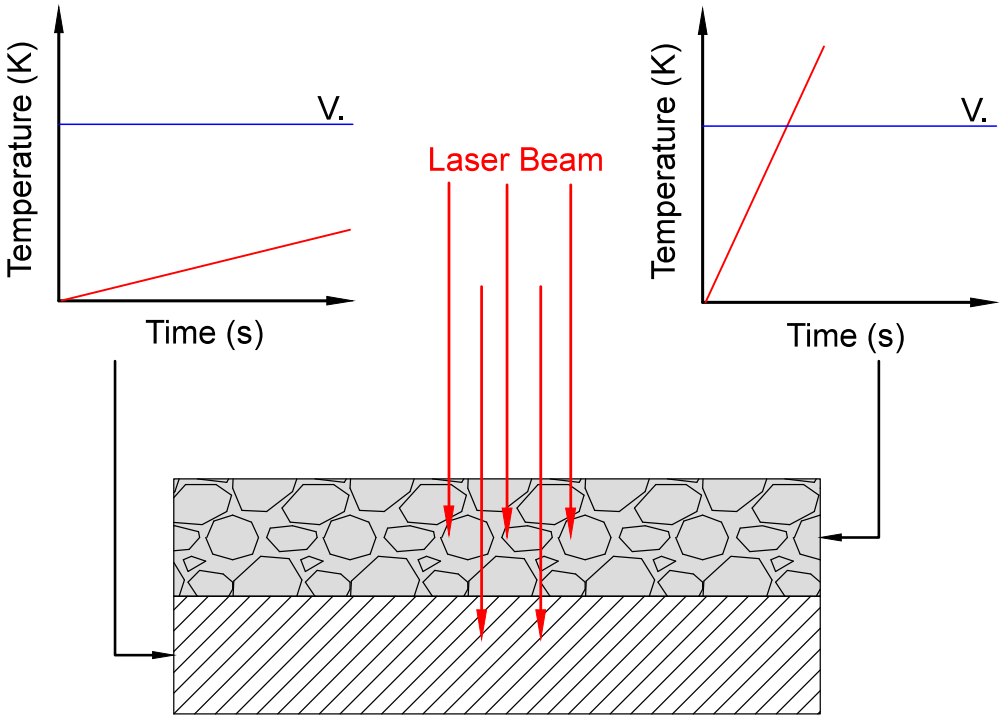

Figure 24: Principal of selective vaporisation. The graphs indicate the temperature difference between the encrustation and substrate, which is due to differential absorption of the incoming laser beam. The blue line (V.) represents the vaporisation point of each material.

2.9.1.2 Spallation

Asmus' subsequent papers introduced the use of high intensity ns lasers in the spallation of contaminant material [124]. By using high intensity (10^7 – 10^{10} Wcm^{-2}) LP laser systems it is possible to induce a different mechanism of laser cleaning, spallation. Using a Q-switched laser it is possible to generate ns pulses (1 – 100 ns); these pulses induce significantly less heat in the substrate than in selective vaporisation, making this a more favourable operating mechanism for conservators. The high intensities of the incoming pulse are sufficient to raise most materials above their vaporisation temperature; within this vaporised material high temperatures of typically 10^4 – 10^5 K are produced. The hot vapour becomes partially ionised and begins to strongly absorb the incoming radiation, creating a plasma just above the surface; shielding the sample from subsequent laser pulses. As the plasma is heated further, extremely high localised pressures of between 1 – 100 kbar are generated near the surface; this causes microscopic compression of the substrate surface. As the pulse ends this pressure is released and the surface relaxes; as it expands a thin layer (1 – 100 µm) is spalled away from the surface, as shown in figure 25.

It is possible to remove a significant amount of material using this mechanism; however the user must carefully control the cleaning process as the high intensity pulses can damage the substrate.

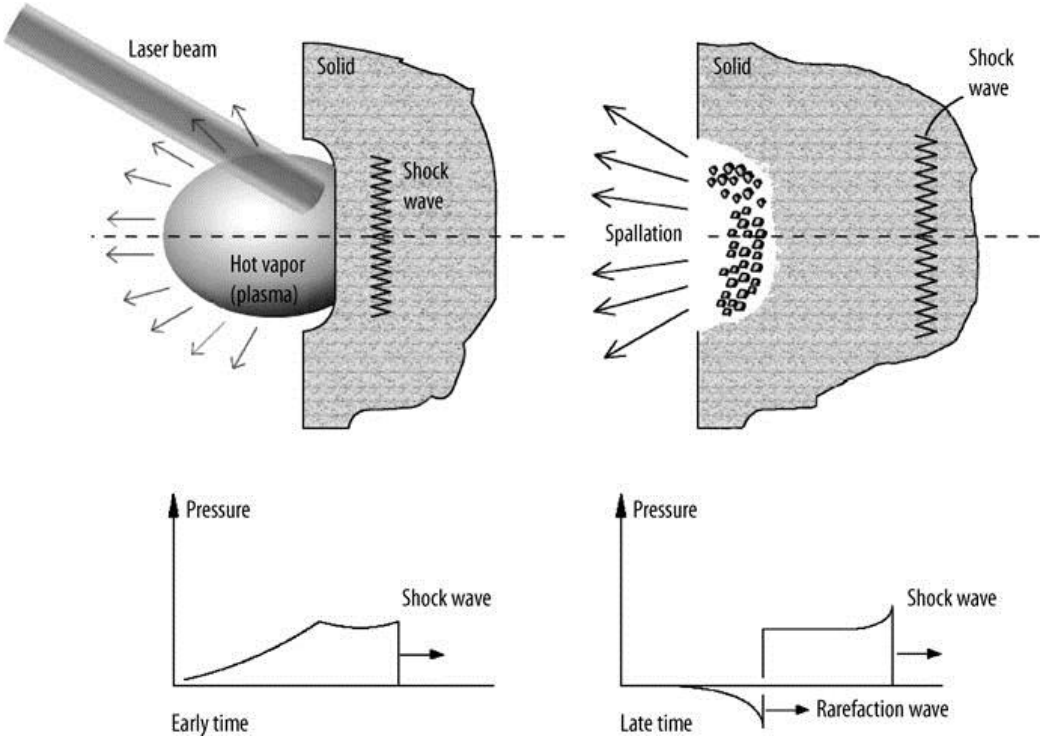

Figure 25: This diagram shows the mechanism of spallation. Image taken from Laser materials processing by Steen [125].

2.9.1.3 Shockwave

Shockwave cleaning [126] also utilises the high pressures generated by ns pulses on the surface of the target material. However, unlike spallation where vaporisation of a small amount of the encrustation is used to generate plasma, shockwave cleaning relies upon air breakdown to generate a high pressure wave above the surface, leading to material ejection. One of the main factors controlling the removal efficiency of this process is the separation between the incoming beam and the material being removed; reducing this distance improves the amount of material removed but the higher pressures experienced by the substrate can lead to surface damage. Figure 26 shows a diagram of the arrangement required for shockwave cleaning, in this configuration one of the main advantages is that the beam does not interact with the target surface minimising the thermal input from the laser and reducing the likelihood of causing damage to the object.

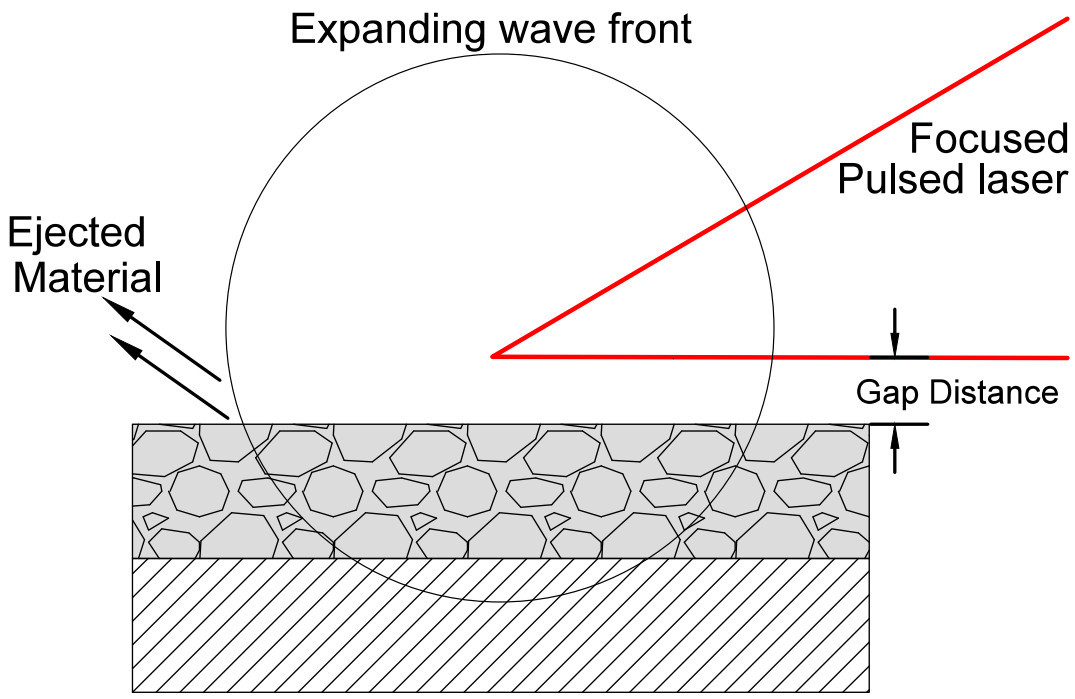

Figure 26: Mechanism of shockwave laser cleaning. A focused pulsed laser is used to breakdown the air directly above the contaminant. The expanding wave front ejects material at the sides.

2.9.1.4 Dry and steam cleaning

Similar to selective vaporisation, dry laser cleaning takes advantage of the difference in absorption between the contaminant and substrate. The difference between these two techniques is that strong absorption in either the substrate or contaminant can be used to induce material removal. When utilising the substrate the incoming beam is strongly absorbed in the sample causing the surface to oscillate; this vibration is sufficient to overcome the Van der Waals (VdW) forces between the contaminant and the surface, enabling removal. In the opposite case, were strong contaminant absorption is utilised, the contaminant will begin to oscillate instead leading to material removal. These vibrations were determined experimentally [127], to be induced by thermoelastic expansion and contraction of the material which experiences stronger absorption.

In steam cleaning [128], a thin film of water is used to cover the surface of the sample; when irradiated the water is quickly heated to well above 373.15 K, causing a change in state. The rapid boiling and subsequent expansion of the water vapour is sufficient to overcome the VdW force of attraction between the contaminant and substrate. Rapid heating of the water can proceed through strong substrate, strong liquid and same liquid-substrate absorption; in all cases irradiation causes rapid boiling and material expulsion, this is shown in figure 27.

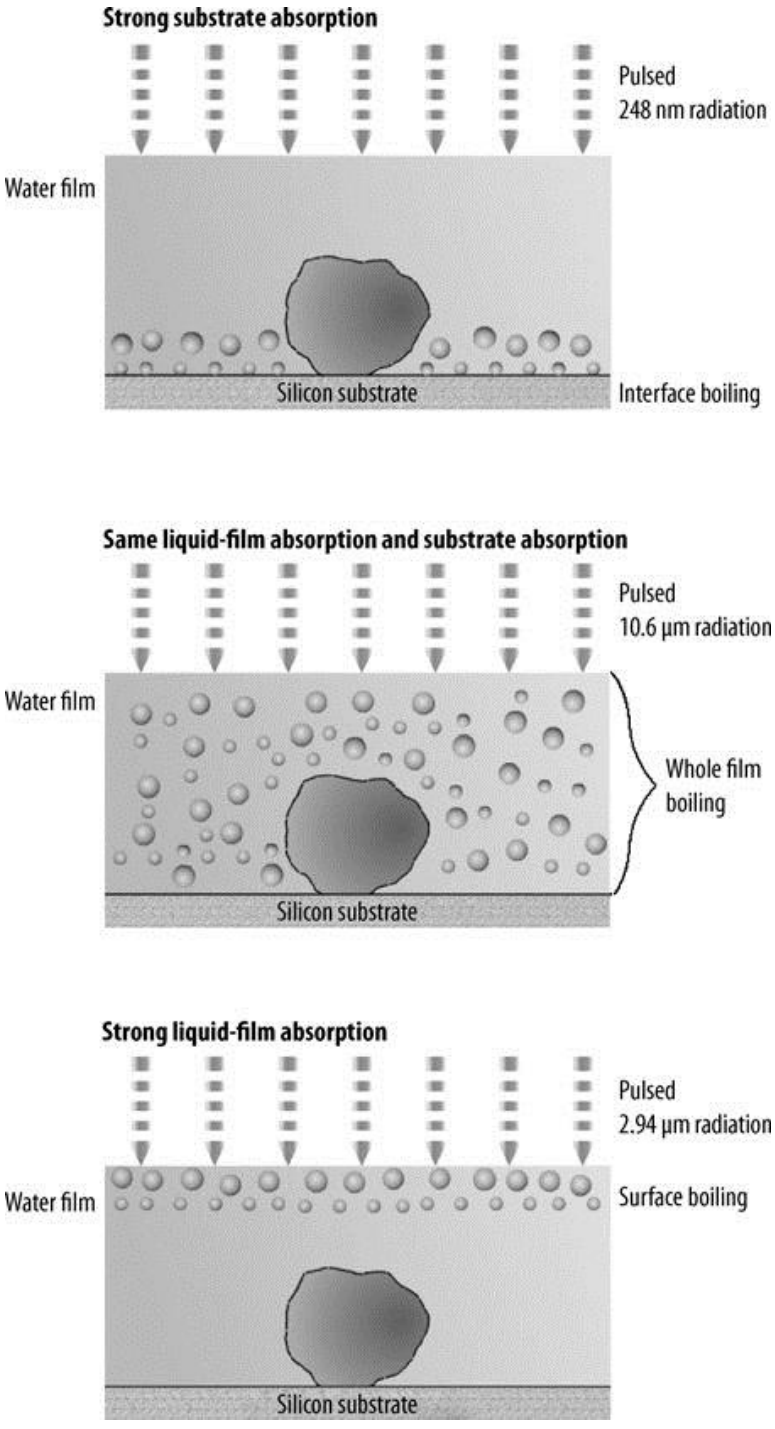

Figure 27: An image showing the mechanism involved in laser steam cleaning for the removal of small particles from the surface of silicon wafers [129].

2.9.1.5 USP cleaning

More recently, new methods of laser cleaning have been studied which utilise USP lasers operating in the ps and fs time scale. Due to the extremely high pulse intensity (>GW) material removal does not occur through conventional rapid heating of the contaminant but through ablation, which is more akin to surface sublimation. One of the key benefits of laser cleaning with these systems is the low thermal loading and near diffraction limited beam size. This enables precision removal with minimal thermalising of the substrate. Using equation 1.4 it can also be shown that the absorption depth of USP is of the order of nanometres. The nano scale absorption, low thermal loading and near diffraction limited beam provides users with a greater degree of control over contaminant removal. However, the trade-off for precision is a significant increase in the time taken to clean an area. This makes ultra-short pulse cleaning unsuitable for extremely thick contaminant layers (>1 mm) or large items. However, new high repetition rate ps and fs lasers may improve the time taken to clean large areas and thick contaminants. Figure 28 shows an example of USP laser restoration; in this work artificial contaminants are removed using USP laser systems and compared to the results achieved when using an ns laser. In this instance, the ns laser is shown to remove a greater amount of material than with fs pulses.

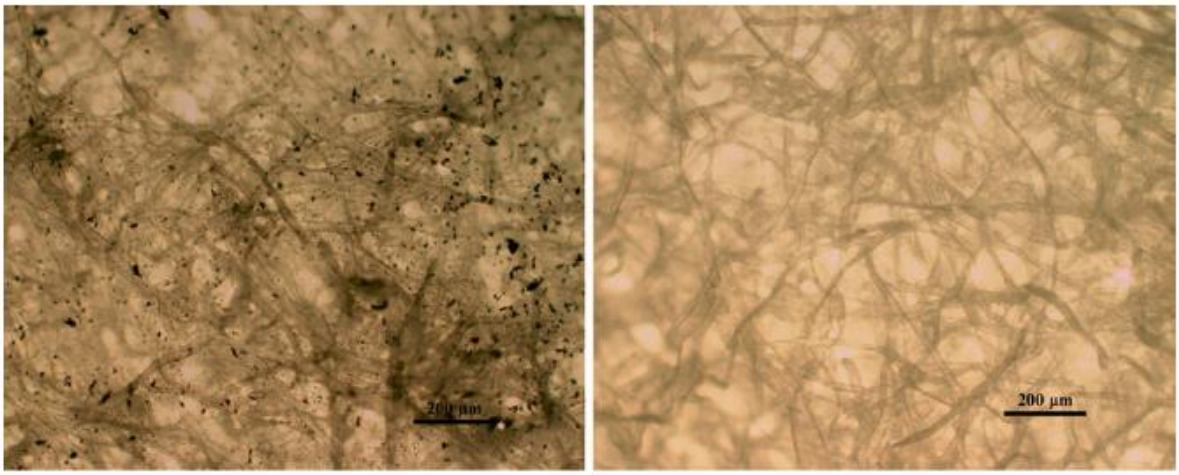

Figure 28: Optical microscopy (OM) images of femtosecond and nanosecond laser cleaned areas of artificially soiled Whatman filter paper at laser fluences of 50% of the damage threshold value of pure paper. (a) 28 fs, 0.10 J/cm2, (b) 8 ns, 5.0 Jcm^{-2} [130].

2.9.1.6 Applications of laser cleaning

The main use of laser cleaning techniques has been in the conservation of artworks and other cultural heritage items. Laser cleaning has been widely applied in this field with several groups dedicated to the use of lasers in cultural heritage being established, examples include the groups at the FORTH Institute of electronic structure and lasers

(IESL), and the Conservation centre in Liverpool. Lasers are currently being used in a wide variety of restoration cases, which build on previous work. A wide variety of items including statues [110], sculptures [131], paintings [132], jewellery [133] and wood [134] have been restored using laser techniques. The advantage of the laser cleaning process method in these case studies was that it, generally, improved the conservation process by reducing the likelihood of causing damage to the surface when compared with more traditional techniques such as sand and water blasting or chemical solvents. Using the laser method also reduced the time taken to complete the project and removed the need for specialist chemical disposal. It is important to note that the laser method did have some drawbacks, such as inducing photo degradation in polymers. This all but prohibits the use lasers in the restoration of paintings, as the induced change in the polymers ultimately degrades the paints used in the picture [126]. When utilising laser cleaning techniques, vaporisation of the surface contaminants also resulted in the production of airborne material which could be inhaled, adversely affecting the health of the conservator [135] if proper extraction and health and safety systems are not in place.

In addition to being used as a restoration tool, lasers have also found widespread use in both microscopic and spectroscopic imaging of the surface using laser spectroscopy techniques such as fluorescence lifetime imaging [136], breakdown spectroscopy [137] and confocal microscopy. Other techniques, such as optical coherence tomography (OCT) [131], second (SHG) and third (THG) [138] harmonic generation allow conservators to visualise the subsurface structure of the sample. These techniques have improved conservation treatments by providing conservators with scientific data containing the exact composition and structure of the piece. This information combined with the skill of the conservators allows them to discern the most appropriate method of restoration. This not only reduces the time taken to complete the project but, importantly, reduces the likelihood of errors, which could cause irreversible damage.

Outside of the conservation field, laser cleaning has also been applied in an industrial capacity. The first industrial application was the removal of particulate debris from the surface of semiconductor wafers (discussed previously). However, lasers have also been applied in degreasing, rust removal and paint removal [139]. The range of items that have undergone laser treatment varies from small components to ship hull cleaning [140]. In many instances the laser method has been used as it can be integrated with a pre-existing production line or because it could improve on other cleaning processes.

2.10 Selective processing of materials using laser sources

The aim of this thesis is too elucidate on the mechanism and application of selective materials processing with USP laser systems. In the previous sections of this chapter the use of selective processing has been indicated in some previous work, such as selective vaporisation for laser restoration and in the fabrication solar cells. The majority of the work in the field of selective processing has been carried out using more traditional CW or LP laser systems, were the mechanisms of ablation are well understood and can be modelled effectively. There is significantly less work available on the application of selective processing using USP lasers. This may be due to a variety of factors including the lack of robust "engineering ready" systems or the technique not being considered viable due to the extremely high intensities produced by near diffraction limited USP systems. Recently, this has begun to change and in several papers the authors have directly referred to being able to remove thin film material without inducing damage effects at the surface [141,142]. By investigating the applicability of selective ultra-short pulse (SUSP) laser materials processing the author hopes to provide researchers with a method of assessing the viability of their SUSP processes, which can be applied to their investigation and enable them to actively identify ideal parameters to utilise this technique in materials processing. Through the application of this method, in a series of case studies, it is hoped that the SUSP is demonstrated to be a viable method for materials processing, by improving on current micro-processing methods and, potentially, giving users access to wholly new ideas.

3 Experimental equipment

In this section the equipment used to undertake experiments and analyse results are introduced; the use of each piece of equipment will be discussed in the relevant chapter.

3.1 Clarke MXR femtosecond laser

A Clarke MXR CPA – 2010 180fs laser system with output wavelengths of 387nm and 775nm was used to remove the flame sprayed layer deposited on to a solar cell. The maximum pulse energy available was ≈1 mJ at a frequency of 1 KHz; this system is compact due to the split level design. The full system consists of a laser head, DT – 505 Pockel cell drivers, ORC–1000 power supply and a closed loop water cooling system (20±1^{o}C). The upper and lower sections of the laser system, figure 29, have two distinct functions; the lower level is used to generate and stretch seed pulses whilst amplification and compression is performed in the upper level.

A solid-state fibre coupled diode laser with an output wavelength of 980nm is used as a pump source for the seed laser. The seed is an Er-doped fibre laser producing a wavelength centred at 775nm; any output dispersion from the seed was eliminated using a compressor. Seed pulses are then frequency doubled and stretched before moving to the upper level where they are amplified. The Pockel cell controls synchronisation between the seed laser and the pump laser for the Ti:Sapphire amplifier. After amplification pulses are compressed before being emitted as ultra-short pulses. The Clarke MXR utilises chirped pulse amplification (CPA) to generate high optical intensities; this technique is discussed in chapter 2.

Figure 29: Clarke MXR fs laser system. This system has a split level arrangement with the seed pulses generated in the lower half before undergoing amplification using CPA in the upper half. The output wavelengths available are 387nm and 775nm the frequency is 1 kHz.

3.2 TOPAS – C

A Light Conversion TOPAS – C (model: 80C1) is a two-stage parametric amplifier of white light continuum; the system consists of several subunits: pump beam delivery and splitting optics (PO), white-light continuum generator (WLG), pre-amplifier (PA1), signal beam expander-collimator (SE) and a power amplifier (PA2). These subunits are combined into a single system with computer controlled translation and rotation stages; allowing fast and accurate positioning of optics for tuning the output wavelength.

Figure 30: TOPAS-C (left) is a compact system for tuning output wavelength. The image on the right shows the TOPAS-C integrated into the Clarke MXR optical path. The laser system is in the background whilst the TOPAS-C is on the left and the Aerotech control stage is on the right.

A 775nm wavelength pulse is split into two components, with a small fraction used to produce white light continuum (WLC). The remaining pump beam and WLC are focussed

into a pre-amplifier crystal; pulses are timed and overlapped non-collinearly inside a non-linear crystal undergoing parametric amplification producing a signal beam. After amplification the residual pump and idler beams are blocked leaving only the signal beam to pass through.

In the next step, the signal beam is expanded and collimated before passing into the power amplifier. Here, pre-amplification pulses can be increased to tens- hundreds of micro-joules provided there is sufficient pump intensity; to achieve this the input beam is reduced in size using a telescope; the beam remains collimated throughout. Finally, the second pump and signal beams are overlapped collinearly to produce well collimated signal and idler beams at the desired wavelength.

Wavelength tuning in pre-amplification is achieved by varying the delay between the white light pulses with respect to the pump pulse and changing the crystal angle to optimise phase-matching. Wavelength tuning in the power amplifier, firstly, requires adjustment of the pre-amplifier wavelength followed by optimising the angle of the second crystal with respect to the secondary input beam.

Once fully calibrated output wavelength tuning was easily controlled using a proprietary software package provided by Light Conversion.

3.3 HighQ picosecond laser

The HighQ picosecond solid-state laser (Model: IC-355-800 ps), figure 31, is a compact and easy to use class IV laser capable of emitting three wavelengths: 1064, 532 and 355nm. The system has a high beam quality, M^2 of ≈1.2[1], can operate at four different frequencies 5, 10, 20 and 50 kHz with a maximum output of 2 Watts at the fundamental wavelength (1064 nm).

The system comprises three main sections: the laser head, controller, and cooling system. The laser head contains the seed laser, regenerative amplifier, pulse picker, Pockel cell, optical isolator and frequency conversion crystals. To generate ten picosecond pulses the system utilises direct diode pumping and semi-conductor saturable absorber mirrors (SESAMs).

[1] Manufacturer quoted value

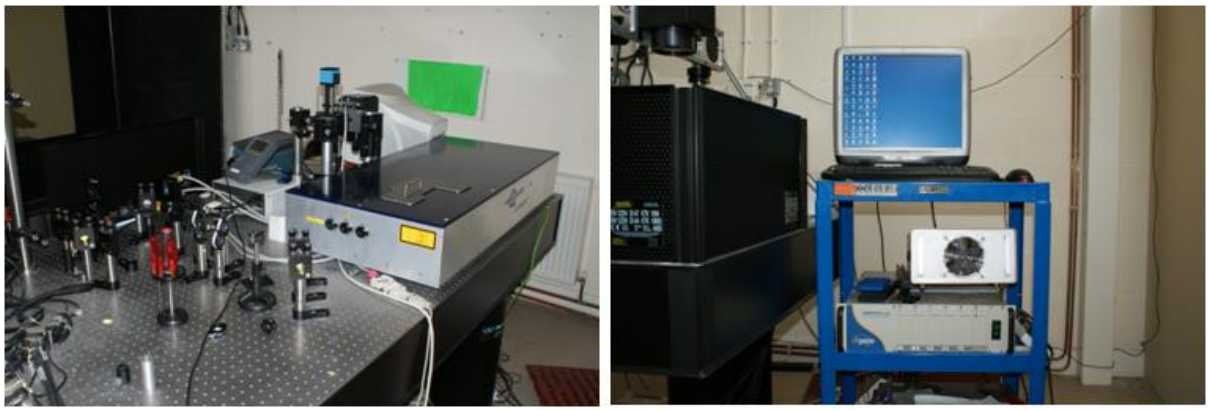

Figure 31: Left: The High-Q laser with three output wavelengths of 355nm, 532nm and 1064nm. Right: control computer (top), power supply for scanning head (middle top) and Aerotech control stage drivers (middle bottom).

HighQ provides users with a graphical user interface (GUI), shown below in figure 32. This software was initiated from the desktop by clicking the "Highqlaser.exe" icon; a communication link between the terminal and laser controller was established through the "open/close port" button.

Using this software the laser can be switched on/off or between standby and active. In standby the seed laser remains active but the trigger for the Pockel cell is disabled preventing pulses from leaving the cavity. Once switched on the system remains in low power mode until the "Pulse Picker enable" box is checked; after this the full power range is accessible. The output power can be altered adjusting the slider control or entering an integer in the range between 300 and 2600 in the edit field.

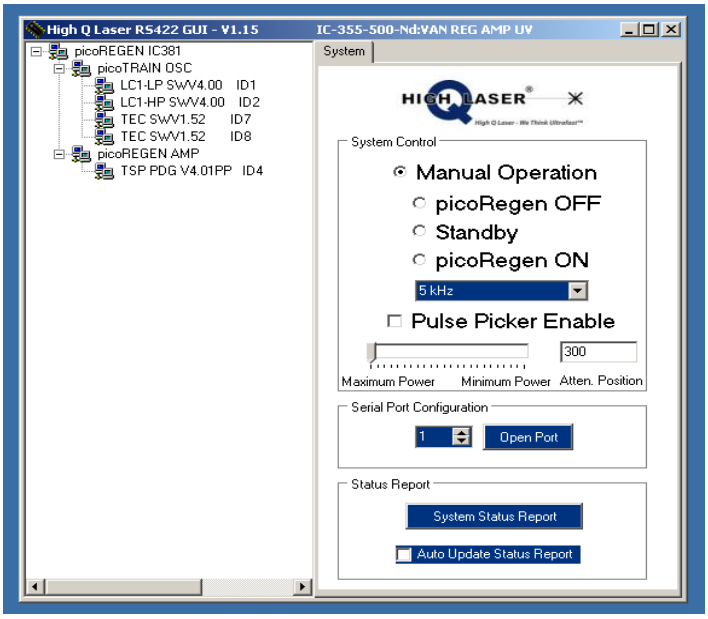

Figure 32: HighQ laser control software. This interface allows the user to switch the system on/off and to control frequency and power.

It was also possible to control the number of output pulses using a function generator. By synchronising with the seed laser and applying a TTL signal at timed interval it was possible to alter the number of pulses emitted; ranging from a single pulse up to and including the maximum frequency.

The HighQ ps laser requires water cooling; a Lauda (model: RE/107) closed loop re-circulating chiller ensures that the temperature remains constant (19^{o}C). To ensure stable performance from the laser water is circulated at a low flow rate and a low pressure.

3.4 Coherent Talisker picosecond laser system

A Coherent Talisker high power ps laser system (figure 33) with an output wavelength of 532nm and a maximum frequency of 40 kHz was used in micro fabrication. High-energy ultra-short pulses (10ps) were produced using a mode locked fibre laser in conjunction with diode pumped solid-state amplifier.

The entire system consisted of a laser head assembly, power supply, harmonics controller, control station and closed-looped water cooling. Full control of the frequency, pulse energy and harmonic wavelength was provided directly by the power supply front panel or the attached computer.

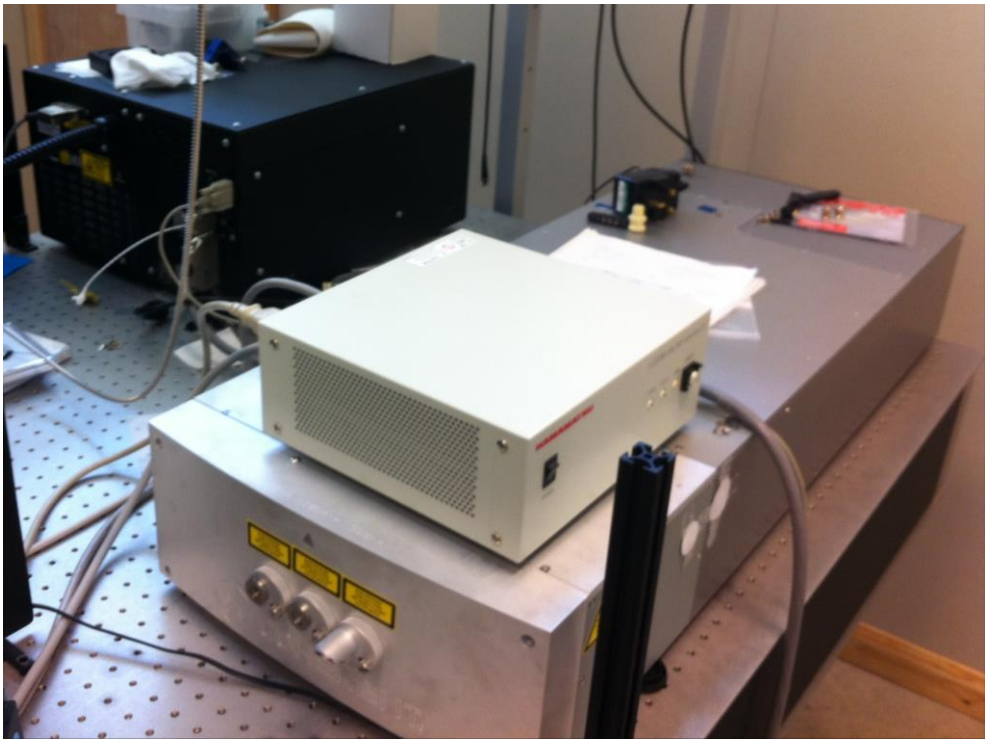

Figure 33: Talisker laser system, the laser controller (black box towards the rear of the image) controlled the system. The laser head is the white and grey slab (in the foreground of the image). In this section of the system the pulses are amplified and can undergo frequency conversion to the desired output wavelength; the three outputs shown are for 1064, 532 and 355nm.

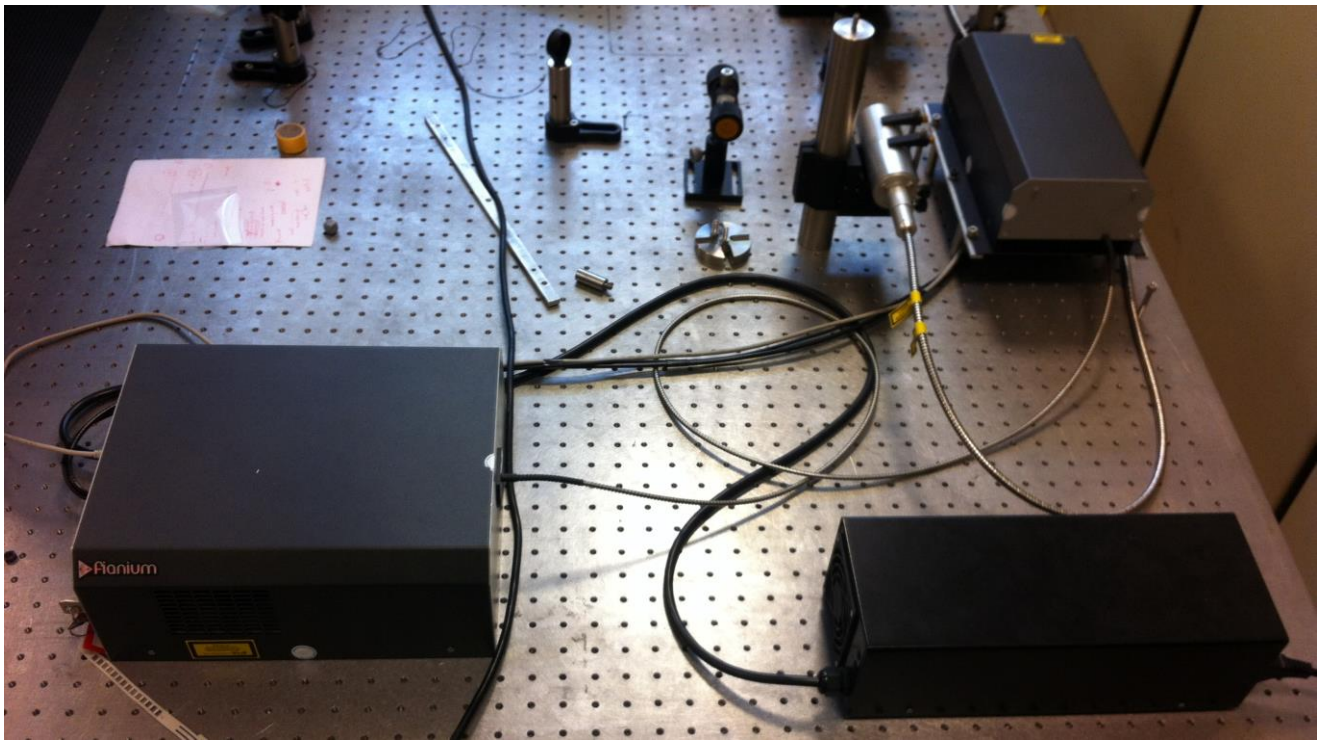

Figure 34: Fianium laser system. The system comprises a power supply (bottom right), a controller, doped fibre oscillator and a laser head. Amplification of the pulse energy takes place after it has left the fibre to prevent photo-darkening.

3.5 Fianium FemtoPower picosecond fibre laser

The Fianium FemtoPower 4μJ is an easy to use, extremely compact and robust 20ps fibre laser system; it is turnkey operated and controlled using software provided with the system. The maximum output power was 2W at a wavelength of 1064nm; there are two output frequencies of 0.2 and 0.5 MHz. The beam quality was excellent with an M^2 value of ≈1.1[2]. The system consisted of three components: the laser controller, doped fibre and laser head. This system uses a rare earth element doped fibre oscillator to produce picosecond pulses; which are subsequently amplified in the remote head before being emitted. A passive cooling system was used by this system.

Upon exiting the laser head the beam was passed through a CVI dual wave 3x beam expander (DWBX-4.0-3x); this device was coated to allow for ≥90 % transmission of IR wavelengths. This telescope corrects for spherical aberration and collimated the output beam. The beam was subsequently passed through a turning mirror and periscope before entering the scanner head for focussing. The scanner head for this system was controlled via the Waverunner software. The Aerotech stage allowed for movement in XYZ; in this system the Z-axis could move through 100mm.

[2] Manufacturer quoted value

3.6 Spatial Light Modulator (SLM)

A Hamamatsu Photonics phase only spatial light modulator (SLM) was used to divide a single input beam into multiple beams for parallel processing. The SLM display (figure 35) is attached to a controller unit and a computer; the LCD acts as a secondary monitor screen. Using the software provide by Hamamatsu, different CGH's can be created and then moved to the second screen (LCD). The CGH's used during processing are shown in the relevant chapter.

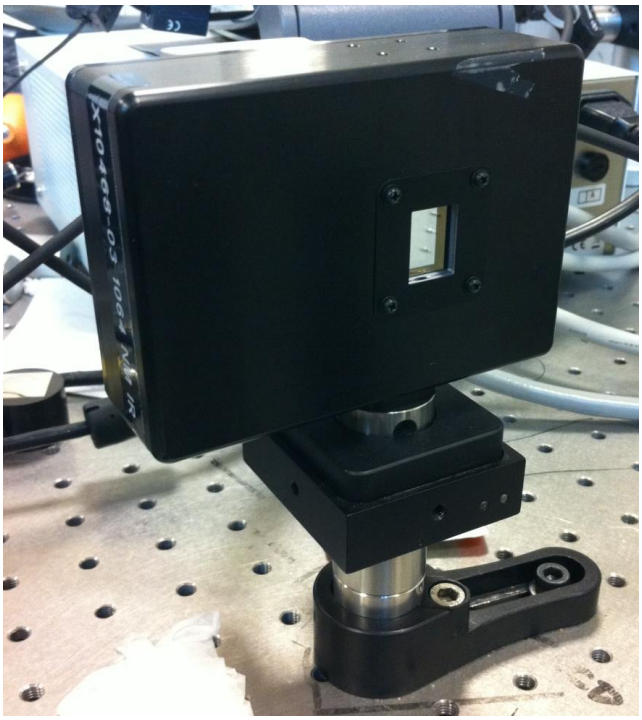

Figure 35: SLM in optical path. Beam is directed onto the LCD were user defined computer generated hologram (CGH) are displayed. The CGH is determined by the user and can be used to generated multiple beams or as a method for pulse shaping.

CGHs created on the computer are converted and displayed on the liquid crystal display by applying a discrete voltage to individual pixels. As a result an electric field associated to each pixel is established causing a change in the refractive index of the liquid crystal. The change in refractive index (Δn) is used to display the hologram and enables modulation of the incoming light. Phase modulation can be described using the following equations:

$$\delta \approx 2\Delta nd \tag{1.16}$$

$$\Delta\varphi = k \cdot \delta \approx \frac{2\pi}{\lambda} 2\Delta nd = \frac{4\pi}{\lambda}\Delta nd \tag{1.17}$$

Where δ is the optical path difference, $\Delta\varphi$ is the phase change, k is the wave number, λ is the wavelength and d is the thickness of the liquid crystal.

The SLM used in this study displays 8 bit CGH, where voltage variation on the CCD pixels has 256 levels (2^8); therefore the phase change of the reflected light will vary as a function of the grey level. Figure 36 shows a near linear increase in phase modulation with increasing grey level.

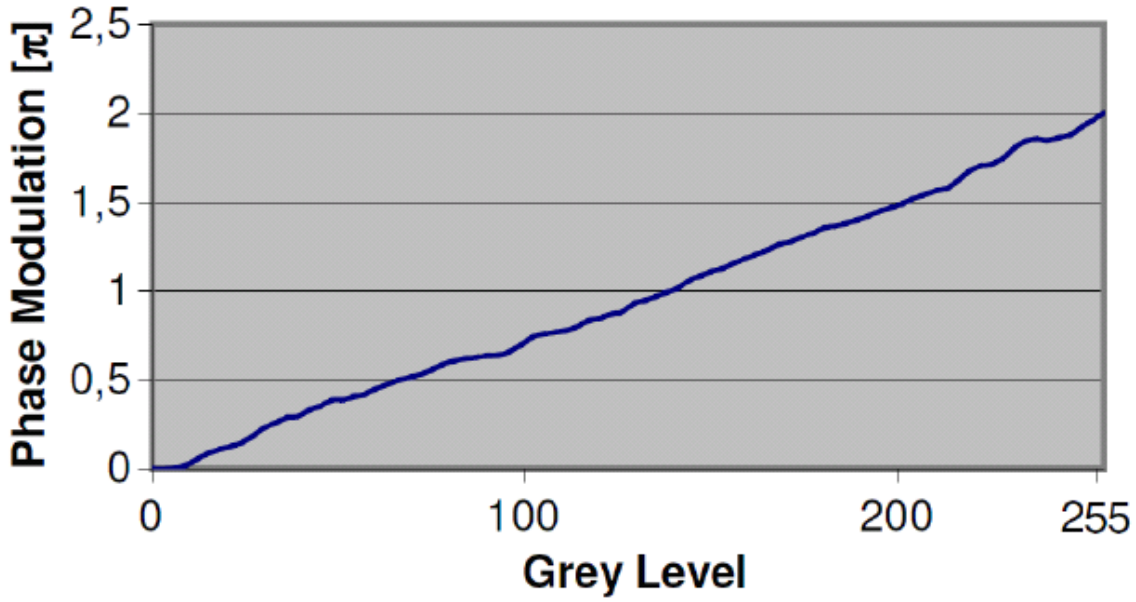

Figure 36: Results measured from a Holoeye SLM showing a near linear increase of the pahse modulation with varying grey level.

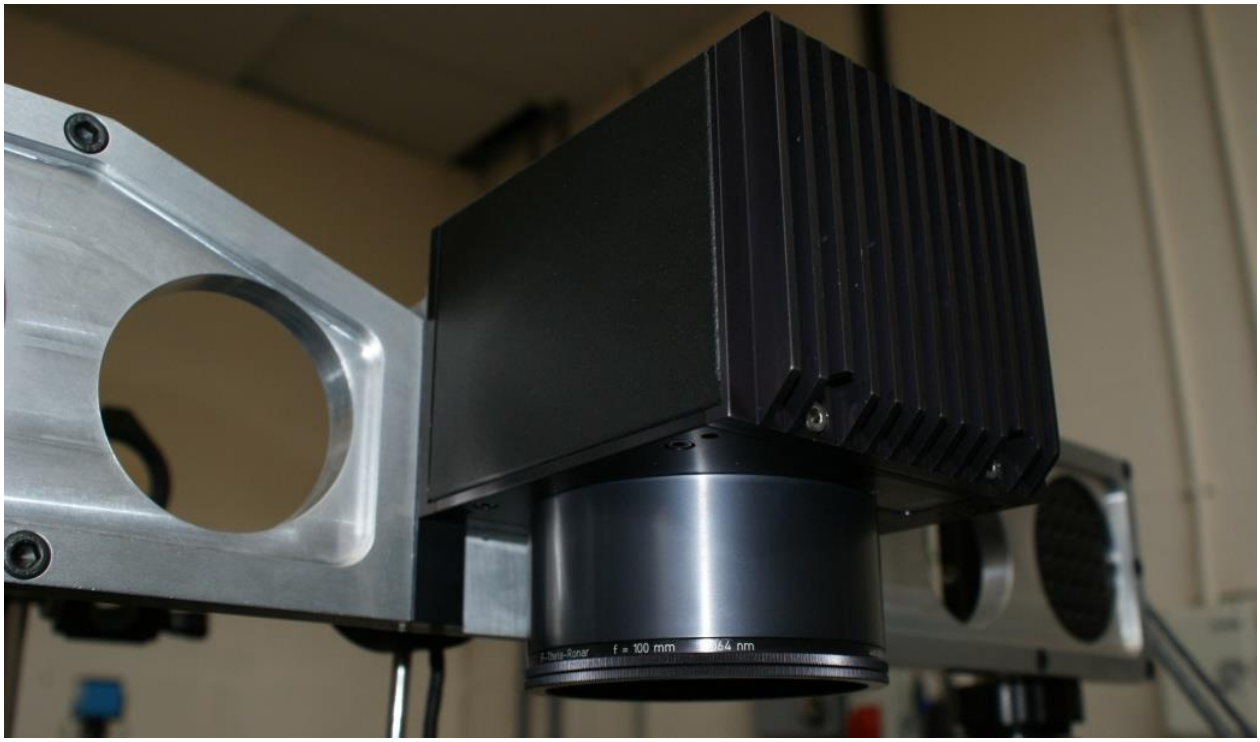

Figure 37: Nutfield scanning head positioned on the HighQ system. Two galvometer mirrors directed the beam through a 100mm flat field lens.

3.7 Nutfield scanning head

To operate the laser beam for both microfabrication and restoration a Nutfield scanning head (model: XLR8) was used. The scanning module consisted of two galvanometers, two optics and integrated driver electronics. Each galvanometer controlled movement in one of either X or Y, whilst flat field lenses were used to focus the beam on the target area. This combination allows the system to be configured to deflect laser pulses for the majority of applications. The maximum working field of the scanning head is 70 x 70 mm, with a resolution of <4 µm. For most of the work undertaken in this study this scanning field was sufficient, in cases where this was too small edge effects were avoided by integrating scanning with movement of the Aerotech stage.

3.8 Aerotech motion and positioning control system

Throughout laser processing accurate control of both the position and location of the sample relative to the beam is very important. Deviation from the required parameters can result in an increase in failure rates of microfabricated devices or damage to a conservation items. To ensure high precision removal of thin films this study used Aerotech stages, Npaq Auto-motion 3200 drivers and the Nview HMI programming interface.

Figure 38: Aerotech stage (left) and driver unit (right). This stage was attached to the HighQ laser and provided movement in 5-axis XYZUA.

The Aerotech stage can provide high accuracy movement through three or five degrees of freedom (figure 38), depending on the laser system, with a resolution of 0.5µm in all directions.

This CNC stage was controlled by the Npaq driver and Nview GUI. Commands were either entered directly into the software using the Nview programming interface or loaded from any other CNC language. Movement of the stage can be defined in two ways, as either absolute co-ordinates (with respect to the table origin) or as relative co-ordinates (with respect to the last position); this allows for both independent and directed axis movement. In addition it was possible to define values for the traverse speed and vector speed (directed movement), acceleration and deceleration and shutter control.

3.9 Scanner application software

During this study two different software programs were adopted to design the microstructures presented later in this thesis: SamLight and Waverunner. SamLight was used for operating the HighQ whilst Waverunner was used on the Fianium system; the user interface for both is very similar. In the grid area in the centre of the screen various patterns can be drawn or loaded from other files. The laser operating parameters such as traverse speed, number of repeat scans, hatch spacing and hatch type can be specified in this software.

3.10 Tektronix AFG 3021B function generator

Figure 39: Tektronic function generator; using this system it was possible to gate the laser to emit a specific number of pulses. This enables the user to produce frequencies up to the maximum produced by the system.

As mentioned, it was possible to extract a specific number of pulses from the HighQ laser system, this cannot be done with the standard software (Highq.exe); to achieve this a Tektronic AFG function generator (figure 39) was used. The AFG can produce different functions including: continuous, square, burst and sine waves. Within these functions it was possible to alter different parameters including frequency, width and delay. By selecting suitable functions and parameters to trigger TTL signals, various pulse frequencies were achieved.

3.11 Analysis Equipment

3.12 WYKO NT1100 White Light Interferometric Microscope

In addition to the Nikon digital microscope a WYKO NT1100 interferometric microscope was employed to collect further information about the surface pre and post processing. The WYKO NT1100 is a non-contact optical profiler which provides accurate images of the surface topography in three planes (XYZ). The resolution in Z was accurate to a few nanometres; this allows for precise measurements to be made. In the XY planes the accuracy was of a micron level. An analysis package called Vision was provided with the microscope, this software allows for dissection and formatting of surface data.

Figure 40: White light interferometry profiling system. A light source was used to illuminate the surface of a target object; interference fringes at the focal plane are used to produce an image. Measurements were initiated and analysed using the Vision software provided.

A white light source is passed through a beam splitter separating the beam into two individual beams of equal intensities. Half the beam is delivered to a reference mirror and the other half to the test surface; the reflected light from both surfaces is then recombined generating an interference pattern. Due to the low coherence of white light, interference fringes are observable only over a short range for each focal position. During a scan several measurements were taken over a user determined range and recorded using the Vision software.

During post processing the software recalls saved data and selects the vertical position corresponding to the peak fringe signal for each point on the surface; the data obtained is decoded and combined creating a complete 3D picture of the surface morphology.

Interferometric measurements were taken by placing a sample on an adjustable XY stage; this ensured the area of interest was illuminated.

The Z position of the stage was altered to ensure that the sample was located at the focal point where interference fringes were observed; the number of observable fringes can be adjusted. Before measurement can take place the objective and field of view (FOV) needed to be checked to ensure that the values shown in the software match the interferometer; this made certain that accurate readings were recorded. For some samples, the amounted of reflected light was increased to ensure a strong enough signal to record an image; in these instances samples were placed on a polished stainless steel surface.

Once at focus and the software parameters had been checked a scan was performed on the sample; following this procedure ensured that measurements were accurate. Using the Vision software data for observing the depth of ablation, surface roughness and topography were obtained.

The system is calibrated at periodic intervals by measuring against a standard sample provided with the microscope and comparing results.

3.13 Phenom Scanning Electron Microscope

Figure 41: SEM area of LLEC. The SEM was a Phenom FEI scanning electron microscope. Samples were loaded into the base unit for optical microscopy before pumping downing for SEM.

A Phenom (FEI) scanning electron microscope (SEM) was utilised to provide detailed surface images at high magnification (min: x24 and max: x24k).

The key features of this system are its small footprint, quick load time (<30 seconds), image quality of up to 2048 x 2048 pixels and high resolution (≈30 nm). Sample control is automated within the system to improve ease of use.

Samples were attached to a specialist sample holder using a double sided adhesive carbon disk; this was then attached to the sample cup and positioned into the SEM. The sample was loaded into the SEM in two stages; initially into an optical microscope and then into a high vacuum chamber for SEM analysis; surface images were taken in both environments. To prevent surface charging occurring on non-conducting samples a sputter coater with a Gold target was used to apply a thin layer to the surface; improving image quality. Several of the image parameters can be altered depending on user requirements;

image capture options were full, topographic A or topographic B. Manual or automatic adjustment of the image focus, contrast, magnification and illumination was possible.

3.14 Energy Dispersive X-ray analysis

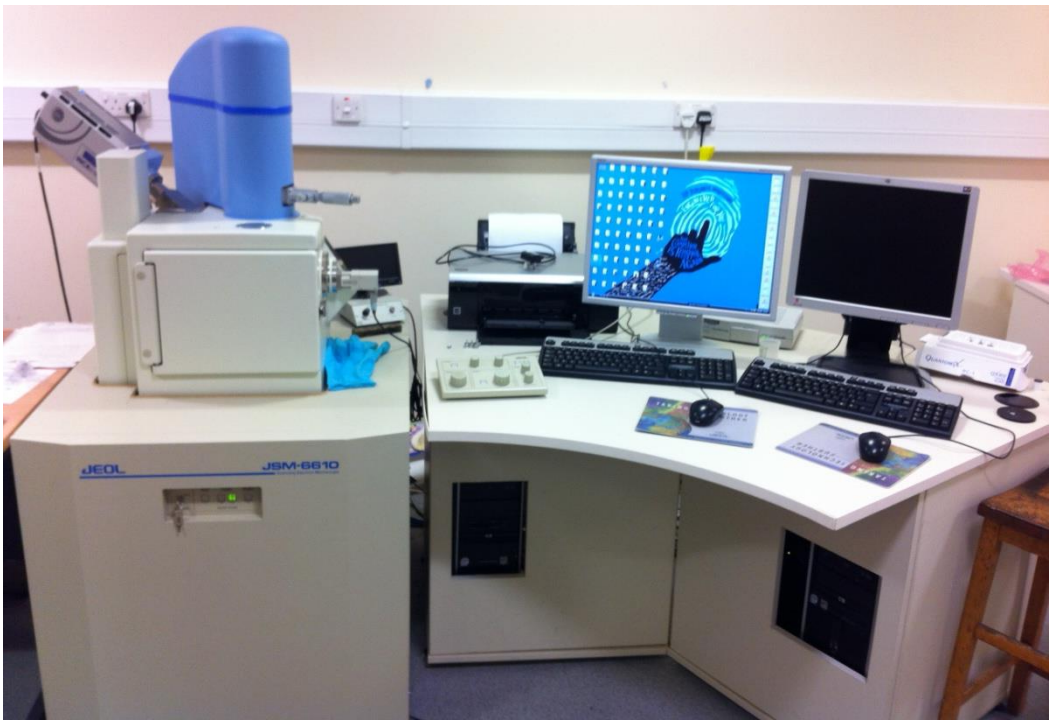

Figure 42: Jeol SEM. In this machine samples are placed into the chamber (left, middle) before being placed under high vacuum. Imaging and magnification is controlled using the computer and monitor on the left of the setup. The second computer and monitor are used to record EDX measurements.

A second SEM (Jeol JSM 6610) was employed with a magnification range of x3 – x300k and a resolution of 3nm; the accelerating voltage of this system can be varied between 0.3 – 30kV. The specimen stage was a 5-axis eucentric goniometer with a maximum displacement of X = 125mm, Y = 100mm, Z = 80mm, T = -10 – 90^{o} (tilt) and R = 360^{o} (rotation).

Samples were placed into a chamber before being evacuated to low pressure; dielectric samples were taped to the sample holder using conductive tape to prevent surface charging. An infrared miniscope attached to the side enabled viewing of the sample whilst under high vacuum.

Attached externally to the Jeol SEM was an Inca X-act EDX (Oxford instruments) analyser; the EDX detector converts the energy of individual x-rays into voltage signals of proportionate size. This Inca system was made up of three main components: x-ray detector, pulse processor and analyser. The first step in analysis was conversion of x-rays to charge using the ionisation of atoms in the semiconductor crystal; secondly the charge signal was converted to a voltage by a FET preamplifier. Finally, the voltage signal is input

to the pulse processor to determine the energy of the x-ray. Results were subsequently displayed using proprietary software as a series of peaks which, using the inbuilt material library, can identify individual elements by x-ray energy.

Figure 43: Oxford Instruments Inca X-act EDX analysis machine. This system was attached to the Jeol 6610 SEM.

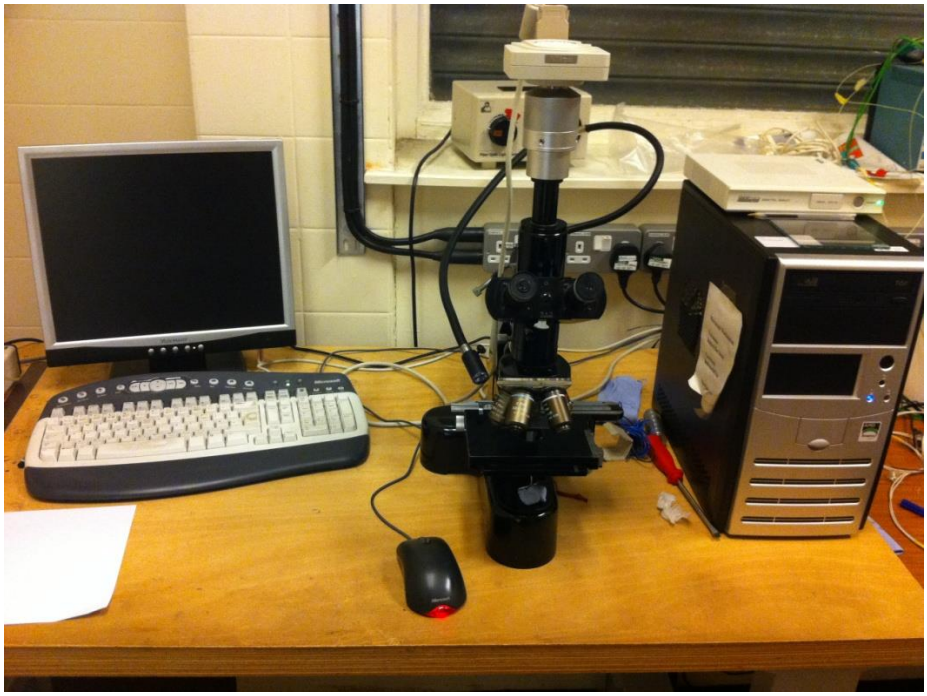

Figure 44: Nikon optical microscopy system. The microscope (centre) rotates to increase magnification; images are taken through the top down camera and transferred to the computer terminal.

3.15 Nikon Digital Microscope

The Nikon microscope provides 2D images of the surface condition before and after treatment with the laser. The microscope has several available magnifications to allow detailed inspection of the surface pre and post processing; these were: x5, x10, x20, x50 and ×100.

The optical microscopy setup comprises three sections: optical microscope, digital camera and Nikon post processing software. The use of a conventional microscope allows the user to observe the surface by adjusting the focus and light to the required conditions; then by switching to the Nikon software the user is able to operate the digital camera to capture, save images and make basic measurements in the XY plane.

The microscope is calibrated regularly by measuring standard samples provided by Nikon; if the measured dimensions do not coincide with those of the samples the system can be adjusted by resetting the scale values of the software.

3.16 Spiricon optical beam profiler

The laser beam profile has a significant effect on the micro-processing quality achieved by laser interaction. In this study, a Spiricon beam profiler (Model LBA-300/400/500PC) was used to inspect the laser beam profile.

Figure 45: Spiricon profiling head. An unfocussed beam passes through a gap (left) where it is split into two components; the majority of the beam passes through but a small portion is diffracted onto the CCD (right). The recorded signal is then displayed on a PC.

This LBA-PC beam profiler system consists of a Spiricon LBA-PC frame grabber card, analysis software, CCIR camera, beam splitter and several neutral density (ND) filters to attenuate the beam; these protect the CCD from damage due to the high optical intensities produced by short and ultra-short pulse lasers even when split.

The CCD has a maximum measurable area is 8 x 8 mm with a pixel spacing of 9.9 x 9.9 µm; this is used to provide high speed, high resolution 2D and 3D intensity profiles and numerical beam profile analysis. To reduce errors in profiling the system monitors the background signal and improves the signal to noise ratio through subtraction of this data; however the beam and some settings on the profiler such as camera gain, camera blooming effect and laser beam attenuation can still impact the accuracy of the measurements. With careful control of the camera an accuracy of ±2% can be achieved.

3.17 Materials and sample preparation

The objective of this thesis is to elucidate on the mechanisms, which enable or prevent selective processing of thin films irradiated with ultra-short pulse lasers. The selective processing method was subsequently applied to four case studies to ascertain the applicability of this technique in a micro processing.

To achieve this, an investigation in to the controlling properties was carried out using samples of indium tin oxide (ITO) coated onto a white float glass substrate. These samples were purchased from Knight optical (WIW5050-I02) with dimensions of 50 x 50 mm; the glass substrate was standard white float glass, with an optical transmission greater than 90% from UV to the near infrared. The float fabrication method produces almost optically flat glass (λ/25 mm). The ITO film was deposited on top of the float glass via vacuum coating up to 20 Ω; the ITO mimics the flatness of the float glass. All of the ITO samples tested had a 100 nm thick film coated on top of the glass substrate. The ITO and glass flatness were also measure using white light interferometry, which recorded surface roughnesses of ≈6 nm and ≈8 nm respectively.

Indium tin oxide (sn-doped In_2O_3) is formed through doping of indium oxide with tin; this produces a cubic bixbyte structure [143,144] in this process the In^{3+} atoms are substituted out of the structure and replaced by tin. Indium tin oxide (sn-doped In_2O_3) is a commonly used TCO material and has found applications in electrically heated windows and EMI shielding. First manufactured in the 1960s, ITO has become very popular with manufacturers due to its near metallic conductivity ($1x10^4$ Ω^{-1} cm^{-1}), transmission (≈95 % in the visible) and stability in most environments. ITO is a semiconducting material with a wide band gap of between 3.5 and 4 eV [145], the high optical transmittance is due to this gap. ITO has a refractive index of 1.96 at 1064 nm. Figure 46 shows the band structure of both sn-doped and undoped indium tin oxide. Doping is observed to reduce the band gap making it easier to generate electron hole pairs increasing conductivity. Due to the wide band gap it is difficult to use 1064 nm pulses (≈1 eV) to promote electrons from the valence into the

conduction band. Therefore, the strong absorption of ITO when irradiated with 1064 nm is attributed to free carrier absorption.

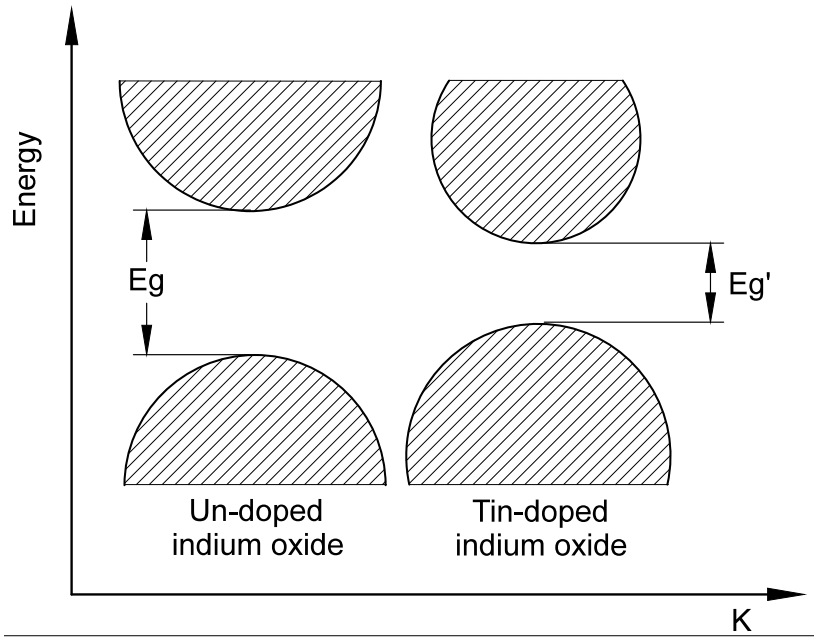

Figure 46: Schematic of the band structure of sn-doped and undoped indium oxide [146]. This shows how the doping process improves conductivity by reducing the band gap allowing more electrons to move into the conduction band.

After determining the controlling parameters, these methods were subsequently applied to four case studies to determine the benefits and limitations of selective processing in micro processing and restoration. The samples used in the case studies were ITO coated glass, a multi-layered thin film solar cell, a pair of Royal gloves and gilded frame sections.

In the second industrial micro-processing case study the fabrication of a low cost thin film was attempted; this cell was developed by Atmos technologies and consisted of several layers deposited on top of a float glass substrate. Combined these layers were used in the conversion of solar energy into electricity, which was then extracted. The cell consisted of four layers; the first two layers were the glass substrate and tin dioxide. These materials were purchased from Pilkington's as standard samples (model number TEC 7) and are commercially available under the TEC glass product name. The TEC series of glasses were developed as a range of products offering high optical transmission and excellent electrical conductivity and thermal properties. These glass products have been used in several applications including heat reflecting, electrochromics, computer screens, photovoltaic cells and shielding applications. In this study the TEC 7 model was selected as it had the lowest resistivity in the TEC series and has been previously used in photovoltaic applications. The thin film deposited on the glass was tin dioxide (SnO_2) which, like ITO, is a transparent

conductive oxide. SnO_2 was chosen in this case due to its excellent optical transparency, conductivity and thermal properties. The SnO_2 film is highly resistant to thermal changes and was an ideal thin film in this application were the subsequent layers are deposited using thermal spraying.

SnO_2 is a semiconducting material with a wide band gap between 3.4 – 4 eV and a refractive index of ≈2.0 [147].

On to this layer a film of silicon and aluminium oxide (≈70% and ≈30% respectively) was deposited using a flame spraying process. Initially, the powdered silicon aluminium mixture was fed into the process area via pressurised lines, when it reached the deposition zone the powder was rapidly heated by passing through an oxyacetylene flame to temperatures just beyond melting point. This viscous liquid is then deposited directly on top of the SnO_2 layer described previously, where it rapidly solidifies producing the flame sprayed oxide (FSO) layer. The SnO_2 film and flame sprayed layer form the p-n junction required to generate charge when solar energy interacts with the surface. This charge can then be extracted as useable electricity. To extract this charge a final layer of aluminium was to be deposited on top of the flame sprayed layer. This metal contact would have been adhered to the flame sprayed layer using physical vapour deposition (PVD). Figure 47 shows the structure of the photovoltaic cell.

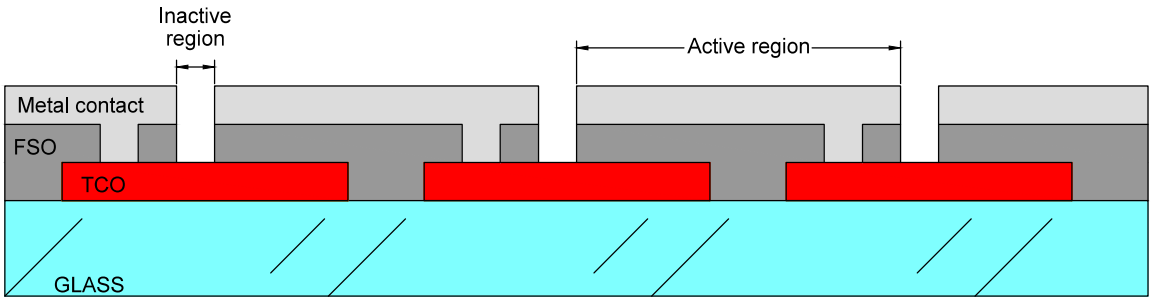

Figure 47: Schematic of the thin film stacked photovoltaic cell manufactured in case study two. Laser processing was used to scribe the TCO and FSO layers.

In case study 3, the use of selective removal in the restoration of a pair of gloves owned by King Charles I was investigated. The glove was treated in two stages; initially restoration of the leather section of the gloves was carried out. Leather is a durable, flame resistant material that is manufactured through the tanning of animal skin; there are several methods of tanning including: Vegetable, chrome, aldehyde, chamois, alum-tawed and rawhide. The gloves in this restoration are a soft cream coloured leather; to achieve this very light shade of leather it is thought that alum-tawed tanning was used. In this method aluminium salts are mixed with a protein binder (e.g. egg yolk); this mixture is then coated

onto the animal skin. One of the advantages of this method is its ability to produce soft, supple leather with excellent durability.

The second stage of restoration was carried out on the decorated gauntlet at the base of the glove, this consisted of several different materials that were combined to create a decorative pattern. The materials used to create the gauntlet were mother of pearl, red dyed silk, silver gilded threads and metals coils. The metal coils were attached to the edge of the gauntlet to provide extra decoration. Figure 48 shows an image of both gloves that were treated with laser radiation during the case study.

Figure 48: King Charles I gloves before laser treatment. The contamination of the white leather is clearly visible in this image. The decorated gauntlet is also shown. These images were taken from "Royal accessory under laser cleaning" by Abdelrazek et al [148].

The final case study was an investigation into the selective removal of bronze gilding from an organic binding layer. To investigate the removal process a series of model samples were fabricated using the method described by White[149]. This process was originally designed for the application of gold leaf gilding. However, as bronze gilding was usually added during restoration treatments as an alternative to gold leaf it was decided that following the gold leaf gilding process and substituting the gold leaf for bronze would provide a structure similar to conservation pieces.

Initially, a wood substrate was coated with a layer of white paint; the purpose of this coating was to act as a barrier preventing the organic binder, which was subsequently applied, from penetrating into the porous wood. If the binding medium penetrates the wood

then the adhesive properties are reduced, as there is less material for the bronze to adhere to. A typical binding medium is oil size; this is a polymer binder made of linseed oil and is a tri-glyceride, which contains a large amount of α-linolenic acid. A high number of unsaturated esters within this molecule make it susceptible to polymerisation upon exposure to air; this process is referred to by gilders as drying. By controlling the number of unsaturated ester groups the time taken to complete polymerisation can be varied; the drying time is then specified on the bottle. In this study, the oil size utilised was C. Robertson and Co. 1 – 2 hour oil size (Gold leaf supplies ref 2055/250). The drying time was important as part way through this process the bronze gilding was applied, if the drying time was too short it would become difficult to accurately apply the bronze gilding resulting in variable quality in the model samples. Similarly if the drying time is too long it increases the likelihood of contaminants becoming adhered to the surface again affecting the sample quality. The 1 – 2 hours drying time was well suited for sample creation, as it allowed for careful application without the risk of contamination due to prolonged exposure to the environment.

As the oil size nears the drying point (completion of polymerisation) the surface viscosity increases and becomes adhesive, at this point the bronze powder was added to the surface using a gilders brush; this is a soft brush that allows for consistent application of the gilding material (Gold leaf supplies ref 3000/2).

Bronze is a commonly used metal alloy that consists mainly of copper with tin as the main additive; however there are several different types of bronze some of which utilise zinc as the main alloying element. Bronze gilding, also called ormolu, is a commonly used substitute for gold leaf due to its similar colour and lower cost; as such it has been applied in many restoration treatments. However unlike gold, bronze is not a noble metal and over time the colour of the bronze changes as the main alloying element, copper, reacts with air forming new copper compounds (e.g. copper oxide or copper carbonate). The change in colour is observable by eye and causes a diminishment in the aesthetics of the piece; although this layer is usually only superficial eventually it can compromise the structure of the object.

These materials are combined to create the model samples, which all testing was carried out on; the structure of the sample is shown in figure 49. This shows the wood base at the bottom coated in the white paint, followed by the oil size and bronze gilding.

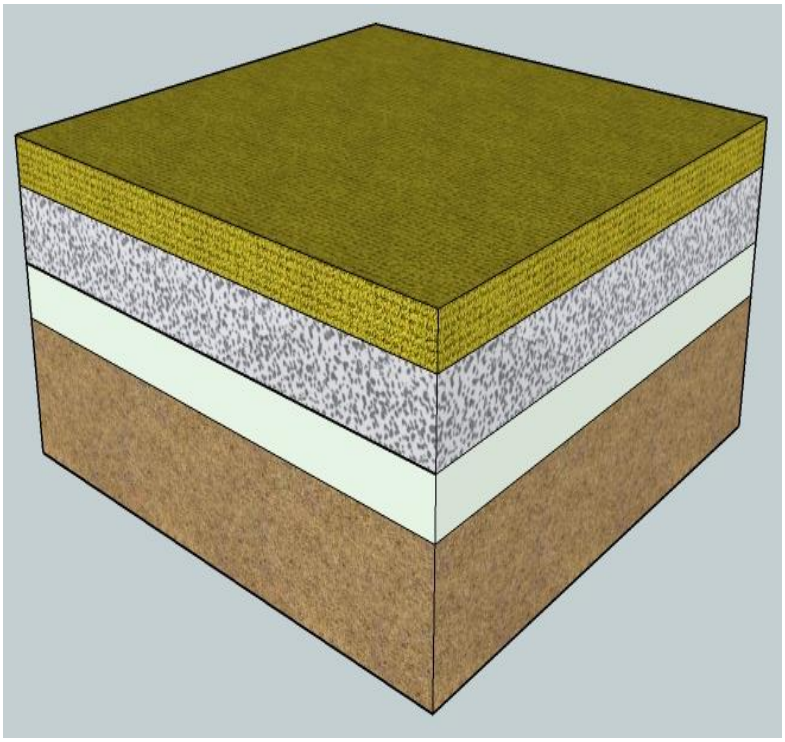

Figure 49: Schematic representation of the cross section of a model sample. The structure beneath the top layer is shown. The sample is comprised of (from top to bottom) bronze gilding, linseed oil, white paint and a wood base.

After completing testing on the model samples the results were applied to two small sections of a gilded frame. Initially these samples were gilded with gold leaf but during subsequent restoration were coated with bronze gilding as a substitute. Over time this gilding has changed in colour and now needs to be replaced. To test the parameters identified on the model samples laser restoration was attempted on these samples.

The experimental procedure for the fundamental investigation of selective removal and subsequent case studies is presented in the relevant chapters.

4 Selective laser processing

Using selective laser processing, material can be removed from multi-layered structures or devices without incurring damage to other materials. Using continuous wave (CW) or long pulses (LP), typically >1 ns, this process depends on differential absorption of the laser wavelength between two layers, evaporating the layer which experiences significant absorption whilst the less absorbing layer experiences a strictly limited increase in temperature, which results in no damage. An early example application of selective removal is conservation. This technique was first introduced in the 1970s by J. Asmus [114] and has since been widely utilised as a key tool for conservators, especially in the restoration of statues. Further to this work, selective laser processing has been actively adopted in CW and LP laser restoration (chapter 2).

With the development of low cost and more robust USP systems the use of these lasers in the micro-fabrication of complex components has seen a widespread increase in areas such as photovoltaic [81] and microelectronic [148] manufacture. Recently, an increase in the reporting of selective materials processing has been observed in papers by Zoppel *et al* [137] and Raciukaitis *et al* [150], indicating an increased interest in ultra-short pulse selective processing.

This chapter investigates the applicability of selective laser processing using USP laser systems. The controlling parameters of selective removal and process tolerances are identified and examined to provide laser users with a detailed insight into selective processing with USP lasers.

Indium tin oxide (ITO) coated on to glass was used as the test material. Initial research focused on determining key factors in achieving selective removal of the ITO by investigating the role of absorption (linear), ablation thresholds, thermal and incubation effects to establish an operating window for selective removal. Investigations on ITO were used to produce guidelines for determining the feasibility of selective removal.

This study investigated selective processing through exploitation of the difference in linear absorption using a 10 ps (HighQ) laser. Investigations were carried out systematically in the following order:

Absorption >> Single pulse >> Multiple pulse

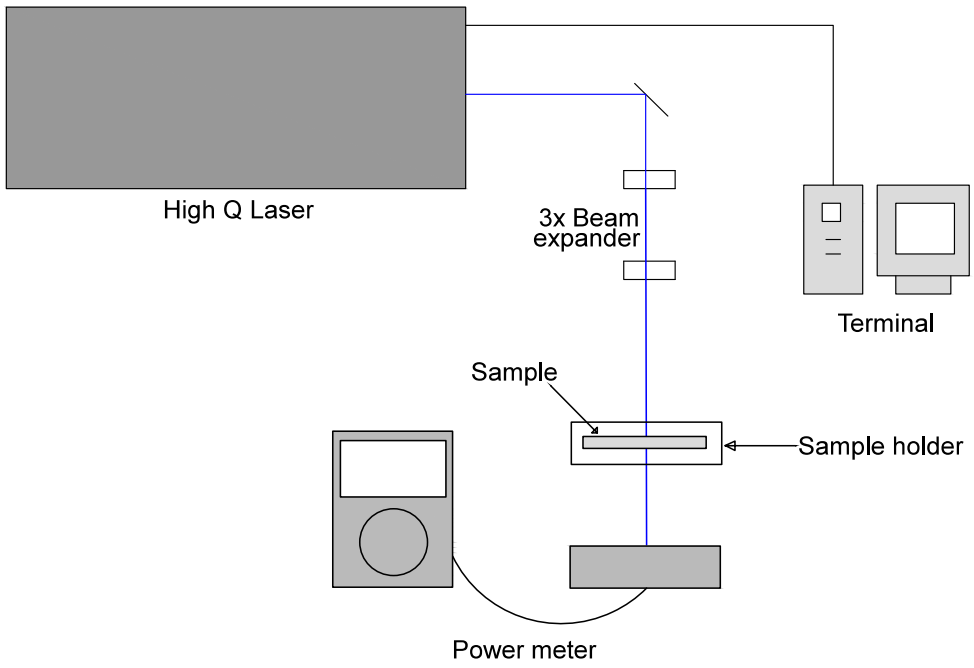

Figure 50: Modified HighQ setup. This optical arrangement was used to determine the absorption coefficient of the ITO thin film and glass substrate. The sample was placed after the beam expander to ensure that the beam was collimated. A Coherent power meter with a Fieldmaster head was used to determine the intensity of the transmitted light.

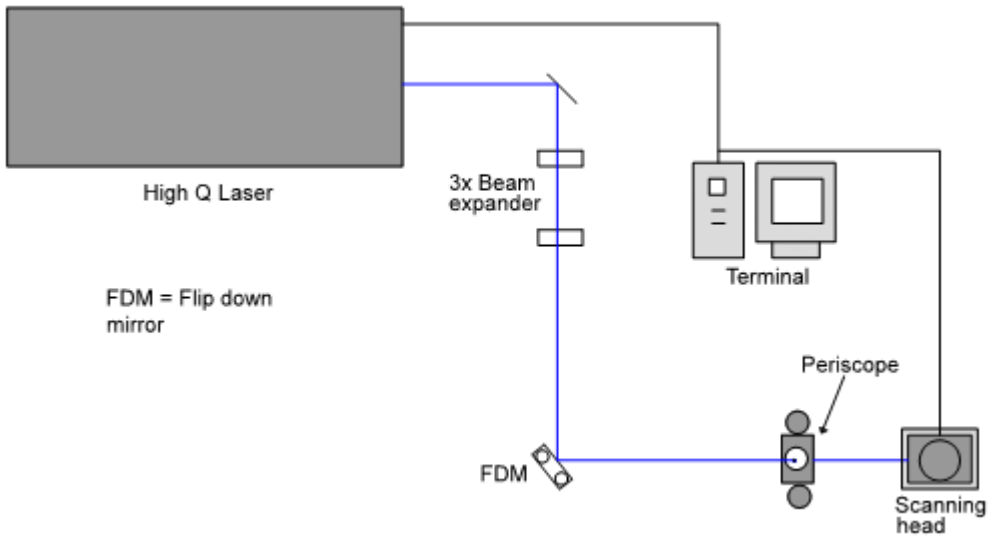

Figure 51: This image shows the standard configuration of the HighQ ps system. Both ITO and glass samples were placed, at focus, on a 5-axis stage under the scanning head during materials processing.

4.1 Experimental procedure

4.1.1 Samples used in investigation

For this fundamental investigation of selective processing, ITO samples vacuum coated on to a white float glass substrate were purchased from Knight optical (WIW5050-I02) with dimensions of 50 x 50 mm. Further details on the ITO and glass used in this study can be found in chapter 3.

4.1.2 Absorption coefficient measurements

The transmission of a monochromatic coherent USP laser source through ITO and glass was recorded; selective removal using CW or LP has previously been shown to have a dependency on the differential absorption rates between the film and substrate. A schematic of the optical arrangement is shown in figure 50.

To accurately determine the linear absorption coefficient, measurements were made using an ITO coated and uncoated glass sample; changes in transmission due to the glass substrate were accounted for to ensure only absorption in ITO was considered. The material properties are presented in detail in chapter 3. Each measurement was performed using a laser repetition rate of 10 kHz using near IR (1064 nm) and visible (532 nm) wavelengths.

4.1.3 Single pulse interaction

A series of single pulse holes were made on the surface using decreasing pulse energies; this allowed for the determination of the single pulse ablation threshold of both ITO and glass. Pulses were separated into individual spots by increasing the traverse speed of the scan head (Nutfield); a schematic of the ablation threshold test is shown below (figure 52). Each scan was 3 mm in length with a traverse speed of 800 mm/s; using a repetition rate of 10 KHz. These parameters were sufficient to clearly separate individual pulses. From each line five ablated craters were selected at random for analysis and measurements were carried out using optical microscopy (Nikon) and white light interferometry (WYKO NT1100).

4.1.4 Multiple pulse interaction

This experiment was undertaken to determine the effects of multiple pulse irradiation on the ablation threshold of both ITO and glass. In this test the number of impinging pulses and fluence were varied. Through the modulation of a pulse picker in the HighQ system it was possible to emit pulse trains with varying pulse numbers. Figure 53 shows a schematic of the multi-pulse test; pulse trains containing a known number of pulses were emitted at a constant fluence at a target sample. Testing was conducted using the function generator (see chapter 3) to modify output pulse trains from the HighQ laser; by substituting a standard

TTL signal with one induced by the function generator it was possible to select the number of output pulses. Four measurements were made at several fluences before determining the average diameter both horizontally and vertically; this data was then used to ascertain the multi pulse ablation threshold and incubation effect.

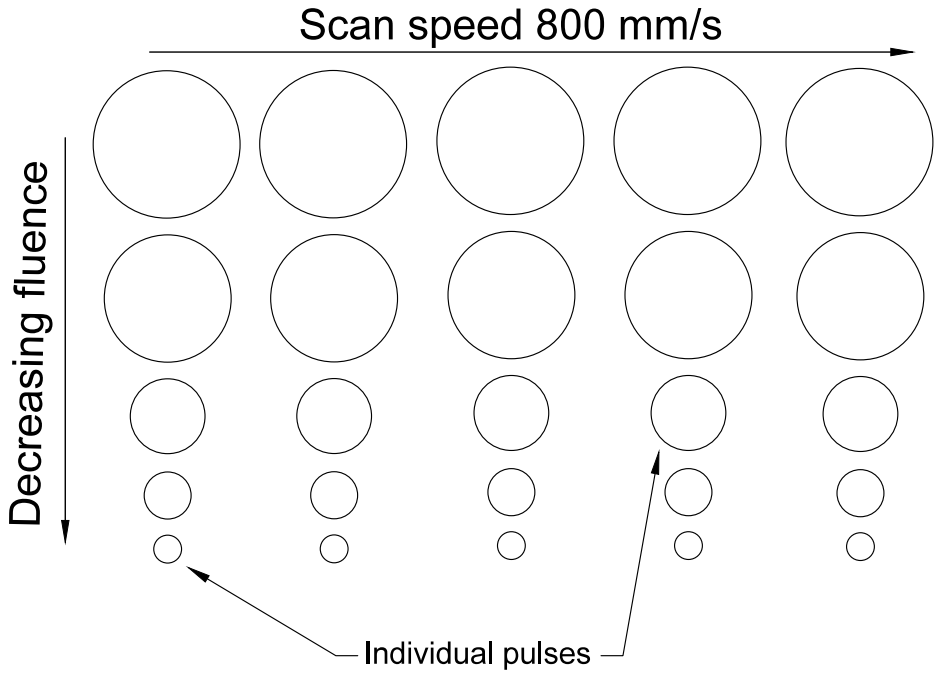

Figure 52: Schematic of single pulse ablation threshold test. Using a repetition rate of 10 kHz it was possible to separate pulses at a traverse speed of 800 mm/s.

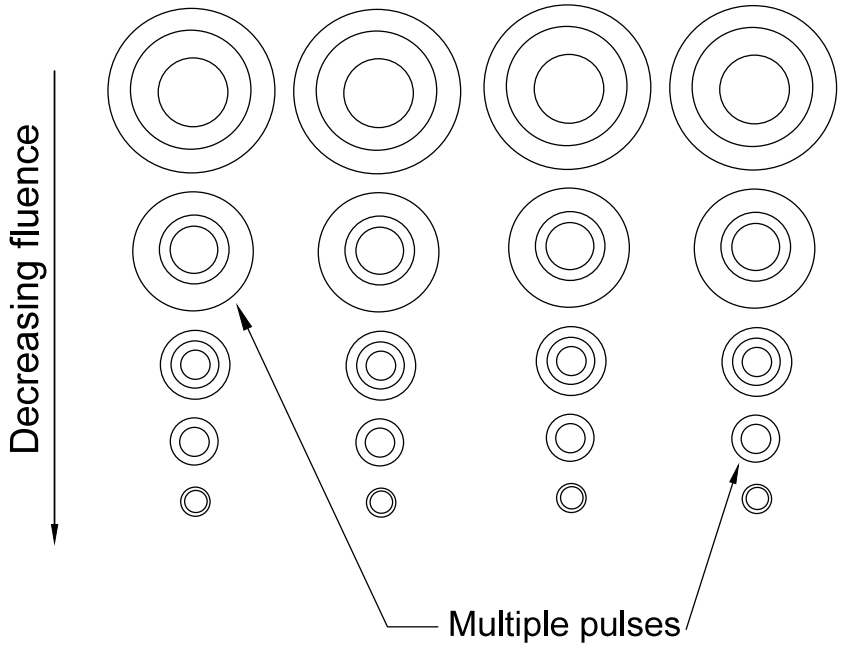

Figure 53: Schematic of the multi pulse ablation threshold test; this technique was used to measure both ITO and glass. The number of pulses per spot (PPS) was set to 6, 10 and 25.

4.1.5 Effect of laser scanning

After determining the ablation thresholds a series of tracks was scanned onto the surface of an ITO sample with varying fluence and pulse overlap. Variation of traverse speed alters the effective number of pulses per spot; the traverse speedwas varied between 5 – 250 mm/s giving a pulse overlap between 2 – 100 PPS. In micro-processing and restoration, scanning of the laser beam will be required to fabricate/restore objects. Each track was measured using optical (OM) and scanning electron microscopy (SEM) before undergoing energy dispersive x-ray spectroscopy (EDX). Using EDX the ablated tracks were examined for their elemental composition in order to determine the extent of ITO removal and determine whether process selectivity was achieved. Using OM five tracks were measured at random points along the irradiation path and averaged in order to obtain an average track width. A schematic of this test is shown in figure 54.

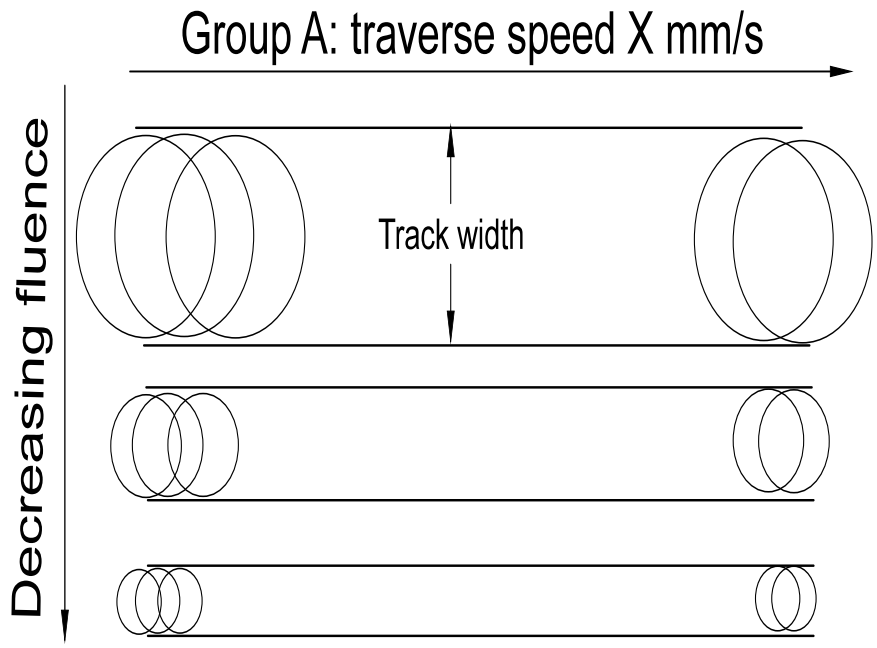

Figure 54: Schematic of multiple pulse ablation threshold testing. Each multiple pulse test was grouped according to the traverse speed (X mm/s) used; within each grouping the fluence was decreased. This was repeated for repetition rates of 5, 10 and 20 kHz.

4.2 Results and Discussion

In this section results from ITO and glass processing are presented. To identify and quantify selective processing using USP the absorption coefficient, single and multi-pulse ablation thresholds and incubation factor were investigated. Using this data the controlling factors of selective processing are determined. Transmission of the laser pulses was measured to determine the absorption properties of both materials before moving on to materials processing. The characteristics of single and multi-pulse ablated craters and tracks were quantitatively analysed; specifically crater diameters, track widths and depth of material removal. The response of both materials to irradiation was investigated to determine the benefits and limitations of selective processing using USP.

Selective material removal using CW or LP laser systems was identified as being dependent upon the difference in absorption coefficients between the target film and the underlying substrate [4]. The absorption mechanism used in these previous investigations relied upon the linear absorption of the incoming beam as peak intensities achieved with LP and CW are insufficient to induce intensity dependent absorption, i.e. nonlinear effects. To begin investigating the use of USP in selective removal the linear absorption coefficients of both the thin film and substrate were measured, when irradiated with ps pulses. The transmitted intensities recorded for ITO and glass when irradiated with 1064 nm and 532 nm USPs are shown below. As the ITO is coated onto the substrate, the change in transmitted power due to glass was recorded using an uncoated white float glass (Knight Optical WGW2515). When measuring the variation in ITO transmitted power the values were adjusted to account for the glass substrate.

Table 1: This table shows the incident (P_0) and transmitted (P_1) power measurements for glass and ITO when irradiated with near IR wavelengths (1064 nm). The transmitted powers for ITO were adjusted to account for the glass substrate.

Determining the absorption coefficient of ITO and glass – Power measurements			
λ = 1064 nm			
Glass		ITO	
P_0	P_1	P_0	P_1
(mW)	(mW)	(mW)	(mW)
1000	980	1000	872
750	676	750	698
500	458	500	462
250	230	250	232
100	93	100	89
75	69	75	69
50	46	50	45
25	24	25	22

Table 2: This table shows the incident and transmitted power measurements for glass and ITO when irradiated with a visible wavelength (532 nm). As in Table 1 ITO data was adjusted to account for the glass substrate.

Determining the absorption coefficient of ITO and glass – Power measurements			
λ = 532 nm			
Glass		ITO	
P_0	P_1	P_0	P_1
(mW)	(mW)	(mW)	(mW)
1000	870	1000	927
750	647	750	678
500	435	500	461
250	217	250	228
200	180	200	185
150	132	150	135
100	86	100	99
50	44	50	44

Before calculating the absorption coefficient the intensity of the impinging and transmitted beam was calculated using the following equation:

$$I = \left(\frac{2E_p}{\pi r^2 T_p}\right) \tag{1.18}$$

Where: E_p = pulse energy, r = beam radius and T_p = pulse duration.

Using equation1.18 incident and transmitted intensities for glass and ITO were calculated; these are shown in table 3 and 4.

Table 3: Intensity of incident and transmitted laser pulses for ITO and glass when irradiated with 1064 nm pulses.

Determining the absorption coefficient of ITO and glass – Intensity calculations			
λ = 1064 nm			
Glass		ITO	
I_0	I_1	I_0	I_1
(Wcm^{-2})	(Wcm^{-2})	(Wcm^{-2})	(Wcm^{-2})
$3.14x10^7$	$3.08x10^7$	$3.14x10^7$	$2.74x10^7$
$2.36x10^7$	$2.13x10^7$	$2.36x10^7$	$2.19x10^7$
$1.57x10^7$	$1.44x10^7$	$1.57x10^7$	$1.45x10^7$
$7.86x10^6$	$7.23x10^6$	$7.86x10^6$	$7.29x10^6$
$3.14x10^6$	$2.92x10^6$	$3.14x10^6$	$2.80x10^6$
$2.36x10^6$	$2.17x10^6$	$2.36x10^6$	$2.17x10^6$
$1.57x10^6$	$1.45x10^6$	$1.57x10^6$	$1.41x10^6$
$7.86x10^5$	$7.55x10^5$	$7.86x10^5$	$6.92x10^5$

Table 4: Intensity of incident and transmitted laser pulses for ITO and glass when irradiated with 532 nm pulses.

Determining the absorption coefficient of ITO and glass – Intensity calculations			
λ = 532 nm			
Glass		ITO	
I_0	I_1	I_0	I_1
(Wcm^{-2})	(Wcm^{-2})	(Wcm^{-2})	(Wcm^{-2})
$3.98x10^7$	$2.85x10^7$	$3.98x10^7$	$3.70x10^7$
$2.98x10^7$	$2.17x10^7$	$2.98x10^7$	$2.72x10^7$
$1.99x10^7$	$1.44x10^7$	$1.99x10^7$	$1.76x10^7$
$9.95x10^6$	$7.36x10^6$	$9.95x10^6$	$9.47x10^6$
$7.96x10^6$	$5.91x10^6$	$7.96x10^6$	$7.20x10^6$
$5.97x10^6$	$4.31x10^6$	$5.97x10^6$	$5.41x10^6$
$3.98x10^6$	$2.89x10^6$	$3.98x10^6$	$3.82x10^6$
$1.99x10^6$	$1.48x10^6$	$1.99x10^6$	$1.91x10^6$

Using Beer's law the data in tables 3 and 4 were used to calculate the absorption coefficient for both materials at 1064 and 532nm. Beer's law calculates the transmitted intensity (I) of the beam after passing through a medium of thickness (z) in air.

$$I = I_0 e^{-\alpha z} \tag{1.19}$$

Where: I_0= initial intensity (Wcm^{-2}), α = absorption coefficient (cm^{-1}).

Equation 1.19 was rearranged to the form:

$$-\alpha = \frac{(ln\, I - \ln I_0)}{z} \tag{1.20}$$

At a wavelength of 1064 nm the absorption coefficient for glass was determined to be 0.65 cm^{-1}, however for ITO it was much greater at $9.95x10^3$ cm^{-1} in good agreement with reported work [151, 152]. This highlights a difference in absorption by a factor of 10^4 between the thin film and substrate. When irradiated with visible (532 nm) light the large gap in absorptivity remained between the two materials; absorption coefficients of $6.67x10^3$ cm^{-1} and 0.70 cm^{-1} were calculated for ITO and glass respectively. The absorption coefficient for ITO at 532 nm is therefore one third lower than at 1064 nm.

These results show that ITO absorption is much stronger in both IR and visible regions than glass, which is almost completely transmissive.

Using the absorption coefficients (α) for both ITO and glass, the depth of absorption (D_p) can also be approximated using equation 1.21.

$$D_p = \frac{1}{\alpha} \tag{1.21}$$

This gives an IR (1064 nm) absorption depth in ITO of ≈0.9 μm and ≈14.1 mm in glass. When irradiated with visible light (532 nm), the absorption depths of ≈2.49 μm and ≈22.3mm were measured for ITO and glass respectively.

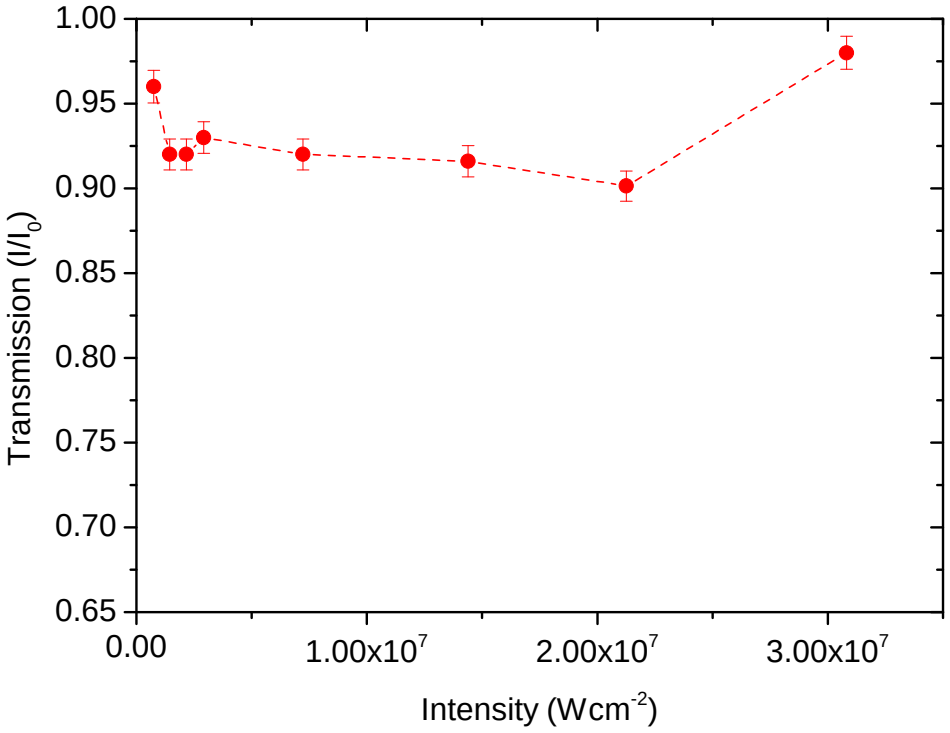

Figure 55: Ratio of transmitted light with increasing intensity. This confirms linear absorption of the IR pulses.

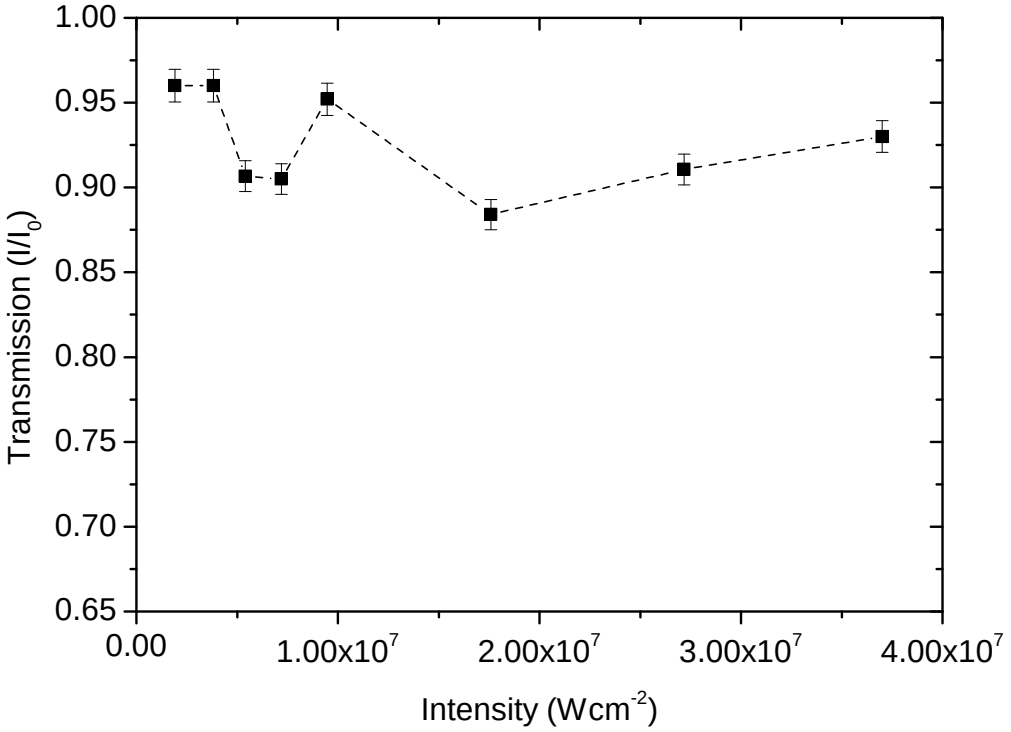

Figure 56: Ratio of transmitted light with increasing intensity. This confirms linear absorption of the visible pulses.

Figures 55 and 56 shows the variation in transmitted light with increasing intensity. These graphs confirm that linear absorption (α) is the dominant mechanism. If non-linear absorption was present the ratio of transmitted light (I/I_0) would decrease as the intensity increased; this is due to the intensity dependence of the non-linear absorption coefficient. This observation is in good agreement with experimental work published by Elim et al[153]. In this paper the nonlinear absorption coefficient of ITO was determined to be ≈0.1 GW/cm. This low absorption coefficient highlights the dominance of the linear absorption mechanism in ITO.

The difference in absorption coefficients was attributed to the response of the electronic structure to incoming energy. ITO is a semi-conducting material with a reduced band gap which easily undergoes excitation from the valence to conduction band. This is in contrast with glass, which is dielectric and has no free electrons (high band gap >6 eV); therefore a higher energy input is required for an electron to undergo a transition. This was discussed in greater detail in chapter 2.

Absorption of IR (1064 nm) radiation by ITO is greater than that observed for visible (532 nm) light, resulting in a substantial difference in absorption coefficients. Conversely the absorption coefficient of IR radiation in glass is extremely low and only slightly improved when using visible light. Therefore in order to produce an efficient selective removal process, subsequent testing was performed using IR radiation only.

4.2.1 Single Pulse ablation threshold

4.2.2 Focussed spot size

Determination of the focal spot size is vital in laser materials processing; specifically for measurement of the absorption coefficient, ablation threshold and depth profiling. The minimum focal spot size ensures maximum energy density during processing; away from this optimum position the result of any measurements can introduce errors.

The focal spot size $(2\omega_0)$ is defined as the distance between two points where the beam intensity equals $1/e^2$ of peak beam intensity. To ensure the beam was located at the focal position the theoretical focal spot size was calculated using equation 1.22 and compared with beam diameters recorded after processing.

$$D_{min} = 2\omega_0 = \frac{4\,f_{LENS}\lambda M^2}{\pi D_{IN}} \qquad (1.22)$$

Where: ω_0 = Radius of beam, f_{LENS} = Focal length of f-theta lens (100 mm), λ = Wavelength (1064 nm), M^2 = Beam quality factor (1.1*) and D_{IN} = Diameter of input beam (as it enters the galvometer) (≈ 6.5 mm).

Using these values the minimum beam diameter $(2\omega_0)$ achievable with the HighQ system was ≈23 µm. As the beam is near Gaussian, results from this theoretical calculation can be directly compared to experimental results using an equation derived by Mannion *et al* [64] wherein the ablated hole diameter is calculated as a function of fluence. By plotting the log of the pulse energy versus the square of the ablated craters, it was possible to determine the effective spot size using the gradient of the slope. Theoretical and effective beam diameters were observed to be approximately equal, confirming that processing was taking place within the focal plane. As the beam is near Gaussian, the ablated crater diameter (D) is related to the fluence using equation [64]:

$$D^2 = 2\omega_0^2 \ln\left(\frac{\phi}{\phi_{th}}\right) \quad (1.23)$$

Where: ω_0 *= Beam radius,* ϕ *= Fluence and* ϕ_{th} *= Ablation threshold.*

Tables 5 and 6 below show data recorded from diameter measurements made on single pulse ablated craters. Using this data it was possible to determine the effective beam diameter and also the single pulse ablation threshold (ϕ_{th}).

Table 5: Data used to calculate the effective beam diameter and single pulse ablation threshold of ITO when irradiated with 10 ps pulse at the fundamental wavelength.

Single Pulse ablation threshold of ITO						
Power	Pulse Energy	Fluence	Beam Diameter	Average Diameter	Diameter squared	Standard deviation
(mW)	(µJ)	(Jcm^{-2})	(µm)	(µm)	($µm^2$)	(µm)
600	60	25.46	24.49	32.40	1049.98	3.26
550	55	23.34		31.12	968.67	2.24
500	50	21.22	Beam Radius	29.61	876.99	1.90
400	40	16.97	(µm)	28.07	788.09	1.58
300	35	12.73	12.25	27.11	734.79	0.41
250	30	10.61		24.98	623.75	0.33
200	20	8.49		24.03	577.34	0.21
150	15	6.37	Frequency	22.82	520.71	0.47
100	10	4.24	(Hz)	19.98	399.12	1.91
75	7.5	3.18	10,000	19.59	383.65	0.55
50	5	2.12		17.05	290.60	0.43
25	2.5	1.06		12.02	144.38	0.41

Table 6: Data used to calculate the effective beam diameter and the single pulse ablation threshold of glass when irradiated with 10 ps pulse at the fundamental wavelength.

Single Pulse ablation threshold of glass						
Power	Pulse Energy	Fluence	Beam Diameter	Average Diameter	Diameter squared	Standard deviation
(mW)	(μJ)	(Jcm^{-2})	(μm)	(μm)	(μm^2)	(μm)
900	90	57.29	20.00	18.15	329.28	1.12
800	80	50.92		16.25	264.19	0.97
700	70	44.56	Beam Radius	15.52	240.96	1.07
600	60	38.19	(μm)	14.82	219.57	0.90
550	55	35.01	10.00	14.67	215.06	0.96
400	40	25.46		11.60	134.49	1.36
350	35	22.28		11.49	131.95	2.08
300	30	19.10	Frequency	8.92	79.48	1.57
250	25	15.91	(Hz)	10.06	101.26	0.92
200	20	12.72	10,000	7.85	61.54	1.76

Figure 57 and 58 are plots of the square of the measured diameters against pulse energy on a logarithmic scale; the gradient of this slope is equal to $2\omega_0^2$. From the gradient produced for ITO and glass an effective beam size of 24 μm (ITO) and 20 μm (glass) was inferred. The ITO value was taken as the most accurate beam size due to the sensitivity of this material to infrared wavelengths. The spread of results in figure 58, for glass, make this data less reliable for determining the beam size. The beam size determined from ITO ablation compares well with the theoretical beam size of 23 μm determined previously, indicating an excellent beam quality.

The effective beam diameter was subsequently used to calculate the fluence impinging on the target using equation 1.24:

$$F_p = \left(\frac{2E_p}{\pi r^2}\right) \tag{1.24}$$

Where: F_p = Peak fluence (Wcm^{-2}), E_p = Pulse energy (J) and r = Beam radius (m).

A plot of D^2 against the calculated fluences was made (figure 59); the ablation threshold of both ITO $\left(\phi_{th}^{ITO}\right)$ and glass $\left(\phi_{th}^{Glass}\right)$ was determined by extrapolation of D^2 to zero. From this it was possible to infer single pulse ablation thresholds of 0.76 and 9.80 Jcm^{-2} for ITO and glass respectively. This confirms a large separation between the energy required to initiate ablation in ITO and glass, by exploiting this difference selective processing may be possible.

These values are expected to be higher than the values obtained for multiple pulses, as incubation effects are not present in this test.

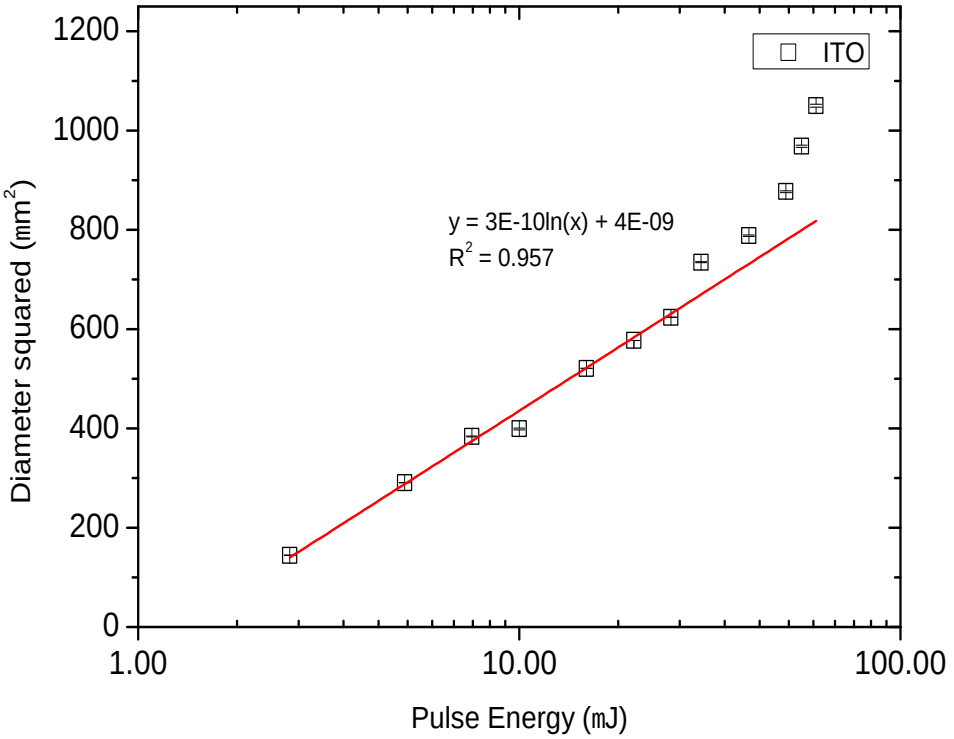

Figure 57: Plot of squared crater diameters vs. pulse energy (log scale) for ITO. The gradient of the slope was used to calculate the effective beam diameter.

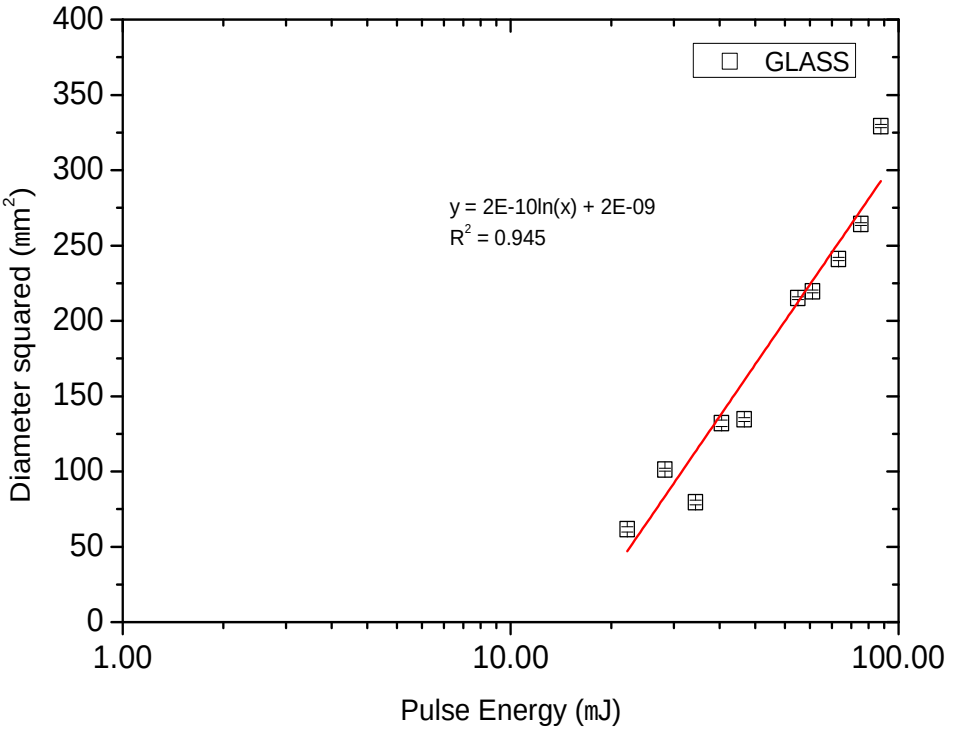

Figure 58: Plot of squared crater diameters vs. pulse energy (log scale) for glass, this test required higher pulse energies to be used due to low absorption of near IR wavelengths. The gradient of the slope was used to calculate the effective beam diameter.

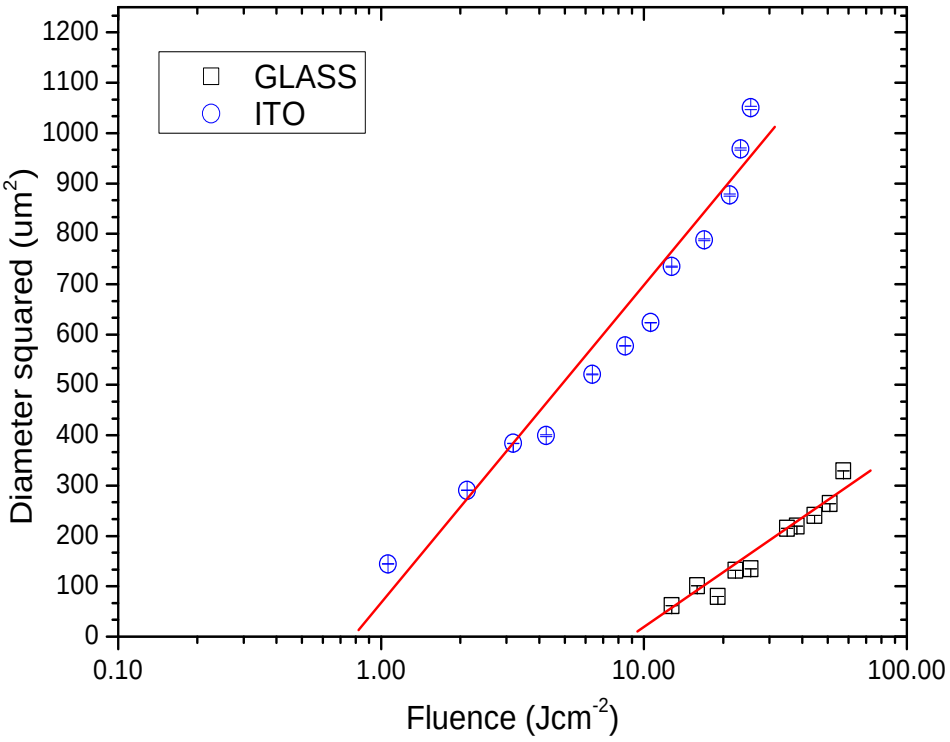

Figure 59: Plot of D^2 vs. fluence for ITO (circles) and glass (squares). The regression lines remained uniform over the experimental range for both sets of data indicating the mechanism of removal remained constant.

The ablation threshold of ITO is comparable to that of previously reported work [136]; it was noted to be similar to the threshold values of metals. The threshold for the dielectric glass was considerably higher than ITO. The ablation threshold for ITO (ϕ_{th}^{ITO}) was recorded to be ≈10 times lower than (ϕ_{th}^{Glass}); this difference was attributed to the vastly different linear absorption coefficients recorded for 1064 nm.

Both trends in figure 59 decrease uniformly indicating that material removal for both samples proceeded in the same manner once ablation was initiated. The separation in threshold values between metals and dielectrics was expected to be large. The metal contains free electrons which can easily be used to initiate ablation whereas the dielectric requires electrons to be promoted from the valence band across and the band gap before ablating the material. The close proximity of ablation thresholds for a metal and semi-conductor would suggest the same ablation mechanism; however no change in gradient was observed indicating that the mechanism proceeds differently.

Slight differences in gradient between ITO and glass were attributed to higher fluences used in determining (ϕ_{th}^{Glass}); this resulted in a larger effective spot size altering the gradient.

The large separation between (ϕ_{th}^{ITO}) and (ϕ_{th}^{Glass}) represents the lower and upper limits of single pulse, selective processing for these two materials. Within this region

removal of the ITO film occurred without damaging the substrate (figure 60). Above (ϕ_{th}^{Glass}) removal of both materials occurred; this is discussed in the next section.

4.2.3 Characterisation of single pulse ablated craters

Figure 60 and 61 are cross-sections and 3D images of single pulse ablation craters recorded using the Wyko white light interferometer (see chapter 3). These images show ablation craters formed on ITO and glass when irradiated using low (2.12 Jcm^{-2}), medium (8.49 Jcm^{-2}) and high (25.46 Jcm^{-2}) fluences. Using the cross-sectional profile it was possible to measure the depth of ITO removal, shown in figure 60. Measurement using the white light system is dependent upon obtaining interference fringes at the surface within a finite focal region. To obtain fringes a tilt may be introduced to the mounting stage, which can cause some angling of results reducing the accuracy. In the majority of cases the tilt is removed by the Veeco software provided with the system; however occasionally a slight slope may remain. The effect of tilting the sample stage can be observed in the images in figure 60, where a visible raised edge with a reciprocal dip, which is especially prominent in the results obtained at lower fluences (A and B). These artefacts also appear in the glass measurements (figure 61) but did not prevent measurement of the ablated craters.

Using figure 60, the average depth of ablation was calculated to be ≈0.05 µm. As this result was observed for both fluences this was taken to be the film thickness. As the depth of removal was shown to be approximately equal for all fluences, this indicates that material removal was achieved selectively because of the linear relationship between impinging fluence and depth of removal (i.e. higher fluence results in more material removal). In figure 60, image (C) shows an instance were the upper limit of selective processing was exceeded; a second raised area at the centre of the crater is clearly visible; the smaller raised area was attributed to interaction between the impinging pulse and glass caused by high fluence at the surface, greater than both (ϕ_{th}^{ITO}) and (ϕ_{th}^{Glass}).

Figure 61 shows the ablated craters used to determine the single pulse ablation threshold of glass. Depth profiles for glass ablation were not recorded as the aim of selective processing was to not damage the substrate; as such only the diameter of the ablated craters were recorded. The depth of ablation on glass was not required as it is the substrate, which should remain unprocessed. The morphology within the ablated crater varied greatly between individual areas and was significantly rougher than that of ITO; this made depth profiles inconsistent. This difference in crater morphology was attributed to the low absorption and thermal diffusivity of glass. Low diffusivity causes any heat generated in the irradiated zone to be confined; this was confirmed by the large heat affected zone (HAZ) surrounding the ablated craters.

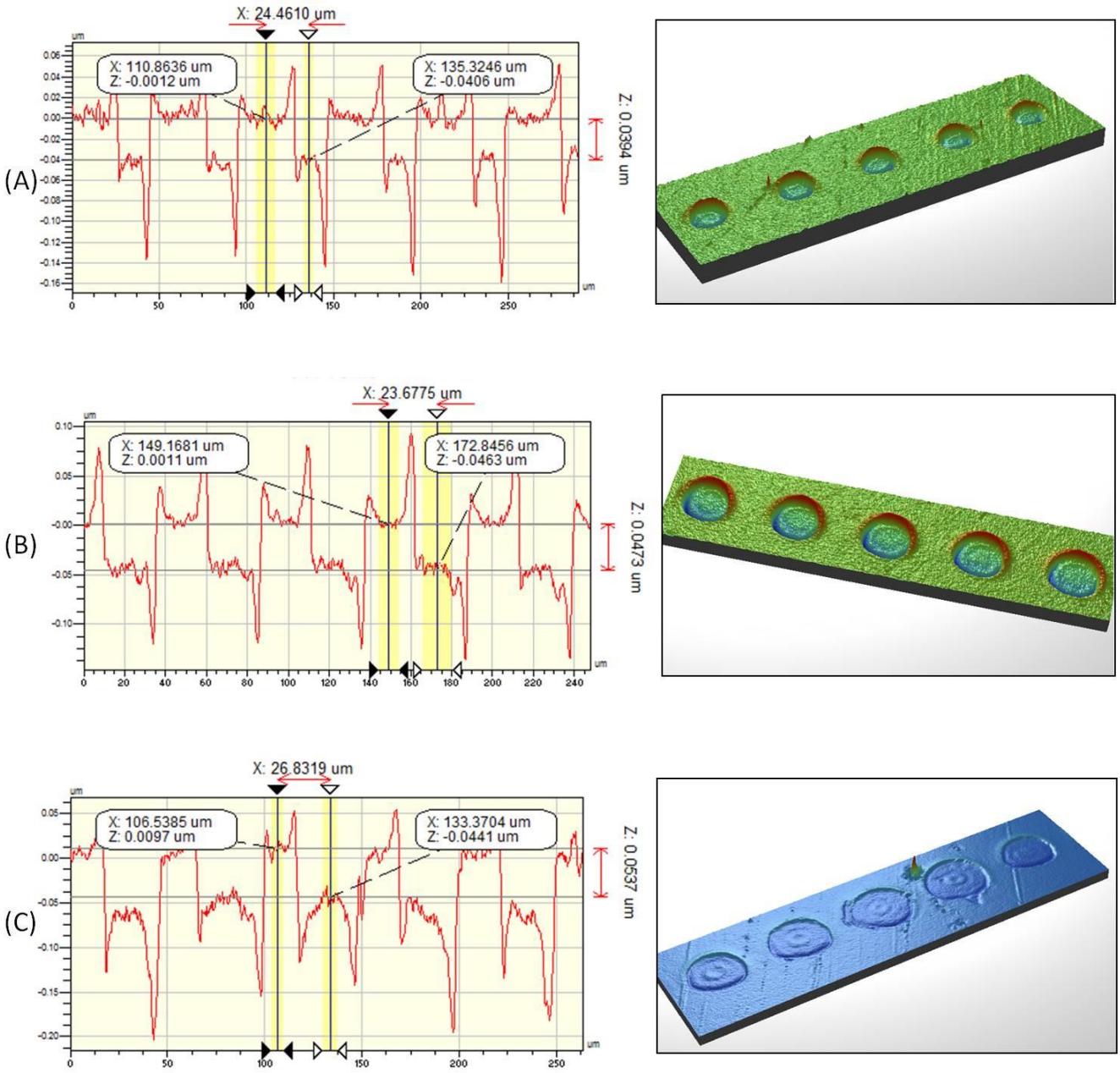

Figure 60: Sample of 5 craters that were used in determining the single pulse ablation threshold of ITO. The fluences shown here are 2.12, 8.49 and 25.46 Jcm^{-2}, for (A), (B) and (C) respectively.

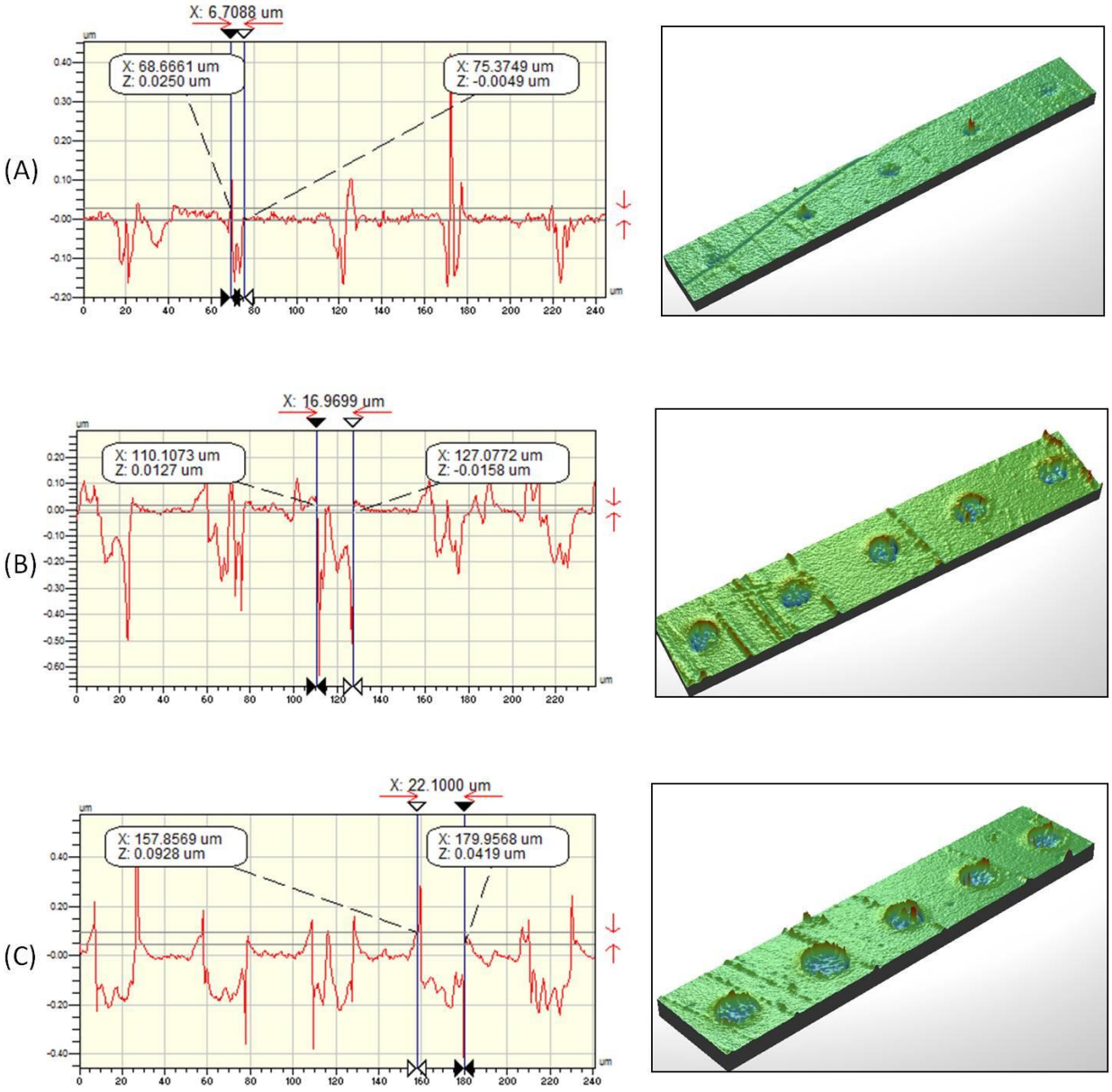

Figure 61: Sample of 5 craters that were used in determining the single pulse ablation threshold of glass. The fluences shown here are 12.73, 38.19 and 57.29 Jcm^{-2}, for (A), (B) and (C) respectively.

4.2.4 Multiple pulse ablation thresholds

When micro processing thin films for industrial/conservation applications these processes often require more than one pulse due to the thickness of the film or the pattern required, this can be observed in both drilling (single position) and scribing (moving position) processes.

The material response to irradiation with either single or multiple pulses has previously been shown in studies by Ashkenasi *et al* and others to be different [67]. In these studies the multi-pulse ablation threshold was determined to be lower than the single pulse; this decrease was attributed to an incubation effect. Successive low fluence pulses impinging on a surface cause minute cumulative changes in the microstructure of the irradiated region. These changes in microstructure eventually lead to increased absorption of the incoming pulses resulting in a lowering of the ablation threshold; a full discussion on the incubation effect can be found in chapter 2.

For selective materials processing to be a viable micro processing technique, the effect of multiple pulse irradiations on the selective processing window identified in the previous section must be investigated.

In this test the multi pulse ablation threshold of ITO and glass were determined using pulse trains of 6, 10 and 25 pulses per spot (PPS). These numbers were chosen because of their applicability to micro processing were the use of thin films only generally requires a few pulses (≤10) to completely remove the film, whilst using excessive pulse numbers can negate the thermal advantages of USP systems.

Figure 63 shows an OM image of the ablated craters made at high fluence with 6 PPS; measurements were made using software provided with the microscope. The horizontal and vertical diameter of each of the craters was measured and the average diameter used to obtain more accurate measurements.

The following tables present the data used to calculate the multi-pulse ablation threshold and incubation effect for ITO (Tables 5, 6 and 7) and glass (Tables 8, 9 and 10).

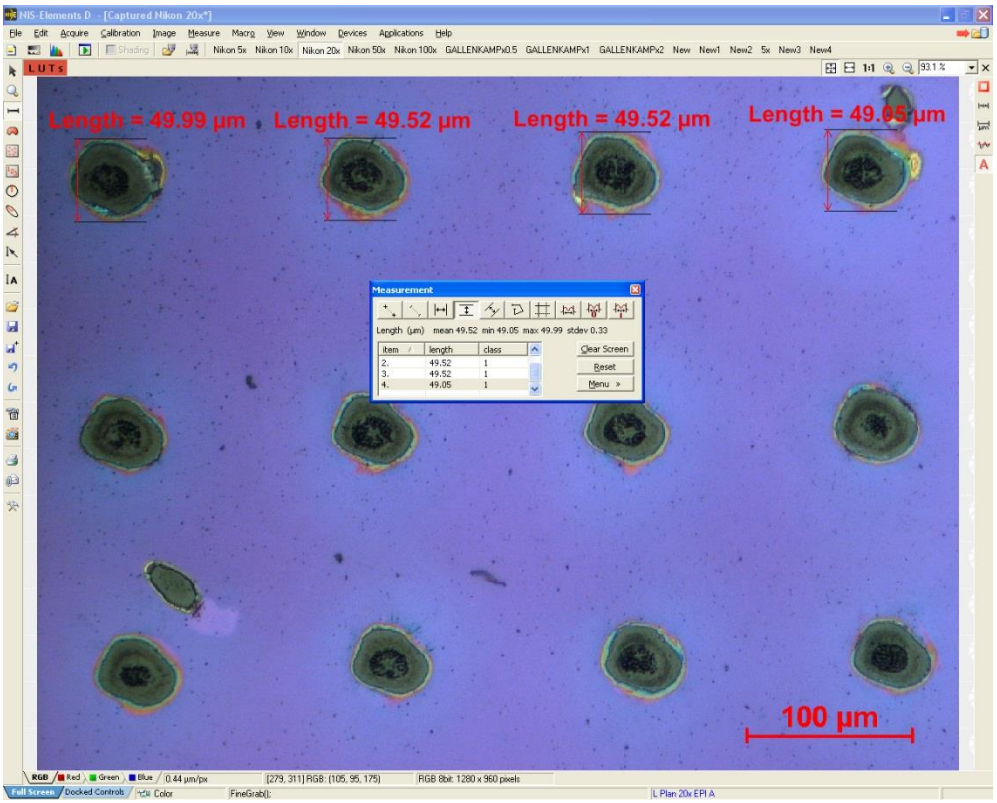

Figure 62: OM images of ablated craters made using 6PPS at x20 magnification. Measurements were made using software provided by Nikon.

Table 7: Six pulse ablation threshold of ITO when irradiated with 1064 nm.

Multi Pulse ablation threshold of ITO (6PPS)						
Power	Pulse Energy	Fluence	Beam Diameter	Average Diameter	Diameter squared	Standard deviation
(mW)	(µJ)	(Jcm^{-2})	(µm)	(µm)	($µm^2$)	(µm)
600	120	50.95	24.49	52.03	2707.25	0.84
550	110	46.70		48.29	2332.29	0.90
500	100	42.46		47.53	2259.46	1.80
400	80	33.97		46.37	2149.95	1.30
300	60	25.47		43.10	1857.18	1.21
200	40	16.98		36.97	1366.50	0.75
100	20	8.49	Frequency	30.31	918.62	0.48
50	10	4.25	(Hz)	25.11	630.39	0.49
25	5	2.12	5000	17.99	323.55	0.87

Table 8: ten pulse ablation threshold of ITO when irradiated with 1064 nm.

Multi Pulse ablation threshold of ITO (10PPS)						
Power	Pulse Energy	Fluence	Beam Diameter	Average Diameter	Diameter squared	Standard deviation
(mW)	(μJ)	(Jcm^{-2})	(μm)	(μm)	(μm^2)	(μm)
600	120	50.95	24.49	53.37	2848.76	4.37
550	110	46.70		48.35	2337.72	0.91
500	100	42.46		49.34	2434.81	3.45
400	80	33.97		47.48	2254.11	1.50
300	60	25.47		44.38	1969.58	2.34
200	40	16.98		37.90	1436.41	0.73
100	20	8.49	Frequency	32.47	1054.22	0.43
50	10	4.25	(Hz)	26.22	687.55	0.55
25	5	2.12	5000	19.21	369.12	0.22

Table 9: Twenty-five pulse ablation threshold of ITO when irradiated with 1064 nm.

Multi Pulse ablation threshold of ITO (25PPS)						
Power	Pulse Energy	Fluence	Beam Diameter	Average Diameter	Diameter squared	Standard deviation
(mW)	(μJ)	(Jcm^{-2})	(μm)	(μm)	(μm^2)	(μm)
600	120	50.95	24.49	53.90	2905.34	1.38
550	110	46.70		53.38	2848.89	2.46
500	100	42.46		50.98	2599.09	2.15
400	80	33.97		47.59	2265.05	1.27
300	60	25.47		44.07	1941.87	0.82
200	40	16.98		31.94	1020.32	0.30
100	20	8.49	Frequency	28.44	808.76	0.48
50	10	4.25	(Hz)	24.41	595.85	0.51
25	5	2.12	5000	19.21	369.07	0.88

Table 10: Ablation threshold of uncoated glass when irradiated with 6 pulses at 1064 nm.

Multi Pulse ablation threshold of Glass (6PPS)						
Power	Pulse Energy	Fluence	Beam Diameter	Average Diameter	Diameter squared	Standard deviation
(mW)	(μJ)	(Jcm^{-2})	(μm)	(μm)	(μm^2)	(μm)
600	120	50.95	24.49	36.44	1327.87	0.50
550	110	46.70		36.15	1306.73	0.84
500	100	42.46		35.39	1252.36	0.82
400	80	33.97		33.58	1127.53	0.67
350	70	25.47		32.82	1077.15	0.77
300	60	16.98		30.95	957.98	0.62
300	50	8.49	Frequency	29.61	876.46	0.65
250	40	4.25	(Hz)	27.86	775.97	0.35
200	20	2.12	5000	19.68	387.25	0.12

Table 11: Ablation threshold of uncoated glass when irradiated with 10 pulses at 1064 nm.

Multi Pulse ablation threshold of Glass (10PPS)						
Power	Pulse Energy	Fluence	Beam Diameter	Average Diameter	Diameter squared	Standard deviation
(mW)	(μJ)	(Jcm^{-2})	(μm)	(μm)	(μm^2)	(μm)
650	130	55.20	24.49	40.99	1680.49	1.36
600	120	50.95		41.05	1685.31	2.43
550	110	46.70		42.28	1787.49	0.99
500	100	42.46		39.48	1558.37	1.72
450	90	38.21		36.50	1332.07	0.96
400	80	33.97		37.02	1370.76	2.03
300	60	25.47	Frequency	33.99	1155.15	1.03
250	50	21.23	(Hz)	32.29	1042.89	2.09
200	40	16.98	5000	28.91	835.57	0.67
100	20	8.49		21.08	444.52	0.52

Table 12: Twenty-five pulse ablation threshold of uncoated glass when irradiated with 1064 nm.

Multi Pulse ablation threshold of Glass (25PPS)						
Power	Pulse Energy	Fluence	Beam Diameter	Average Diameter	Diameter squared	Standard deviation
(mW)	(μJ)	(Jcm^{-2})	(μm)	(μm)	(μm^2)	(μm)
650	130	55.20	24.49	48.47	2349.34	2.40
600	120	50.95		47.89	2293.09	1.72
550	110	46.70		45.84	2101.42	2.11
500	100	42.46		44.32	1964.48	2.18
450	90	38.21		43.33	1877.60	3.33
400	80	33.97		38.95	1517.20	2.14
300	60	25.47	Frequency	37.14	1379.47	1.16
250	50	21.23	(Hz)	34.81	1211.39	1.13
200	40	16.98	5000	31.18	972.35	1.76
100	20	8.49		22.66	513.42	0.43

From figures 63 and 64 a decrease in ablation threshold can be observed in comparison to those recorded using single pulses. The observed accumulation effect has previously been explained using an incubation model [67]. From this model a power law relationship between the ablation threshold fluence for N pulses (ϕ_{th}^{N}) and the single pulse threshold (ϕ_{th}^{1}) was identified, equation 1.25.

$$\Phi_{th}(N) = \Phi_{th}(1)N^{S-1} \quad (1.25)$$

The incubation coefficient (S) represents the extent to which incubation will affect the material being irradiated; if incubation effects are strong then S will tend towards zero; if incubation is not present S will be equal to 1. To determine the pulse dependent ablation threshold (ϕ_{th}^{N}) equation 1.24 was combined with 1.25 to produce a modified ablation threshold equation 1.26 [65].

$$D = \omega_0 \sqrt{2} \ln\left(\frac{\Phi_0}{\Phi_{th}(1) N^{S-1}}\right) \quad (1.26)$$

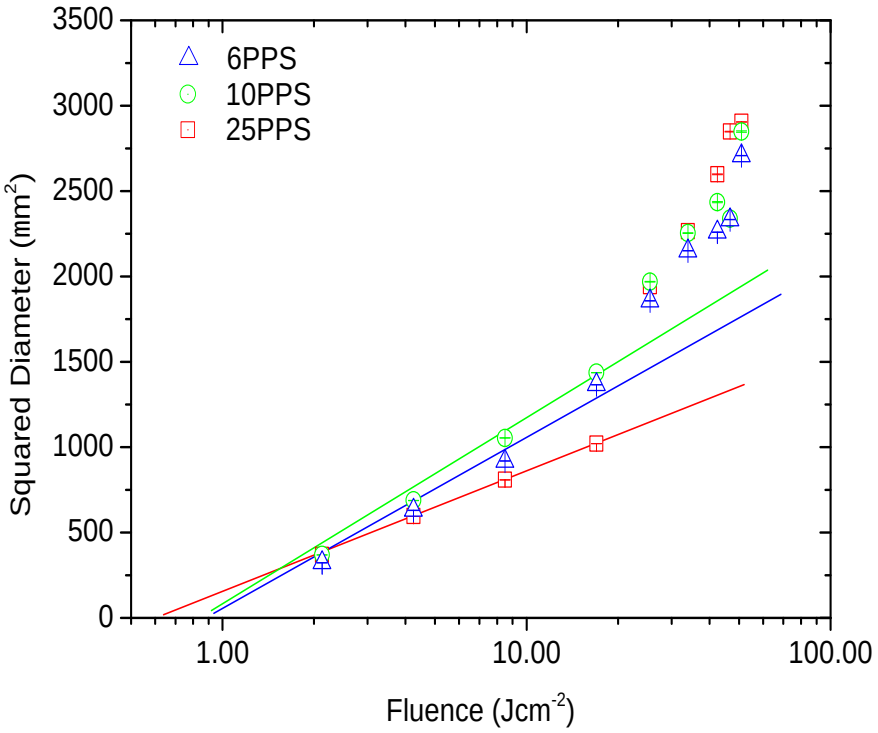

Figure 63: Measurement of multi-pulse ablation threshold of ITO when irradiated with 6, 10 and 25 PPS. All processing was undertaken at 1064 nm with an oscillator repetition rate of 5 kHz.

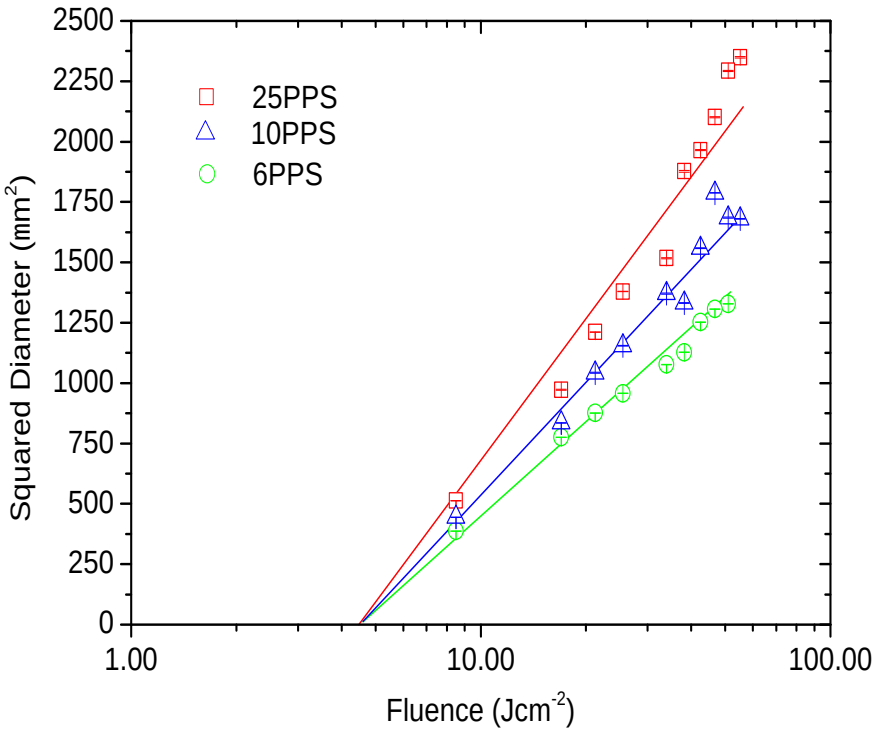

Figure 64: Measurement of multi-pulse ablation threshold of glass when irradiated with 6, 10 and 25 PPS. All processing was undertaken at 1064 nm with an oscillator repetition rate of 5 kHz.

The multi-pulse ablation thresholds determined for ITO and glass when irradiated with 6, 10 and 25PPS are shown in table 13; these are compared to the single pulse threshold determined previously.

Table 13: Multi-pulse ablation threshold and effect of incubation on ITO. Pulse trains of 6, 10 and 25 PPS were used; the single pulse ablation threshold is provided for comparison.

Number of Pulse per spot (PPS)	Ablation threshold (ϕ_{th}^{N})	Incubation effect (S)
1	0.76 Jcm^{-2}	-
6	0.76 Jcm^{-2}	1.00
10	0.75 Jcm^{-2}	1.00
25	0.65 Jcm^{-2}	0.77

Table 14: Multi-pulse ablation threshold and effect of incubation on glass. Pulse trains of 6, 10 and 25 PPS were used; the single pulse ablation threshold is provided for comparison.

Number of Pulse per spot (PPS)	Ablation threshold (ϕ_{th}^{N})	Incubation effect (S)
1	9.9 Jcm^{-2}	-
6	4.7 Jcm^{-2}	0.58
10	4.7 Jcm^{-2}	0.68
25	4.7 Jcm^{-2}	0.77

The incubation effect is measured between zero and one [65], when S is equal to one no incubation effect is present; this is discussed in detail in chapter 2. Tables 13 and 14 show that incubation had no effect on the ablation threshold of ITO up to 10 PPS; however an incubation effect was observed when using 25 PPS. The low impact of incubation on the ablation threshold of ITO was attributed to strong absorption of near IR radiation. This makes it relatively simple for a single impinging laser pulse to promote electrons between the donor level provided by the dopant and conduction band to initiate ablation; consequently increasing the number of impinging pulses would have minimal effect.

When irradiated with 25 PPS the ablation threshold of the ITO film was observed to alter distinctly above ≈16 Jcm^{-2}; this change in gradient indicates a change in ablation mechanism similar to the change observed in metals [146]. In the case of metals this effect was attributed to the onset of strong ablation [154], as discussed in chapter 2.

The incubation effect on glass resulted in a distinct change in (ϕ_{th}^{N}) for glass between single and multiple pulses (6, 10 and 25 PPS). The ablation threshold for the three tested pulse numbers was determined to be equivalent (4.7 Jcm^{-2}), confirming that incubation as a result of multi-pulse irradiation was limited. This is in good agreement with the calculated S values and previous reported experimental data [67], which indicated that the effect of incubation was reduced as the number of pulses was increased.

4.2.5 Characterisation of multi-pulse ablation

Figures 65 and 66 are optical images of ITO and glass, respectively, after irradiation with multiple pulses. Figure 65 shows the ablated craters created on ITO when irradiated with 10 PPS, whilst figure 66 shows the effect of using 25 PPS on uncoated glass. Ablation of the ITO film and glass substrate was observed when irradiated with high fluences (figure 65), resulting in a large outer crater where the fluence was only sufficient for ITO ablation and an inner crater where both ITO and glass were removed. Thermal effects induced on the ITO film during irradiation were observed at higher fluences with a faint ring indicating were the film had been modified; these effects were not as prominent as those observed on glass. With low fluence only ITO removal was observed; lowest image in figure 65.

On the uncoated glass, light scattering around the ablated craters can be observed. This effect was attributed to either the formation of a HAZ, due to the low thermal conductivity of glass (0.96 $Wm^{-1}K^{-1}$) [155] in comparison to other materials such as ITO (3.2 $Wm^{-1}K^{-1}$) [156], or the re-deposition of ablated material. Re-deposited material would consist of tiny glass fragments that were not effectively extracted during processing. As the lowest fluence used in testing was above (ϕ_{th}^{N}) but well below (ϕ_{th}^{1}) this confirmed that the ablation threshold had been reduced as a result of multi-pulse irradiation.

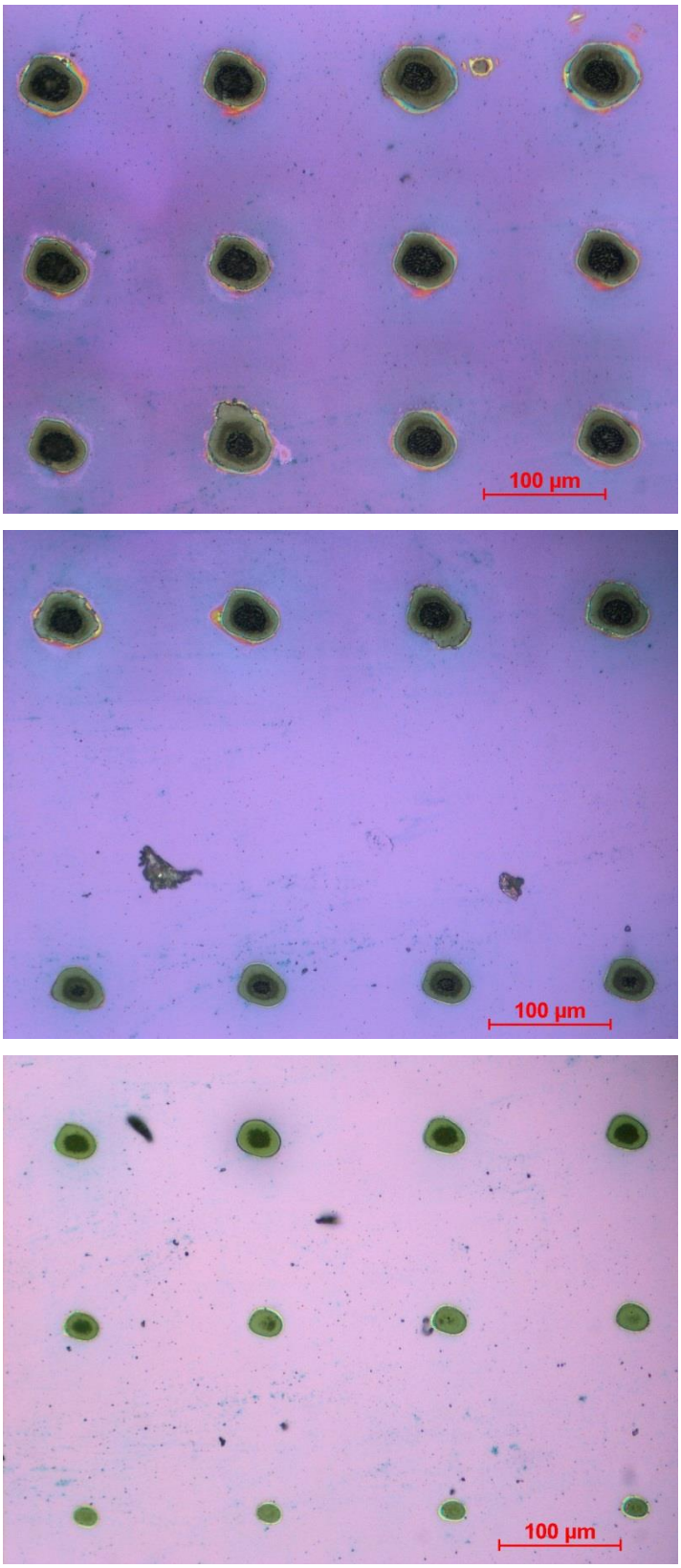

Figure 65: OM images of ablated craters made on ITO using 10 PPS. The fluence in these three images decreases from 50.95 Jcm^{-2} (top) to 2.12 Jcm^{-2} (bottom). In the middle image one row of data is missing due to an error; this data was retaken later and used in the final results.

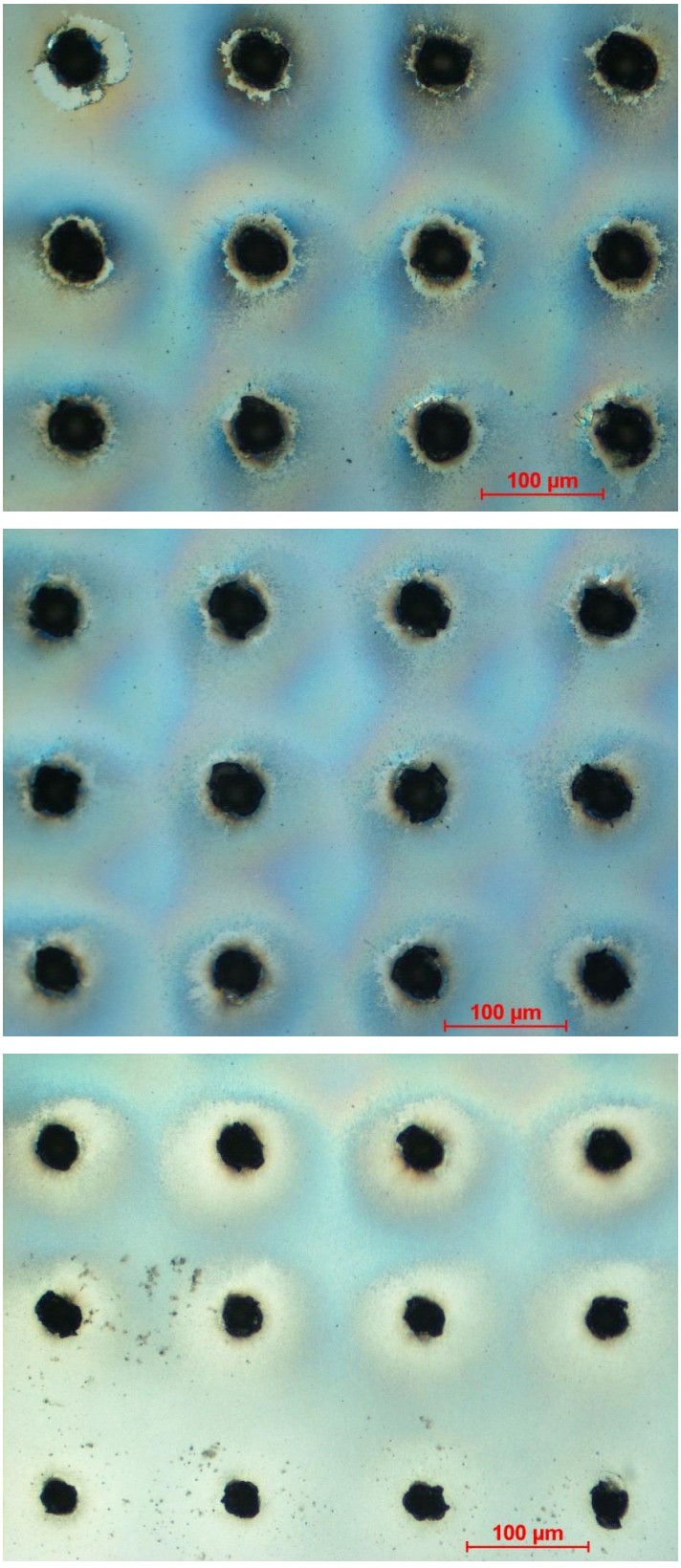

Figure 66: OM images of ablated craters made using 25 PPS on glass. The fluence decreases from top to bottom; this encompasses all fluences between 55.20 and 8.49 Jcm^{-2}. At the highest fluences (top) thermal effects around the crater edge are clearly evident. These effects are clearly observable at the lowest fluence of 8.49 Jcm^{-2}.

4.2.6 Effect of scanning on ITO ablation

Materials processing can be carried out in either a stationary or variable position. In the previous testing laser ablation threshold measurements were made using a stationary position with direct control over the number of impinging pulses. In this section the effect of traversing the beam across the sample is investigated to determine if varying the interaction time alters the selective processing window.

To observe the effect of track processing, ITO coated glass samples were examined using SEM and EDX; using SEM high magnification images were recorded to observe if any damage occurred during processing. As ITO is conductive, recording images of this surface was possible however when imaging glass it is more challenging as some charging effects were present at the surface. A build-up of electrostatic charge on the sample surface causes this effect; occurring readily on materials with a low/no electrical conductivity; in this instance glass.

EDX measurements were also undertaken to examine the elements present within the processed regions. From the EDX data, indium and silicon signals were used to represent the ITO and glass respectively.

Figure 67 shows the SEM image and EDX spectra recorded for an unprocessed section of the ITO coated glass sample. The SEM image shows the uniformity and flatness of the ITO film deposited on to the glass; a surface contaminant is shown in the central part of the lower section of the image. The EDX spectra obtained for the unprocessed region (lower section of figure 67) shows strong peaks for indium and tin; these peaks were attributed to ITO. The result of the unprocessed samples was subsequently compared against processed regions to identify the change in signal intensity. A strong silicon peak was also observed; this was attributed to glass substrate underneath the ITO thin film. The energy of the incoming electrons was 10 keV, this was sufficient to penetrate the thin film and move into the glass; this accounted for the strong silicon peak.

Figure 68 shows SEM images of ablated tracks made during multi-pulse testing at a repetition rate of 10 kHz; these images show the effects of using high or low degrees of overlap and increasing the fluence. These images were taken from across the testing range to provide an overview of the effect of irradiation. Images A, C and E show tracks made at 5 mm/s respectively; whilst B and C are images of tracks made using a high traverse speed (250 mm/s). Image F was recorded at 50 mm/s due to the low fluence it was not possible to observe ablation at greater speeds.

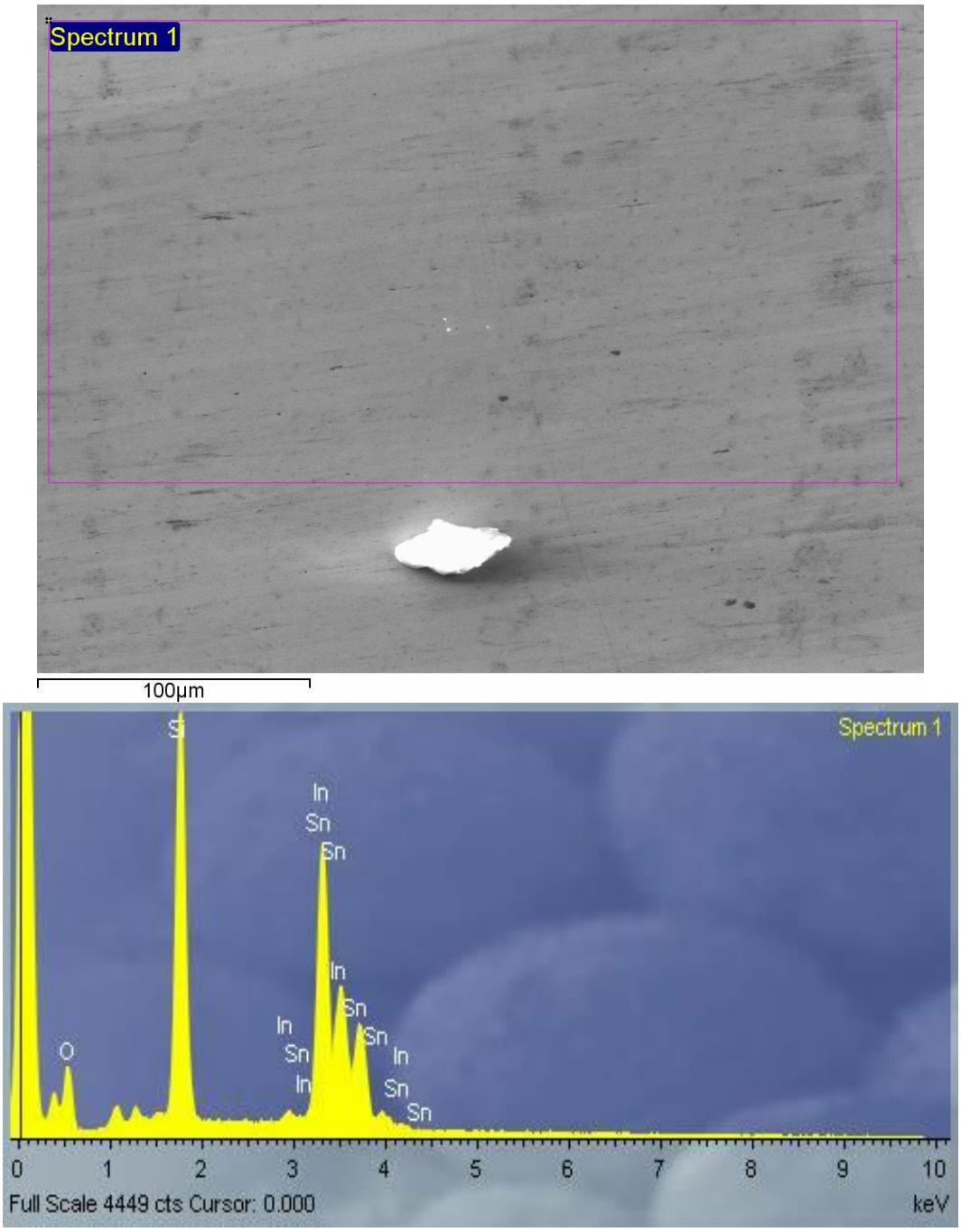

Figure 67: This SEM image (top) and EDX spectra (bottom) were recorded on an unprocessed section of the ITO sample. The ITO coating is shown to be highly flat; the white particulate in the middle of the lower area of the sample is a contaminant introduced when exposed to air.

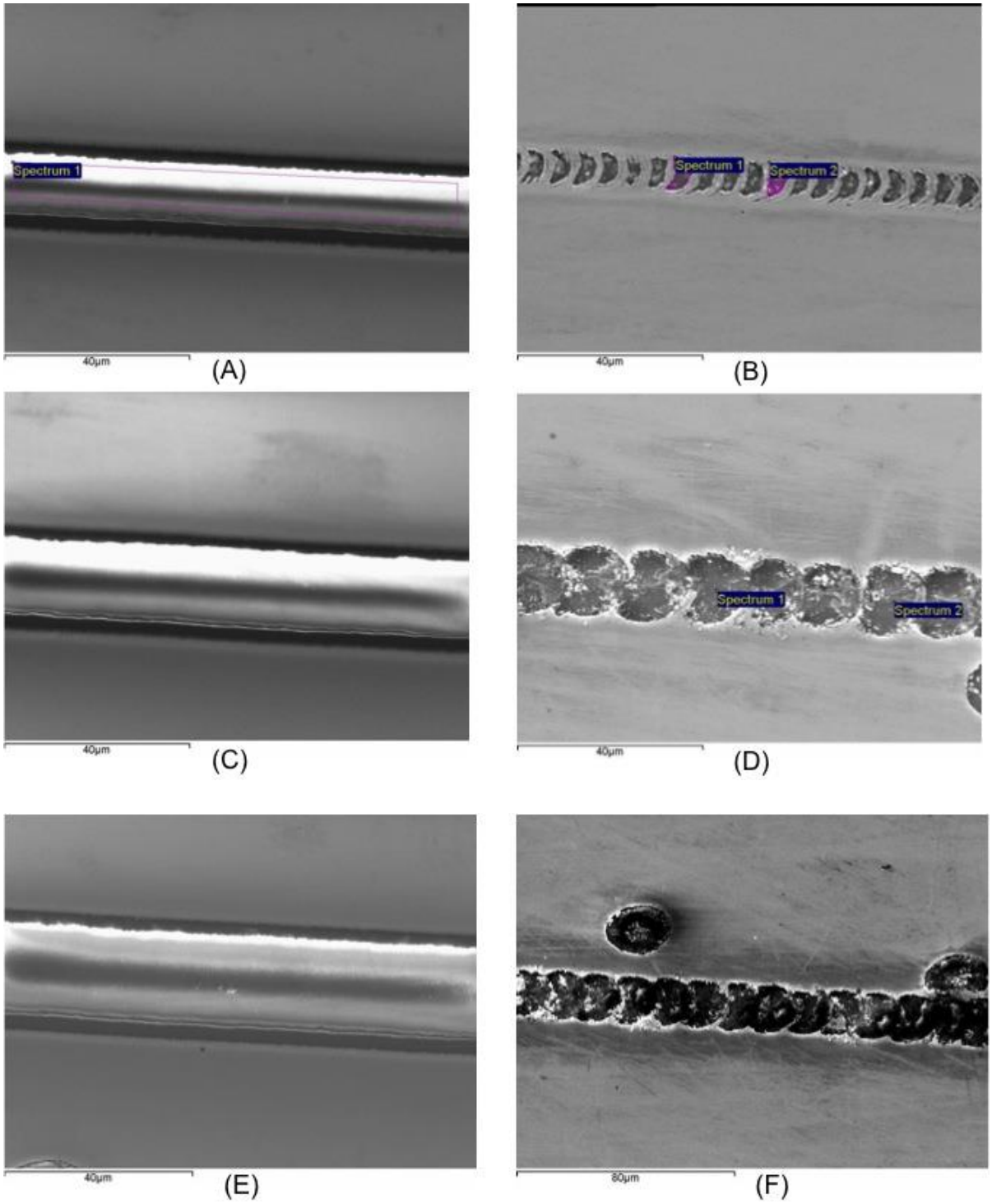

Figure 68: SEM images of ablated tracks used in pulse overlap testing. Images A, C and E show the effect of using high pulse overlap (approx. 100 pulse per spot) with decreasing fluence; 1.43 Jcm^{-2} (A & B), 0.48 Jcm^{-2} (C & D) and 0.32 Jcm^{-2} (E and F). The regions enclosed by the purple line were subjected to EDX; measurements are shown in images A, B and D.

Table 15: This table shows the indium abundance recorded after irradiation with a constant fluence of 1.43 Jcm^{-2} at traverse speeds between 5-250 mm/s. The abundance recorded at zero is taken from an unprocessed region and used as the reference for calculating the percentage change in abundance.

Traverse speed (mm/s)	-	5	5.55	6.25	7.10	8.40	10	12.40	16.40	25	50	100	250
No. of pulses (Approx.)	-	100	90	80	70	60	50	40	30	20	10	5	2
Indium abundance (recorded)	133475	4798.90	4656.70	4348.80	4386.80	4702.20	4376.20	4438.70	4288.80	4397.30	3926.20	3926.20	9709.10
Indium abundance (reference)	133475	133475	133475	133475	133475	133475	133475	133475	133475	133475	133475	133475	133475
% Change	0	96.40	96.51	96.74	96.71	96.48	96.72	96.67	96.79	96.71	97.06	97.06	92.73

Table 16: This table shows the indium abundance recorded after irradiation with a constant fluence of 0.48 Jcm^{-2} at traverse speeds between 5-25 mm/s; above this speed the interaction time was insufficient to induce ablation. The abundance recorded at zero is taken from an unprocessed region and used as the reference for calculating the percentage change in abundance.

Traverse speed (mm/s)	-	5	5.55	6.25	7.10	8.40	10	12.40	16.40	25
No. of pulses (Approx.)	-	100	90	80	70	60	50	40	30	20
Indium abundance (Recorded)	133475	5042.00	5051.80	4848.20	5067.00	4559.10	3749.10	4262.70	3874.80	15545.80
Indium abundance (Reference)	133475	133475	133475	133475	133475	133475	133475	133475	133475	133475
% Change	0	96.22	96.21	96.37	96.20	96.58	97.19	96.81	97.10	88.35

Table 17: This table shows the silicon abundance recorded after irradiation with a constant fluence of 1.43 Jcm^{-2} at traverse speeds between 5 – 250 mm/s. The reference abundance was taken from an unprocessed region and highlights the increase in silicon signal as ITO was removed from the surface.

Traverse speed (mm/s)	5	5.55	6.25	7.10	8.40	10	12.40	16.40	25	50	100	250
No. of pulses (Approx.)	100	90	80	70	60	50	40	30	20	10	5	2
Silicon abundance (recorded)	229809.40	227.470.30	228843.30	228629.2	229212.80	230769.70	231243.70	233508.70	235495.80	244274.6	244274.6	228317.10
Silicon abundance (reference)	95365.00	95365.00	95365.00	95365.00	95365.00	95365.00	95365.00	95365.00	95365.00	95365.00	95365.00	95365.00

Table 18: This table shows the silicon abundance recorded after irradiation with a constant fluence of 0.48 Jcm^{-2} at traverse speeds between 5-25 mm/s; above 25 mm/s the fluence was too low to initiate ablation. The reference abundance was taken from an unprocessed region and highlights the increase in silicon signal as ITO was removed from the surface.

Traverse speed (mm/s)	5	5.55	6.25	7.10	8.40	10	12.40	16.40	25
No. of pulses (Approx.)	100	90	80	70	60	50	40	30	20
Silicon abundance (recorded)	230978.30	251368.80	251304.40	250180.50	248405.50	247080.80	246571.10	245927.30	244460.00
Silicon abundance (Initial)	95365.00	95365.00	95365.00	95365.00	95365.00	95365.00	95365.00	95365.00	95365.00

The silicon and indium values shown in tables 15 – 18 were recorded using EDX spectra; the tables show the variation in elemental signal between ablated tracks made using 10 kHz with a constant fluence of 1.43 Jcm^{-2} and 0.48 Jcm^{-2}. These tables show the variation in indium and silicon signal within the ablated tracks. From the spectra, indium and silicon were used to ascertain the effect of ablation on the ITO and glass respectively. Indium was chosen however; tin would also have been suitable. In the unprocessed sample spectrum, a strong signal from silicon was detected. This prohibited the use of oxygen as an indicator of material removal as it is present in both ITO and glass, with no method for differentiating between the two signals.

By comparing the variation of indium and silicon signals to the ones recorded in the unprocessed region it was possible to determine the percentage change in elemental abundance. These measurements were possible even where low pulse numbers (250 mm/s, approx. 2 pulses) were used; wherein over a 90% decrease in indium signal was observed. Increasing the number of incoming pulses did not vary the signal significantly; with the maximum signal reduction being between 96 – 97%.

Using this data, pie charts were created to visualise the variation in in signal for indium and silicon at different traverse speeds.

Figure 69 shows a pie chart indicating the variation in indium on the surface of the ITO after irradiation with a fluence of 0.48 Jcm^{-2}; the traverse speeds (pulse overlap) were altered during testing. With the exception of 250 mm/s, each section of the chart is approximately the same size (i.e. the indium abundance after irradiation is similar); indicating that below 250 mm/s the amount of indium removed became independent of pulse number. The small difference in percentages between slices was attributed to detector variations, as there was no cumulative decrease in indium signal as the traverse speed was lowered. The larger percentage observed for 250 mm/s (green section) was attributed to the high traverse speed, reducing the overall interaction time thus removing less ITO.

Figure 70 shows a pie chart of silicon variation (glass) after the ITO layer was irradiated using multiple laser pulses. The chart shows the silicon signal recorded for each measurement as a percentage total of the whole chart. Each section of the chart is approximately equal in size indicating that the silicon signal remained almost uniform across test regions. This uniformity suggests that the glass substrate remained intact throughout processing; i.e. ITO was selectively removed from the surface.

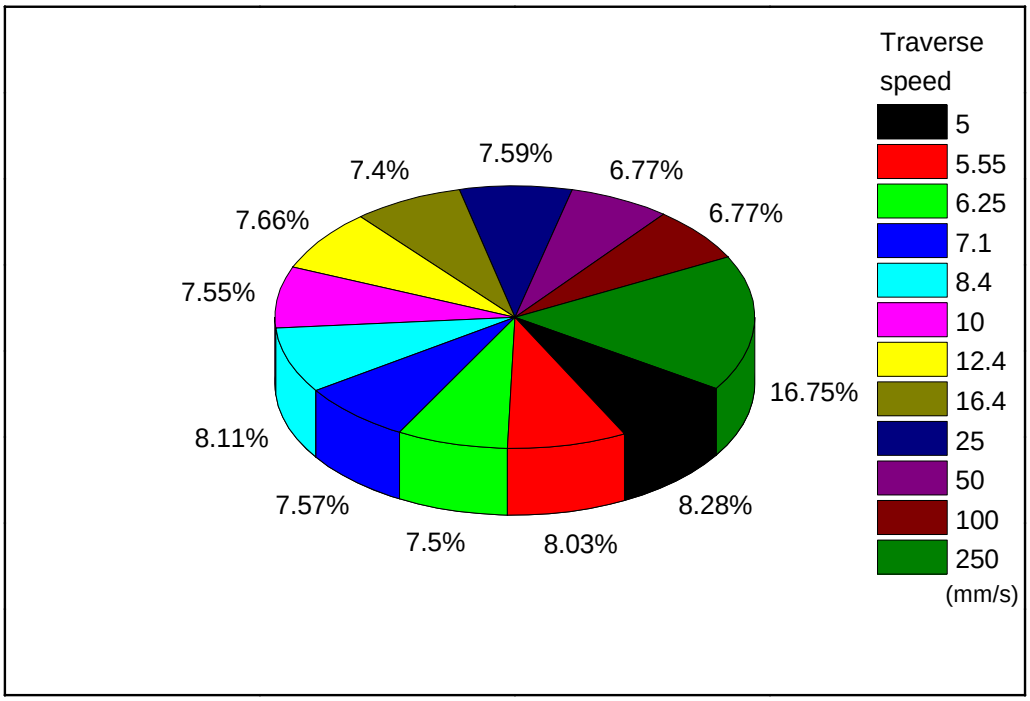

Figure 69: Pie chart showing the relative abundance of indium after irradiation with a constant fluence of 1.43 Jcm^{-2} with traverse speeds ranging between 5 – 250 mm/s.

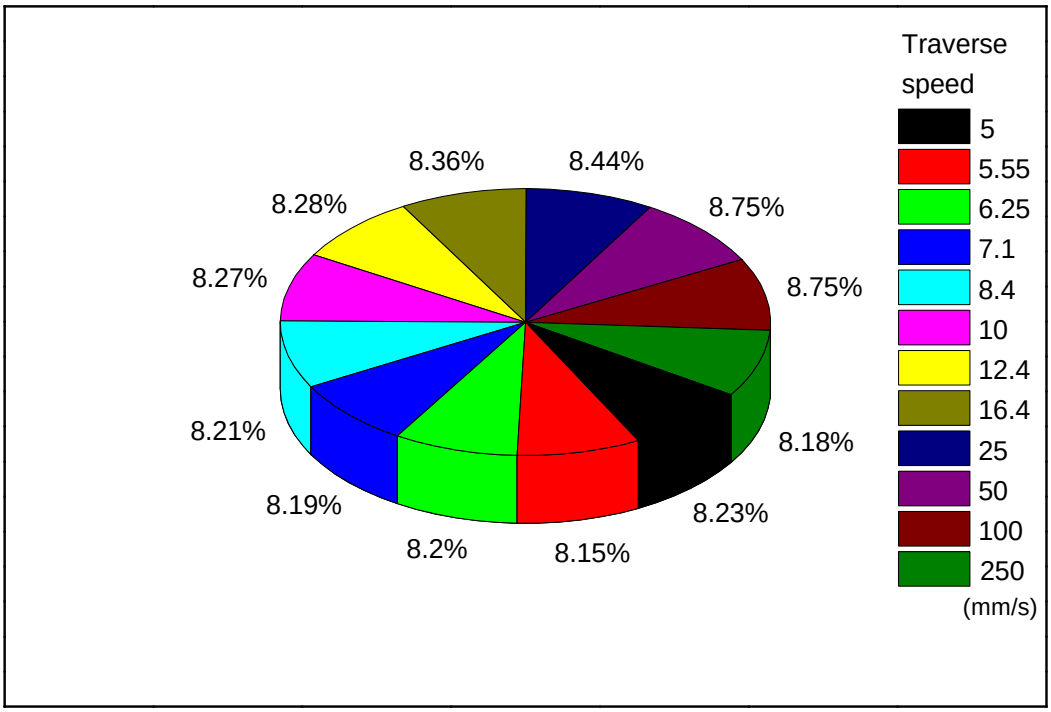

Figure 70: Pie chart showing the relative abundance of silicon after the surface ITO layer was irradiated with a constant fluence of 0.48 Jcm^{-2} at traverse speeds ranging between 5 – 250 mm/s.

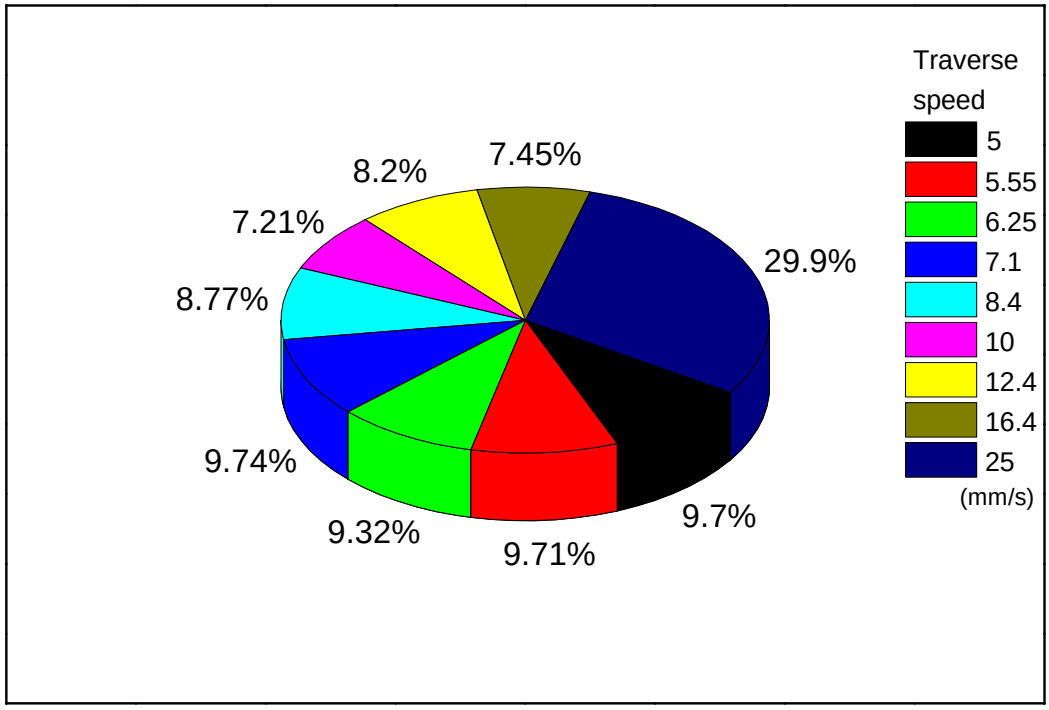

Figure 71: Pie chart showing the relative abundance of indium after the surface ITO layer was irradiated with a constant fluence of 1.43 Jcm^{-2} at traverse speeds ranging between 5 – 250 mm/s.

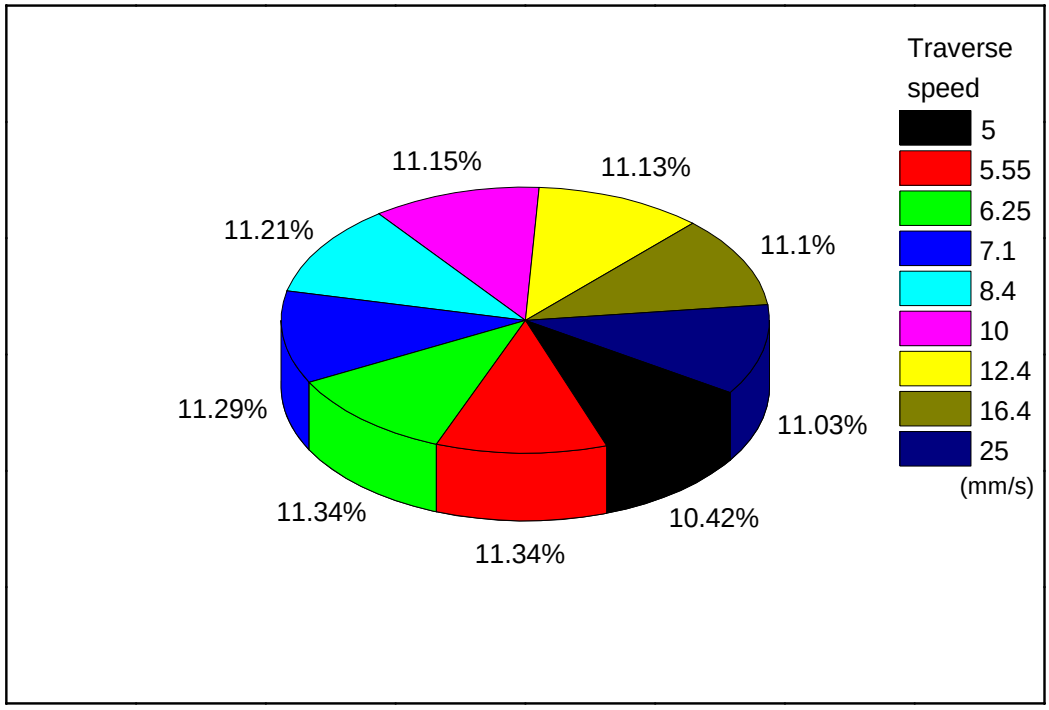

Figure 72: Pie chart showing the relative abundance of silicon after irradiation with a constant fluence of 0.48 Jcm^{-2} at traverse speeds ranging between 5 – 250 mm/s.

Figure 71 shows the abundance of indium remaining on the surface after irradiation with a constant fluence of 1.43 Jcm^{-2} and varying pulse overlap; in this test the highest traverse speed, which produced an identifiable track was 25 mm/s, above this speed no material modification occurred at this fluence. Figure 71 shows that when using a traverse speed of 25 mm/s a larger amount of indium remained adhered to the surface when compared to results shown in the rest of the chart. Similar to the result observed in figure 69, the larger amounts of indium remaining on the surface of the sample were attributed to the small interaction time; reducing the amount of ITO removed. At traverse speeds of 16.40 mm/s and below the amount of material removed was independent of pulse number; although more variation was observed these differences were minimal (up to 2.53 % variation between signals).

As previously observed, the silicon signal recorded after processing was almost uniform indicating that no glass had been removed from the irradiated regions; this again highlights the selective removal of ITO from glass.

When viewing the SEM images for both high and low fluences no observable modification in the centre of the processed areas was observable; this contributes to the assertion that ITO removal was selective.

4.3 Summary

Selective processing previously observed by other authors and applied in long pulse (LP) and continuous wave (CW) materials processing has been investigated using USP laser systems. For the LP/CW regimes, selective processing is dependent upon differential absorption between a thin film and substrate; leading to a rapid increase in temperature in the film causing vaporisation. The substrate positioned underneath the film only experiences a small temperature rise, which is insufficient to induce damage.

SUSP processing was also determined to be dependent upon the difference in absorption between two materials. In SUSP processing the difference in absorption causes the ablation of material whilst the other material remains undamaged. As mentioned in chapter 2, ablation is caused by rapid thermalisation of the irradiated area. Within this region were maximum light absorption and minimal thermal conduction occurs; rapid heating induces a very high transient thermo-elastic stress which exceeds the fracture limit of the thin film [42].

By measuring the absorption coefficient of an ITO coated glass sample, a distinct difference in absorption between ITO and glass was identified. To test the effect of differential absorption rates single pulse ablation threshold tests were undertaken on both ITO and glass, resulting in vastly different ablation thresholds; 0.76 and 9.80 Jcm^{-2} for ITO and glass respectively. In the region separating $\left(\phi_{th}^{1}\right)$ for ITO and glass, only the removal of

ITO was observed; *i.e.* the surface was selectively processed. This was confirmed by measurement of the depth profiles of the ablated craters, were a depth of removal of ≈0.05 μm was observed independent of fluence. Once the threshold for glass ablation was exceeded, selectivity was lost and damage to both ITO and glass was observed. For single pulses, only ITO removal occurred up to (ϕ_{th}^{1}) of glass. This is the maximum separation achievable for selective processing these two materials using single pulses. When above the ablation threshold of glass, selective removal was not possible. From this it is clear that the ablation threshold of both materials enclose the region were selective removal can occur.

Thin film materials processing with a single pulse is rare in micro-processing, as the products being fabricated require drilling or scribing, which cannot be achieved with single pulses. In these instances processing generally requires several pulses to complete the removal process. The need for multiple pulses could impact the applicability of selective processing in micro processing and restoration. To determine the effect of multiple pulse ablation the previous single pulse test on ITO and glass was expanded to include 6, 10 and 25 pulses per spot (PPS). This number of PPS provided a sufficient range to ascertain the effects of multi pulse ablation. The ITO coated onto glass showed no alteration in ablation threshold between 1 and 10 PPS, however a slight reduction in the threshold was observed at 25PPS. When the glass was subjected to multiple pulse irradiations the ablation threshold was found to substantially reduce, from 9.80 Jcm^{-2} to 4.70 Jcm^{-2}. The reduction in threshold was attributed to a previously reported incubation effect [65, 67]. The incubation effect occurs as the result of microstructural modifications induced by successive pulses; these changes cause a cumulative increase in pulse absorption, this makes it easier to initiate surface ablation. From these results it was clear that the selective processing window would be altered by multiple pulse irradiations.

Figure 73 shows the lower and upper limits for single (A) and multi-pulse (B) selective processing of ITO coated glass. The change in threshold value for glass (B) between single and multiple pulse irradiations is highlighted. The (ϕ_{th}^{1}) of ITO represents the lower selective processing limit, as this is the minimum amount of energy input required to remove the film.

The upper selective processing limit was determined to vary depending on whether single or multiple pulses were used during processing; the upper limit for single pulse irradiation was determined to be (ϕ_{th}^{1}) of glass. When irradiated with multiple pulses the upper limit became equivalent to (ϕ_{th}^{N}) of glass, this value was lower than single pulse irradiation. The lowering of the ablation threshold was attributed to the effect of incubation within the glass.

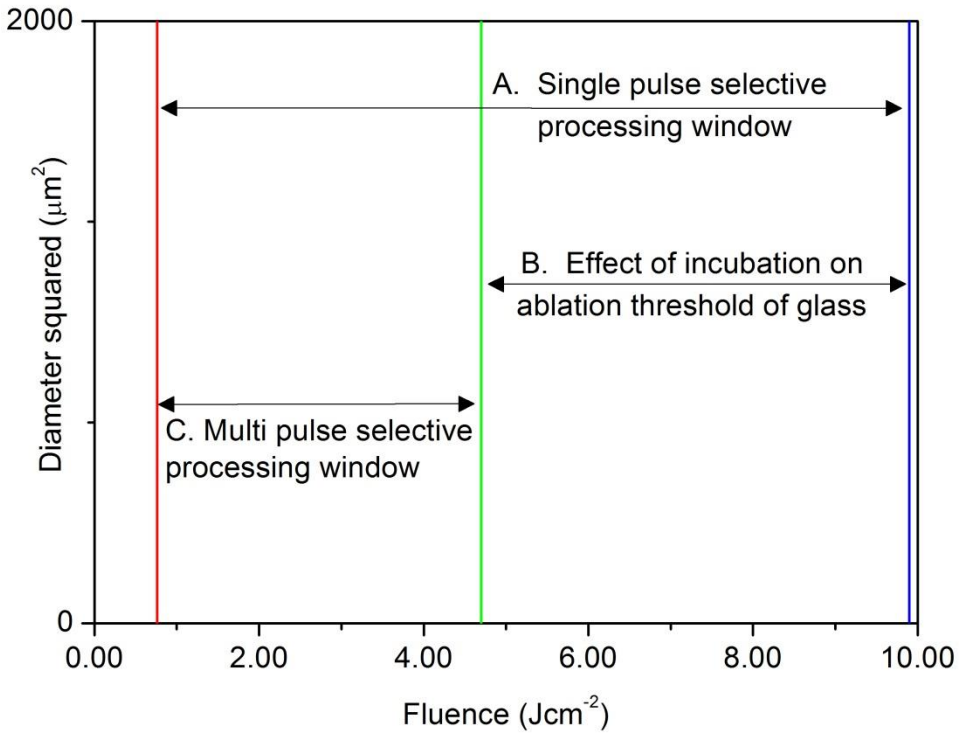

Figure 73: The single pulse ablation threshold of ITO (red) and glass (blue) are combined with the multi-pulse threshold of glass (green) to indicate the selective processing windows available for single and multiple pulses. The effect of incubation on the ablation threshold of glass is indicated.

To test the effect of scanning on selective processing a series of small scanned lines was made on the surface of ITO at varying traverse speeds. These scanned lines were subsequently examined using SEM and EDX techniques, to image surface conditions and determine the elements present. Under high magnification, SEM images showed no distinct modification of the surrounding unprocessed areas, highlighting the quality of processing achievable. There was also no indication of damage on the glass surface. EDX spectra of the area within the ablated tracks were recorded, with the signals for indium and silicon used to represent ITO and glass respectively. The indium signal was shown to decrease by over 90% even at low fluences and high traverse speeds; however it was not possible to remove 100% of the indium; this has previously been reported in work by Yavas *et al* [145] which indicated at shorter wavelengths that some substrate absorption enabled complete film removal.

The silicon peak was also monitored for both high and low fluences to determine process selectively. When compared to an unprocessed sample the detected signal was observed to increase significantly as ITO was ablated. The silicon signals recorded in processed areas were combined to determine the relative effect of traverse speed on signal variation; these were presented in the form of a pie chart to facilitate ease of comparison. It was observed that the intensity of the peak corresponding to silicon remained constant regardless of the traverse speed used to remove ITO.

5 Applications of selective processing

Chapter 4 provided a fundamental study of selective ultra-short pulse (SUSP) processing in order to determine the applicability of this technique for laser materials processing of samples commonly used in this field, something not previously well defined at these pulse durations. The aim of this study was to identify a processing window and the factors controlling the size of this region such as absorption, fluence and scan speed. Through this investigation we were able to provide a set of general guidelines for SUSP processing.

Although we have analysed the parameters determining SUSP processing, it is imperative to show how this technique works not only in theory but when applied to samples generally used in this field; showing this to be a viable process for micro fabrication and laser restoration.

Herein four case studies are presented, two of which were undertaken on transparent conductive oxides (TCO), which are commonly used in photovoltaics [81] and touch panel technology [159]. Two further case studies were focussed on laser restoration; in these instances traditional techniques had proven unsuccessful and conservators were in need of a new tool to continue their work. Through investigation of these applications we were able to identify the benefits and limitations of using SUSP processing.

In all application tests the basic structure of the sample was the same, i.e. a substrate coated with a thin layer of material; a detailed description of each sample is given in the relevant section.

5.1 Micro processing

Micro processing describes the fabrication of a functional device within a size range of 1 micron to 1 mm. This manufacturing process can be additive or subtractive and has traditionally been applied using mechanical force or etching. More recently, the use of lasers in this technique has become more prevalent, due to the benefits that can be provided including higher quality structures, simplified manufacturing processes and removing the need for hazardous chemicals.

The following case studies analyse the use of ultra-short pulses for use in the manufacture of a thin film circuit and a photovoltaic cell.

5.2 Parallel processing of ITO functional circuits using ultra-short pulses

In device manufacture there is a requirement to be able to fabricate large numbers of devices in short time intervals. When using micro processing techniques, one method of

reducing production time is to divide a single incoming beam into multiple (N) beams using a spatial light modulator (SLM). This component contains a liquid crystal display (LCD), which once integrated into the optical arrangement, displays a computer-generated hologram (CGH). This is used to modify the beam path of incoming light; thereby allowing the user to generate multiple beams, which can be used to parallel process samples (also referred to as multi beam processing).

In this study we have utilised a simple binary grating to create multiple beams, producing conditions similar to Young's double split experiment. As light interacts with the hologram reflected beams interfere both constructively and destructively. In regions of constructive interference this results in bright spots (orders), which can be used in materials processing.

One complication observed in parallel processing (PP) is the variation of diffracted beam uniformity. This variation can cause manufacturing problems such as under scribing, due to low power in the diffracted beam or conversely, substrate damage caused by high power in the diffracted beam.

By determining the selective processing window for the sample prior to processing the SUSP technique eliminates the possibility of damaging the substrate. In addition if the reflected beam has a low power the user can rescan or increase the fluence.

In the present study, we have used a simple grating hologram, however we are aware that several holograms of varying complexity are available and can be utilised with SLMs in order to produce multiple beams with different properties, an example of an alternative CGH is the Gerchberg-Saxton algorithm [160].

5.2.1 Experimental procedure

The selective processing window previously determined for ITO coated glass samples (chapter 4) have been applied herein for use in parallel processing.

Areas of ITO coated glass samples (100 nm thick ITO coating) were hatched in order to create the circuits used in this study, i.e. pulses overlapped in both X and Y directions, as illustrated in figure 74. This ensures that no cross boundary conductivity occurs within the circuit. In the previous chapter, a series of scans was applied to ITO coated glass using different fluences and traverse speeds; this data was then used to determine the track width required.

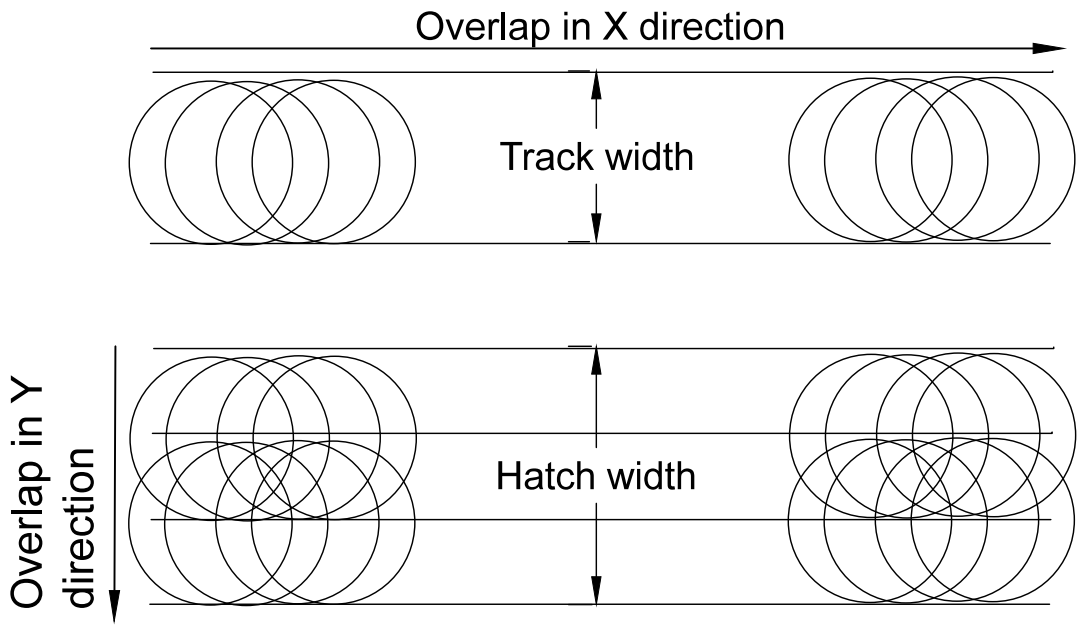

Figure 74: Schematic representation of hatching. Overlapping in X produces a single track, whilst overlapping in both X and Y is used to create a hatch area.

As previously discussed, we have determined that there is no incubation effect observed for ITO, up to and including 10 pulses per spot (PPS). In addition, the change in ablation threshold observed for glass, which is altered by incubation, is known thereby providing a complete selective processing window. By operating within these parameters, a series of square hatches (3x3 mm) was produced by varying the overlap in the Y direction and fluence.

After processing the square areas, the conductivity between the processed regions and ITO film was tested in order to determine whether the parameters used were acceptable for use in circuit manufacture.

Once the optimum parameter was determined, a full circuit was fabricated. The design consisted of a simple circuit track (figure 75) with two enlarged pads positioned at each end of the track. Using these pads the conductivity in the circuit and across scribed boundaries was checked.

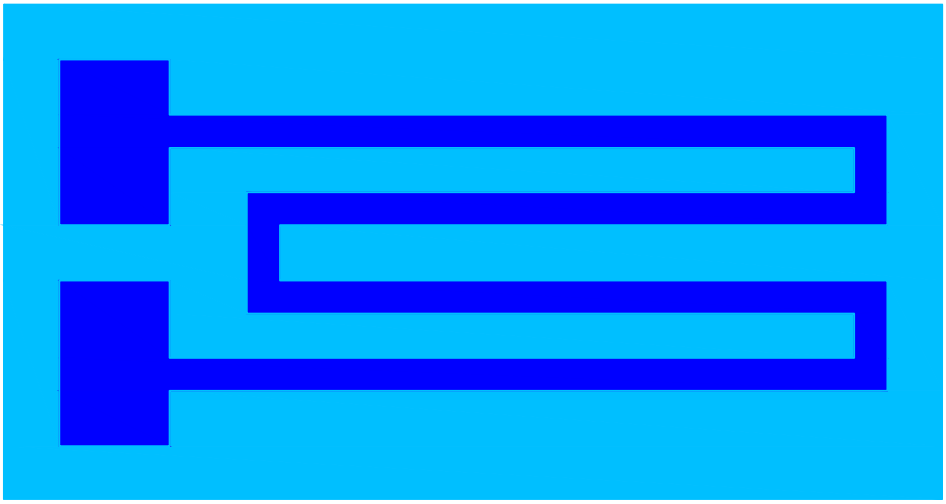

Figure 75: A schematic representation of the simple circuit fabricated on to the ITO coated glass, wherein areas that have not been irradiated are shown in dark blue; areas that were processed using an USP laser are shown in light blue.

Once the optimum processing parameters were determined and verified using a single beam to produce an individual circuit, the optical arrangement of the HighQ system was modified so as to include an SLM, as shown in figure 76.

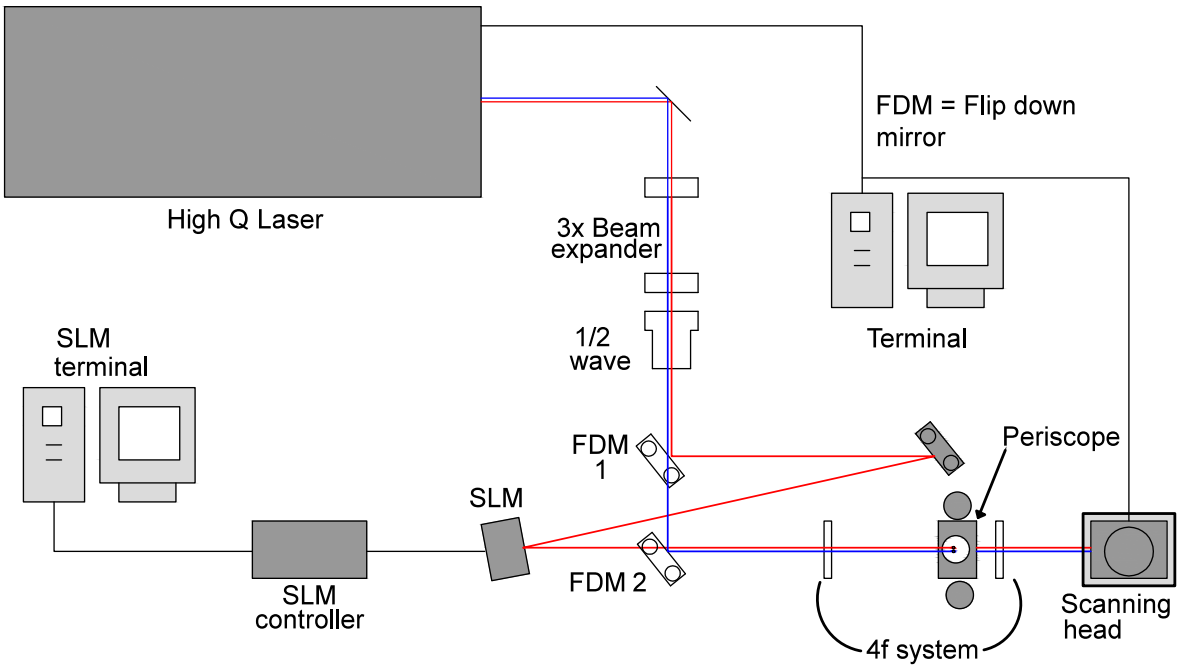

Figure 76: Schematic representation of the modified HighQ optical arrangement used in the present study. This setup retains all the components used previously but includes the addition of an SLM, two FDMs and a 4f optical system. For parallel processing FDM 2 was folded so as not to obstruct the beam path after being reflected from the SLM.

By adjusting the flip down mirrors (FDM) it was possible to switch between single and multi-beam processing with minimal realignment of the optical path required. The Fourier,

also referred to as 4f, optical system was used to translate the image produced by the SLM into the focal plane of the focussing optic.

The SLM terminal was used to generate holograms (CGH), which were displayed on the LCD; these acted as diffraction gratings. Due to the curvature inherent to LCOS SLMs the reflected wave can become distorted [161]. To minimise the effect of distortion, the angle of incident light on the SLM was kept small (<15°).

By varying the greyscale of the CGH, the number of orders produced and the intensity of each beam could be varied.

A sample of the binary grating used in this study is shown in figure 77. The numbers of pixels within the grating period were varied so as to determine whether the resulting diffraction angle guided both first order beams toward the scanning galvanometer; higher orders (> ±1) generated by the SLM were lost due to the angle of diffraction being too great.

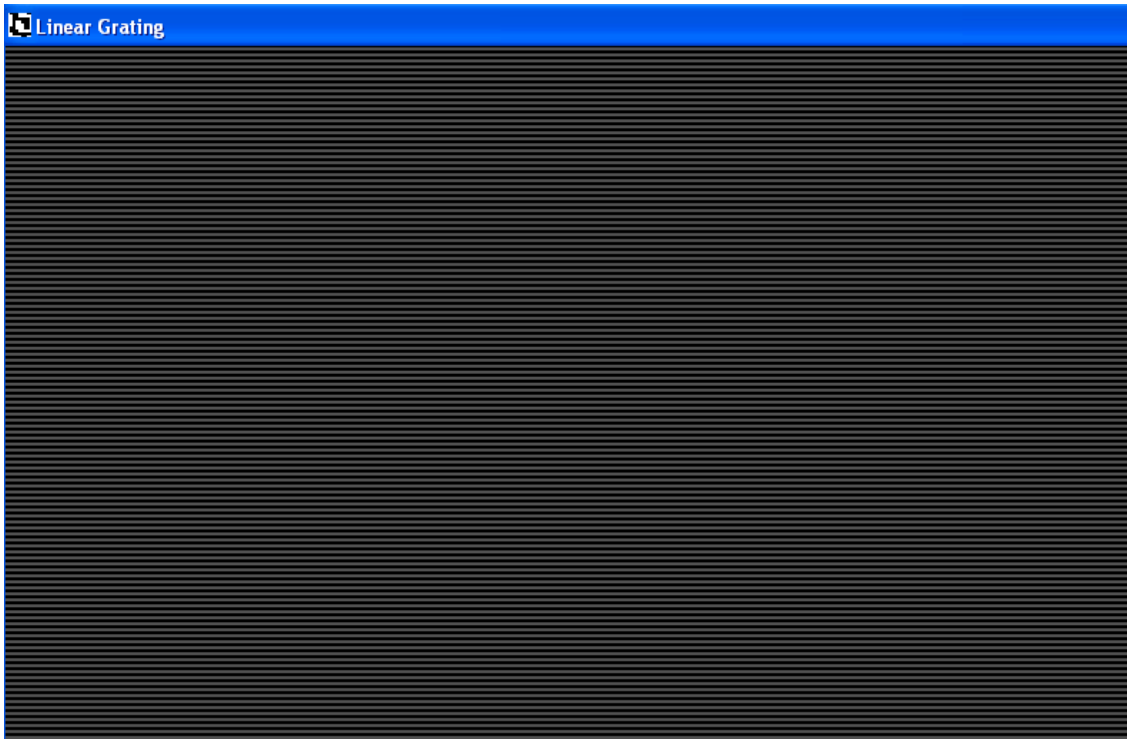

Figure 77: Image of the binary linear grating used to generate multiple beams for parallel processing. The grating period was set to one pixel to ensure that both first order-diffracted beams could be guided to the scanning head.

Before parallel processing was undertaken the uniformity of the diffracted beams was measured. To prevent the fabricated circuits from overlapping, the zero order beam was blocked and processing was continued using only the first order diffracted beams. The uniformity of the multiple beams was determined through the measurement of the power in each order. In this test both the zero beam and one of the first order beams were blocked. The process was reversed in order to measure the corresponding first order power. A Spiricon image of the diffracted beams is shown in figure 78.

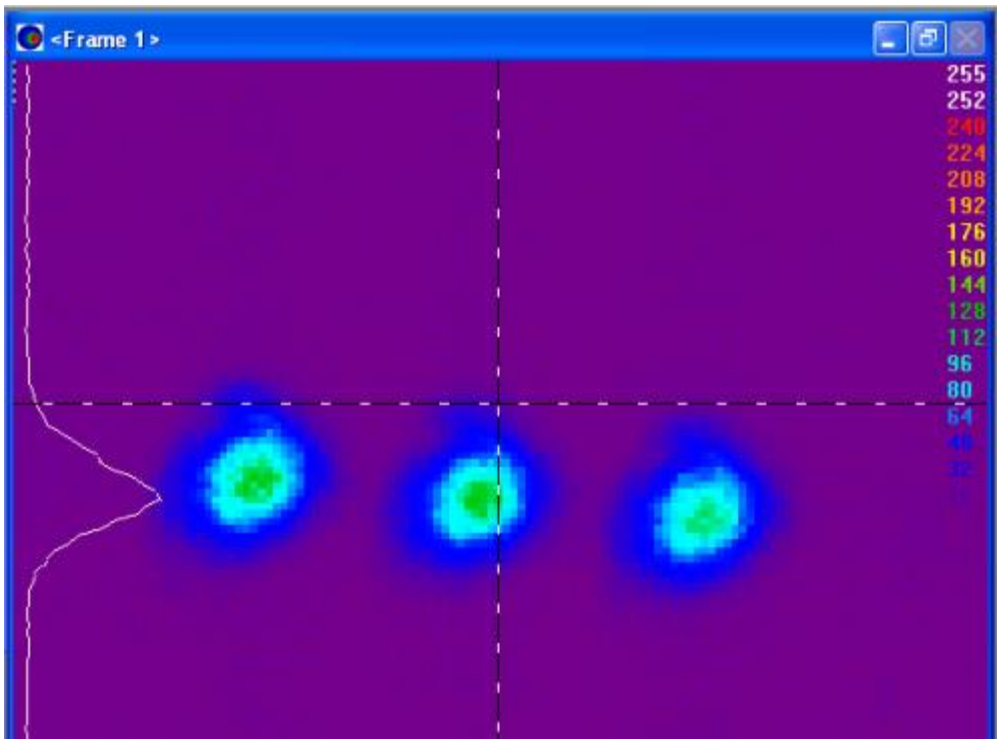

Figure 78: Spiricon image of the three beams generated using a simple binary grating. The centre spot is the zero order beam, whilst the spots to the far left and right are the first order diffracted beams used in circuit fabrication.

5.2.2 Results and discussion

5.2.2.1 Single beam processing

From the previous investigation (chapter 4), a fluence of 4.24 Jcm^{-2} and traverse speed of 32 mm/s were chosen to fabricate the ITO circuit. At this traverse speed the ablation threshold of glass is expected to be 4.70 Jcm^{-2}, therefore processing with this fluence should allow us to remain within the selective processing window. Using this combination of parameters circuits were produced quickly and accurately, something that would benefit manufacturers.

To test the effect of overlapping pulses in both X and Y directions, a series of small (3x3 mm) hatches was made using a fluence of 4.24 Jcm^{-2}, onto ITO coated glass sample with increasing overlap. The surface roughness of a sample of unprocessed and uncoated glass was analysed using white light interferometry imaging (figure 79); the surface roughness was recorded as ≈3.54 nm.

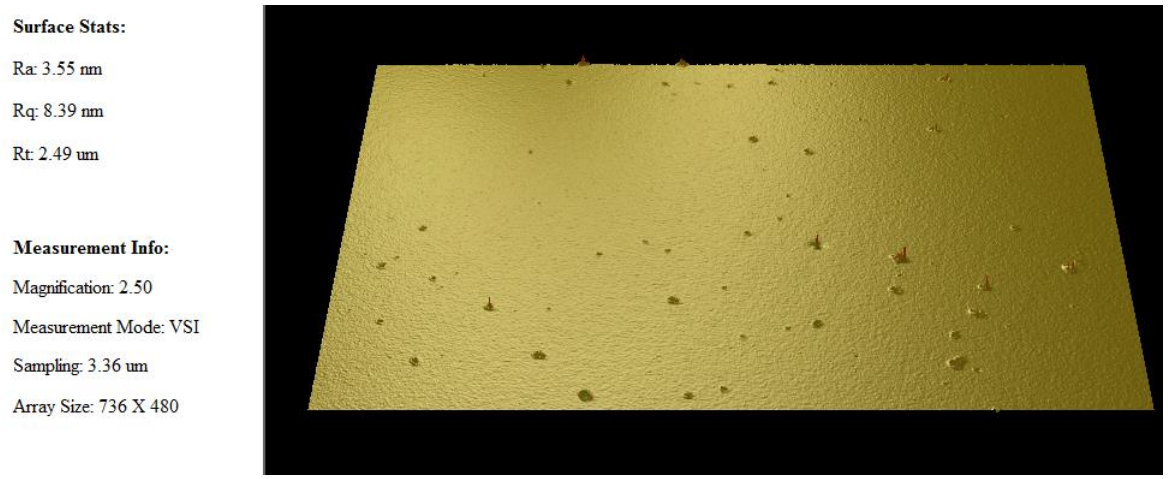

Figure 79: A white light interferometry image showing the surface of an unprocessed, uncoated glass sample. These measurements were recorded at x50 magnification.

The pulse overlap of the hatch in the Y direction was increased between 70 – 95 %. Figure 80 shows the white light interferometry profiles for the different percentage overlaps. The surface roughness (Ra) was decreased from 14.08 nm to 6.42 nm as the percentage overlap of the hatch was increased. As the laser produces a Gaussian (TEM_{00}) shaped pulse, increasing the overlap ensures that a larger area of the sample is exposed to the highest fluence at the peak of the pulse, therefore more material is effectively removed, decreasing the surface roughness of the sample.

From these images it is possible to confirm that no observable damage occurred to the glass substrate as a result of the processing method used. Any resulting damage to the glass, such as cracks and deep holes, would appear as black areas within the processed regions as an insufficient amount of light is returned to the detector and an image cannot be produced.

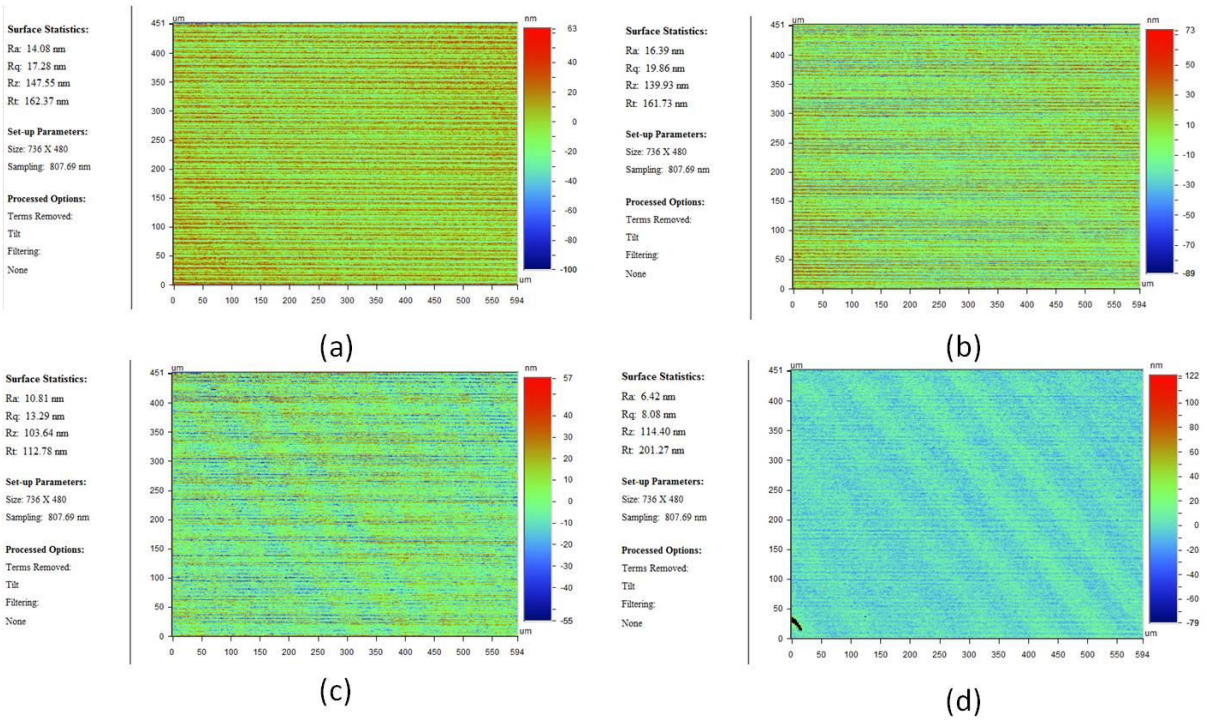

Figure 80: White light interferometry image of an ITO coated glass sample, processed using an overlap of (a) 70%, (b) 80%, (c) 90% and (d) 95%.

The surface roughness of the processed ITO coated glass samples was recorded using white light interferometry measurements and compared directly with uncoated glass. Figure 81 shows the comparison between the surface roughness of these samples.

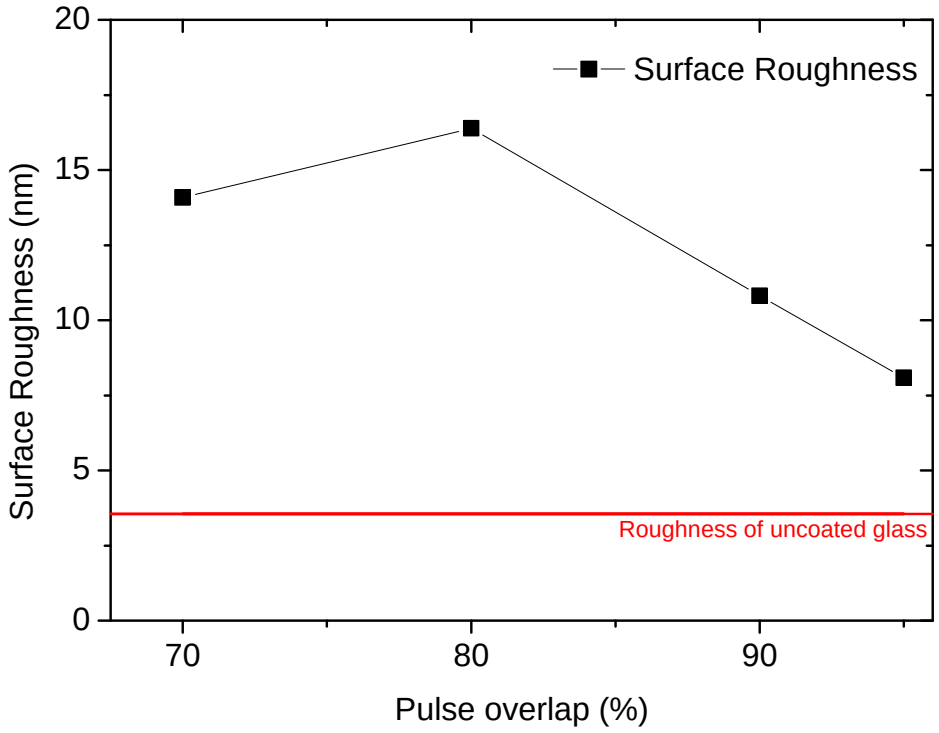

Figure 81: A comparison between the surface roughness of the processed ITO coated areas with increasing pulse overlap. The red line represents the surface roughness recorded for uncoated glass.

These results show that the surface roughness of the processed ITO coated glass samples remained higher than that of the uncoated glass, even when the pulse overlap was increased. This was attributed to some ITO remaining on the surface of the substrate after irradiation. This effect was also observed in chapter 4 on ITO coated glass samples scanned in a single line. This was expected, as Yavas *et al* has shown that complete removal of ITO from glass is only possible when using UV wavelengths but cannot be achieved with visible or infrared wavelengths [145].

Whilst the surface roughness tends to decrease as the pulse overlap is increased, a higher Ra value was measured when using an overlap of 80 % compared to 70 %. This may be attributed to the percentage overlap being insufficient to produce a larger average peak fluence region. Therefore the small differences observed between these two samples may be attributed to natural variance.

Despite the fact that some ITO remained on the glass substrate after processing the surface roughness was of the order of nm, indicating no damage to the glass substrate. From these results we have shown that overlap at this fluence and traverse speed had no effect on the damage threshold of glass and that selective surface processing remained viable.

5.2.2.2 Parallel processing

After determining the optimum parameters for producing a simple circuit with a single beam, the SLM was inserted into the optical path and used to parallel process the ITO coated glass sample. To ensure no overlapping between circuits occurred the zero order beam was blocked leaving the +/- first order beams to be used in processing.

The transmitted power of each beam is determined by the CGH, therefore before processing, the grayscale was varied in order to minimise the power distribution between the first order beams, as shown in table 19. There are two grayscale controls available for adjusting the SLM output, each of these affect the contrast of the adjacent grating periods, therein altering the path of the reflected rays. In this test, grayscale one (G1) was varied whilst grayscale two (G2) remained constant. As grayscale two was set to zero, the contrast between adjacent periods was increased with increasing values of G1. The change in contrast between the grating periods affects the interference of the reflected rays. By varying the contrast we were able to identify which parameters produced the most uniform power distribution.

Table 19: Variation of transmitted power when altering G1. Only the first orders were used in processing, however zero order data has been included for completeness.

Variation in power between diffracted first orders when G1 was varied			
G1	-1 (mW)	0 (mW)	+1 (mW)
210	183	228	124
200	183	236	134
180	179	255	152
160	165	288	167
140	148	337	168
130	135	319	159
120	122	390	155
100	94	465	129
80	66	554	93
60	39	625	57
40	19	627	26
20	5	650	9

Table 19 shows that varying the contrast between G1 and G2 has a significant effect on the transmitted power distribution of the diffracted orders. However, equivalent power distribution between orders was not possible. For parallel processing to be used as a micro manufacturing technique, the variation in power needs to be taken into consideration when determining the processing parameters, as variation in uniformity can affect the quality of processing.

By utilising SUSP processing it is possible to negate the effects of non-uniformity in transmitted beams. By increasing the overall fluence the user can ensure that there is sufficient power in both diffracted beams to achieve materials processing, provided that the highest fluence remains within the selective processing window.

Figure 82: Images of the ITO coated glass surface after parallel processing with a G1 value of 160. The image on the left shows both fabricated circuits. The right hand image is provided to show the size of the circuits hatched.

In order to highlight the benefits of selective processing, in this example we have produced simple ITO on glass circuits, using both uniform and non-uniform beams. The grayscale was varied to produce multiple beams with near uniform (160) and disparate (100)

powers. Figure 82 shows two circuits fabricated using a grayscale value of 160, a fluence of 4.24 Jcm^{-2} and a traverse speed of 32 mm/s, these values are below the multi-pulse ablation threshold value for glass (as determined in chapter 4). This greyscale produced highly uniform beams with a variation in intensity between orders of <2 %.

This test was repeated with a grayscale value of 100; providing a greater disparity in transmitted powers (30% between orders). The conductivity of the circuits produced using both uniform and non-uniform beams were checked with a potentiometer; no conductivity between processed and unprocessed ITO regions was detected for either circuit. Figure 83 shows the white light interferometry profile of the processed regions for the parallel circuits produced using non-uniform first order beams. Generally, disparity in beam power would lead to a difference in the amount of ITO removed by each beam; however we have shown that when using SUSP the average depth of film removal produced by each beam is in good agreement. In addition no damage to the substrate was observed despite the higher fluence of one of the diffracted beams.

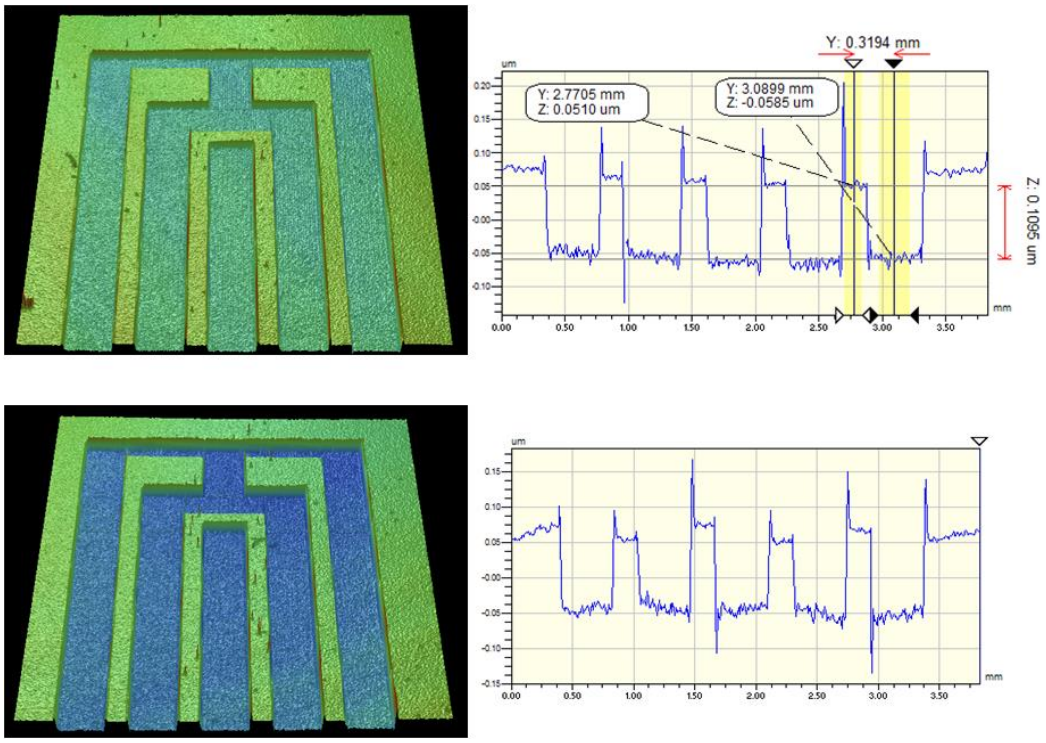

Figure 83: White light interferometry profile of circuits produced using non-uniform beams. These circuits were produced using first order diffracted beams whilst the zero order beam was blocked. This prevents overlapping of the circuits.

5.2.3 Summary

Herein, we have shown that the selective processing parameters for ITO coated glass samples, as determined previously (chapter 4); can be applied for use in parallel processing of small circuits onto ITO glass samples. This was achieved by determining the

optimum pulse overlap to ensure no cross boundary conductivity occurred. An electrically addressed SLM was used in conjunction with a CGH in order to generate multiple beams. By varying the number of pixels in the grating period of the LCD we were able to successfully direct both the zero order and first order beams towards the processing region.

Using multiple beams the applicability of SUSP in parallel processing with both uniform and non-uniform first order diffracted beams was demonstrated. In order to achieve this we analysed the effect of the varying the contrast between grating periods on the uniformity of the transmitted power distribution. Thereby we were able to select appropriate grayscale values for the production of both uniform and non-uniform beams.

Uniform and non-uniform beams were used in the parallel processing of a simple circuit; in the case of non-beam uniformity SUSP was utilised to ensure that the circuit was successfully manufactured, despite the disparity between the first order beams. The resulting circuit was successfully processed using beams with intensity variations of ≈1% and 30%. Examination of the processed areas shows uniform material removal from the surface using both uniform and non-uniform beams. Using a spatial light modulator and selective processing the time for circuit fabrication has been reduced by half; by increasing the number of diffracted orders this could be further increased providing a high speed micro processing solution.

This case study showed how SUSP processing can be incorporated within a different micro processing technique, in this instance parallel processing. The results obtained in this study imply that SUSP could be used in conjunction with more complex CGHs to produce a greater number of beams. This would reduce manufacturing time and costs whilst still achieving the same high quality results observed in etching and LP/CW laser direct write techniques.

5.3 Selective processing of PV cells

Solar cells are used to harness light from the sun and convert it into electricity, a detailed discussion of how solar cells function is provided in chapter 2. The use of solar cells as an alternative method of power generation has seen a large increase in recent years in homes, businesses and solar farms. Currently, there are two main obstacles to wider uptake in solar cell technology, the cost of manufacturing solar cells and conversion efficiency. Thin film solar cells have a conversion efficiency of up to approximately 20%. This efficiency is lower than that observed for other common types of solar cells, such as crystalline silicon and multi-junction cells, which have optimum efficiencies of 25 % and 43.5 % respectively [162]. Despite the lower efficiency, uptake of thin film solar cells has been largely successful due to the relatively low manufacturing costs; this produces a lower overall cost per Watt (CPW).

A new solar cell manufacturing process based on proprietary deposition techniques aims to reduce the overall CPW by decreasing photovoltaic (PV) cell manufacturing costs, whilst matching current efficiency standards. Lower manufacturing costs are achieved through the use of simple, low cost equipment, which does not need skilled labour and requires little maintenance. The cell consists of three layers: a metal contact, flame sprayed oxide (FSO) and a transparent conductive oxide (TCO); these layers were deposited onto a glass substrate. The cells were originally designed to be manufactured at large size (>1x1m^2), producing larger cells increases the area in which electron-hole pairs can be formed and useable electricity generated. However, the increased distances travelled by charge carrying electrons resulted in a low overall efficiency, as charge was lost due to recombination.

One method of improving charge extraction is to reduce the distance between the point at which free electrons are generated and where charge is extracted. Herein, laser scribing of thin film and flame sprayed layer was undertaken to separate charge areas, by reducing the area through which electrons can travel this maximises the extraction efficiency of the cell.

To keep the CPW as low as possible processing was initially attempted using a single laser system, to facilitate this, a jig was fabricated to ensure that the sample could be registered at the same point during each processing run. The use of a single system is advantageous as it reduces manufacturing costs, which in turn keeps the CPW within acceptable limits.

5.3.1 Experimental procedure

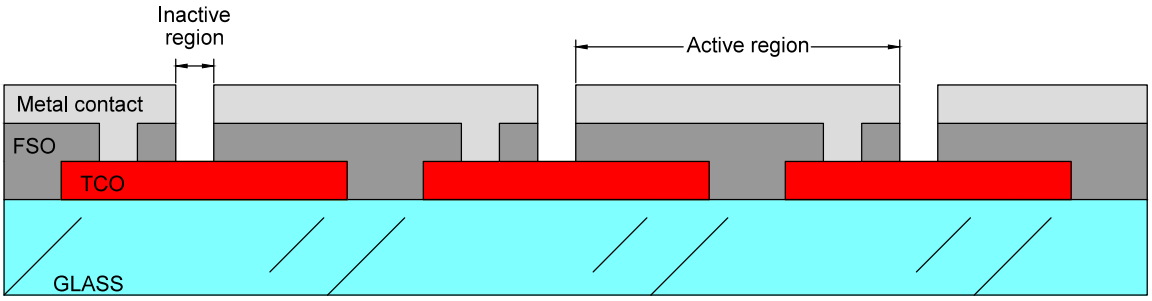

Figure 84: Schematic of stacked PV cell; laser processing was to be used to create the inactive regions through selective scribing of the TCO, FSO and metal contact. This reduces the likelihood of recombination, improving cell efficiency.

Experimental studies were carried out on two of the three layers comprising the PV cell, namely the TCO and the FSO oxide layers which are used in charge generation. The structure of the photovoltaic cell (figure 84) consists of three layers, the TCO, FSO and metal contact. To produce a functioning cell these layers require scribing to ensure that the metal contact layer, which extracts the potential difference, is in contact with both the FSO and

TCO layers [163]. The photovoltaic cell fabricated herein utilises the above structure to ensure efficient charge generation.

To produce this photovoltaic cell commercially available transparent conductive oxide (TCO) coated glass samples (TEC7) where purchased from Pilkingtons. The TCO layer was first scribed to create individual cells; thereby exposing the glass. The manufacturer stated TCO film thickness was 500 nm. The separation required between charge generation areas for this PV cell was 250 microns. In order to achieve this, the Aerotech stage was programmed using G code software, which controls the speed and direction of the stage, the hatch was repeated until this track width was achieved. This process was repeated at 20 mm intervals across the sample.

After scribing the TCO layer to create the platform for the individual cells, the samples were coated using a thermal spraying technique. Powders fed in by a hopper are heated above the melting point and quickly deposited on to the surface of the scribed TCO layer. The oxide layer was then allowed to solidify, in air, by rapid cooling. After depositing this layer scribing was required at a position slightly offset from the regions in which the TCO layer was removed (see structure of PV cell in figure 84). In order to achieve this, a jig was created (figure 85) to ensure that the samples could be registered in the same position even if removed multiple times. This combined with the high precision of the Aerotech stage (±5 µm) allowed for precise control over the scribed area.

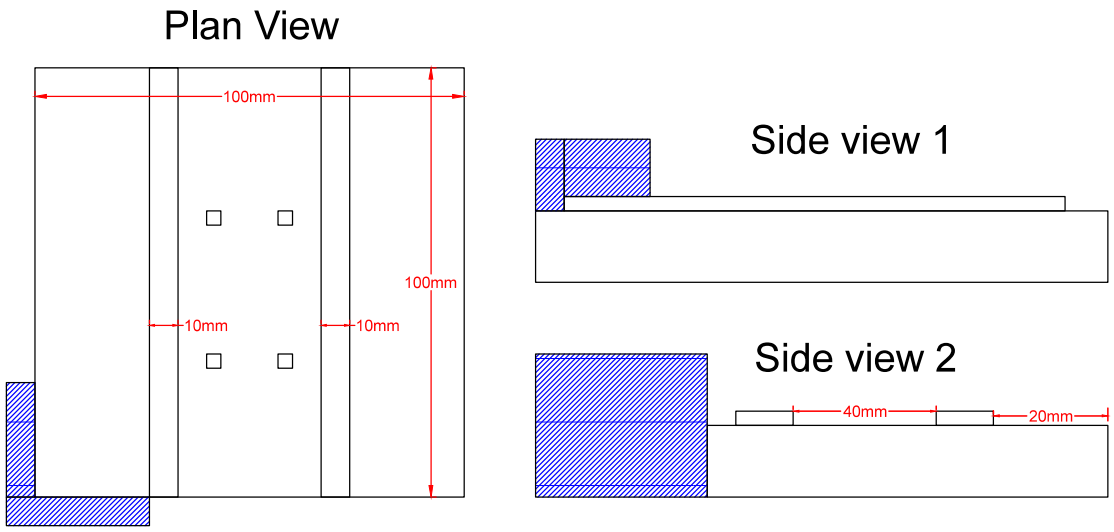

Figure 85: A schematic representation of the jig created to assist in registering the PV samples. The blue area represents the registration point.

5.3.2 Results and discussion

The TCO used in the present study was fluorine doped tin dioxide (F-SnO_2); this material has similar properties to ITO, as used in chapter 4 and chapter 5. To establish whether selective processing was feasible for the TCO sample, the absorption coefficient

and ablation threshold were determined experimentally and subsequently compared to the values previously recorded for glass (chapter 4). Through this it was possible to determine the selective processing window for F-SnO_2 and glass; using the optical arrangement presented in chapter 4.

The absorption coefficients were measured using the HighQ and Coherent Talisker lasers systems, at a wavelength of 1064 nm and 532 nm respectively. The input beam diameter was ≈9 mm for the HighQ and ≈8 mm for the Talisker. Both samples were placed after a beam expander, the HighQ and Talisker using a magnification of x3 and x4 respectively, ensuring that the beam was collimated.

By using a collimated beam it is possible to accurately determine the intensity of the pulses. The incident (I_0) and transmitted (I_1) intensity at wavelengths of 1064nm and 532nm respectively are shown in tables 20 and 21.

Using equation 1.3, the absorption coefficient of F-SnO_2 at 1064 nm was determined to be $2.87x10^3$ cm^{-1} ±4%; whilst for glass absorption remained low at 78.10 cm^{-1} ±7%. This low absorption recorded for glass was in good agreement with results presented in chapter 4. Using 532 nm the absorption coefficient of F-SnO_2 was measured to be $1.94x10^3$ cm^{-1} ±15 %; for glass the absorption coefficient was 51.21 cm^{-1} ±5%. This result was found to be in good agreement with other values determined for glass in this thesis (chapter 4).

From these results it was observed that, similar to ITO, absorption was improved when using IR wavelengths in comparison to visible light. Therefore F-SnO_2 scribing was carried out using 1064 nm radiation. Figures 86 and 87 show how the transmission ratio varies with increasing impinging intensity (I_0). The transmission is shown to be independent of intensity for both 1064 nm and 532 nm, confirming linear absorption of the beam for both wavelengths.

Table 20: Impinging and transmitted intensities recorded for 1064 nm radiation on glass and F-SnO_2. As F-SnO_2 was coated on to the glass surface, the intensity values were adjusted to factor in the glass substrate.

Determining the absorption coefficient of F-SnO_2 and glass – Intensity calculations			
λ = 1064 nm			
Glass		F-SnO_2	
I_0 (Wcm^{-2})	I_1 (Wcm^{-2})	I_0 (Wcm^{-2})	I_1 (Wcm^{-2})
$9.95x10^5$	$7.56x10^5$	$9.95x10^5$	$8.55x10^5$
$1.99x10^6$	$1.53x10^6$	$1.99x10^6$	$1.73x10^6$
$4.97x10^6$	$3.96x10^6$	$4.97x10^6$	$4.30x10^6$
$9.95x10^6$	$7.58x10^6$	$9.95x10^6$	$8.65x10^6$
$1.49x10^7$	$1.14x10^7$	$1.49x10^7$	$1.30x10^7$
$1.99x10^7$	$1.56x10^7$	$1.99x10^7$	$1.71x10^7$

Table 21: Impinging and transmitted intensities recorded for 532 nm radiation on glass and F-SnO_2. As F-SnO_2 was coated on to the glass surface, the intensity values were adjusted to factor in the glass substrate.

Determining the absorption coefficient of F-SnO_2 and glass – Intensity calculations			
λ = 532 nm			
Glass		F-SnO_2	
I_0 (Wcm^{-2})	I_1 (Wcm^{-2})	I_0 (Wcm^{-2})	I_1 (Wcm^{-2})
$8.16x10^5$	$6.76x10^5$	$8.16x10^5$	$7.36x10^5$
$9.95x10^5$	$8.95x10^5$	$9.95x10^5$	$8.95x10^5$
$1.75x10^6$	$1.39x10^6$	$1.75x10^6$	$1.55x10^6$
$2.49x10^6$	$2.09x10^6$	$2.49x10^6$	$2.29x10^6$
$3.73x10^6$	$3.08x10^6$	$3.73x10^6$	$3.43x10^6$
$4.97x10^6$	$4.13x10^6$	$4.97x10^6$	$4.58x10^6$

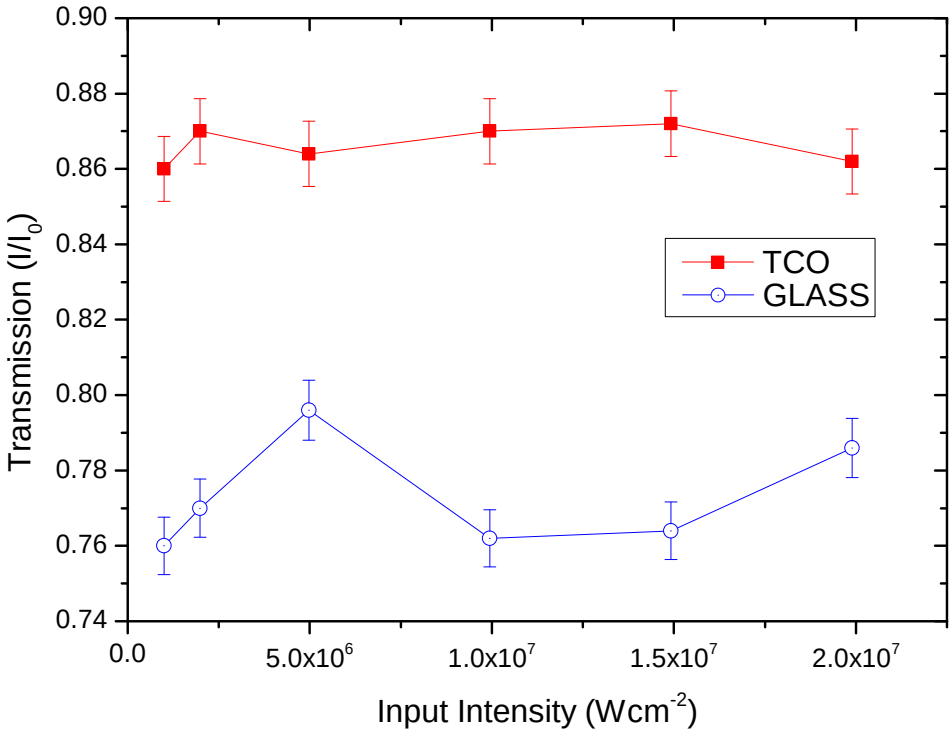

Figure 86: The variation of transmission ratio against impinging intensity for both the TCO and glass sample, irradiated using the HighQ laser operating at a wavelength of 1064 nm.

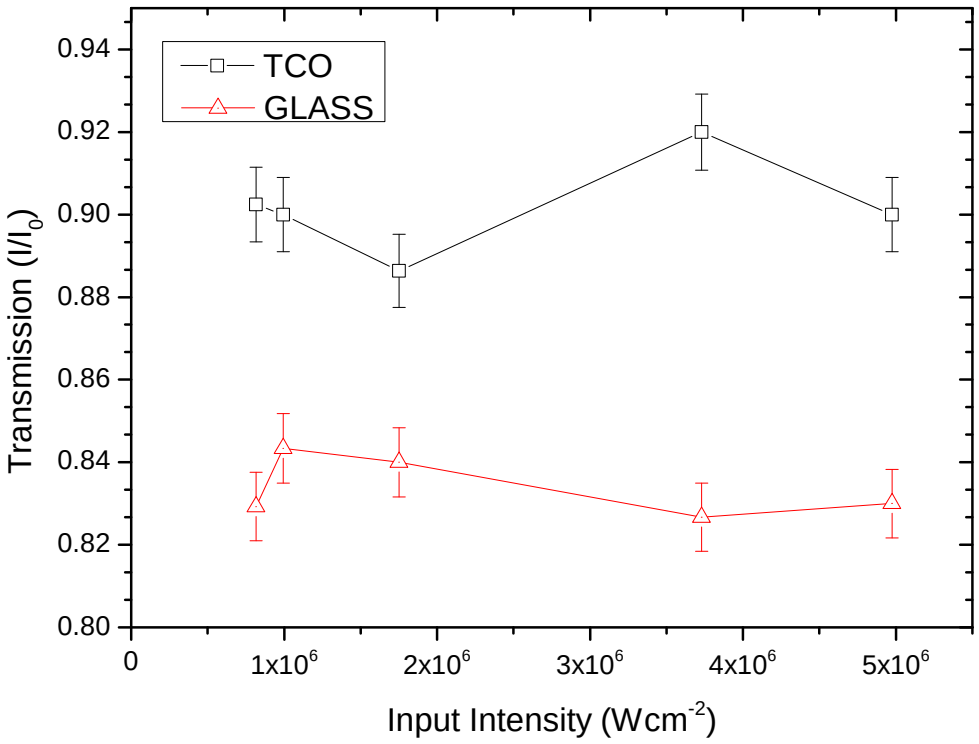

Figure 87: The variation of transmission ratio against impinging intensity for both the TCO and glass sample, irradiated using the Talisker laser operating at a wavelength of 532 nm.

5.3.2.1 Single Pulse Ablation threshold

The optical microscope (OM) images of the resultant ablated craters produced are shown below (Figure 88); these were used to determine the ablation threshold of the F-SnO_2. To determine the diameter of individual ablated craters in images A, B and C measurements were recorded in both the horizontal and vertical dimensions, using the Nikon microscope (chapter 3), and averaged. These individual measurements were subsequently combined with the average diameters recorded for the four other individual ablated craters, made at the same fluence. These were averaged to provide an average ablation diameter at each fluence value.

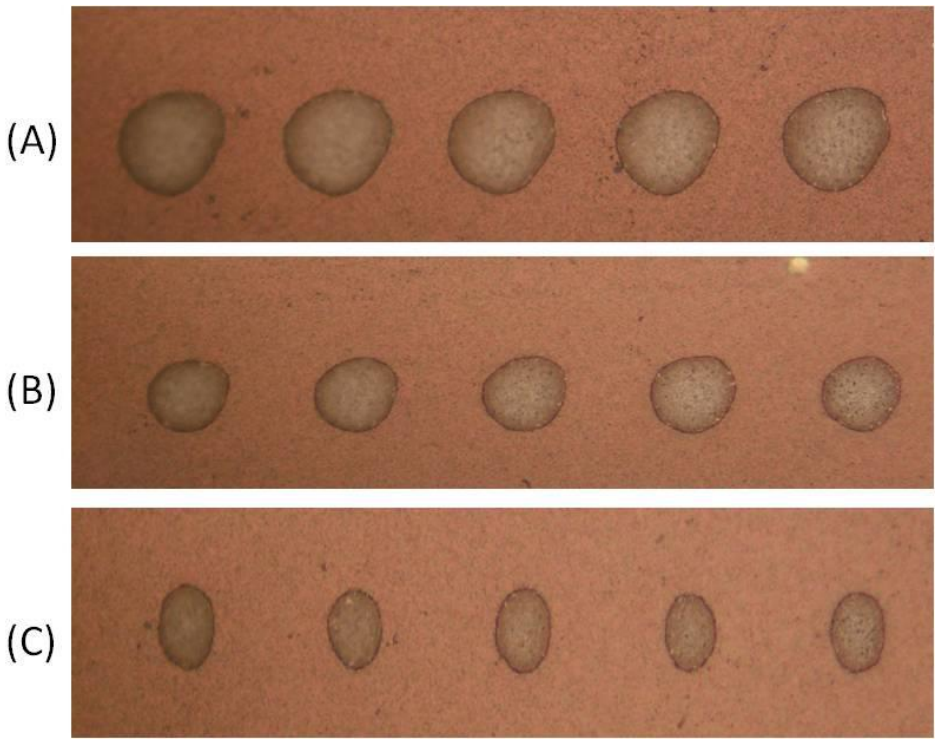

Figure 88: Optical microscopy images of single pulse ablation craters produced using fluences of (A) 31.83 Jcm^{-2}, (B) 22.28 Jcm^{-2} (B) and (C) 12.73 Jcm^{-2} in the TCO layer.

Figure 89 shows a plot of the single pulse ablation threshold of F-SnO_2; when combined with the multi-pulse data gained for glass the selective processing window, which was established to be 1 – 9.80 Jcm^{-2}, depending on the number of pulses. This window is smaller than that observed for ITO, due to the single pulse ablation threshold of F-SnO_2 being greater than ITO. However, the threshold separation was still large enough for SUSP to proceed. At high fluences a change in the gradient of the slope indicates a modification in the mechanism for material removal; this was attributed to the transition to a "strong" ablation regime [147] were thermal effects enhance material removal rates. This effect is also observed in other transparent oxides, such as ITO.

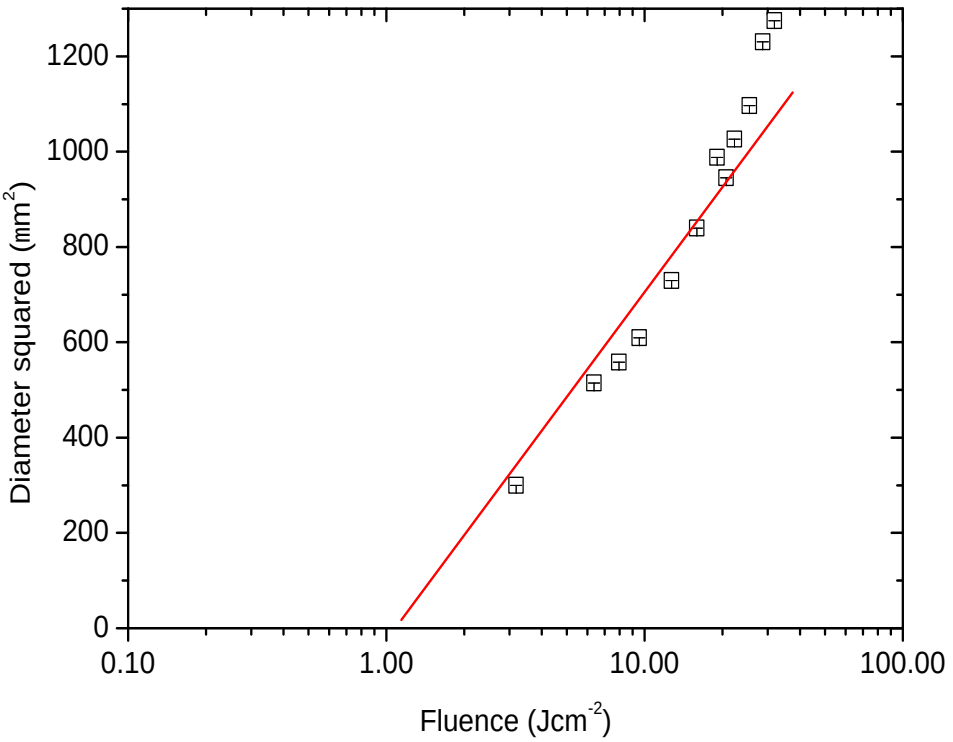

Figure 89: Illustrating the effect of increasing fluence on the diameter squared of the ablated craters. Extrapolation of the curve to zero indicates the single pulse ablation threshold of F-SnO_2 to be ≈1 Jcm^{-2}.

From these results it was determined that the parameters used previously for ITO samples were suitable for selectively processing F-SnO_2. The transparent conductive oxides, ITO and F-SnO_2 were observed to have similar ablation thresholds; 0.76 and 1.02 Jcm^{-2} respectively. As a result the processing parameters applied in the previous section (parallel ITO processing) where tested in the processing of F-SnO_2. This was possible due to the fluence being greater than the ablation threshold but below the damage threshold for glass when using N pulses.

Due to the size of the sample (100 mm x 100 mm) processing could not be completed using the Nutfield scanning head, which has a limited scope of translation. Therefore, the Aerotech stage was programmed to move in discrete steps to create a series of scribed lines that completely remove conductivity between areas adjacent to the processed region.

Firstly, a single scan of the surface was carried out with a fluence of 4.09 Jcm^{-2} and a traverse speed of 32 mm/s (figure 90). This gives a pulse overlap of approximately 7 PPS, which as shown in previous case studies on ITO, this was sufficient to completely remove the layer and remain inside the selective processing window.

Using a single surface scan it was not possible to removal all of the TCO film from the glass substrate. This was confirmed by the white light image shown in figure 90 and conductivity detection across processed boundaries. To overcome this test was repeated with two scans, the result is shown in figure 91. To improve the material removal rate per

scan it may be beneficial to process the TCO layer from the reverse side of the sample. i.e. through the glass substrate. Previously reported work has suggested that removal from the reverse side is more efficient than front side removal [164,165].

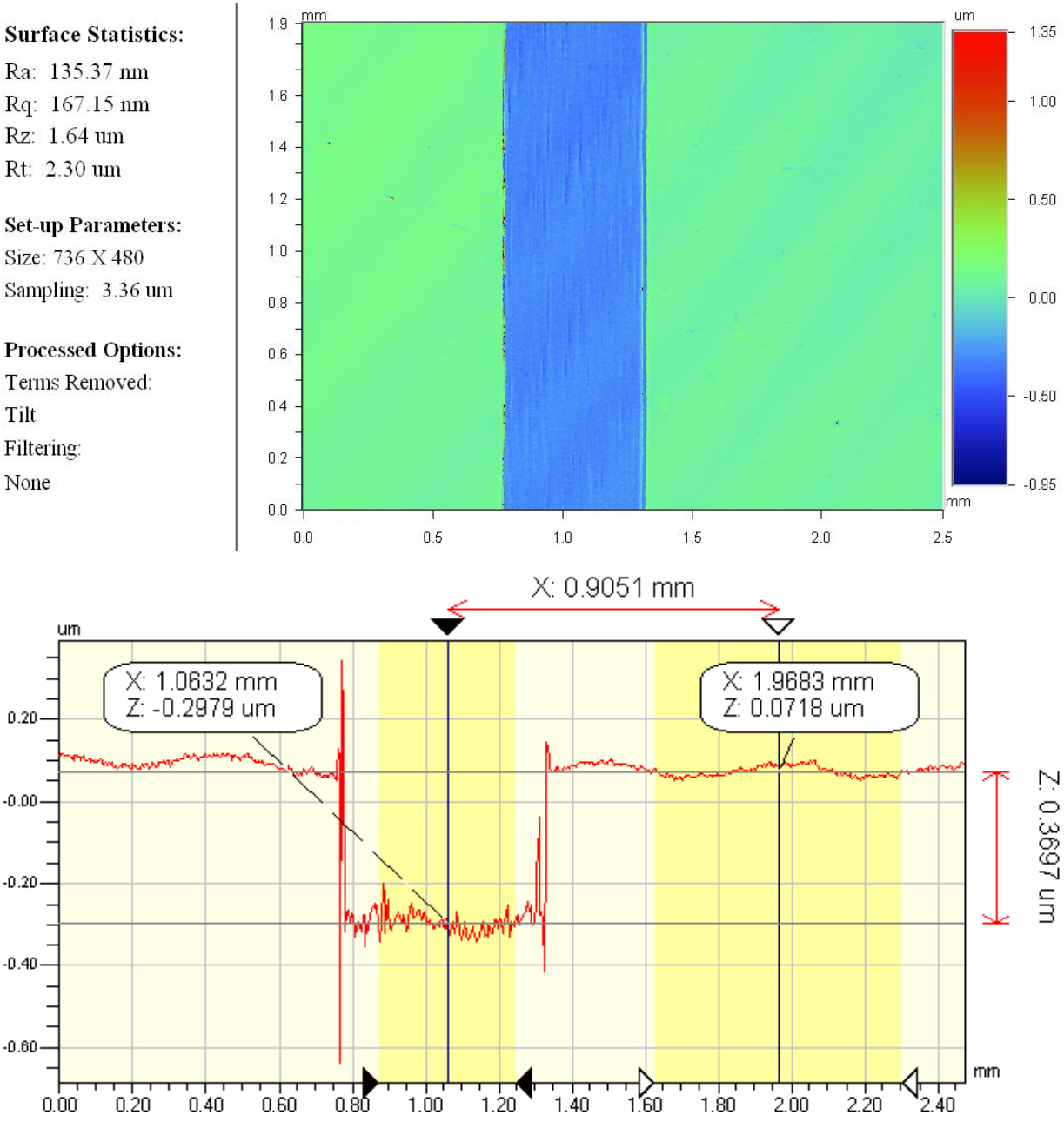

Figure 90: White light interferometry image (cross section) of TCO that was processed with a single scan of the surface (Top). The X profile (bottom) shows that a scribe of 370 nm deep was possible with a single scan. There is no observable damage to the surrounding material.

Figure 91 shows the results of scribing the F-SnO_2 surface twice, with a fluence of 4.09 Jcm^{-2} and a traverse speed of 32 mm/s. This gives a pulse overlap of approximately 7 PPS, which as shown in previous case studies on ITO, this was sufficient to completely remove the layer and remain inside the selective processing window. Here, a ≈250 micron wide track has been scribed into the TCO coated layer with no observable damage to the surrounding area. This highlights the ability of USP to provide a precision

processing tool. Figure 92 shows the depth profile obtained from this track, measurements were taken at three different locations to showcase the repeatability of this process. The depth recorded is ≈500 nm; this is equivalent to the layer thickness recorded by Pilkingtons. Within the ablated tracks the roughness can be observed to be very low. By scanning the surface twice it was possible to remove conductivity across the boundary, indicating that the interface between the TCO and glass has been reached.

These scribes were repeated across the 100x100 mm samples at 20 mm intervals to create the basic structure. After processing the TCO, the samples were returned to Atmos technologies were they were coated in a flame sprayed oxide (FSO). The attempted processing of this layer is subsequently discussed.

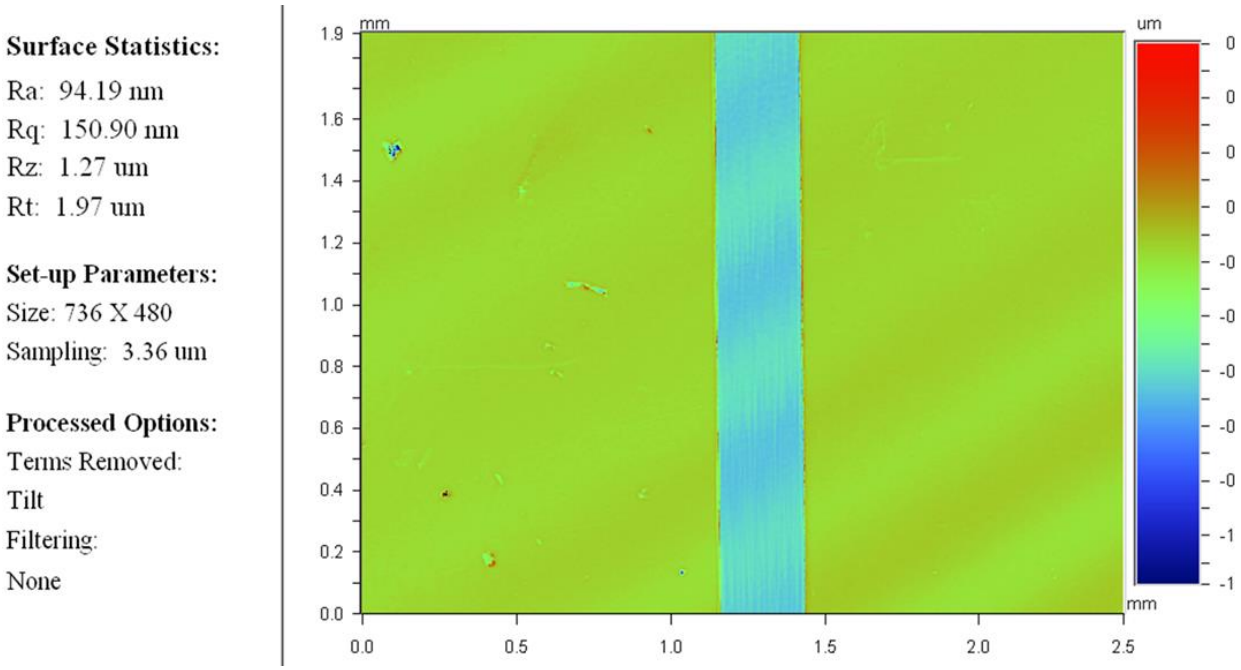

Figure 91: White light interferometry image of scribe made in TCO coated glass.

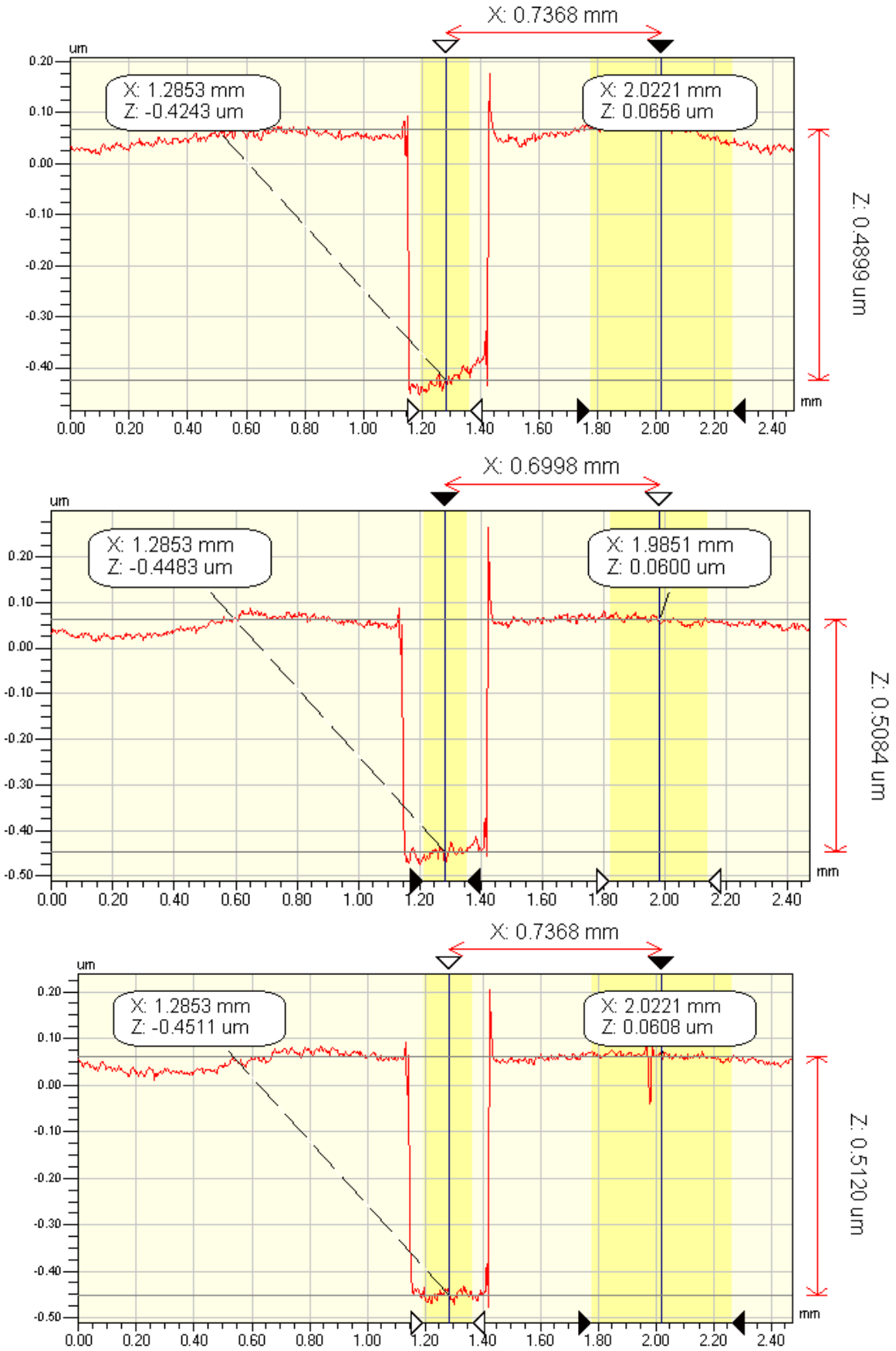

Figure 92: X profiles obtained from White light interferometry at different locations. In this test the TCO surface was scanned twice to increase ablation and remove conductivity between across the boundary.

5.3.2.2 Processing of FSO layer

After scribing the TCO coated glass, the samples underwent a second deposition process, so as to apply a secondary coating layer comprising a flame sprayed oxide (FSO). In this process a compound containing silicon (≈70%) and aluminium (≈30%) was deposited using a flame spraying technique. Figure 93 depicts the surface of the sample after the addition of the FSO layer. By analysing the surface of the FSO coated sample under magnification (x10), the topography was shown to be extremely rough. Due to the high surface roughness it was not possible to get the whole illuminated area of the FSO layer into the focal plane of the microscope (as shown in figure 93 (right)).

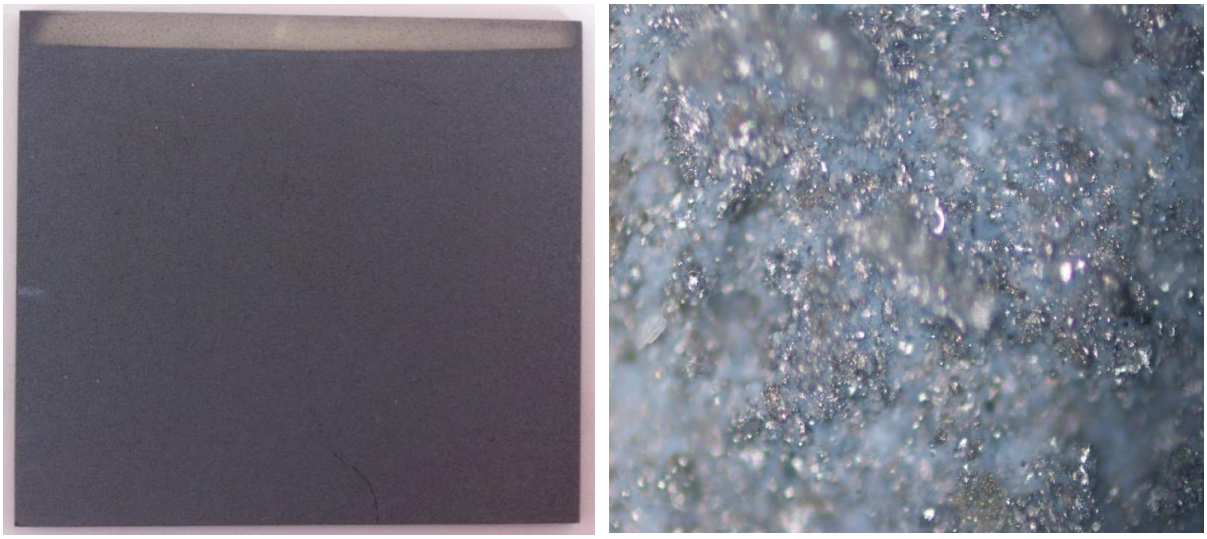

Figure 93: Images the FSO layer deposited on to the PV cell. The photograph shows the entire cell coated in FSO (left) and a magnification of the FSO surface (right), taken using the Nikon microscope at x10 magnification; even at this relatively low level the high surface roughness was apparent.

5.3.2.3 Measurement of absorption coefficient

Unlike previous samples, the FSO coating is opaque and so prevents measurement of transmission. The detector was therefore repositioned to record the reflected intensity from the sample. These results are then used to ascertain the absorption coefficient of the material. However, the surface of the FSO was highly scattering and so prevented measurement of any reflected power. The high level of scattering observed is produced by the rough surface of the deposited FSO layer (figure 94).

Figure 94 shows the extent of the surface scattering produced when irradiating the FSO material using a green HeNe laser (532 nm). The high surface roughness, attributed to the deposition method, was analysed through the use of OM and SEM imaging techniques.

When utilising flame spraying the powder is melted before being deposited on the surface; however the use of a flame causes inhomogeneous heating of the powder. As a direct consequence, cooling of the deposited layer varies across the sample; this makes it difficult to deposit a uniform layer.

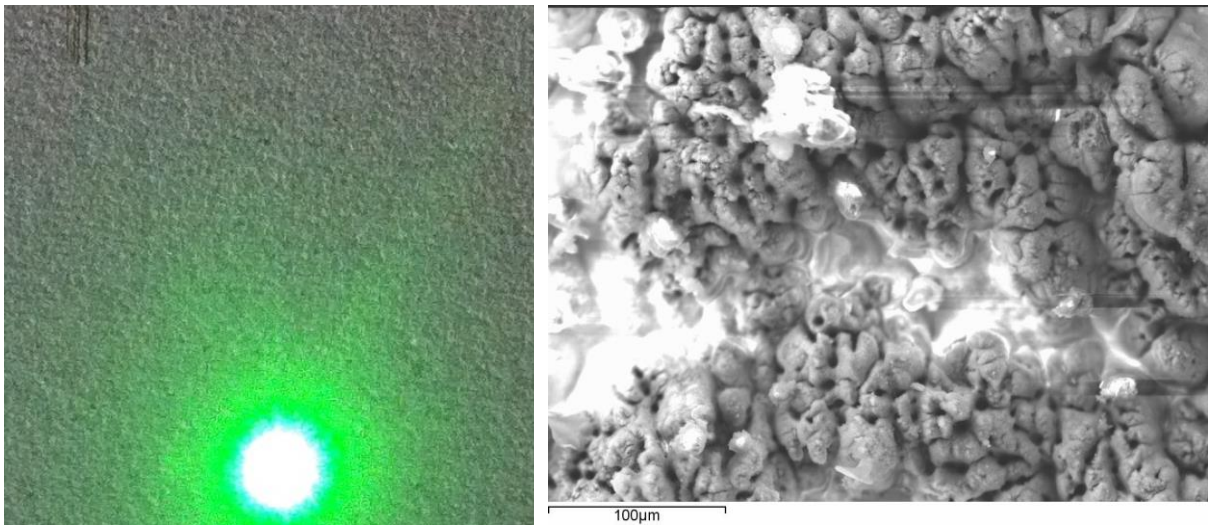

Figure 94: Left: Imaging of the scattering effect of the FSO layer produced using a HeNe laser at 532nm. Right: SEM image of the surface roughness of the FSO layer.

As measurement of the absorption properties of the FSO material was not possible, the next stage of testing was to determine the ablation threshold. However, the extremely high surface roughness (figures 93 and 94) coupled with the small focal spot (≈25 µm) prevent the characterisation of individual spots. In order to overcome this, a series of scans with an overlap of approximately 3 pulses per spot were used in conjunction with decreasing fluence. The ablation threshold was said to be equivalent to the point at which a plasma was no longer visible at the surface. Table 22 shows the results obtained for picosecond (ps) and femtosecond (fs) lasers, using wavelengths in the IR and visible regions.

Table 22: Approximate ablation thresholds of the FSO layer deposited on the PV cell.

Laser system	Wavelength (nm)	Ablation threshold (Jcm^{-2})
HighQ 10 ps	1064	≈2.5
Talisker 10 ps	532	≈2.4
Clarke MXR 180 fs	775	≈2.0

Once the approximate ablation threshold was determined for all three lasers systems (table 22) a series of small hatches was made to ascertain whether efficient material removal was achievable with a ps laser system. IR (1064 nm) light from the HighQ ps laser when impinging on the FSO layer had minimal effect on the surface as no material ablation was observed at lower fluences, the power was increased to determine whether ablation could be achieved. Upon increasing the fluence to greater than 50 Jcm^{-2} no observable increase in material removal was shown; however a heat-affected zone (HAZ) was clearly distinguishable.

Using visible light enabled some material removal, however despite the approximate ablation threshold being determined as 2.40 Jcm^{-2}, to achieve any significant removal of the FSO layer high fluences were required.

It was considered that selective processing would not be viable as the fluence required to remove a significant amount of the FSO was well in excess of the ablation threshold of the TCO underneath. This indicates that when the boundary interface between the FSO and TCO was reached, the subsequent laser pulses would also ablate the TCO layer. The effect of using high fluence can be observed in figure 95 where before achieving complete removal the use of several scans at high fluence caused a thermal build up within the substrate leading to fracture. The red circle indicates the point where the fracture began; from here it propagated in both directions splitting the sample into two pieces.

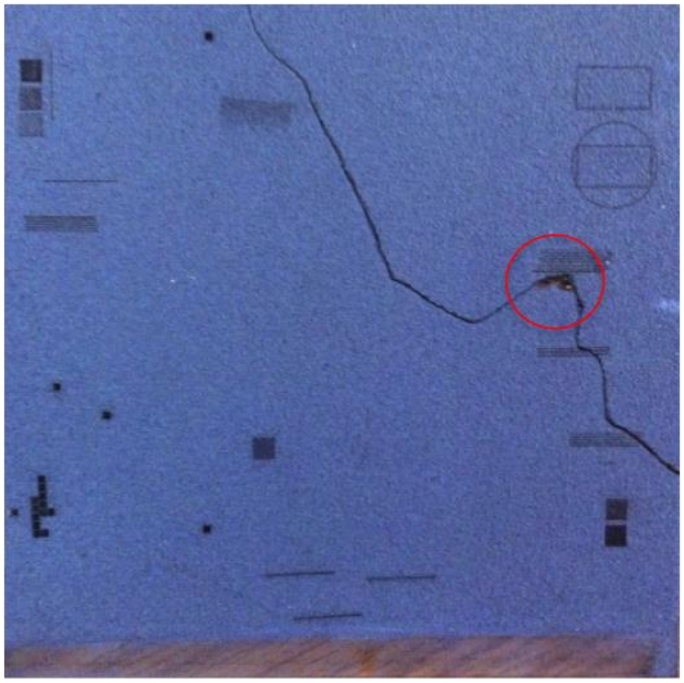

Figure 95: Image of fractured sample, the red circle indicates where the failure initiated. This damage propagated across the sample. The average power used here was 5 W with greater than 50 surface scans being used, leading to thermal build up and subsequent failure.

After testing the samples using a ps laser, the samples were then tested using the Clarke MXR fs system. Testing using fs pulses was carried out to investigate whether the extremely high pulse intensities and significantly smaller thermal effects obtainable with these pulse durations could enable efficient material removal.

Testing was carried out by scribing two small hatches on the surface of the cell using pulse energies of 15 and 30 µJ. As the intensity of the fs pulses are increased compared to ps pulses, this improved processing efficiency and enables material removal, exposing the FSO/TCO interface. To examine the effects of processing these areas were illuminated from the back to show transmission. Figure 96 illustrates the resultant surface after testing.

Whilst transmission of some light was observed, there were several dark regions where no transmission occurred. These dark regions were attributed to FSO that remained adhered to the surface. The residual material indicates that it is not possible to uniformly remove FSO from the surface of the cell. Consequently, more pulses are required.

Non-uniform removal of the FSO layer would require further irradiation in order to fully expose the FSO/TCO interface. Therefore, inefficient removal of this material increases the likelihood of damaging the TCO layer beneath. The residual FSO on the surface was attributed to the combination of high surface roughness and low material removal rate.

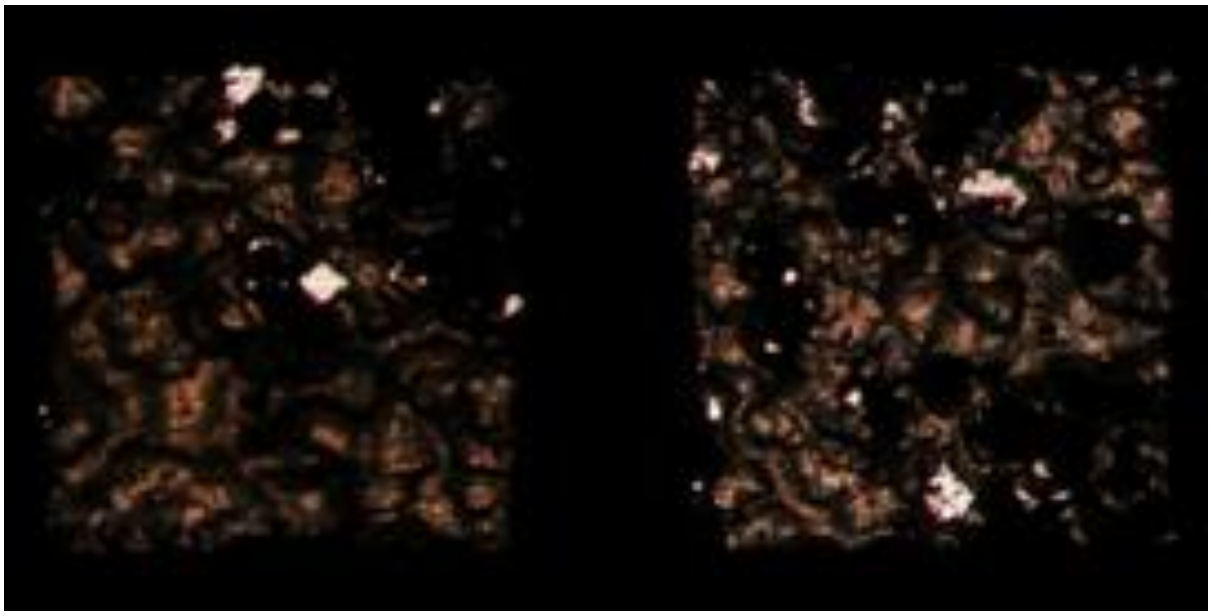

Figure 96: Optical microscopic image showing the transmission of light through FSO layer after processing with the Clarke MXR fs laser system. Fluence of 6.11 Jcm^{-2} (left) and 12.22 Jcm^{-2} (right) were used in processing. The dark regions signify areas of no transmittance, which are attributed to FSO remaining on the surface of the cell.

5.3.3 Summary

In this case study, the SUSP processing of a low cost solar cell was undertaken with the aim of creating an integrated solution for the manufacture of individual photovoltaic cells. The cell structure was a four-layer system consisting of a glass substrate, transparent conductive oxide (TCO), flame sprayed oxide (FSO) and a metal contact layer. Laser scribing was used to remove areas of both the TCO and FSO layers so as to enable efficient charge extraction from the PN (positive/negative) junction.

The sample cell was held in place using a bespoke jig designed to ensure registration of the sample was consistent. Using the techniques identified in chapter 4, the linear absorption coefficient and ablation threshold of the TCO layer were determined and compared to glass to ensure that selective processing was possible.

TCO was processed using a wavelength of 1064 nm with a traverse speed of 32 mm/s and a fluence of 4.09 Jcm^{-2}, similar to ITO. This produced a series of non-conducting tracks across the sample.

After processing the TCO layer, scribing was performed on the FSO layer. Measurement of the absorption coefficient in both transmission and reflection was not possible due to the layer being opaque and having a high surface roughness. The ablation threshold was calculated to be approximately 2.5, 2.4 and 2.0 Jcm^{-2} using the HighQ, Coherent Talisker and Clarke MXR fs laser respectively. Processing at 1064 and 532 nm with ps pulses showed no significant FSO removal from the surface. One reason for this may be low absorption of the incident pulses by the FSO layer, this layer was predominantly silicon based, which has low absorption coefficients in both the visible and IR parts of the spectrum.

Fs processing at 775 nm resulted in removal of the FSO layer exposing the FSO/TCO boundary interface. This is due to the ultra-high intensities provided by focussed fs pulses (≈$TWcm^{-2}$), at these intensities it is possible for non-linear absorption to occur. This could account for why surface processing was only possible with fs pulses; when non-linear processes occur the absorption coefficient is a function of the intensity and becomes almost completely independent of the material properties. However, the high surface roughness prevented uniform removal (figure 96). The inconsistent removal combined with the high fluence required to process the FSO layer negated the use of selective processing, as the powers required to remove this layer would result in damage to the TCO and glass. From this it was determined that selective laser processing was not a suitable fabrication technique for this photovoltaic cell.

A limitation of selective processing was identified in this study. The structure of the cell prevented selective processing as the material with the lower ablation threshold (TCO) was deposited beneath a material with a higher ablation threshold (FSO).

6 Laser Restoration

In the previous case studies discussed, SUSP was used to investigate the ablation of thin films for the creation of a small circuit and the fabrication of PV cells. In these investigations the thin films being studied were optimised for laser processing i.e. they were of a known composition and, in most cases, were almost optically flat.

Laser cleaning is a term applied to the removal of an unwanted film from the surface of a multi-layered structure. This technique was first discovered in the 1970s by Asmus *et al* [114] and to date has been used for both conservation and industrial applications.

Since its inception, laser cleaning has found a widespread use in the field of conservation, were several different cleaning mechanisms can be utilised in the restoration of various items, such as statues, buildings, metal sculptures and paintings. In these instances, the use of a laser reduces the time taken to complete the restoration project. In addition, this method often negates the requirement for chemical restoration processes, which can further damage the conservation item and pose a health risk to the conservator.

In industrial laser cleaning, micron sized surface debris is removed from silicon wafers thereby reducing the number rejected wafers and the number of failures. An example of when a failure can occur is the use of silicon wafers within computer processors, in this instance the contaminant causes a localised thermal build up, which eventually severs the connections inside the processor due to overheating. Here, the major advantage of the laser method is its ability to generate sufficient force to overcome the Van der Waals force of attraction between micron sized particles and the substrate. Removing contaminants on such a small scale had previously been proven to be extremely difficult when using more traditional techniques. These methods are unable to overcome the Van der Waals force between the particle and substrate, as this force of attraction increases as the particle size decreases.

More recently, ultra-short pulse lasers have been utilised in laser cleaning projects [126]. The key advantage of these lasers is the low thermal input to the substrate and the near diffraction limited spot size of the beam, which allows for accurate material removal.

The subsequent case studies herein, investigate the use of SUSP with samples that have varying compositions and surface roughness. Laser restoration (or cleaning) was one of the first areas to actively utilise selective removal with continuous wave (CW) or long pulse (LP) lasers, therefore the application of SUSP to this field is a good test of the capabilities of this technique. Here the restoration of a pair of gloves previously owned by King Charles (I) and an investigation into the removal of unwanted bronze gilding are presented.

USP lasers were applied to the restoration of a pair of gloves, previously commissioned for King Charles I (figure 97). The gloves are part of a private collection and were previously exposed to the environment. As a result of the storage conditions the gloves became tarnished with surface contaminants such as carbon and sulphur. These deposits are easily observable on the surface of the gloves in figure 97.

Previously, successful conservation of objects comprising different materials has proven to be difficult due to the different responses of each material to laser and chemical treatment. On this item, in particular, the intricate detailing on the cuff meant that highly precise restoration techniques were required to prevent damage.

This difficulty presents an opportunity to demonstrate the applicability of SUSP as a restoration technique. Using a HighQ 10 ps laser operating at the fundamental wavelength of 1064 nm the power, traverse speed and pulse overlap were varied to enable the selective removal of environmental contaminants on the surface of the gloves. Removal of the deposited contaminants was imperative, firstly in order to improve the aesthetics and secondly to prevent any further degradation of the piece.

6.1 King Charles (I) gloves

6.1.1 Experimental procedure

This restoration was carried out in partnership with Fayoum University (Fayoum, Egypt), The Courtauld institute (London, UK), the National Research Council (Florence, Italy) and The Natural History Museum (London, UK).

This investigation was performed using the HighQ laser system operating at a wavelength of 1064 nm. This wavelength was selected due to the reduced possibility of inducing photo degradation, when compared to wavelengths in the visible and especially UV range. The optical arrangement used is shown in chapter 3. The base plate of the Aerotech stage was modified to accept a steel platform, which was used to hold the gloves in position throughout treatment. The laser was operated with a repetition rate of 10 kHz throughout testing; the range of fluences used was between 0.62 and 6.80 Jcm^{-2}. Due to the high surface roughness and inhomogeneity of the contamination, individual pulses could not be determined. As a result, a series of hatches (2 mm x 2 mm) with a constant separation of 6 µm were used to ascertain whether material removal had occurred. The traverse speed (1650, 825 and 300 mm/s) and the number of scans (1 – 20) was varied so as to identify a processing window. Treated areas were then examined for signs of damage using both OM and SEM imaging techniques.

Figure 97: King Charles I gloves before laser treatment. The contamination of the white leather is clearly visible in this image. The decorated gauntlet is also shown [143].

The object under investigation was a pair of Royal gloves, previously owned and worn by King Charles I. The measured dimensions of the gloves are 32 cm x 9 cm and are comprised of white leather, silver, dyed silk and metal thread. At the base of the glove is a highly decorated gauntlet; this area also underwent restoration. The gloves were displayed in a private collection where they were exposed to the environment. In addition to the contaminants previously discussed, two further contaminants were found firstly, the nails that had held the gloves in position had corroded and stained the surface with rust and secondly, under the gauntlet part of the glove a fungal growth was detected, as shown in figure 98.

Before treatment of the gloves, a series of small samples were collected from the damaged areas or sections were the material had fallen away. For the leather, several samples of uncoated material were made and irradiated before commencing the restoration.

Figure 98: A photographic image showing an area of fungal growth located beneath the gauntlet section of the glove. The red circle highlights the rust staining [143].

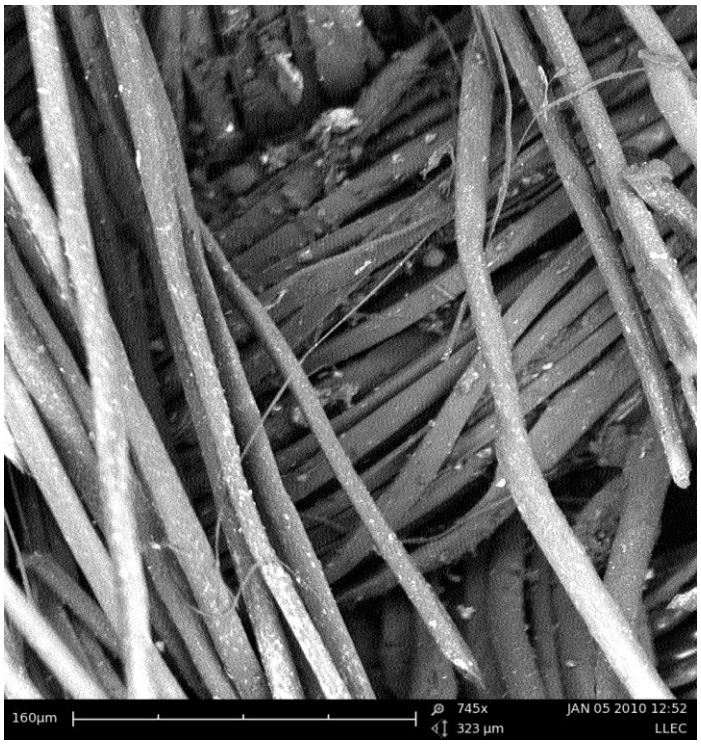

Figure 99: An SEM image showing the dust contaminates deposited on the dyed fabric of the gauntlet.

6.1.2 Result and Discussion

Initial tests were performed using high traverse speeds (1650 and 825 mm/s). These tests showed no observable material removal; this was attributed to the extremely low overlap (< 1 PPS) and the interaction time being insufficient to remove contamination even at the highest fluence. These high speeds were analysed in order to determine whether it was possible to remove the loosely bound contaminants from the surface, thus minimising exposure. By reducing the traverse speed to 300 mm/s the pulse overlap was increased to be just greater than 1 PPS. These parameters were found to be sufficient for contaminant removal.

Prior to restoration of the gloves, the suitability of an USP laser with these materials was tested. The hatch pattern, described above, was used on small sample sections of leather. These areas were irradiated with increasing fluence to determine the damage threshold of the leather; the tested fluences ranged between 0.42 – 6.80 Jcm^{-2}. Figure 100 shows the effect of increasing the fluence at 0.42, 4.89 and 6.80 Jcm^{-2}. The figures show that at the lowest fluence material removal was negligible. At 4.89 Jcm^{-2} and above damage to the leather was observed; this is shown in in figure 100 (B) and (C) where removal of the upper layer has exposed the collagen fibres underneath. Figure 100 (C) illustrates the effect on the leather sample when the fluence was twice the damage threshold; the laser-scanning pattern can clearly be seen.

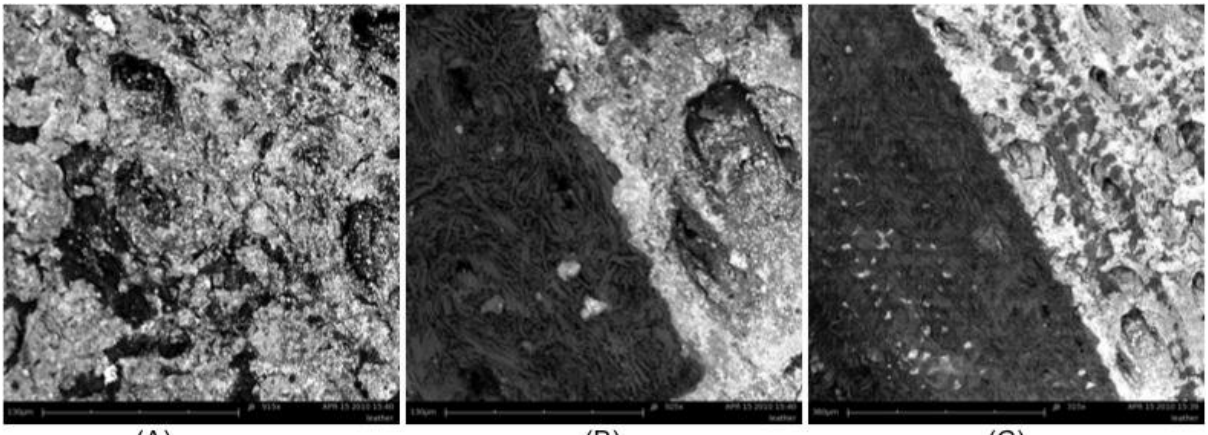

Figure 100: SEM images of samples of white leather taken from the gloves, wherein the processing parameters comprise a fluence value of (A) 0.42 Jcm^{-2}, (B) 4.89 Jcm^{-2} and (C) 6.80 Jcm^{-2}.

Processing the sample using a fluence of 4.10 Jcm^{-2} resulted in the removal of surface contaminants without damaging the leather surface. Figure 101 shows the section of glove under SEM imaging. The contaminants have been removed from the surface whilst the leather dermal layer has remained undamaged. Some hair follicle protrusions can be observed on the right hand side of the image. The SEM magnification could not be

increased further than x450, due to the charging effect associated with non-conducting surfaces, which obscured the image.

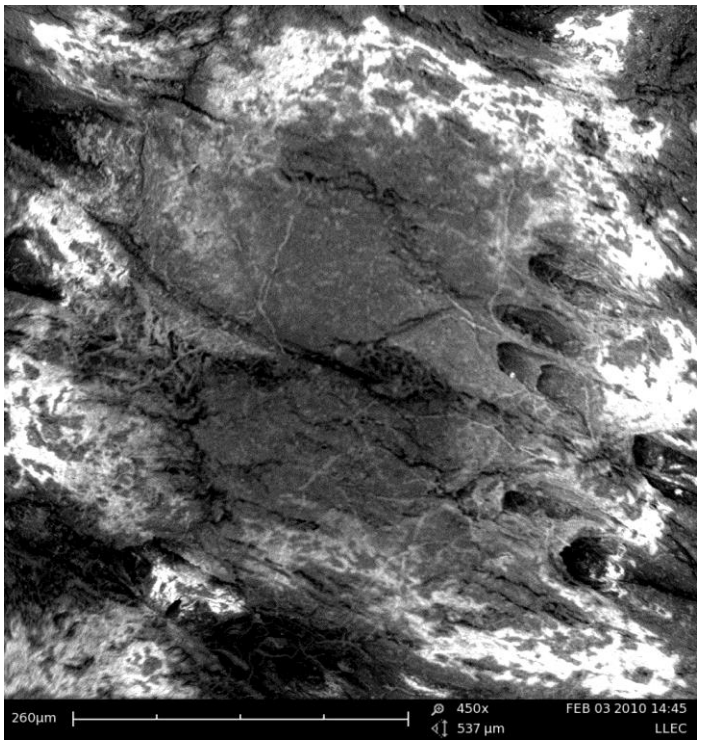

Figure 101: An SEM image showing the leather section of the glove after cleaning. The contaminants have been removed from the sample and, even under high magnification, no damage to the leather was observed.

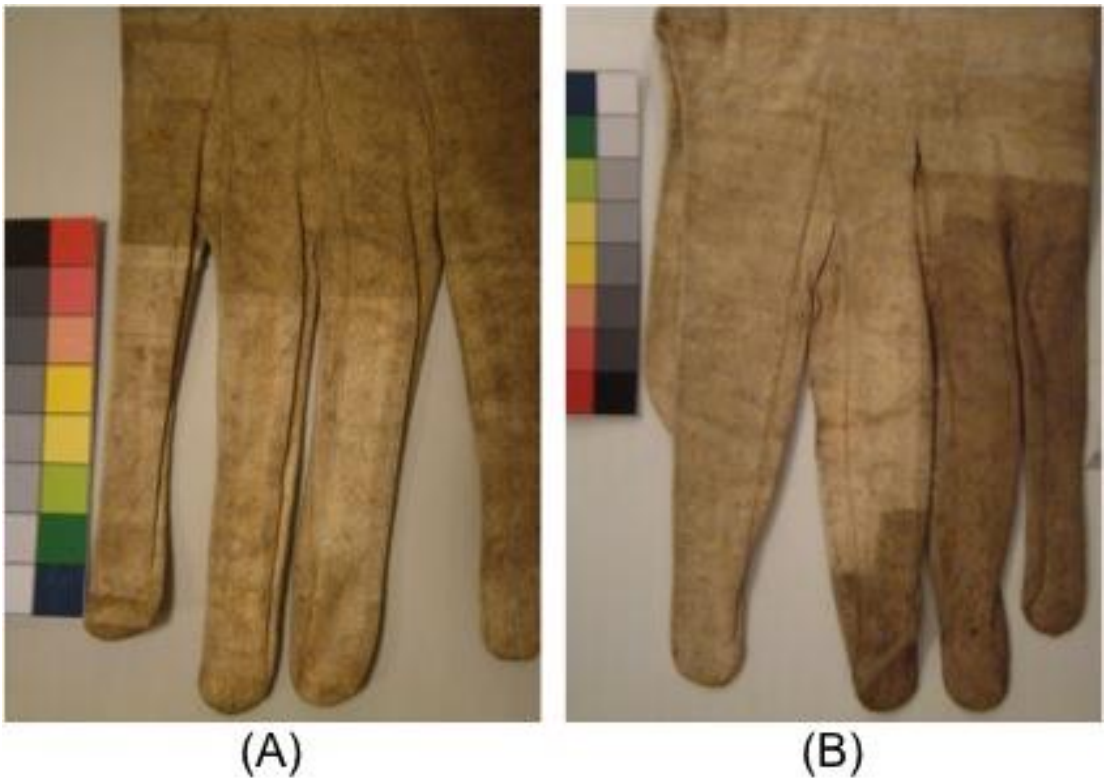

Figure 102: Photographic images of the leather area of the King Charles I gloves during restoration, using a fluence of 4.10 Jcm^{-2}. Image (A) shows the glove in an early stage of the leather restoration. The colour scale is provided for comparison.

Figure 102 shows that whilst it is possible to remove the majority of the contaminant material, complete removal is not possible. This was attributed to the complex fibrous structure of leather; dirt can remain in areas where it is difficult or not possible for the laser to irradiate. Therein the surface retains some or all of the contaminants producing varied removal. However, a distinct improvement in the surface can be clearly observed when compared to an unprocessed region. Figure 103 show sections of restored leather using an x80 magnification.

Figure 103: An image showing a section of leather restored using a fluence of 4.10 Jcm^{-2} when viewed at x80 magnification. No surface damage was observed, however some small contaminant deposits remain on the surface.

The leather sections of both samples were restored using a fluence of 4.10 Jcm^{-2}; this was sufficient to remove the majority of the surface contaminants. However, when irradiated at this fluence, the fungal and rust staining observed under the gauntlet and on the glove remained clearly visible. For these materials laser restoration was not sufficient, therefore these sections underwent chemical treatment after the laser restoration process was completed.

After processing the leather section of the glove, testing moved to the gauntlet. This provided a greater challenge due to the variety of materials used and the complexity of the embroidered pattern. Figure 104 [143] is an image of the embroidered gauntlet and shows the complexity of the pattern and the different materials used during construction.

Before restoration of the gauntlet, testing was performed on several samples in order to determine whether using USP lasers was viable. The samples used to test the viability of

laser restoration were taken from the gauntlet in areas where damage due to aging had occurred; this enabled testing without risking further damage to the gloves.

Testing was split into three areas, dyed fabric, gilded stitching and metal coils. Figure 105 shows images of all three types of sample before undergoing restoration.

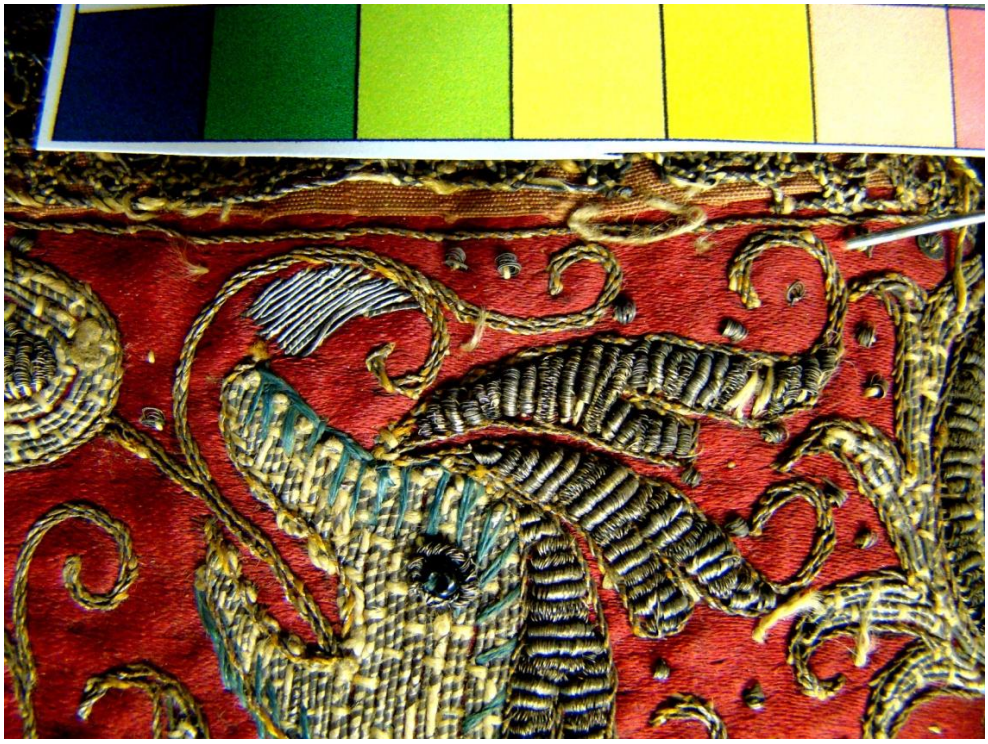

Figure 104: A photographic image highlighting the complexity of the gauntlet. The red dyed fabric, gilded fibres and gemstone eye of the animal can be observed and must be considered during irradiation.

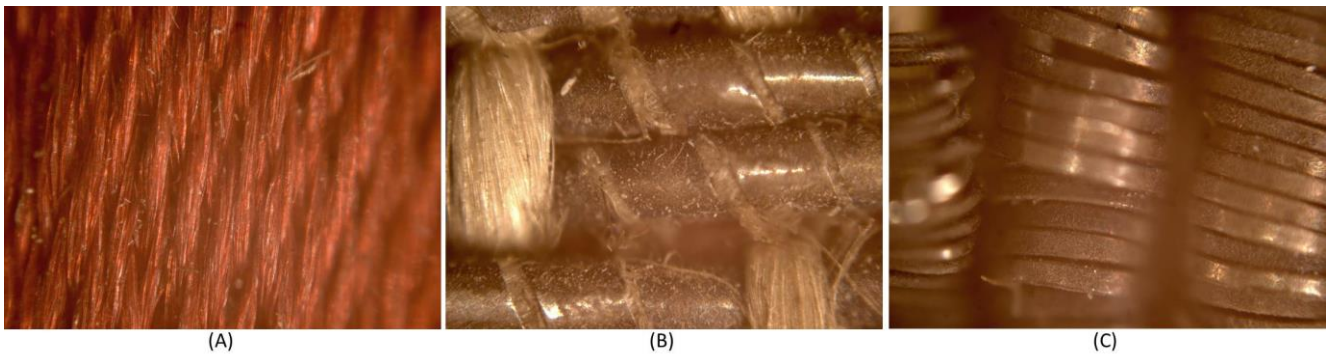

Figure 105: Optical microscopic images of the untreated sections of the gauntlet; (A) dyed fabric, (B) gilt silver fabric and (C) coiled silver metal. These images were provided by Fayoum University.

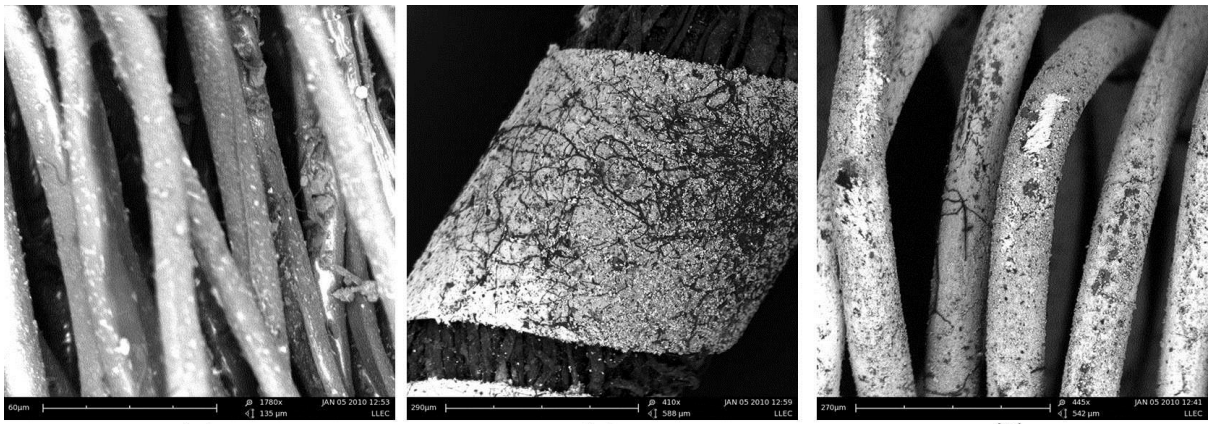

Figure 106: SEM images showing sections of the gauntlet that had been removed from the glove. The contaminants on the surface of the (A) dyed fabric, (B) gilded fabric and (C) metal coils are clearly visible.

Figure 106 shows three sections of the gauntlet imaged using SEM; in all three images the contaminants are clearly visible. These three sections where irradiated using a fluence 4.10 Jcm^{-2}, this was used previously to restore the leather section of the glove.

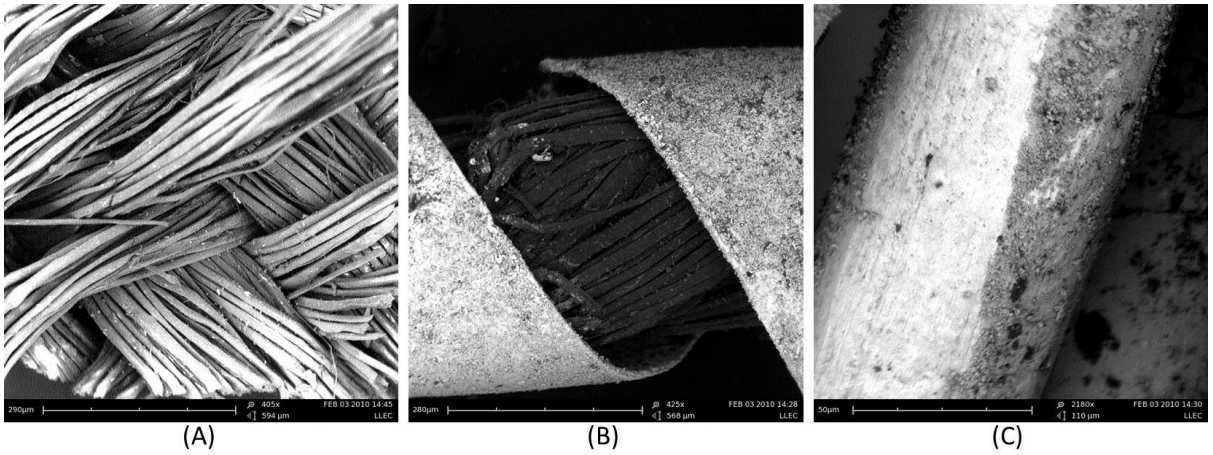

Figure 107: SEM images of the (A) dyed fabric, (B) gilded fabric and (C) metal coil, after irradiation.

The effect of irradiation using a fluence of 4.10 Jcm^{-2} on the different materials, which comprise the glove's gauntlet, can be seen in figure 107. It is immediately apparent that some of the surface contamination had been removed. Laser irradiation of the dyed fabric (figure 107 (A)) showed that it was possible to remove the majority of the contamination without damaging the fibres. This was also seen for the gilded fabric (figure 107 (B)) where a distinct reduction in contaminants was observed without causing damage the fibres that the gilding was wound around. In figure 107 (C) the coil shows a clear distinction between the treated and untreated areas with a visible change in surface colour. With regards to each of the three samples shown in figure 107, complete removal of contamination was not possible. This was attributed the 3D structure of the objects which underwent restoration treatments. The gloves were placed normal to the incident beam and hence it was only

possible for the system to treat the areas exposed to the incoming beam. Other areas would not have experienced material removal; this is most easily observed in figure 107 (C) were the distinction between exposed and hidden areas is distinct. From these tests it was determined that this fluence (4.10 Jcm^{-2}) was suitable for selective removal of the gauntlet; therefore the remaining untreated areas were restored using this fluence.

After laser treatment, the gilt silver thread was further examined using SEM and energy dispersive x-ray (EDX) spectroscopy techniques to determine whether contaminant removal had been successful. Figure 108 shows a sample section of gilt silver thread, which had been partially cleaned. The spectra for the treated and untreated section are provided. By comparing these two spectra a distinct decrease in surface contamination was observed in the treated region, this is shown by the absence of peaks attributed to the surface contaminants, such as carbon and sulphur, in the EDX spectra. The SEM image provided in figure 108 shows no damage to the irradiated region, indicating that material was selectively removed from the surface.

The final section of the glove was the embroided threads, which were attached to the end of the gauntlet. Samples of these coils were obtained from sections, which had come away from the glove. Figure 109 shows the coils after irradiation using a fluence of 4.10 Jcm^{-2}. In figure 109 (A) the coil has been partially cleaned, whilst in image (B) the coil has been fully cleaned. To complete the cleaning process required turning the sample to ensure that all parts were irradiated.

Similar to previous tests in micro processing, laser cleaning could not remove the entire contaminant and trace amounts remained on the surface. The residual contamination was attributed to the layer thickness varying and the 3D geometry of the sample. Throughout testing no observable damage to the leather or gauntlet was observed under high magnification SEM. This confirmed the selectivity of the restoration treatment.

Using the parameters identified on the test samples full laser restoration of the gloves was undertaken using the HighQ 10 ps laser system operating at 1064 nm. A fluence value of 4.10 Jcm^{-2} at a traverse speed of 300 mm/s and a hatch spacing of 6 µm were used.

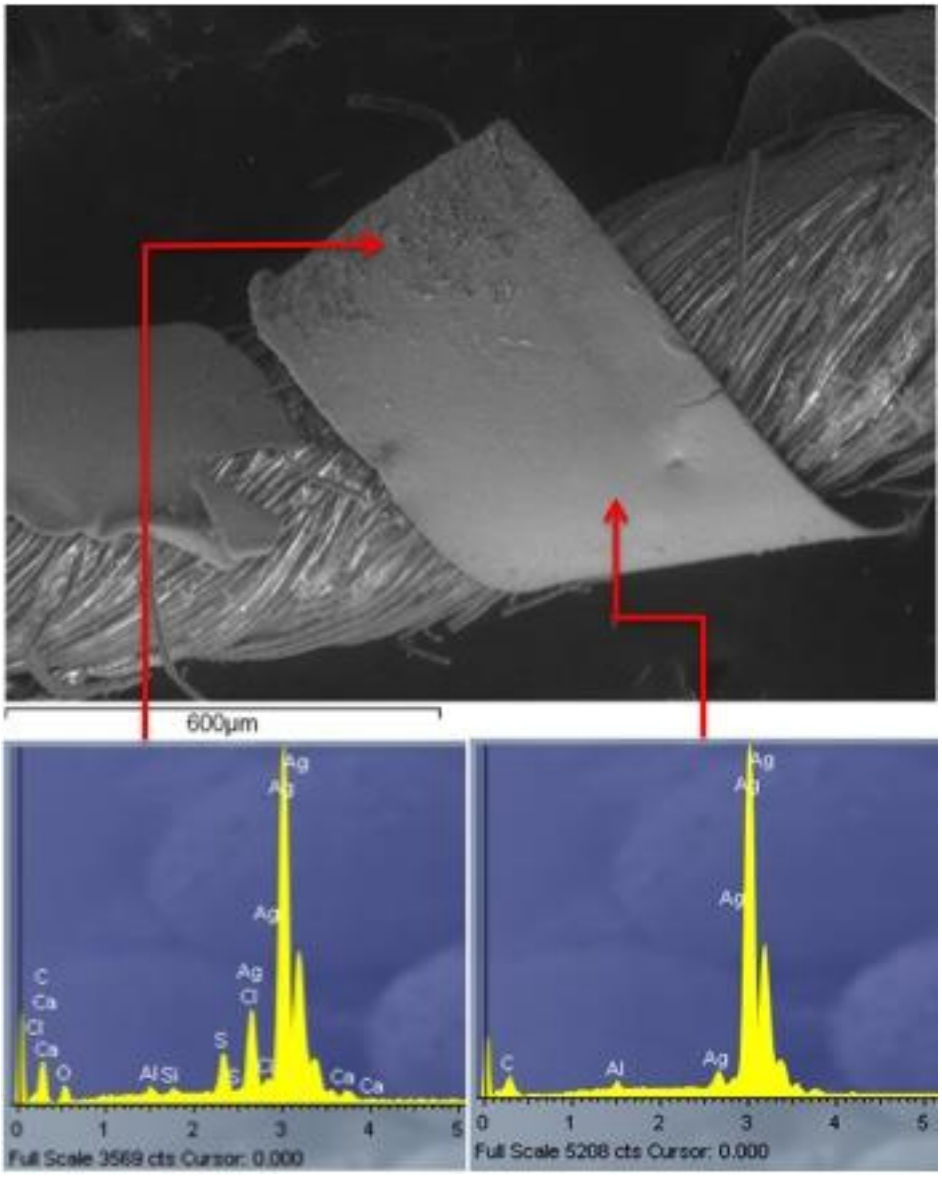

Figure 108: An SEM image of a partially restored gilt silver thread. EDX spectra were recorded for both treated (right) and untreated (left) regions, as shown above. These images were provided by Fayoum University [143].

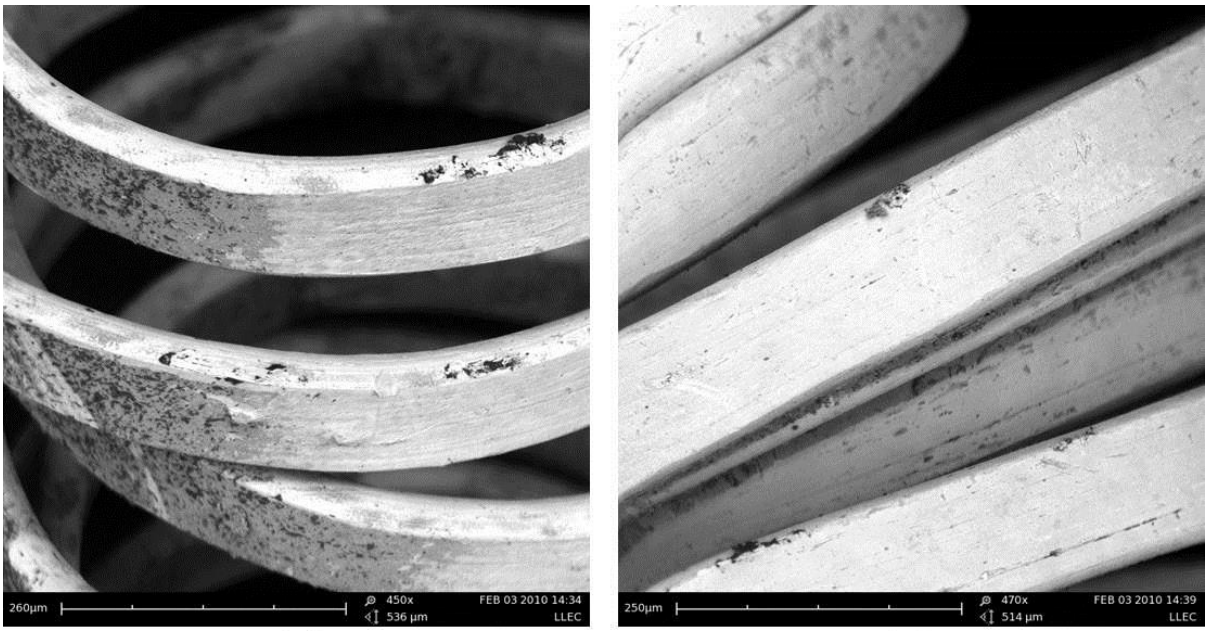

Figure 109: SEM images of the coils attached to the edge of the gauntlet. Image (A) shows partial cleaning of the coil whilst (B) shows the coil after treatment was finished. Both treatments used a fluence of 4.07 Jcm^{-2}.

6.1.3 Summary

In this case study, SUSP restoration was carried out on a pair of gloves, commissioned for King Charles I. Contamination through particulate deposition was observable on the main body (leather) and gauntlet (mixed materials). LP/CW laser restoration was not viable in this instance due to the high thermal loading and shockwave attributed to these cleaning mechanisms (as discussed in chapter 2). SUSP was utilised in order to remove surface contaminants from all sections of the glove, as ultra-short pulses do not induce the aforementioned thermal and shock effects.

Several small samples were taken from damaged areas of the glove and examined to ensure contaminant removal and the selectivity of the restoration process. EDX spectroscopy (figure 108) was used to show the variation in carbon and sulphur (contaminants) signals between processed and unprocessed regions. The selectivity of the restoration process was confirmed through examination of these samples using high magnification SEM; in these images contaminant removal without damaging the substrate was clearly observed.

The upper limit of fluence which may be used on the leather sections of the glove was determined to be 4.89 Jcm^{-2}. Above this fluence, damage to the leather, caused by laser ablation was clearly observable (figure 100). Using a fluence of 4.10 Jcm^{-2}, a value below the damage threshold, with a traverse speed of 300 mm/s (>1 PPS) selective removal of the surface contaminants adhered to the leather was achieved (figure 103). Complete removal of the surface contaminants was not possible; this is attributed to the 3D structure of

the collagen fibres of the leather section of the glove. This complex structure prevents irradiation of the entire contaminated fibre; as a result some material remains adhered.

SUSP laser restoration was also applied to the gauntlet, which has a detailed and intricate pattern. This decoration was created through the use of several different materials including dyed fabric, gilded thread and mother of pearl (figure 104). Laser restoration with ultra-short pulses has an advantage over CW/LP and chemical cleaning techniques, as the micrometre beam diameters achievable enable highly precise material removal without continual exposure of other parts of the gauntlet. Continual exposure increases the likelihood of damage occurring. SUSP restoration of the gauntlet section, including the attached embroided threads, was carried out using a fluence of 4.07 Jcm^{-2}. This was also used in the restoration of the leather section. By using a single fluence the time taken to complete the restoration project was reduced.

6.2 Removal of unwanted bronze gilding

One of the challenges facing modern conservation projects is the effect of previous restorations; in some cases these were ill conceived and lead to poor results [166, 167]. In other instances advances in technology and understanding have given rise to changes in general restoration practice rendering previous techniques redundant; this is observed in every conservation specialism.

A prime example is the use of bronze gilding as a substitute for gold leaf; chosen because of its similar colour and substantially lower cost making it readily available to conservators. However, over time the bronze gilding becomes tarnished due to environmental contaminants and oxidisation. In time a distinct contrast between original and new gilding becomes clearly visible. Therefore, it is now necessary to remove the tarnished bronze gilding and replace these areas with new gold leaf. To date, two different methods have been employed in order to try and successfully remove this layer: mechanical and chemical [152]. Both techniques have had limited success; mechanical removal of bronze gilding was difficult as the gilded layer is thin, often leading to damage of the underlying materials when treated. Examples of mechanical removal include the use of abrasive papers or a hammer and chisel. Chemical removal has also proven difficult due to the treatment process not being selective. In many cases bronze gilding was only applied as a partial restoration, i.e. a mixture of the original gold and newer bronze gilding. Application of a chemical in this case can lead to damage of original gold leaf gilding and other materials present in the treated region. Finally, both mechanical and chemical methods are extremely labour intensive and time consuming with no guarantee of successfully restoring the object.

This difficulty presents an opportunity for laser restoration; as discussed in chapter 2 the removal process involves no physical contact between the restoration tool and the conservation object. The small spot size allows precision control of the beam location and no chemicals are required. In addition, advances in the manufacture of picosecond laser have allowed the production of robust systems suitable for use outside conventional laboratory environments. The present case study investigates the application of SUSP restoration techniques. Herein, laser restoration was carried out on model samples; wherein the fluence, traverse speed and number of scans were varied in order to determine a potential selective processing window. This was subsequently applied to the restoration of sections of gilded frame to determine if the SUSP technique could be utilised in this application.

6.2.1 Experimental procedure

A Fianium FemtoPower fibre laser was used in this study. The optical arrangement and a brief specification of the system are provided below. A detailed specification can be found in chapter 3. The Fianium FemtoPower fibre laser (figure 110) was selected due to its small footprint, maintenance free turnkey operation and relatively low cost, thereby making it a viable choice for conservators who are often operating within limited budgets.

Ultra-short pulses (20 ps) laser cleaning was applied to both model and real gilded frame samples with the aim of selectively removing the bronze gilding adhered to a common binder (oil size). Oil size is the adhesive material used by conservators to adhere gold, bronze and other materials to the surface of the object undergoing the gilding process; in this study the oil size is linseed oil. Due to the high intensity at the surface (≈42 GW/cm2), the samples were processed using IR radiation as this reduced the likelihood of inducing photo degradation in the oil size when compared to processing with either visible or UV wavelengths [168]. Using a fixed repetition rate (0.2 MHz) and a beam diameter of approximately 25 μm fluence values of 0.41, 0.82 and 1.22 Jcm^{-2} were produced. The number of scans was increased between 1 and 30. In order to determine whether processing was selective, results were analysed using a combination of optical microscopy (OM), scanning electron microscope (SEM) and energy dispersive x-ray spectroscopy (EDX).

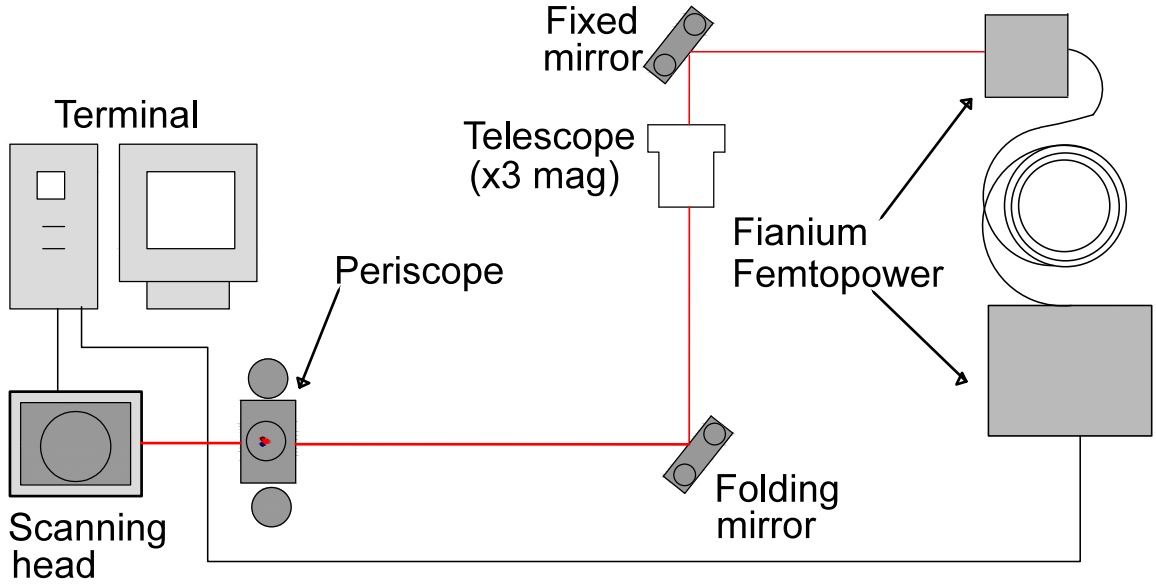

Figure 110: Schematic representation of the optical arrangement for the Fianium FemtoPower 20 ps fibre laser.

Before treatment of the real gilded frame pieces, a series of model samples were created to investigate the applicability of SUSP laser restoration. Figure 111 and 112 show the model samples fabricated using the method described by White [144]. Initially a thin layer of white paint was applied to the wood surface and allowed to dry; this prevented the oil size from being absorbed into the porous wood. Absorption of the oil size in to the wood is problematic as this reduces the amount of material which can be retained on the surface. As a consequence, the gilding powder would easily flake away from the surface, affecting the results obtained from laser cleaning.

Oil size (linseed oil) was applied to the painted surface. Linseed oil readily polymerises in air, and so was fully dry within one hour. Other oil sizes, which dry at different rates, are available. Before drying is completed the oil size layer becomes tacky, enabling it to act as an adhesive. At this point bronze gilding powder was applied to the surface using a horsehair gilders brush and was allowed to completely dry overnight. The horsehair gilders brush is used to apply Gold leaf gilding and so in this study it was used to apply the bronze gilding. After drying any excess material was brushed away also using the gilder's brush. This process was repeated for all model samples.

Once the optimum processing parameters were identified, the investigation moved on to removal of the bronze gilding from real test samples.

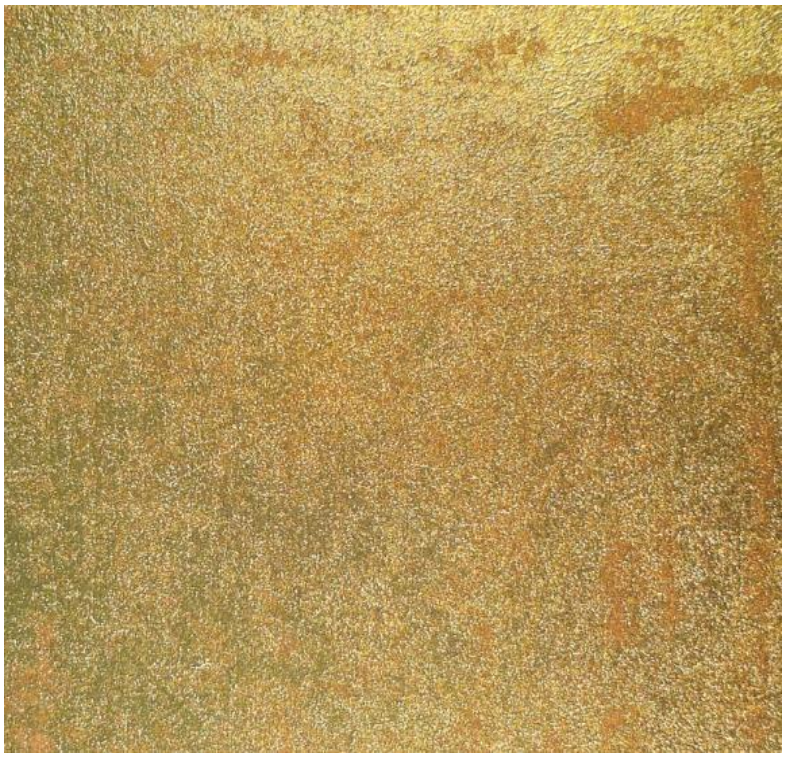

Figure 111: Optical microscopic image of the top surface of a model sample before undergoing irradiation.

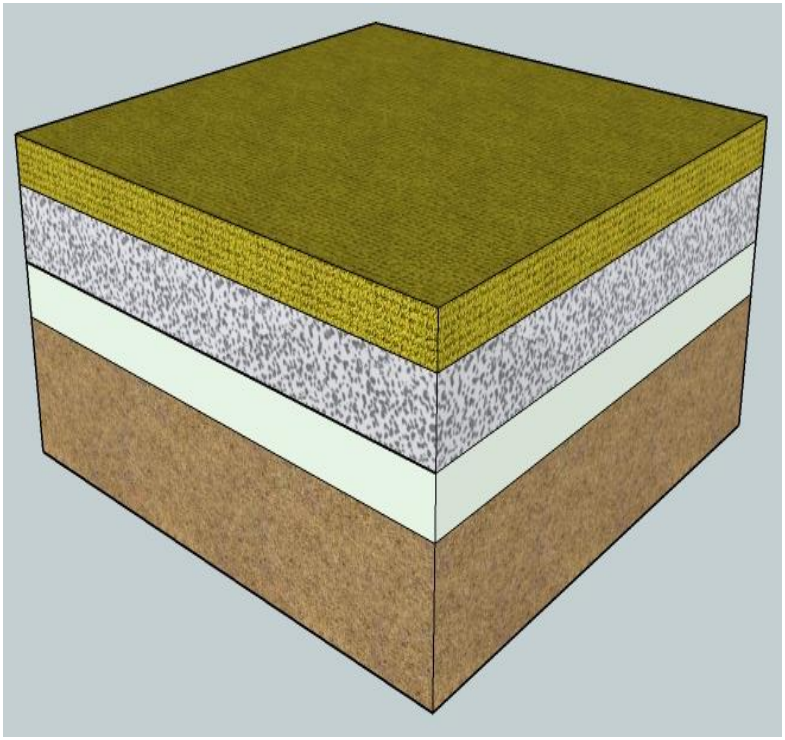

Figure 112: Schematic representation of the cross section of a model sample. The structure beneath the top layer is shown. The sample is comprised of (from top to bottom) bronze gilding, linseed oil, white paint and a wood base.

In order to determine the applicability of selective USP restoration of unwanted bronze gilding, three variables were investigated; these were fluence, traverse speed and number of scans. The Fianium system produced a maximum pulse energy of 3 µJ, therefore testing was undertaken at 1, 2 and 3 µJ; which corresponds to fluences of 0.41, 0.81 and 1.22 Jcm^{-2} respectively. The traverse speed (250, 500 and 5000 mm/s) and number of scans (1, 2, 5, 8, 10, 15, 20, 25 and 30) were varied to investigate the effect of increased interaction time and multiple surface irradiations on selective processing.

6.2.2 Results and discussion

The surface of a model sample before irradiation is shown in Figure 113; this is representative of all the model samples. The bronze flakes vary in size and shape and are adhered to the oil size in an irregular pattern due to the method of application (discussed above). The dark regions show sections of the surface were no bronze is attached; in these areas the oil size is exposed. The white edges observed on some flakes were attributed to a build-up of surface charge; this effect is common in SEM imaging. Figure 114 shows the EDX spectra for an unprocessed surface, the strong copper and zinc signals are attributed to the bronze. The titanium signal was attributed to the white paint used in the sealant layer, whilst the carbon and oxygen signals were attributed to the oil size

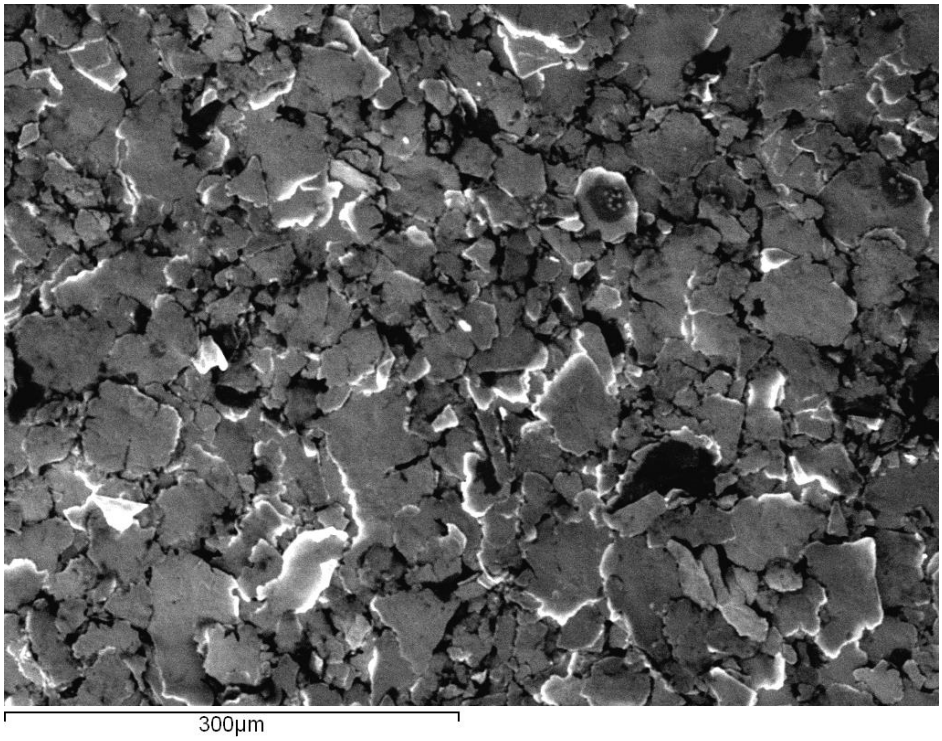

Figure 113: High magnification (x500) SEM image of the surface of a model bronze guild coated sample before irradiation. The black areas of the image show patches were no bronze flakes are adhered; exposing the oil size beneath.

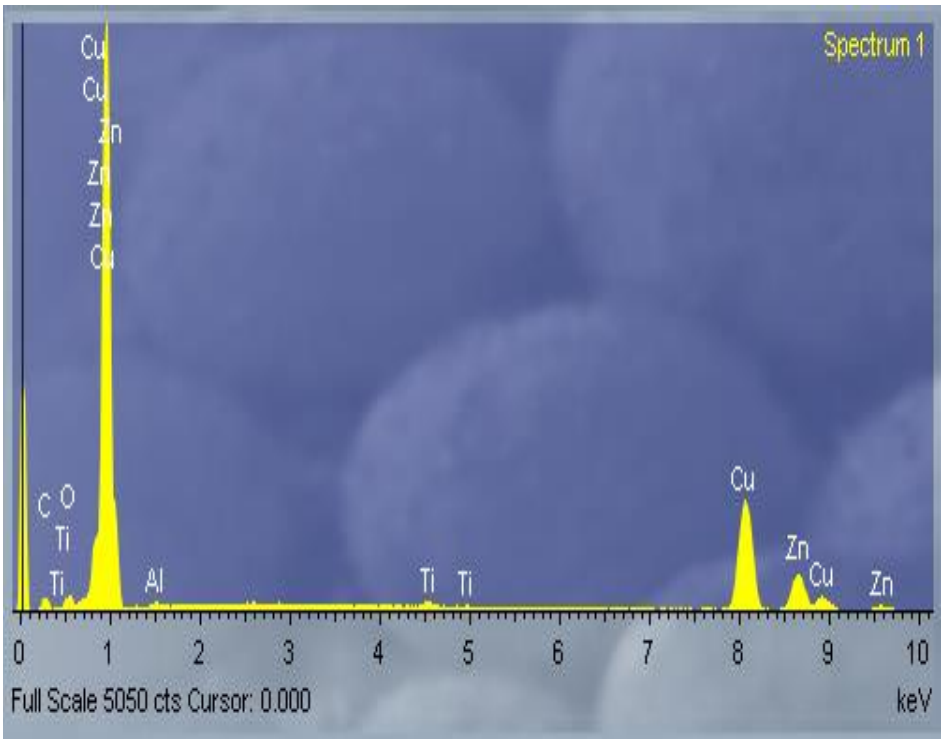

Figure 114: EDX spectrum of a model bronze gilded coated sample before irradiation.

The OM images of the sample surface when irradiated using a fluence of 0.41 Jcm^{-2} (Figure 115), demonstrate the effect of the lowest fluence tested. Figure 115 (A) shows the results obtained at the highest traverse speed (5000 mm/s); the effects of irradiation using this fluence and traverse speed are minimal. Increasing the number of scans has no observable effect on the bronze gilded layer. The lack of material removal was attributed to the combination of low fluence and short interaction time, due to the high traverse speed, prevented removal of the bronze gilding.

Surface effects were observed in figure 115 (B); in this test the interaction time was increased by x10 through reduction of the traverse speed (500 mm/s). Initially, for low scan numbers (<10) the observable effects were weak. However, for scan numbers greater than ten surface effects were easier to observe with a distinct darkening of irradiated areas. This darkening indicates that the gilding was removed from the surface revealing the oil size underneath.

Using the lowest traverse speed (250 mm/s), surface modification was clearly observable in all test areas except for a single scans. The OM image of the sample showed that the bronze gilding remained adhered to the surface, even when irradiated at the lowest traverse speed and the maximum number of tested scans, i.e. the interaction time of the beam with the sample was at the maximum available in this test.

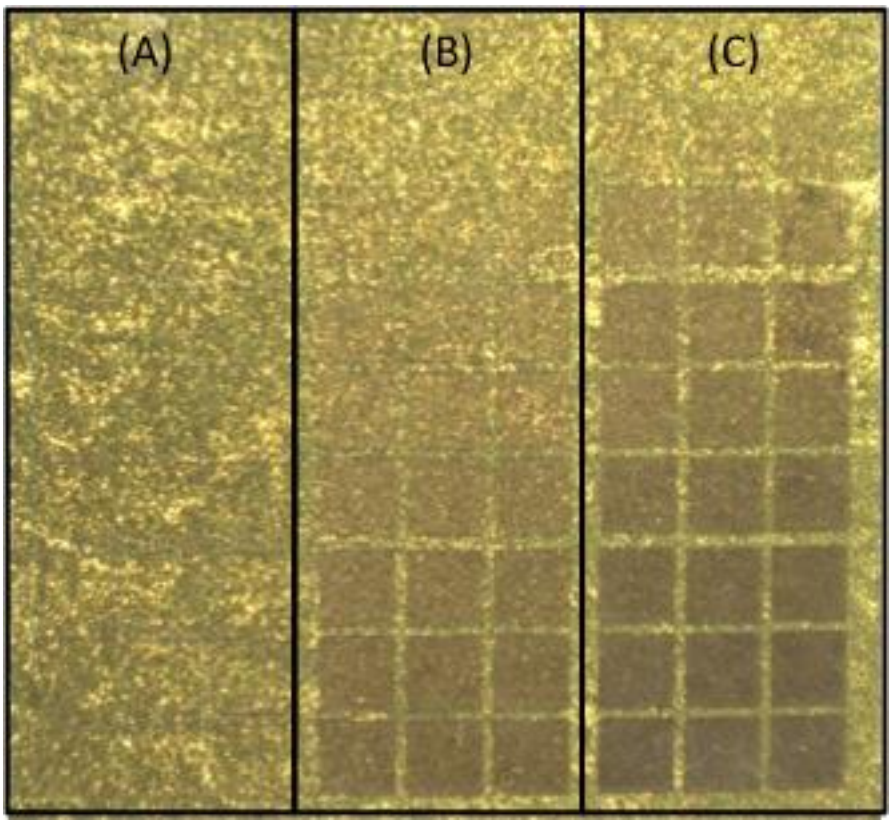

Figure 115: Photographic image of a model sample irradiated using a fluence of 0.41 Jcm^{-2}. This image shows all the tests undertaken at this fluence with each test being repeated three times. Each column represents testing at traverse speeds of (A) 5000, (B) 500 and (C) 250 mm/s. In each test grouping the number of scans was increased from one to thirty (top to bottom).

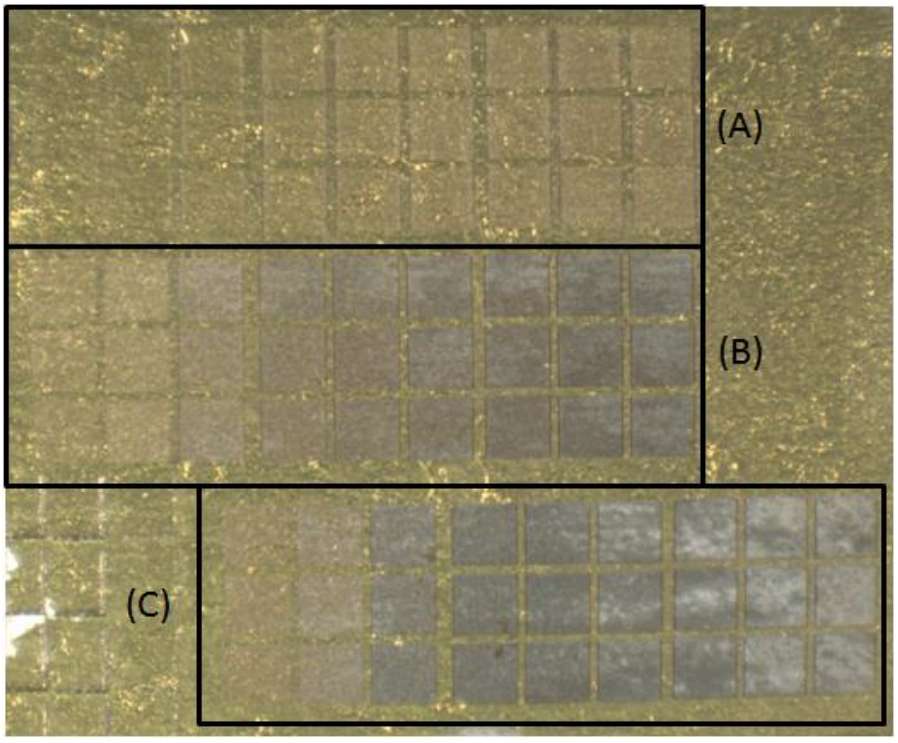

Figure 116: Photographic image of a model sample after irradiation using a fluence of 0.81 Jcm^{-2}. The number of scans is increased from one to thirty (left to right). The traverse speeds used were (A) 5000, (B) 500 and (C) 250 mm/s.

Using a fluence of 0.81 Jcm^{-2}, removal of the gilded layer was possible using a traverse speed of 5000 mm/s (figure 116); however this was only observable when using several surface scans. Increasing the number of surface scans is not always detrimental to the process, however with excessive scans damage to the oil size layer relating to a thermal build up at the surface can occur. Similar, to results recorded at a fluence of 0.41 Jcm^{-2} complete removal of the gilded layer was not possible using the highest traverse speed of 5000 mm/s (figure 116 (A)). This was again attributed to the fluence and interaction time being insufficient to induce ablation of the bronze gilding.

Using a traverse speed of 500 mm/s (figure 116 (B)) removal of the gilded layer was evident as the number of scans increased. Removal was also possible using a traverse speed of 250 mm/s; this was observed with increasing scans from left to right. The majority of bronze gilding was removed below 10 scans, after this the oil size layer is gradually removed exposing the white paint of the sealing layer. Exposure of this layer can be easily observed in figure 116 (C) where the surface was irradiated 25 and 30 times. From a conservators perspective it would be more beneficial to use a higher traverse speed (500 mm/s) as this reduces the interaction time of the laser with each point at the surface, minimising the likelihood of causing damage.

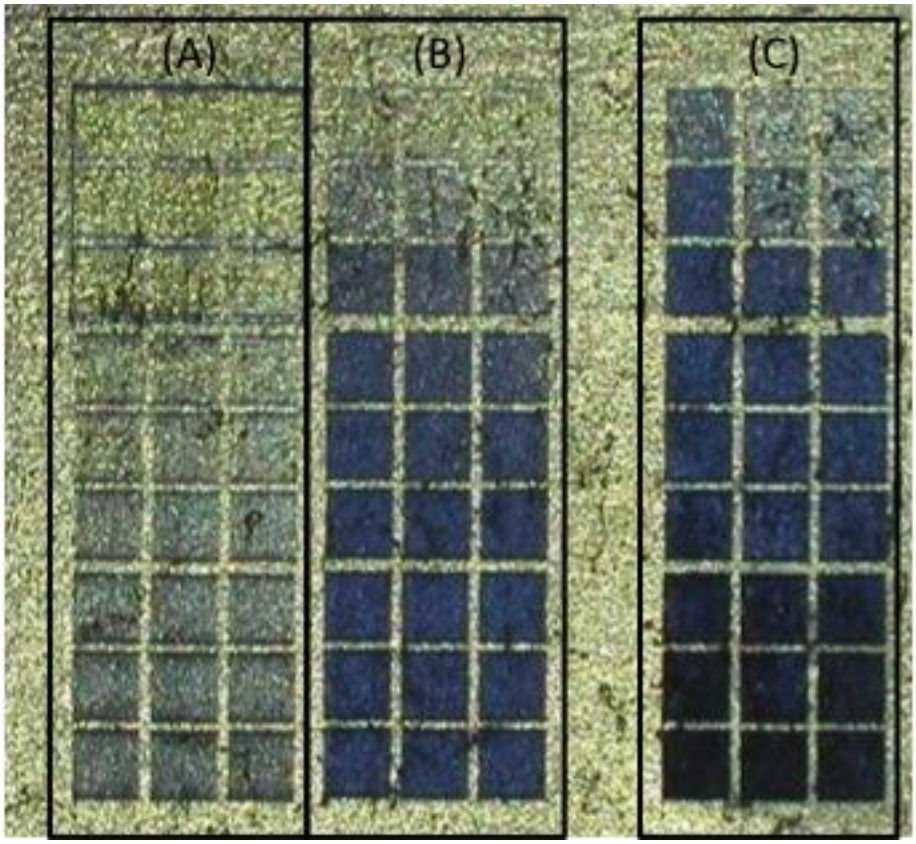

Figure 117: Photographic image of the model sample irradiated using a fluence of 1.22 Jcm^{-2}. Each column represents testing at traverse speeds of (A) 5000, (B) 500 and (C) 250 mm/s. In each test grouping the number of scans was increased between one and thirty from top to bottom.

Figure 117 is an image of the results obtained when irradiating a model sample with a fluence of 1.22 Jcm^{-2}, which is the highest fluence tested in this study. Using this fluence resulted in removal of the gilded layer even when irradiation was carried out at the highest traverse speed (5000 mm/s). However, similar to previous tests at this traverse speed complete removal of the gilded layer was not observed.

Upon irradiating the sample using a traverse speed of 500 mm/s, the majority of the gilded layer was removed after 5 scans. Subsequent scans produced darkened regions where interaction with beam has resulted in removal of the gilding layer. Within these regions, after ablation, some bronze particulates re-deposited onto the surface of the sample. Re-deposition of the gilding removal is not ideal as the purpose of this conservation treatment was to remove the gilded layer.

At the lowest traverse speed of 250 mm/s, removal of the gilded layers was easily observable. At this fluence complete removal of all the layers comprising the model sample was observed. Complete ablation of the sample layers decreases the likelihood of using SUSP in the conservation of gilded frames, as it is an important requirement of the restoration process that the oil size layer remains undamaged after laser treatment.

After initial testing, further examination of the samples irradiated with fluences of 0.81 and 1.22 Jcm^{-2} was carried out using SEM imaging in order to determine the extent of gilding removal and inspect the surface condition of the oil size. Further, EDX spectroscopy was used to analyse the surface of the sample so as to determine the elements remaining in the processed region and identify the boundaries between individual layers (gilding/oil size, oil size/white paint and white paint/wood).

Testing on the sample produced using the lowest fluence (0.41 Jcm^{-2}) was discontinued, as these parameters were unable to initiate a significant amount of material removal from the surface.

The SEM image and EDX spectra recorded from an area processed using a fluence of 0.81 Jcm^{-2} and a traverse speed of 5000 mm/s is shown below. The test area was processed using the maximum number of scans (30). The SEM image shows that a significant amount of the bronze flakes remained adhered to the surface after irradiation. The strong signals for copper and zinc (bronze) recorded in the EDX spectra confirms that complete removal of the gilded layer was not possible. Therefore, this parameter (fluence/traverse speed (0.81 Jcm^{-2} and 5000 mm/s)) combination was deemed unsuitable for use in laser restoration.

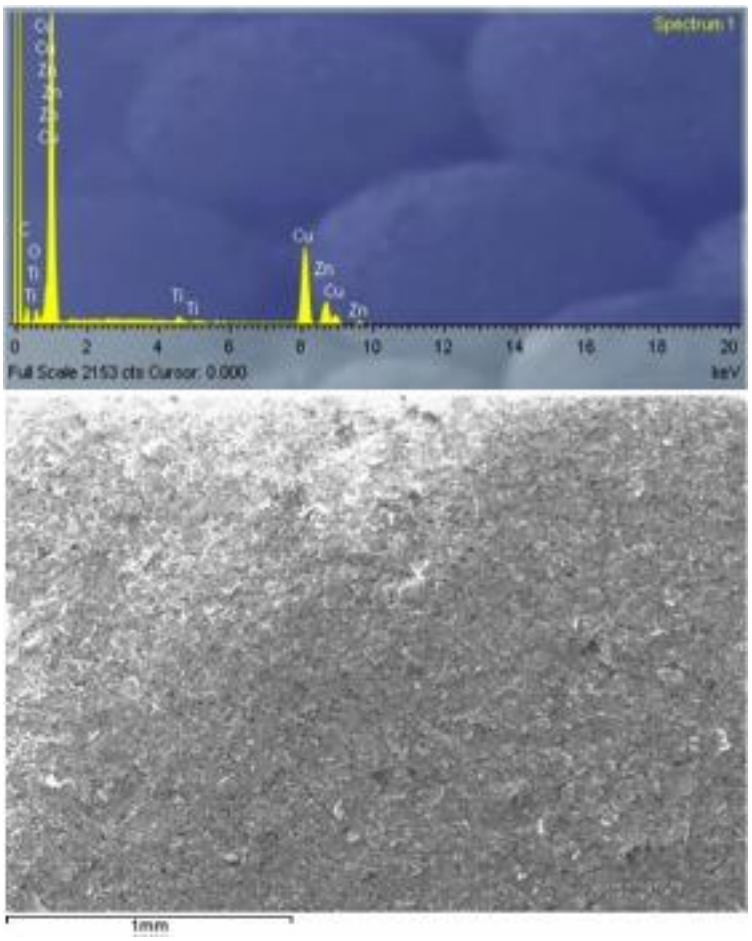

Figure 118: SEM image (x50) taken after irradiation with a fluence of 0.81 Jcm^{-2} using a traverse speed of 5000 mm/s with the maximum 30 scans (bottom). This image was used to obtain the EDX spectra shown (top), the accelerating voltage used was 15 keV.

Using the EDX technique, areas processed with a fluence of 0.81 Jcm^{-2} and traverse speed of 5000 mm/s were scanned to determine the elements present on the surface. For these samples copper, carbon and titanium were used as the main identifying elements for the bronze, oil size and white paint respectively. The graph in figure 119 shows the variation in signal for these elements. The most abundant elements in both the oil size and wood were carbon; therefore it was important to be able to identify each materials contribution to the EDX signal, thereby reducing the possibility of erroneous results. In order to monitor contributions from wood, the titanium signal was utilised. This layer was coated directly on top of the wood; therefore, before any significant contributions to the carbon signal could be made, this sealing layer would have to be exposed and removed by the beam. This would correspond to variations in titanium signal.

Using the highest traverse speed (5000 mm/s) the copper signal was decreased by 20.70 % over the 30-scan range, when compared to signal recorded for the untreated area. The change in signal for both copper and carbon was observed to be inversely proportional; this was attributed to exposure of the oil size to incident x-rays after bronze gilding had been removed. From figure 119 the titanium signal remained approximately uniform across the 30

scan range; this indicates there was no removal of the painted layer and therefore any contributions to the carbon signal caused by the wood would be insufficient to significantly affect the carbon signal.

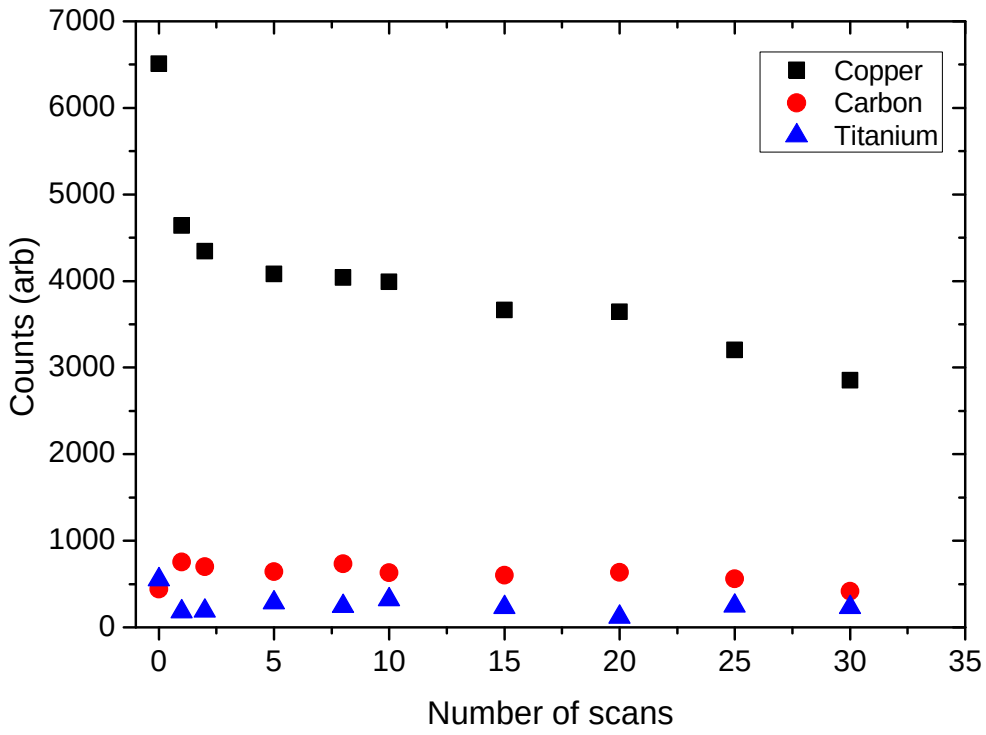

Figure 119: A graph showing the variation in elemental signal recorded for a processed bronze sample when irradiated with 0.81 Jcm^{-2} using a traverse speed of 5000 mm/s.

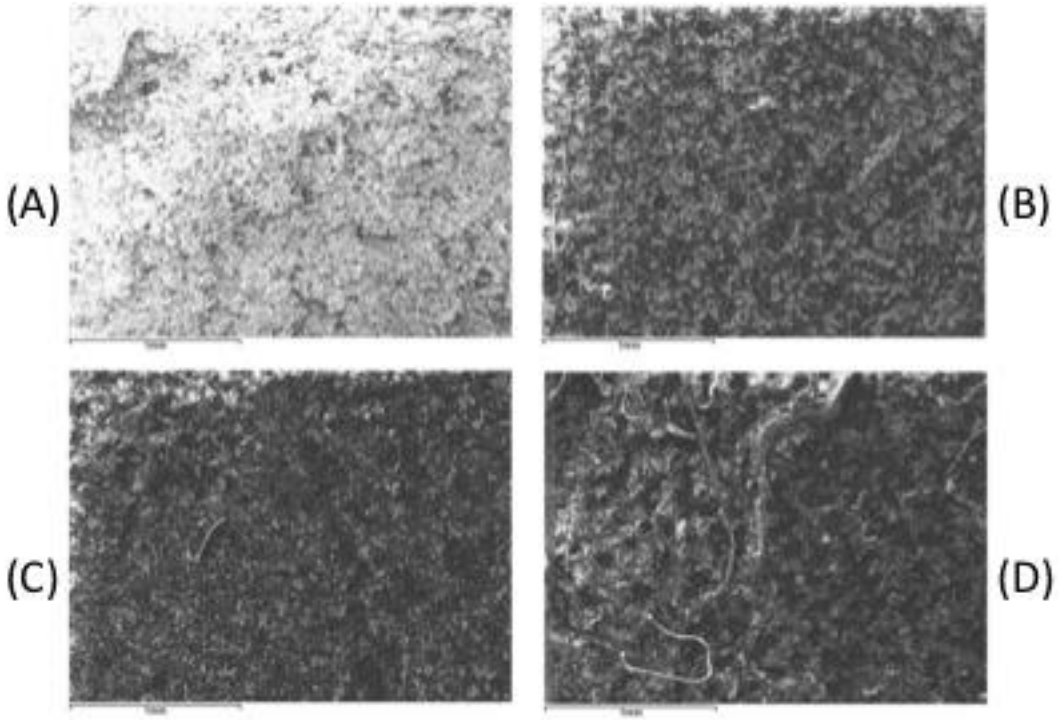

Figure 120: SEM images of areas irradiated with a fluence of 0.81 Jcm^{-2} using a traverse speed of 500mm/s (≈10 PPS); the number of scans used was varied between 1 and 30. These images show an overview of the scanned areas (A) 1 scan, (B) 10 scans, (C) 20 scans and (D) 30 scans.

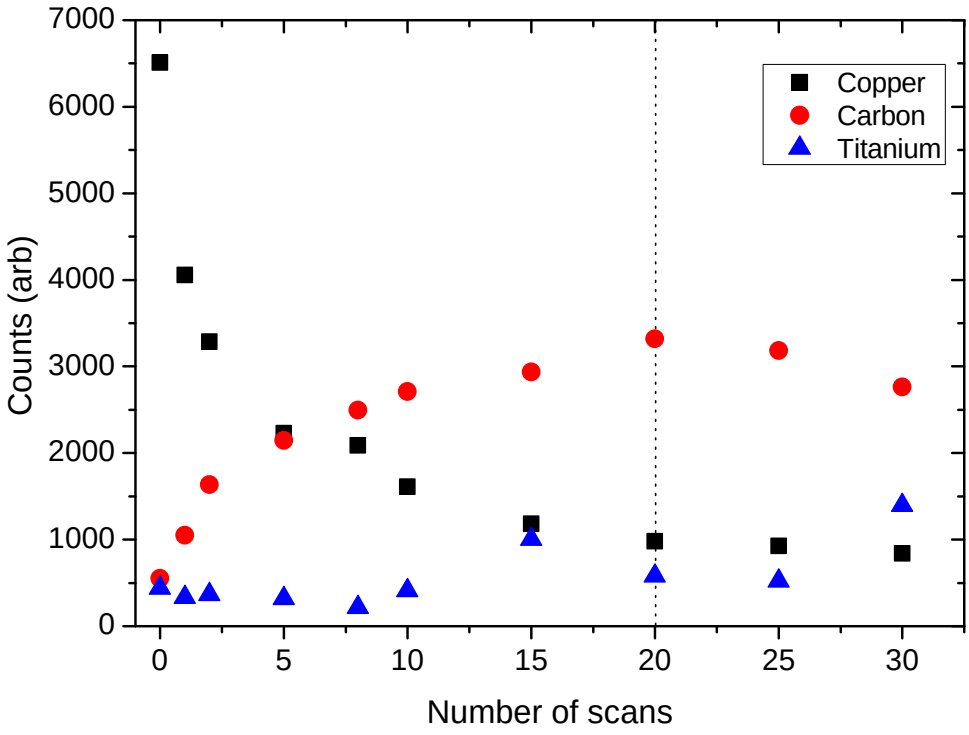

Figure 121: A graph showing the variation in elemental signal recorded for a processed bronze sample when irradiated with 0.81 Jcm^{-2} using a traverse speed of 500 mm/s.

The SEM images in figure 120 show that removal of gilding was possible with increasing scan number; this exposed the oil size beneath. For images (C) and (D) fibres were present on the surface, these were attributed to horsehair from the gilders brush becoming attached to the surface when fabricating the sample.

The results of the EDX spectra at a traverse speed of 500 mm/s are distinctly different to the results obtained at 5000 mm/s. The copper signal was reduced by 87 % over the 30-scan range, confirming that removal of the gilded layer was possible; however trace amounts remained on the surface. The carbon signal rises to maxima at 20 scans coinciding with the copper minimum; again highlighting the inverse relationship between the two signals. This point (highlight by the dotted line in figure 121) was taken to be the interface between the gilded layer and oil size. functional

At this interface, processing would ideally cease, as the purpose of this study was to utilise SUSP to remove the unwanted bronze gilding. After 20 scans the carbon peak began decreasing, indicating removal of the oil size by subsequent scans. This assertion is supported by the increase in titanium (white paint sealing layer) signal between 20 and 30 scans. Until this point (20 scans) the titanium signal remained approximately uniform; ruling out significant contributions to the carbon signal from the wood before 20 scans. The titanium signal increased quickly between 25 and 30 scans, whilst the carbon signal continued to decrease between 20 and 30 scans. This confirms that the carbon signal was mostly generated by the carbon atoms in the linseed oil.

Figures 122 and 123 show the effect of using the lowest traverse speed (250 mm/s). With functional parameters it was possible to remove all the layers of the model sample. This resulted in exposure of some of the wood, as seen in figure 122 (D). Removal of the gilded layers was observed after a single scan, as indicated by the darkened regions where bronze flakes had been removed. Removal using a single scan with a lower traverse speed (therefore a greater number of pulses per spot) was more distinct compared to single scan results observed using higher traverse speeds; this was due to the increased number of surface interactions as the laser dwells in one area for a longer time. In figure 122 (C) and 122 (D), the round holes that appeared in the processed area were attributed to localised increased absorption, resulting in greater removal. This effect is likely to be caused by incubation, which was discussed previously (chapter 4). Incubation results in a lowering of the local ablation threshold through the accumulation of microscopic changes in molecular structure which adjust the refractive index of the material increasing absorption. The localised increase in absorption is attributed to random defects within the microstructure, in these regions the effect of incubation is increased as absorption in this area is greater than the surrounding material.

The effect of irradiation using a fluence of 0.81 Jcm^{-2} with a traverse speed of 250 mm/s; the scan number was increased between 1 and 30 on the surface of the bronze gilded samples is shown in figure 123. Similar to figure 121 a high rate of decline was observed for the copper signal as the scan number increased. Over the 30-scan range the copper (bronze gilding) peak decreased by 100 %. After 8 scans the copper (bronze gilding) peak was reduced by 96 %; the subsequent scans removed the remaining trace amounts and removing the layers beneath.

The peak carbon signal was detected at 8 scans, as this coincided with the copper minima this was determined as the gilding-oil size interface (dotted line at 8 scans). Surface scans between 8 and 25 resulted in a decrease in signal strength; this was attributed to removal of the oil size layer from the surface.

This was supported by the variation in titanium signal, which reached its maxima coinciding with the carbon minima; this was identified as the interface between the oil size and sealing layer (dotted line at 25 scans).

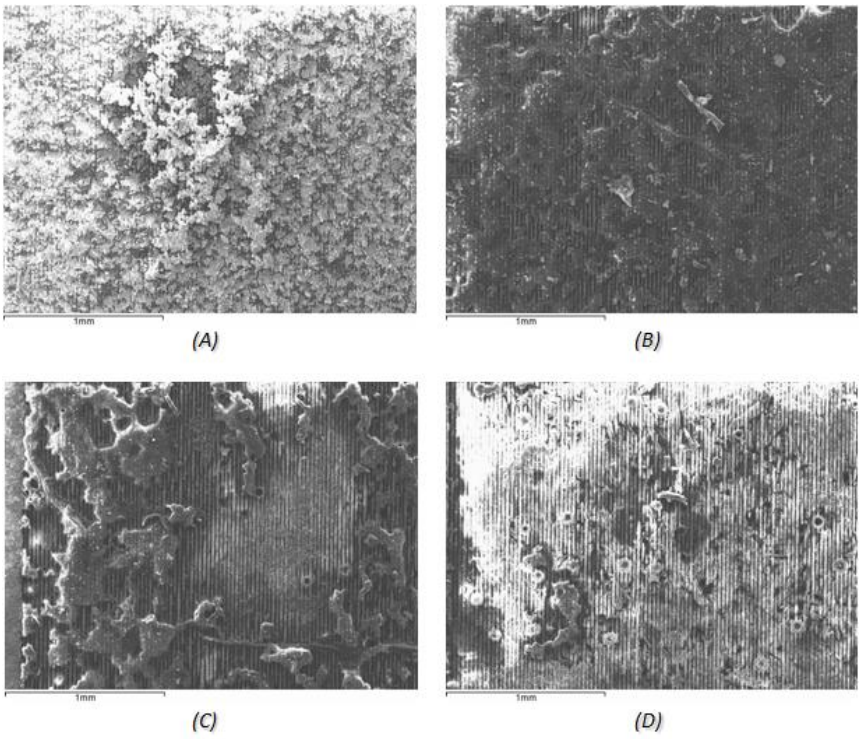

Figure 122: SEM images of areas processed using a fluence of 0.81 Jcm^{-2} using a traverse speed of 250 mm/s (≈ 20 PPS). The number of scans is increased between 1 and 30; here the results of (A) 1 scan, (B) 10, (C) 20 and (D) 30 scans are shown.

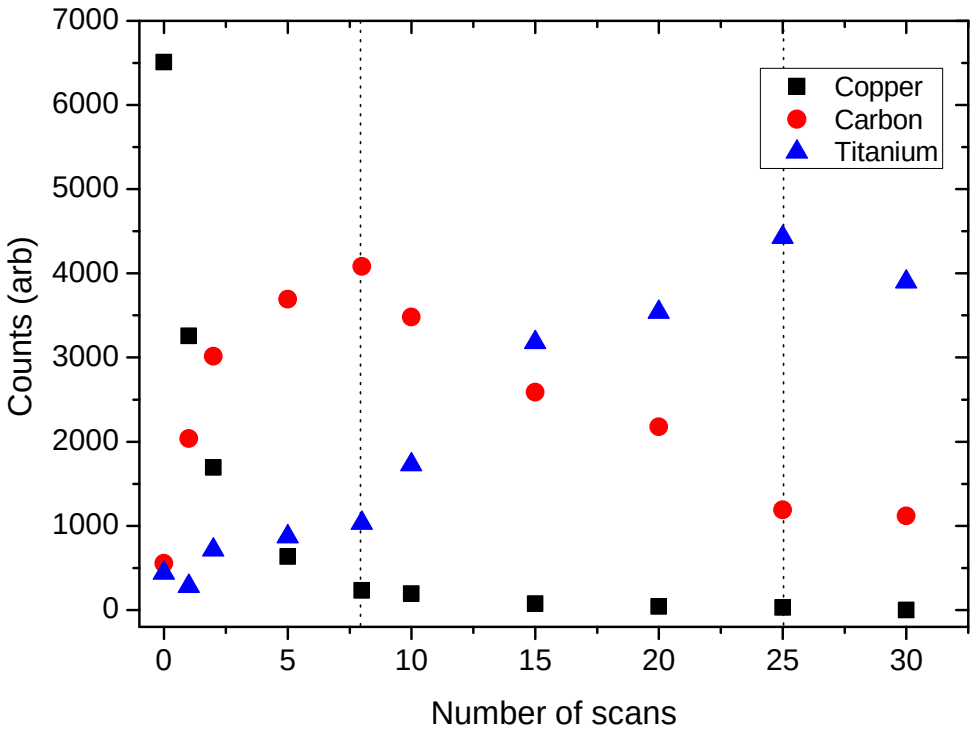

Figure 123: Graph showing the variation in elemental signal obtained when irradiated with a fluence of 0.81 Jcm^{-2} using a traverse speed of 250 mm/s. The dotted lines represent the boundaries of bronze/oil size (left) and titanium/wood.

The effect of increasing the fluence to 1.22 Jcm^{-2} is shown in figures 124 and 125. These SEM images show that using a traverse speed of 5000 mm/s, significant removal of the gilded layer was not possible. In areas were removal had occurred the oil size layer was exposed. Figure 125 shows the change in elemental composition of the surface of the sample after irradiation. Over the 30-scan range the overall decrease in copper signal was 20.71 %. This was approximately equivalent to the change in signal recorded with a fluence of 0.81 Jcm^{-2} and traverse speed of 5000 mm/s Again, a correlation between copper signal decrease and carbon increase was observed, whilst the uniformity of the titanium signal minimises the likelihood of contributions to the carbon signal from the wood.

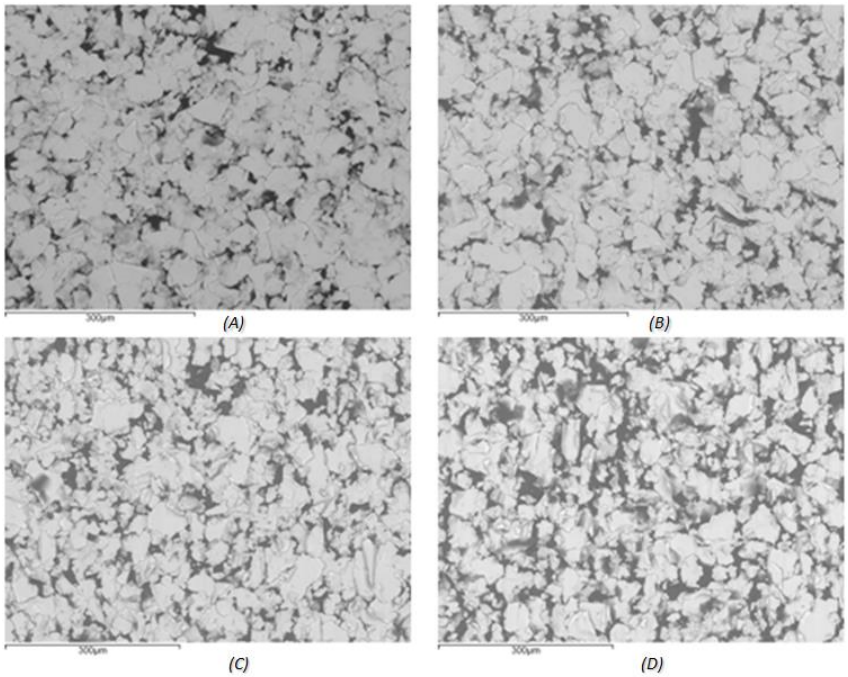

Figure 124: SEM images of areas irradiated at a fluence of 1.22 Jcm^{-2} with a traverse speed of 5000 mm/s. This image shows the result of (A) 1 scan, (B) 10, (C) 20 and (D) 30 scans.

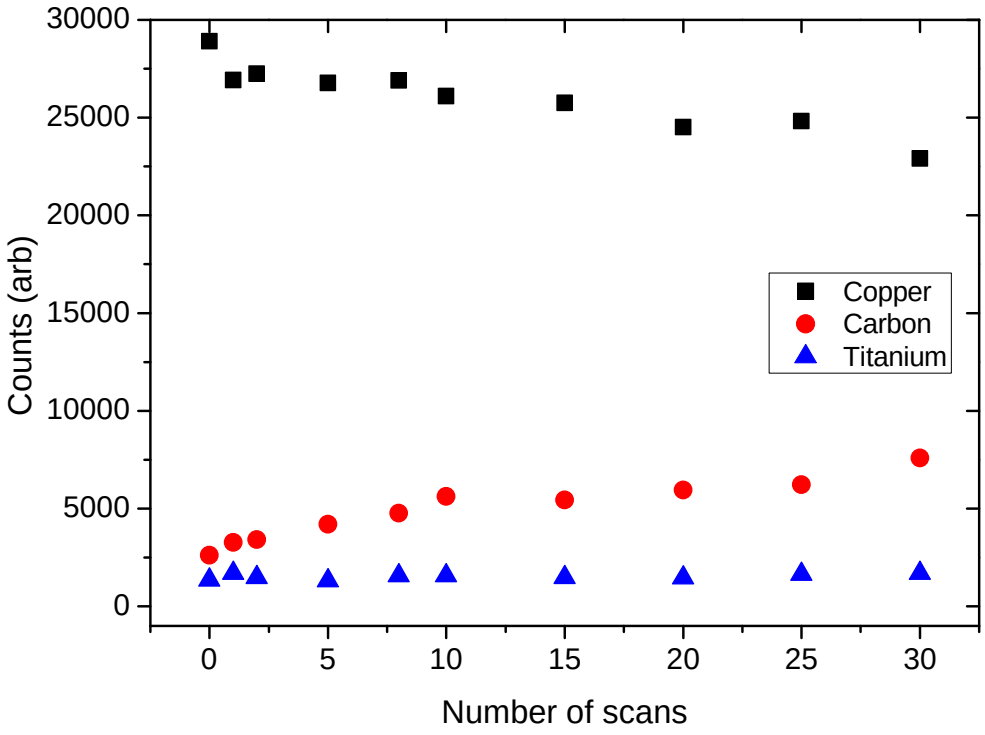

Figure 125: Graph showing the variation in elemental signal obtained when irradiated with a fluence of 1.22 Jcm^{-2} using a traverse speed of 5000 mm/s.

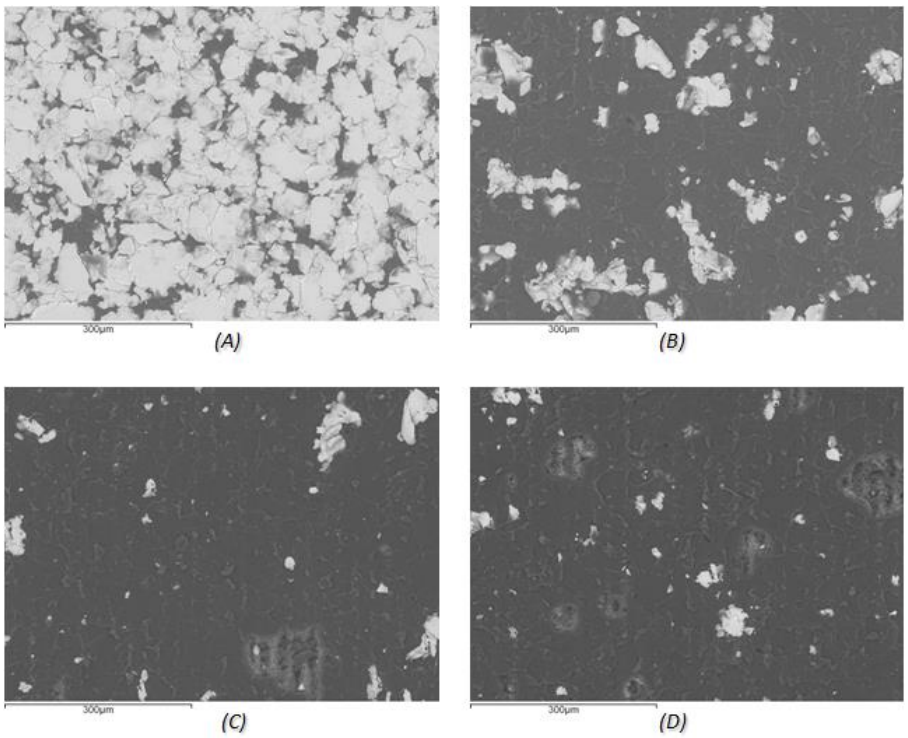

Figure 126: SEM images of areas irradiated at a fluence of 1.22 Jcm^{-2} with a traverse speed of 500 mm/s. This image shows the result of (A) 1 scan, (B) 10, (C) 20 and (D) 30 scans. Some bronze particulates and damage attributed to thermal effects can be observed in (C) and (D).

Figure 126 shows the effect of irradiation using a fluence of 1.22 Jcm^{-2} using a traverse speed of 500 mm/s; with this combination of parameters material removal was clearly observed. Removal was initiated using a single scan. After 10 scans (figure 126 (B)) the majority of the gilding had been removed with only trace amounts of bronze particulates remaining. The rate of bronze removal decreases over the subsequent 20 scans (C and D) as there was less material to remove. In images (C) and (D) damage to the oil size layer was observed in the form of surface blistering, attributed to thermal build up in the interaction zone caused by cumulative irradiation.

Figure 127 shows the variation in the surface composition when processed using a fluence of 1.22 Jcm^{-2} using a traverse speed of 500 mm/s. The copper signal was reduced to trace amounts after 10 scans, a reduction in the signal of 90.92 %. Over the remaining 20 scans this signal did not vary greatly producing an overall decrease of 97.50 %.

At 10 scans the carbon signal reached a maximum, this again coincided with the copper minimum (i.e. the interface boundary between gilding and oil size), from the previous test using a fluence of 0.81 Jcm^{-2} and traverse speed of 500 mm/s. It was expected that the carbon peak would begin to decrease as the beam removed the oil size; however the carbon peak remained uniform over the subsequent scans suggesting that removal using these parameters was selective over the 30-scan range. Any potential error in carbon signal was

excluded by examining the titanium signal, which did not vary significantly across the test range.

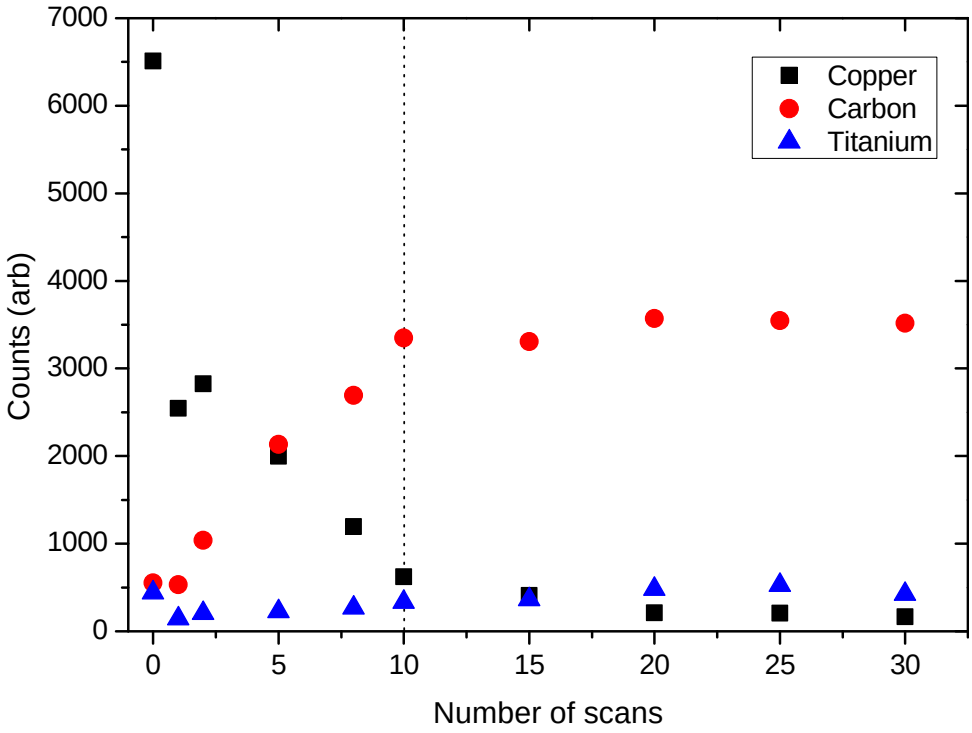

Figure 127: Graph showing the variation in elemental signal obtained when irradiated with a fluence of 1.22 Jcm^{-2} using a traverse speed of 5000 mm/s. The dotted lines represent the boundaries of bronze/oil size.

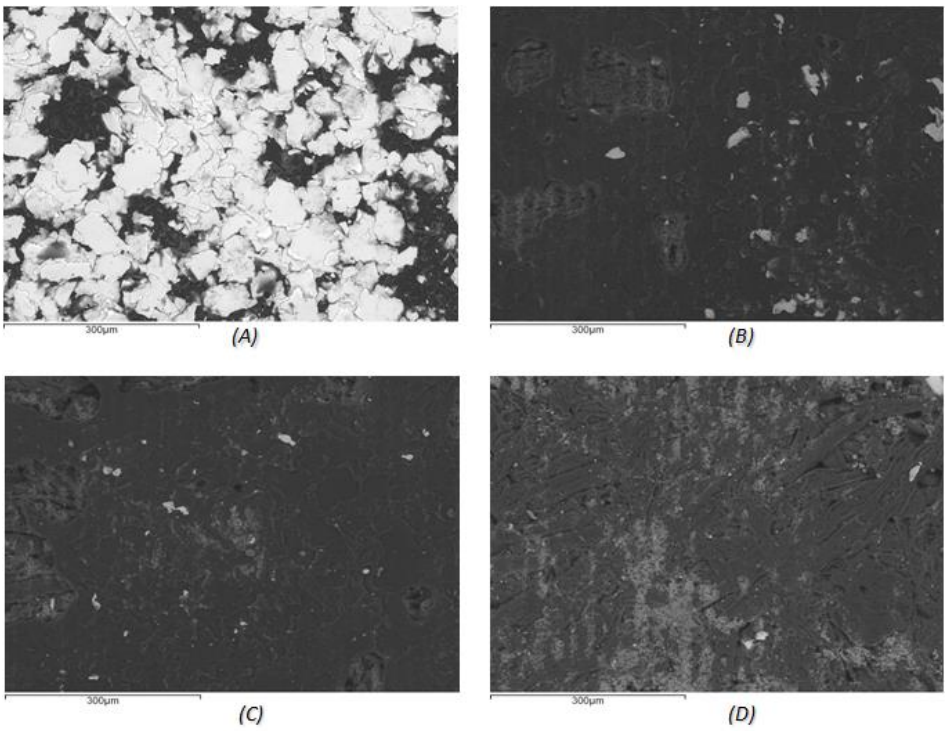

Figure 128: SEM images of areas processed using a fluence of 1.22 Jcm^{-2} with a traverse speed of 250 mm/s. This image shows the result of (A) 1 scan, (B) 10, (C) 20 and (D) 30 scans.

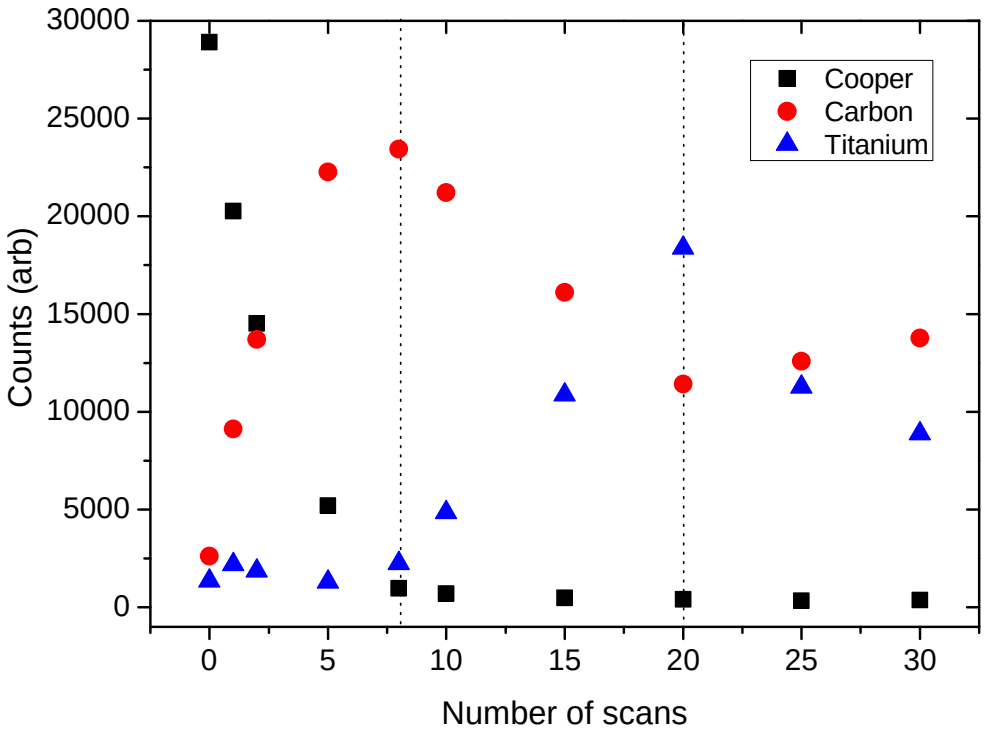

Figure 129: Graph showing the variation in elemental signal obtained when irradiated with a fluence of 1.22 Jcm^{-2} using a traverse speed of 250 mm/s. The dotted lines represent the boundaries of bronze/oil size (left) and titanium/wood (right). The dotted lines indicate the gilding/oil size interface (left) and oil size/sealing layer interface (right).

The SEM images recorded for areas treated with a fluence of 1.22 Jcm^{-2} with the lowest traverse speed of 250 mm/s (20 PPS) are shown in figure 128. Decreasing the traverse speed to 250 mm/s reduced the number of scans required to remove the gilding to 8. Subsequent scans with these parameters lead to complete removal of all the layers comprising the model sample. This can easily be observed in figure 128 (B), (C) and (D), were blistering of the oil size (B) and removal of both the oil size and sealing layer where observed (C and D). In image (D) the fibres of the wood base are clearly visible. Although the majority of the gilded material was removed some trace particulates, attributed to re-deposition, were observed. Re-deposition occurs when some of the ablated material is not efficiently extracted and the kinetic energy imparted during ablation is insufficient to remove the remaining particulate from the interaction zone.

Figure 129 shows the variation in surface composition when using a fluence of 1.22 Jcm^{-2} and a traverse speed of 250 mm/s (20 PPS). The majority of the gilded layer was removed between 1 and 8 scans. The signal reduction after 8 scans was measured to be 96.67 %, after 30 scans the gilding signal was reduced to 98.70 %.

The gilding/oil size interface was reached after 8 scans, this is shown by change in copper removal rate (962 counts (at 8 scans) and 375 counts (30 scans)) and the carbon maximum (23443 counts), as indicated by the dotted line (figure 129, left). Between 8 and 20 scans the carbon signal decreased from this maximum as the oil size was removed.

The decrease in carbon coincides with an increase in titanium signal confirming removal of the oil size due to laser treatment. Between 20 and 30 scans this trend was reversed with the carbon signal increasing whilst the titanium signal declined; this was due to removal of the sealing layer exposing the wood.

Across all the samples analysed using SEM and EDX peaks and troughs were observable as the surface chemical composition varied due to irradiation. Material removal was identified from all the samples was shown and a trend linking the maxima and minima of adjoining layers was identified; these were distinguished using dotted lines.

In this study, copper and carbon were used to identify the gilding/oil size boundary. The maxima and minima combinations of both the materials corresponded to the interface between each layer. The carbon/titanium and the titanium/carbon signals were used to identify the oil size/sealing and the sealing/wood interfaces respectively.

Figure 130 below shows the effect of using the selective processing parameters identified in figure 127 for the treatment of actual bronze gilded samples. These samples were from sections of gilded frames were the damage already sustained required removal and replacement of part of the frame. Using a fluence of 0.81 Jcm^{-2}, a traverse speed of 500 mm/s and an upper scan limit of 20 scans the item was treated. These optimum parameters were determined from the combination of SEM images, to view the effects of laser material interaction, and also by monitoring the copper (bronze gilding) and carbon (oil size) signals to identify when the boundary between the gilding and oil size was reached. By identifying the layer boundaries and monitoring the change in elemental signal it was possible to determine that SUSP could be utilised in laser restoration. The 20-scan limit was introduced due to the slight decrease in carbon signal identified in figure 121. When using a higher fluence and a 500 mm/s traverse speed carbon removal did not occur; this variation was attributed to non-uniformity in the gilding layer resulting in different thicknesses.

Figure 130: Using a fluence of 1.22 Jcm^{-2} with a traverse speed of 500 mm/s and a maximum 20 scans, the gilded frame section was irradiated to test the use of laser treatment on real conservation items. The bronze gilding on the surface was removed revealing the wood base and some gold leaf, which had previously been covered hidden due to the addition of the second gilded layer.

Using a fluence of 0.81 Jcm^{-2} and traverse speed of 500 mm/s removal of the bronze gilded layer was undertaken on part of the bronze gilded layer, as shown in figure 130. No damage was observed in the treated areas and it was also possible to reveal some original Gold leaf that has been covered by the bronze gilding during previous restorations. This sample had no sealing layer between the wood and oil size layer preventing the use of SEM and EDX to measure elemental signal variation.

6.2.3 Summary

In this study removal of unwanted bronze gilding, something that has proven difficult using traditional methods was investigated. Several model samples were fabricated in order to test the applicability of USP lasers and selective processing for the restoration of gilded objects. The use of a low fluence (0.41 Jcm^{-2}) resulted in minute gilding removal at all traverse speeds. By increasing the fluence to 0.81 and 1.22 Jcm^{-2} removal was possible at all traverse speeds, with the exception of 5000 mm/s.

Selective removal of the bronze gilding was achieved using a fluence of 0.81 or 1.22 Jcm^{-2} with a traverse speed of 500 mm/s; this indicates that once above the threshold for material removal that the traverse speed (effective number of pulses per spot) was the controlling factor in selective processing.

Utilising SUSP in the restoration of gilded frames is difficult to apply, due to the unique structure of each surface; i.e. the gilding composition will vary across the surface. This makes it difficult to identify a set of consistent parameters that could be utilised across the rest of the test surface. If the surface composition of the objected was mapped, using a technique such as optical coherence tomography (OCT), before starting the restoration

process then it may be possible to utilise this technique; however, this requires further investigation.

Using the optimised parameters identified through testing model samples, laser restoration was applied to sections of bronze gilded frames. The use of the optimised parameters resulted in the removal of the unwanted bronze gilding exposing the polymer underneath and some previously concealed gold leaf gilding (figure 130). Upon inspection of the wood base and oil size layers, no observable damage was detected. Processing of the frame section was problematic due to the shape and size, which made it difficult to ensure that the restoration was carried out uniformly. Therefore, the size and shape of the item must also be considered when using this technique in gilding removal.

7 Conclusions and future work

In this study, selective materials processing with ultra-short pulses have been investigated. To fully understand this process, a study into the properties that enable selective removal was carried out. These were determined by investigating the steps involved in materials ablation with ultra-short pulses.

The determinant factors, identified in the first stage of testing, were then applied in four case studies which aimed to highlight both the benefits of ultra-short pulse selective processing and identify any potential limitations to this technique. The case studies consisted of two micro processing and two restoration techniques.

7.1 Selective materials processing with ultra-short pulses

An empirical investigation into the application of selective materials processing with ultra-short pulses was carried out to determine whether this technique was feasible and what parameters influenced this method of materials processing. The following conclusions are presented.

By studying the linear absorption of ITO coated glass samples it was possible to identify a distinct separation between the absorption coefficients at both 1064 nm and 532 nm. ITO was found to have a much greater absorption coefficient (9.95×10^3 cm^{-1} and 6.67×10^3 cm^{-1},1064 nm and 532 nm respectively) than glass (0.65 cm^{-1} (1064 nm) and 0.70 cm^{-1} (532 nm)).

The impact of these vastly different absorption coefficients was observed by experimentally determining the ablation threshold of both ITO and glass. These values were used to identify a selective ultra-short pulse (SUSP) processing window. Using the single pulse ablation threshold of ITO $\left(\phi_{th}^{ITO}\right)$ and glass $\left(\phi_{th}^{Glass}\right)$ (0.76 and 9.80 Jcm^{-2} respectively), selective processing with a fluence (Φ) was possible. To achieve selective processing for single pulses the fluence used must be greater than the ablation threshold of the ITO but less than the ablation threshold of the glass.

Multi-pulse ablation threshold tests were carried out to determine the effect of increased pulse numbers on the selective processing window. The ablation threshold of ITO was found not to alter significantly when irradiated with 6 and 10 pulses; however a lower threshold (0.65 Jcm^{-2}) was observed when irradiated with 25 pulses.

The ablation threshold of the glass substrate was found to varying significantly when irradiated with multiple pulses compared to the single pulse case. The ablation threshold of glass was determined as 4.70 Jcm^{-2} for 6, 10 and 25 pulses. This decrease was attributed to incubation effects, which increase absorption, reducing the ablation threshold. This alters

the size of the selective processing window. In the multi–pulse case the criteria for selective processing requires that the lower fluence is greater than the single pulse threshold of ITO (0.76 Jcm^{-2}) and less than the multi-pulse threshold of glass.

Finally, the effect of scanning the surface of the thin film was investigated using SEM and EDX measurements. SEM images were used to examine the ablated tracks under high magnification; this showed the precision ablation achievable with ultra-short pulses (USP) as minimal thermal effects were observed. When using high traverse speeds the quality of track processing was reduced significantly, with individual pulses overlapping each other.. These high speeds reduce the likelihood of creating a consistent track.

To confirm selective ablation, tracks were examined using EDX. By monitoring both the indium and silicon signals it was possible to show indium removal at all traverse speeds, resulting in approximately the same amount of material removal (i.e. independent of pulse number). EDX measurements of the silicon signal (attributed to the glass substrate) remained unchanged during processing, confirming the selectivity of the process.

SUSP processing has been carried out successfully using 10 ps pulses. Similar to the selective processing with continuous wave (CW) or long pulse (LP), the linear absorption coefficient (α) was identified as the determinant factor in achieving selective processing. The difference in absorption is observed experimentally by a distinct difference between ablation thresholds. By exploiting this difference SUSP processing was possible. The use of multiple pulses reduces the ablation threshold of the glass substrate, due to an incubation effect. In this instance the upper limit for selective processing is reduced.

7.2 Parallel processing of a small ITO circuit

Using the parameters identified in chapter 4, the selective parallel processing of ITO to create small functional circuits, with picosecond pulses, was carried out. By utilising the difference in ablation thresholds of ITO and glass, removal of the thin layer was possible with no observable damage to the substrate; confirmed by optical microscope and white light profiling. The lower threshold for processing was taken as the ablation threshold of ITO (0.76 Jcm^{-2}). The upper limit for processing was dependent on the traverse speed used.

Both single and multi-beam circuits were tested for conductivity with no cross boundary current detected. The circuit conductivity recorded for single and parallel processed circuits highlight the repeatability of this process. Through the introduction of an SLM and the application of a CGH, the time taken to manufacture the circuits was halved. The application of more complex holograms could allow for the fabrication of greater numbers simultaneously. This enables the fabrication process to be more energy efficient, quicker and cheaper, especially when compared to current methods.

7.3 Fabrication of a low cost solar cell

Using the principles identified in chapter 4 the selective process of a multi layered photovoltaic structure was carried out. The absorption coefficient of F-SnO_2 was determined to be much greater than glass ($2.87x10^3$ cm^{-1} in comparison to 78.1 cm^{-1} at 1064 nm). This gave rise to a distinct difference in ablation thresholds, which could be exploited for the purposes of SUSP processing.

Using a fluence of 4.09 Jcm^{-2} a hatch, width 250 microns, was scribed into the surface of the F-SnO_2 to fabricate several cells which could be connected in series. It was not possible to complete this with a single scan and the area required a second scan run; this was attributed to the ≈500 nm layer thickness. After a second scan the conductivity between scribed areas was measured to be zero. White light images showed a uniform material removal with no observable substrate damage, which could possibly reduce cell efficiency. This process was repeated for 5 scribes across the sample (100 x 100 mm).

After processing the F-SnO_2, a flame sprayed oxide was deposited on top of the structured surface. Attempts to follow the steps outlined in the SUSP approach were unsuccessful due to the opacity and high surface roughness of this layer. An approximate ablation threshold was determined by monitoring plasma generation near the surface. Using fluences above these values in both IR (1064 nm) and visible (532 nm) showed minimal surface modification. This was attributed to low absorption and high surface roughness. Excessive scanning with 532 nm at high power resulted in a failure fracture of the surface.

FSO removal was achieved with fs processing of the surface; however this required high pulse energies which were sufficient to damage the F-SnO_2 and the glass. Observation of the processed areas, in transmission, showed inconsistent material removal attributed to the high surface roughness. Material removal with fs pulses was attributed to the extremely high intensities inducing non-linear absorption at the surface. In the non-linear case absorption is dependent upon the intensity of the incoming pulse and as such would not be able to differentiate between different materials within the solar cell structure.

This case study highlights the difficulty of using SUSP processing in low absorbing mediums, where the material underneath has a lower ablation threshold than the material being processed.

7.4 Restoration of a Royal accessory

The laser restoration of a pair of gloves commissioned by King Charles I underwent laser restoration to remove surface contaminants from the gloves. To minimise the likelihood of inducing photo degradation, restoration was carried out using a wavelength of 1064 nm. To minimise the interaction between the laser pulses and sample, the effect of traverse speed was tested. At high traverse speeds material removal was not observed, upon reducing the speed to 300 mm/s (approx. 1 pulse per spot at 10 kHz) contaminant removal was possible. Restoration of the leather section of the glove was possible up to fluences of 4.89 Jcm^{-2}; above this damage to the surface of the leather was clearly observable revealing the fibres beneath. This was confirmed using high magnification SEM images.

These parameters were subsequently applied to the cuff of the glove. This section of the glove is highly decorated and consisted of several different materials. SEM images of these areas showed that selective removal from these materials was possible. The remaining conservation was carried out using a fluence of 4.10 Jcm^{-2} at a traverse speed of 300 mm/s; treatment was completed within 3 days. This significantly reduced the time taken to usually restore these delicate objects. Laser removal of some iron staining and fungal growth on the leather section of the glove was not treatable with the laser; this was removed later using more traditional chemical methods.

7.5 Removal of bronze gilding

In this study removal of unwanted bronze gilding was carried out using an ultra-short pulse fibre laser (20 ps). Traditionally restoration of gilded objects has proven difficult due to the thinness of the gilding and the partial use of bronze gilding on some objects.

Several model samples were created to facilitate the process of laser treatment before moving onto actual gilded samples. Selective removal of the gilding was achieved at fluences above 0.81 Jcm^{-2}; below this fluence no material removal was observed in testing. The effect of traverse speed of the process was also studied, using high speeds of 5000 mm/s there was insufficient interaction time to induce significant gilding removal from the surface. Removal of the gilding layer increased significantly, when the traverse speed was reduced to 500 mm/s, this increased the interaction time tenfold. At the lowest tested traverse speed (250 mm/s) the interaction time was sufficient to induced removal of all the layers of the model sample over the 30 scan range, making this speed unsuitable for restoration. The optimum processing parameters were determined by EDX analysis of the surface; using a fluence of 0.81 Jcm^{-2} and traverse speed of 500 mm/s selective processing was achievable over a small area.

Using the selective removal parameters identified on the model samples a pair of gilded frame offcuts were treated using the laser. This removed the bronze contaminant without damaging the material underneath.

SUSP processing was difficult on this sample due to the surface morphology and composition of the samples treated. Variations in surface composition are accounted for by the process selectivity; however increasing exposure of the material underneath will eventually lead to ablation as the threshold is lowered. Similarly the morphology of conservation objects poses a problem due to the finite focal region of a laser; this makes it more difficult to accurately undertake restoration treatments.

7.6 Future work

Several recommendations are made as result of this work:

The main factor in achieving selective materials processing was determined to be the linear absorption coefficient (α), however the effects of utilising nonlinear absorption in selective processing are unknown. In nonlinear processes the degree of absorption is dependent upon the square of the intensity of the impinging pulse. This would mean that optical pulse would not differentiate between materials; negating the selective processing.

Viable micro processing in industry requires high repeatability with high throughput, selective processing provides a reliable method for surface structuring; however, the effect of using high repetition rates (>0.1 MHz) are unknown. Using high pulses numbers generates thermal effects in the processing region, regardless of the pulse width. An increase in surface temperature when processing could alter the selective processing window.

Throughout this thesis a Gaussian beam profile has been used, this is not fundamentally the best beam profile for selective materials processing as the intensity is peaked at the centre. The use of beam shaping to produce other shapes, such as top hat, could improve the selective processing window.

Selective ablation in parallel processing can be utilised to overcome differences in beam uniformity, this could allow the use of less memory intensive holograms and reduce failure rates. The application of ultra-short pulses in laser conservation has begun to be investigated more intensively due to the precision removal and low thermal impact of these systems. Selectively processing objects presents great benefits as enables the restoration of more delicate items, previously considered unsuitable for laser treatment and minimises the risk of damage. However, the unique surface composition of restoration items means that a method for characterising the surface and sub-surface structure is required before widespread uptake could take place.

8 References

[1] Luk Yanchuk B. "Laser Cleaning". World Scientific Pub Co Inc; 1st edition (December 2002)

[2] Kane D. M. "Laser cleaning II". *Volume 4 of International Workshop on Laser Cleaning: IWLC*

[3]Application_note_described_on_http://www.liverpoolmuseums.org.uk/conservation/technologies/casestudies/sculpture/palmhouse/index.aspx.

[4] Asmus JF, Munk WH, Murphy CG (1973) Studies on the interaction of laser radiation with art artefacts. Proc Soc Photo-Opt Instrum Eng 41:72–76

[5] Shirk M.D. Molian P.A. "A review of ultrashort pulsed laser ablation of materials". Journal of Laser Applications / Volume 10 / Issue 1 1998.

[6]Shirk M. D. Molian P.A. and Malshe A. P. "Ultrashort pulsed laser ablation of diamond". J. Laser Appl. 10, 64 (1998)

[7] Malinauskas M. Danilevičius P. and Juodkazis S. "Three-dimensional micro-/nano-structuring via direct write polymerization with picosecond laser pulses" Optics Express, Vol. 19, Issue 6, pp. 5602-5610 (2011)

[8] *Einstein, A. 1916. Zur Quantentheorie der Strahlung. Physik. Gesell. Z¨urich Mitt. 18: 47-62*

[9] Ladenburg, R. 1928. Untersuchungen ¨uber die anomale Dispersion angeregter Gase I. Teil. Zur Pr¨ufung der quantentheoretischen Dispersiondformel. Z. Phys. 48: 15-25

[10] Maiman, T.H. 1960a. Speech by Dr. Theodore H. Maiman, Hughes Aircraft Company, at a Press Conference at the Hotel Delmonico, New York, July 7, 1960. URL: http://www. hrl.com/lasers/pdfs/maiman 60.07.07.pdf, accessed on March 9, 2011

[11] Maiman, T.H. 2000. The Laser Odyssey. Laser Press, Blaine, WA

[12] Taylor, Nick (2000). *LASER: The inventor, the Nobel laureate, and the thirty-year patent war*. New York: Simon & Schuster. pp. 125–128. ISBN 0-684-83515-0.

[13] Patel, C.K.N. 1964. Continuous-Wave Laser Action on Vibrational-Rotational Transitions of CO2. Phys. Rev. 136: A1187-A1193

[14] Sun Z. Ion J.C. "Laser welding of dissimilar metal combination Review". Journal of Materials Science, Volume 30, Issue 17, September 1995, Pages 4205-4214

[15] Karatas C. Keles O. Uslan I. Usta Y. "Laser cutting of steel sheets: Influence of work piece thickness and beam waist position on kerf size and stria formation". Journal of Materials Processing Technology, Volume 172, Issue 1, 20 February 2006, Pages 22-29

[16] Geiger, M. Vollertsen F. "The mechanisms of laser forming". CIRP Annals - Manufacturing Technology, Volume 42, Issue 1, 1993, Pages 301-304.

[17] Griffiths J. Edwardson S.P. Dearden, G. Watkins K.G. "Finite element modelling of laser forming at macro and micro scales". Physics Procedia, Volume 5, Issue PART 2, 2010, Pages 371-380.

[18] Lin J. Steen W.M. "An in-process method for the inverse estimation of the powder catchment efficiency during laser cladding". Optics and Laser Technology, Volume 30, Issue 2, 1998, Pages 77-84.

[19]Singh, J. Laser-beam and photon-assisted processed materials and theirmicrostructures (Review) Journal of Materials Science Volume 29, Issue 20, October 1994, Pages 5232-5258

[20] Geusic, J.E., H.M. Marcos and L.G. Van Uitert. 1964. Laser Oscillations in Nd-Doped Yttrium Aluminum Yttrium Gallium and Gadolinium Garnets Appl. Phys. Lett. 4: 182-184

[21] Hooker S. Webb C. "Laser Physics". Oxford master series in atomic, optical and laser physics. Oxford University press 2010.

[22] P. M. Paul et al. Generation of a train of attoseconds pulses from high harmonic generation. Science 292, 1689 (2001);

[23] Collins, R.J., D.F. Nelson, A.L. Schawlow, W. Bond, C.G.B. Garrett and W. Kaiser. 1960. Coherence, Narrowing, Directionality, and Relaxation Oscillations in the Light Emission from Ruby. Phys. Rev. Lett. 5: 303-305

[24] Hellwarth, R.W. 1961. Control of Fluorescent Pulsations. in Advances in Quantum. Electronics, edited by J. Singers. Columbia Press, New York, 334

[25] McClung, F.J. and R.W. Hellwarth. 1962. Giant Optical Pulsations from Ruby. J. Appl. Phys. 33: 828-829

[26] Shi W. Leigh M. Zong J. and Jiang S. "Single-frequency terahertz source pumped by Q-switched fiber lasers based on difference-frequency generation in GaSe crystal". OPTICS LETTERS, Vol. 32, No. 8, April 15, 2007.

[27] Both images taken from the RP Hpotonics website.

[28] W. E. Lamb Jr., "Theory of an optical laser", Phys. Rev. 134 (6A), A1429 (1964)

[29] Hargrove, L.E., R.L. Fork and M.A. Pollack. 1964. Locking of He-Ne Laser Modes Induced by Synchronous Intracavity Modulation. Appl. Phys. Lett. 5: 4-5

[30] D. J. Kuizenga and A. E. Siegman, "FM and AM mode locking of the homogeneous laser – Part I: theory", IEEE J. Quantum Electron. 6, 694 (1970)

[31] Images taken from: Hooker S. and Webb C. Laser Physics. Oxford master series in atomic, optical and laser physics. Oxford University press ISBN 9780198506911

[32] Image reproduced from laser physics. Hooker S. and Webb C. Laser Physics. Oxford master series in atomic, optical and laser physics. Oxford University press ISBN 9780198506911

[33] H. W. Mocker and R. J. Collins, “Mode competition and self-locking effects in a Q-switched ruby laser”, Appl. Phys. Lett. 7, 270 (1965)

[34] Image taken from RP Photonics.

[35] H. A. Haus, “Theory of mode locking with a fast saturable absorber”, J. Appl. Phys. 46, 3049 (1975)

[36] K. Sala *et al.*, “Passive modelocking of lasers with the optical Kerr effect modulator”, IEEE J. Quantum Electron. QE-13 (11), 915 (1977).

[37] Ursula Keller *et al*. Semiconductor Saturable Absorber Mirrors (SESAM’s) for Femtosecond to Nanosecond Pulse Generation in Solid-State Lasers. IEEE JOURNAL OF SELECTED TOPICS IN QUANTUM ELECTRONICS, VOL. 2, NO. 3, SEPTEMBER 1996 435

[38] Strickland, D. and G. Mourou. 1985. Compression of Amplified Chirped Optical Pulses. Opt. Commun. 55: 447-449

[39] Image taken from University of Michigan, dept of engineering.

[40] Steen W. M. “Laser Materials Processing”. Ed. 3 Springer-Verlag

[41] Bado P. Clark W. Said A. “Micromachining handbook”. www.cmxr.com, 2011

[42] Karnakis D. Kearsley A. Knowles M. “Ultrafast laser patterning of OLEDs on flexible substrate for solid-state lighting”. Journal of laser Micro/Nanoengineering, vol 4, 3, 2009

[43] Stuart B. C. “Nanosecond to-femtosecond laser induced breakdown in dielectrics”. Phys. Rev. B, Vol 53, Issue 4, 1996

[44] Beer A. “Bestimmung der Absorption des rothen Lichts in farbigen Flüssigkeiten (Determination of the absorption of red light in colored liquids)”. Annalen der Physik und Chemie, vol. 86, pp. 78–88.

[45] Goeppert-Mayer M (1931). "Über Elementarakte mit zwei Quantensprüngen". Ann Phys 9 (3): 273–95.

[46] Jayabalan J. Singh A. Oak S. M. “Single-shot measurement of nonlinear absorption and nonlinear refraction”. Applied optics, vol 45, 16, 2006

[47] I. Zavestovskaya, P. Eliseev. O. Krokhin, N. Men’kova. “Analysis of the nonlinear absorption mechanism in ablation of transparent materials by high intensityand ultra short laser pulses. Applied Physics A: Material science and processing, 92, 4, pp 903 -906. (2008).

[48]Ready J.F. and Farson D. F. “LIA Handbook of Laser Materials Processing”. Magnolia Publishing Inc, Orlando, 2001

[49] Demtröder W. “Laser Spectroscopy: Basic Concepts and Instrumentation”. 3rd Edition Springer-Verlag, Berlin 2003.

[50] Hohlfeld J. Grosenick D. Conrad U. and Mattias E. Applied Physics A 60, 137, 1995.

[51] A. Y. Vorobyev and C. Guo, Physical Review B. 72(19). (2005), 195422.

[52]A. Y. Vorobyev, V. M. Kuzmichev, N. G. Kokody, P. Kohns, J. Dai and C. Guo, Applied Physics *A*. 82. (2006), 357.

[53] P. Lorazo, L. Lewis and M. Meunier. "Short-Pulse Laser Ablation of Solids: From Phase Explosion to Fragmentation". Physical Review Letters, Vol. 91. No. 22. (2003)

[54] J. Yang, Y. Zhao, N. Zhang, Y. Liang and M. Wang, Physical Review B. 76. (2007)

[55] M. E. Povarnitsyn, T. E. Itina, M. Sentis, K. V. Khishchenko and P. R. Levashov, Physical Review B. 75(23). (2007), 235414.

[56] B. H. Christensen and P. Balling, Physical Review B. 79(15). (2009), 155424.

[57] Y. Yao, H. Chen, W. Zhang. "Time scale effects in laser material removal: a review". Int J Adv Manuf Technol 26: 598–608 (2005).

[58] S. Nolte, C. Momma, H. Jacobs, A. Tünnermann, B. N. Chichkov, B. Wellegehausen and H. Welling, Journal of the Optical Society of America B. 14. (1997), 2716.

[59] M. Schmid, B. Neuenschwander, V. Romano, B. Jaeggi, U Hunziker. "Processing of metals with ps-laser pulses in the range between 10 ps and 100 ps". Proc. SPIE 7920, Laser applications in Microelectronic and Optoelectronic Manufacturing XVI. (2011)

[60] Yong Gan and J. K. Chen. "An atomic-level study of material ablation and spallation in ultrafast laser processing of gold films". J. Appl. Phys. 108, 103102 (2010).

[61] A. Lemke and D. Ashkenasi. "Picosecond Laser Induced Colour Centres: Stress-free Markings and Choice of Guiding Optics". JLMN, Volume 6, No. 1. (2011)

[62] S. Amoruso. G. Ausanio. A C Barone. R Bruzzese. L Gragnaniello. M Vitiello. and X Wang. "Ultrashort laser ablation of solid matter in vacuum: a comparison between the picosecond and femtosecond regimes". J. Phys. B: At. Mol. Opt. Phys. 38 (2005) L329–L338

[63] A. Rosenfeld, M. Lorenz, R. Stoian and D. Ashkenasi, Applied Physics A. 69. (1999), S373.

[64]D. Ashkenasi, M. Lorenz, R. Stoian and A. Rosenfeld, Applied Surface Science. 150.(1999), 101.

[65] J. Bonse, P. Rudolph, J. Krüger, S. Baudach and W. Kautek, Applied Surface Science. 154/155. (2000), 659.

[66] X. C. Wang, G. C. Lim, H. Y. Zheng, F. L. Ng, W. Liu and S. J. Chua, Applied Surface Science. 228. (2004), 221.

[67] X. Liu, D. Du, and G. Mourou. "Laser Ablation and Micromachining with Ultrashort Laser Pulses". IEEE JOURNAL OF QUANTUM ELECTRONICS, VOL. 33, NO. 10, OCTOBER 1997

[68]E. Coyne, J. Magee, P. Mannion and G. O'Connor, *Proceedings of SPIE*. 4876. 487.

[69] P. T. Mannion, J. Magee, E. Coyne, G. M. O'Connor and T. J. Glynn, Applied Surface Science. 233. (2004), 275.

[70] S. Baudach, J. Bonse, J. Krüger and W. Kautek, Applied Surface Science. 154/155. (2000), 555.

[71] Ashkenasi D. Lorenz M. Stoian R. Rosenfeld A. "Surface damage threshold and structuring of dielectrics using femtosecond laser pulses: the role of incubation". Applied Surface Science 150, 101 – 106, 1999

[72] S. I. Anisimov, A. M. Bonch-Bruevich, M. A. El'yashevich, Y. A. Imas, N. A. Pavlenko and G. S. Romanov, Soviet Physics-JETP. 11. (1967), 945. 131.

[73] S. I. Anisimov, B. L. Kapeliovich and T. L. Perelman, Soviet Physics-JETP. 39. (1974), 375.

[74] T.Q. Qiu, C.L. Tien. "Short-pulse laser heating on metals". International Journal of Heat and Mass Transfer, Volume 35, Issue 3, March 1992, Pages 719–726

[75] B. J. Alder and J. W. Wainwright, Journal of Chemical Physics 31. (1959), 459.

[76] Lewis L. J. Perez D. "Laser ablation with short and ultrashort laser pulses: Basic mechanisms from molecular-dynamics simulations". Applied Surface Science, Volume 255, Issue 10, 1 March 2009, Pages 5101–5106

[77] D. C. Rapaport, ed. *The art of molecular dynamics simulation*. (2004), Cambridge, University Press: Cambridge.

[78] Schafer C. Urbassek H. M. Physical Review B. 66. 2002

[79] P. Rai-choudhury, ed. Handbook of Microlithography, Micromachining, and Microfabracation. (1997), SPIE Optical Engineering Press: Washington, N. P. Mahalik, Micromanufacturing and Nanotechnology. (2006), Berlin: Springer.

[80] G. Mohamed, *MEMS : Design and Fabrication.* (2005), USA: CRC Press.

[81] R. Lipkin, Science News. 144. (1993), 197. E. J. Garcia and J. J. Sniegowski, Proceedings of the Seventh International

Conference on Solid-State Sensors and Actuators (Transducers '93). (1993), 763. E. J. Garcia and J. J. Sniegowski, Sensors and Actuators A. 48. (1995), 203. J. J. Sniegowski and E. J. Garcia, IEEE Electron Device Letters. 17. (1996), 366. A. H. Epstein and S. D. Senturia, Scicence. 276. (1997), 1211. J. Pekola, R. Schoelkopf and J. Ullom, Physics Today. 57. (2004), 41. T. M. Squires and S. R. Quake, Reviews of Modern Physics 77. (2005), 977.

[82] M. Reichling and H. Gronbeck. "Harmonic heat flow in isotropic layered systems and its use for thin film thermal conductivity measurements". . Appl. Phys. 75 (4), 15 February 1994.

[83]Philip D. Rack, Paul H. Holloway. "The structure, device physics, and material properties of thin film electroluminescent displays". Materials Science and Engineering: R: Reports, Volume 21, Issue 4, January 1998, Pages 171–219.

[84] P. F. Baude et al. "Pentacene-based radio-frequency identification circuitry". Appl. Phys. Lett. 82, 3964 (2003).

[85] Peter Peumans, Aharon Yakimov, and Stephen R. Forrest. "Small molecular weight organic thin-film photodetectors and solar cells". J. Appl. Phys. 93, 3693 (2003).

[87] Inzelt G (2008) Conducting polymers a new era in electrochemistry. Monographs in electrochemistry DOI: 10.1007/978-3-540-75930-0

[88] C.G. Granqvist, A. Hultaker. "Transparent and conducting ITO films: new developments and applications". Thin Solid Films 411 (2002) 1–5.

[89] Tindioxide based transparent semiconducting films deposited by the dip-coating technique. Sekhar C Ray, Malay K Karanjai, Dhruba DasGupta

[90] Effects of AFM-based nanomachining process on aluminum surface. Te-Hua Fanga, Win-Jin Changb,

[91] J. W. Lee et al. "Comparison of plasma chemistries for dry etching thin film electroluminescent display materials". J. Vac. Sci. Technol. A 16, 2177 (1998).

[92] J. M. Bustillo et al. "Surface Micromachining for Microelectromechanical Systems". Proc. Of IEEE, Vol. 86, No. 8, 1998.

[93] G. Kovacs et al. "Bulk Micromachining of Silicon". Proc. Of IEEE, Vol. 86, No. 8, 1998

[94] N.J. de Jager, W.J. Perold , U. Büttner. "An effective fabrication method for ultra thin aluminum structures". Thin Solid Films, 520, 1768–1770 2012.

[95] R. G. H. Lammertink et al. "Nanostructured Thin Films of Organic: Organometallic Block Copolymers: One-Step Lithography with Poly(ferrocenylsilanes) by Reactive Ion Etching". Adv. Mater. 2000, 12, No. 2

[96] Xinghua Lia, Takashi Abeb,*, Masayoshi Esashic. "Deep reactive ion etching of Pyrex glass using SF6 plasma". Sensors and Actuators A 87 (2001) 139 – 145.

[97] Kyoung Hwan K. Youn-Kyoung B. Hwan-Jin J. Mohan S. and Hee-Tae J. "Cylindrical posts of Ag/SiO2/Au multi-segment layer patterns for highly efficient surface enhanced Raman scattering". Nanotechnology 23 (2012) 315302 (7pp).

[98] I.W. Rangelow. "Reactive ion etching for high aspect ratio silicon micromachining". Surface and Coatings Technology 97 (1997) 140–150.

[99] E.W. Becker, W. Ehrfeld, P. Hagmann, A. Maner, D. Münchmeyer. "Fabrication of microstructures with high aspect ratios and great structural heights by synchrotron radiation lithography, galvanoforming, and plastic moulding (LIGA process). Microelectronic Engineering, Volume 4, Issue 1, May 1986, Pages 35–56.

[100] Saile V. "LIGA and its Applications". Wiley-VCH 2009.

[101] D. Lim et al. "Fabrication of microfluidic mixers and artificial vasculatures using a high-brightness diode-pumped Nd:YAG laser direct write method". *Lab Chip,* 2003, 3, 318–323.

[102] W Perriea M Gilla G Robinsonb P Fox W O'Neill. "Femtosecond laser micro-structuring of aluminium under helium". Applied Surface Science Volume 230, Issues 1–4, 31 May 2004, Pages 50–59

[103] M. C. Gower, Optical Express. 7. (2000), 56.

[104] Kim K.R. Back K.Y. et al. "A laser selective etching process for Next Generation Flexible Display". Proc. Of the laser microfabrication conference, ICALEO, 2006

[105] M. Halbwax et al. "Micromachining of semiconductor by femtosecond laser for integrated circuit defect analysis". Applied Surface Science 254 (2007) 911–915

[106] Tai-Wook K. "Comparison of multilayer laser scribing of thin film solar cells with femto, pico and nanosecond pulse durations". *Proc. SPIE*. 7409, Thin Film Solar Technology (August 20, 2009)

[107] Martin A. Green et al. "Solar cell efficiency tables (version 39)". Prog. Photovolt: Res. Appl. 2012; 20:12–20

[108] Image taken from www.intellectualtakeout.org on 20/08/2012.

[109] David C. Duffy et al. "Rapid Prototyping of Microfluidic Systems in Poly(dimethylsiloxane)". Anal. Chem. 1998, 70, 4974-4984

[110] Holger Becker, Laurie E. Locascio. "Polymer microfluidic devices". Talanta 56 (2002) 267–287

[111] S. E. Lyshevski, Nano- and Micro- Electonmechanical Systems: Fundamentals of Nano- and Microengineering. (2005), London: CRC Press.

[112] Serap Çelen. "Laser micro-machined semi-slinky like MEMS structures: Novel interface coolers". Optics & Laser Technology, Volume 44, Issue 7, October 2012, Pages 2043–2048.

[113] Yuanyuan Dong, Rajeev Nair, Raathai Molian and Pal Molian. "Femtosecond-pulsed laser micromachining of a 4H–SiC wafer for MEMS pressure sensor diaphragms and via holes". J. Micromech. Microeng. 18 (2008) 035022 (9pp)

[114]Taken from www.prior-ip.cpm Patent Number: 3786907 Country: United States. Issue Date: Jan 22, 1974.

[115] K.G. Watkins, Steen el at. "Laser materials Processing". 3rd Edition, page: 417, Springer, 2010.

[116] Cooper M.I. Emmony D.C. Larson J. Characterization of laser cleaning of limestone, Optics and Laser Technology

Volume 27, Issue 1, February 1995, Pages 69-73

[117] Georgiou S. Zafiropulos V. Anglos D. Balas C. Tornari V. Fotakis, C. "Excimer laser restoration of painted artworks: Procedures, mechanisms and effects". Applied Surface Science, Volume 127-129, May 1998, Pages 738-745.

[118] Moropoulou A. Polikreti K. Ruf V. Deodatis G. "San Francisco Monastery, Quito, Equador: Characterisation of building materials, damage assessment and conservation considerations". Journal of Cultural Heritage, Volume 4, Issue 2, April 2003, Pages 101-108.

[119] Asmus JF, Munk WH, Murphy CG (1973) Studies on the interaction of laser radiation with art artefacts. Proc Soc Photo-Opt Instrum Eng 41:72–76

[120] Zapka W, Zeimlich W, Tam AC. "Efficient pulsed laser removal of 0.2 mm sized particles from a solid surface". Appl Phys Lett, 58:2217, 1991.

[121] Tam AC, Leung WP, Zapka W, Zeimlich W. "Laser cleaning techniques for the removal of surface particulates". J Appl Phys 71:3515 1992.

[122] Asmus JF (1978) Light cleaning – laser technology for surface preparation in the arts. Technol Conserv 13:14.

[123] Steen el at. "Laser materials Processing". 3rd Edition, pages: 419 – 423, Springer, 2010.

[124] Asmus J. F. "MORE LIGHT FOR ART CONSERVATION". IEEE Circuits and Devices Magazine, Volume 2, Issue 2, March 1986, Pages 6-15.

[125] K.G. Watkins, Steen el at. "Laser materials Processing". 3rd Edition, pages 424, Springer, 2010.

[126] Lee JM, Watkins KG (2001) Removal of small particles on silicon wafer by laser-induced airborne plasma shock waves. J Appl Phys 89:6496–6500

[127] Tam AC, Leung WP, Zapka W, Zeimlich W (1992) Laser cleaning techniques for the removal of surface particulates. J Appl Phys 71:3515

[128] K. Imen, S. J. Lee, and S. D. Allen. "Laser-assisted micron scale particle removal". Applied Physics Letters, Volume 58, Issue 2, 1991, Pages 203-205.

[129] Tam AC, Leung WP, Zapka W, Zeimlich W (1992) Laser cleaning techniques for the removal of surface particulates. J Appl Phys 71:3515

[130] S. Pentzien, A. Conradi, R. Koter, J. Krüger. "Cleaning of artificially soiled paper using nanosecond, picosecond and femtosecond laser pulses". Appl Phys A (2010) 101: 441–446.

[131] Siano S. Salimbeni R. "The Gate of Paradise: Physical optimisation of the laser cleaning approach". Studies in Conservation, Vol 46, 4 (2001)

[132] Castillejo M. Martin M. Oujja M. Silva D. Torres R. " Analytical study of the chemical and physical changes induced by KrF laser cleaning of tempera paints". Anal. Chem, 74, 2002

[133] Garbacz H. *et al.* "Effect of laser treatment on the surface of copper alloys". Applied Surface Science, Volume 257, Issue 17, 15 June 2011, Pages 7369-7374

[134] Gaspar P. et al. "A study of the effect of the wavelength in the Q-switched Nd:YAG laser cleaning of gilded wood". Journal of Cultural Heritage 1, 2000

[135] Ostrowski R. Marczak J. Strzelec M. Barcikwski S.. " Nano and microparticles emission during laser cleaning of stone". Proc. SPIE 6598, Laser technology 8: applications of lasers 2007

[136] Comelli D. et al. "Fluorescence lifetime imaging and spectroscopy as tools for non-destructive analysis of works of art". Applied Optics, Vol 43, 10, 2004

[137] Radavn R. et al. "Lasers in the conservation of artworks VIII". CRC press, 2010

[138] Filippidis G. et al. "Nonlinear imaging microscopy techniques as diagnostic tools for art conservation studies". Optics letters, Vol 33, 3 2008

[139] Daurelia G. Chita G. Cinquepalmi M. "New laser cleaning treatments: cleaning, derusting, deoiling, depainting, deoxidising and degreasing". Proc. Of lasers and optics in manufacturing". Paper, 1997

[140] Farsari M. et al. "Clean Art". Industrial laser solutions for manufacturing, 2005

[141] Xiao S. Fernandes S. A. Ostendorf A. "Selective patterning of ITO on flexible PET substrate by 1064nm picosecond laser". Physics Procedia 12, 2011

[142] Zoppel S. Huber H. Reider G.A. "Selective ablation of thin Mo and TCO films with femtosecond laser pulses for structuring thin film solar cells". Applied Physics A, 89, 2007

[143] J. C. C. Fan and J. B. Goodenough, "X-Ray Photoemission Spectroscopy Studies of Sn-doped Indium Oxide Films"Journal of Applied Physics, 48(8), 1977, pp. 3524 - 3531

[144] M. Quaas, C. Eggs, H. Wulff. "Structural studies of ITO thin films with the Rietveld method". Thin Solid Films, Volume 332, Issues 1–2, 2 November 1998, Pages 277–281

[145] N. Balasubramanian and A. Subrahmanyam, "Electrical and Optical Properties of Reactively Evaporated Indium Tin Oxide (ITO) Films - Dependence on Substrate Temperature and Tin Concentration", Journal of Physics D: Applied Physics, 22, 1989, pp. 206 - 209

[146] L. Gupta, A. Mansingh and P. K. Srivastava, "Band Gap Narrowing and the Band Structure of Tin Doped Indium Oxide Films", Thin Solid Films, 176, 1989, pp. 33 - 44

[147] Tindioxide based transparent semiconducting films deposited by the dip-coating technique. Sekhar C Ray, Malay K Karanjai, Dhruba DasGupta

[148] Abdelrazek Elnaggar *et al*. "Picosecond Laser Ablation for the Cleaning of Metal Decorations and Leather of Charles I's 17th C. Gloves". *In press* 2011

[149] K. White. "Oil gilding process". The Carving Path, www.thecarving path.net. Nov. 2010.

[150] Raciukaitis G. Gecys P. Gedvilas M. Regelskis K. and Voisiat B. "Selective Ablation of Thin Films with Picosecond-Pulsed Lasers for Solar Cells". International symposium on High Power Laser ablation, American institute of Physics, 2010.

[151] Molpeceres C. et al. "Microprocessing of ITOand a-Si thin films using ns laser sources". J. Micromech. Microeng 15, 2005.

[152] Yavas O. Takai M. "Effect of substrate absorption on the efficiency of laser patterning of indium tin oxide thin films". J. Applied Physics, Vol 85, 8, 1999

[153] Elim H. & Zhu F. "Carrier concentration dependence of optical Kerr nonlinearity in indium tin oxide films". Applied Physics B, vol 82, issue 3, 439 -442, 2006.

[154] Stoian R. Ashkenasi D. Rosenfeld A. & Campbell E. "Coulomb explosion in ultrashort pulsed laser ablation of Al_2O_3". Phys. Rev. B 62, 13167–13173, 2000

[155] Taken from the "Engineering Toolbox", Engineering toolbox.com

[156] Yagi T. et al. "Analysis on thermal properties of tin doped indium oxide films by picosecond thermoreflectance measurement". Journal of Vacuum Science and Technology A, Vol 23, Issue 4.

[159] Shih-Feng Tseng *et al.* "Laser scribing of indium tin oxide (ITO) thin films deposited on various substrates for touch panels". Applied Surface Science 257 (2010) 1487–1494

[160] D. Liu et al. "High-speed uniform parallel 3D refractive index micro-structuring of poly(methyl methacrylate) for volume phase gratings". Appl Phys B (2010) 101: 817–823

[161] Ambs P. et al. "Spatial light modulators for information processing: Applications and overview". 6th Euro-American workshop on Information Optics, pg 25 – 30, 2007.

[162] Image of solar cell efficiencies taken from National Renewable Energy Laboratory.

[163] Shah A. "Thin-film silicon solar cells". Micro and Nano technology, CRC press, 2010

[164] Matylitsky V. Huber H. Kopf D. "Selective removal of transparent conductive oxide layers with ultrashort laser pulses: front- vs. back-side ablation". International Congress on Applications of Lasers & Electro-Optics, M903: 1022-1027, 2011

[165] Beyer S. Tonrnari V. Gornicki D. "Comparison of laser induced front- and rear side ablation". Proceedings of SPIE, 5063: 202-207, 2002

[166] Powell C. Mallinson F. Allen Z. "Overview of the gilded objects treated for the British Galleries". Conservation Journal, Autumn 2001, Issue 39

[167] Dabrowa B. "The conservation of three gilded frames for the new paintings galleries at the Victoria and Albert Museum". Conservation Journal, Spring 2004, Issue 46

[168] Castillejo M. "Analytical Study of the Chemical and Physical Changes Induced by KrF Laser Cleaning of Tempera Paints". Anal. Chem. 2002, 74, 4662-4671